THE ROLE OF RHODIUM IN THE ANDRUSSOW PROCESS

C.R. BICKNELL

A thesis submitted in partial fulfilment of the requirements of The Nottingham Trent University for the degree of Doctor of Philosophy

August 1997

ABSTRACT

The Andrussow process is used industrially to synthesise hydrogen cyanide from methane, air and ammonia using a multilayer platinum-rhodium gauze catalyst.

$$CH_4 + NH_3 + 1\ ^1/_2\ O_2 \rightarrow HCN + 3\ H_2O$$

Oxygen conversion is normally complete. The reaction is, however, normally < 65% selective with by-products including H_2 CO, CO_2 and N_2. When using a fresh platinum-rhodium catalyst, the initial selectivity to HCN is normally low but selectivity increases with time to reach a maximum of 65% (from methane) and then decays until renewal of the gauze pack is required. The catalyst pack undergoes extensive restructuring during the activation process. The role of rhodium is not well understood either in terms of peak selectivity or on its effect on activation. The above reaction was, therefore, studied by constructing and using a laboratory microreactor to

(a) measure the effect of rhodium concentration on peak selectivity.
(b) measure the effect of rhodium concentration on the activation of gauze catalysts.
(c) prepare samples of partially and fully activated catalyst for characterisation.

Microreactor results of fully activated catalysts show that the selectivity to HCN from methane and ammonia for the pure platinum catalysts is greater than for rhodium containing catalysts. Pure platinum catalysts are, however, less active than rhodium containing catalysts and require the furnace which surrounds the reactor tube to be at a higher temperature to reach peak selectivity. Although pure platinum catalysts are less active than platinum-rhodium catalysts, through changing the furnace temperature the maximum HCN yield for pure platinum catalysts, at 55% was 10% higher than the maximum yield of HCN for platinum-rhodium catalysts.

Activation studies show that pure platinum gauze catalysts have a high initial selectivity to HCN but show little further activation. Under the activation conditions investigated platinum-rhodium catalysts exhibit a low initial selectivity to HCN, but after an activation period of ca. 30 hours, have a selectivity within 2 % of the selectivity of pure platinum catalysts.

Characterisation of catalysts throughout the activation process shows that the activation process is essentially independent of catalyst morphology. The surface rhodium concentration of unused platinum-rhodium gauze catalysts is above the bulk concentration but during the activation process the surface concentration of rhodium decreases to below the bulk concentration. The rhodium surface concentration after extensive activation is found to be within experimental error of published values for atomically clean alloy surfaces.

Characterisation of a catalyst removed from an industrial reactor shows that the formation of a multilayer thickness of carbon occurs and, due to a simple site blocking mechanism, may be a factor in the deactivation of platinum-rhodium catalysts under industrial conditions.

ACKNOWLEDGEMENTS

Firstly I wish to thank my academic supervisor Prof. Richard Joyner and my Industrial supervisors Dr. Sean Axon and Steve Frank for their guidance over the past few years. I also wish to thank ICI Acrylics R&T and the EPSRC for funding the project. Other people who have taken an active part in the project, to whom I am indebted include -

Dr. D. Briggs and Dr. I Fletcher for their involvement in time of flight secondary ion mass spectrometry and Dr. Peter Beahan and Dr. David Batchelor for their involvement with the scanning Auger microscopy. I wish to thank my family who have had to put up with me when things have not been going my way. I also want to thank my co-workers at the Leverhulme Centre, Liverpool University and at the Catalysis Research Laboratory, Nottingham Trent University for the help they have given me.

1. INTRODUCTION

2. MICROREACTOR DESIGN

5. CHARACTERISATION - UNUSED GAUZE

6. CHARACTERISATION - INDUSTRIAL SAMPLES

7. CHARACTERISATION - LABORATORY SAMPLES

1. Introduction

1.1 General Introduction

Of particular interest to industrialists is the functionalisation of light saturated hydrocarbons (from natural gas) to form reactive feedstocks for chemical manufacture. At present, the major use of methane within industry is as a fuel, primarily due to the technical difficulties in activating the molecule.

The simplest, and usually the cheapest method of functionalising a saturated hydrocarbon is to carry out a partial oxidation. This can result in several possible products such as an unsaturated alkene (oxidative dehydrogenation), or a more esoteric structure like the formation of maleic anhydride from butane. At present, there are three main types of process utilising methane as a feed, the oxidation processes for the production of hydrogen cyanide and acetylene, the chlorination or oxychlorination processes for the production of chloromethanes and the steam reforming process for the production of syngas. Of these, the most widespread is the reforming process for the production of hydrogen and carbon oxides from methane. Downstream processing results in a wide range of possible products from ammonia, as in the Haber process, to gasoline via the methanol synthesis and methanol to gasoline processes.

Currently there are few selective oxidation processes that utilise methane as a feed, primarily due to the fact that methane is very stable and therefore commonly requires very high temperatures to activate the molecule. The stability of methane is primarily caused by its saturated nature i.e. the lack of empty π^* orbitals into which donation of electrons may occur. The stability of methane almost certainly means that any partial oxidation products, such as methanol, are likely to be much more reactive than methane itself. This indicates that kinetic control of reaction products is crucial in the successful utilisation of methane in partial oxidation situations where the partial oxidation product may react further.

One of the few processes that have successfully used methane as a feed is the Degussa process, whereby hydrogen cyanide is manufactured from ammonia and methane. The process is notable as the selectivities from methane are high at 90+%. This is primarily due to the simplicity of the chemistry - the reaction proceeds via the endothermic dehydrogenation of the feeds and subsequent surface reaction between nitrogen and carbon containing surface species. The Degussa process is described by equation 1.1.

$$CH_4 + NH_3 \rightarrow HCN + 3\,H_2 \qquad \Delta H = 252\ kJ\ mol^{-1}$$

Equation 1.1: The Endothermic Formation Of Hydrogen Cyanide From Methane And Ammonia

In the Degussa process, the catalyst is deposited onto the inside wall of a ceramic tube. The reactor tube is then held within a furnace at ca. 1500K. The reactant gas is fed through the reactor tube which is normally ca. 2 cm in diameter and 2 m long. The first and last 25% of the length are the heating and cooling portions and much of the reaction occurs in the centre of the tube. Typically, the rate limiting factor becomes the transfer of heat from the furnace to the tubes. Typical composition of the reactor product is as shown below.

HCN	NH_3	CH_4	H_2	N_2
23	2.7	2.4	71.2	0.9

Table 1.1: Typical Exit Gas Composition For The Degussa Process (vol. %).

The financial success of the Degussa process, which is technically very difficult to carry out, due to the materials problems with heat transfer at such high temperatures, is critically dependant on utilisation of the liberated hydrogen.

An alternative method for the production of hydrogen cyanide from methane and ammonia is the Andrussow process where oxygen is also added to the reactant mixture. Here, the reactant gases are mixed and passed over a platinum-rhodium gauze catalyst of similar form and composition as those used for ammonia oxidation. The reaction is highly exothermic, removing the need for external heating of the catalyst. The Andrussow reaction is shown in equation 1.2. Other than the steam reforming process, the Andrussow process is by far the most industrially important process utilising methane as a feedstock, and the process dominates the industrial production of hydrogen cyanide world-wide.

$$CH_4 + NH_3 + 1\ ^1/_2\ O_2 \rightarrow HCN + 3\ H_2O\ \Delta H = -482\ kJmol^{-1}$$

Equation 1.2 : The Andrussow Reaction - The Formation Of Hydrogen Cyanide From Methane, Ammonia and Air.

In comparison with the Degussa process, the Andrussow process has a major technical advantage, as the temperatures required for the formation of hydrogen cyanide are supplied by the partial oxidation process, alleviating the need for a furnace to heat the catalyst. Indeed the Andrussow reactor commonly operates at an adiabatic temperature of 1350 K or more. The exit gases must, however, be cooled quickly to prevent secondary reaction. Heat removal is achieved by placing a heat exchanger immediately below the reactor and a by-product of the process is a great deal of high temperature steam from the heat exchanger. Once the HCN product has been removed, further heat is liberated by burning the remaining product gas which contains mainly N_2, H_2 and CO.

Under normal operating conditions, using a multilayer pack of platinum-rhodium gauze catalyst, the reaction is between 60 and 80% selective for hydrogen cyanide from ammonia. As the conversions for methane are > 95% and > 85% for ammonia, the yields are correspondingly high, at 55-75% (from ammonia).

HCN	NH_3	CO_2	CO	CH_4	H_2	O_2	N_2	H_2O
5.9	1.6	0.4	4.4	0.5	7.5	0.1	56.7	23

Table 1.2: Typical Exit Gas Composition For The Andrussow Process (vol. %).

The stoichiometric air requirement for the Andrussow process is 1.5 moles of oxygen per mole of methane assuming a 1:1 ratio of methane to ammonia. Feed gas mixtures are typically around 1.1:1 oxygen to methane, as these conditions give the highest yields of HCN. The reactor is, therefore, operating under highly reducing conditions, a fact that is demonstrated by the high concentration of hydrogen and carbon monoxide in the products and almost complete oxygen conversion.

In industry the reaction proceeds over a bed of platinum-rhodium gauze catalyst which may be in excess of 4 metres in diameter and between 0.5 and 3 centimetres deep. The catalyst of choice is currently a 90% Pt - 10% Rh alloy (82.6 atomic% Pt, 17.4 atomic% Rh), supplied in woven sheets with a wire diameter of either 60 or 72 μm. The weave density of the sheets is very high and typically there are 13 wires per

centimetre in both weave directions. The reactants, at a pressure of up to 2 bar absolute, are passed over the gauze at a velocity of ca. 1 metre per second. With corrections for changes in temperature from ambient to 1350 K, and the void fraction, this equates to a contact time of less than 1 millisecond.

A number of alternative catalyst systems have been investigated, including platinum supported on beryl[1] and platinum supported on alumina monoliths[2], but these catalyst systems are not as selective as the gauze catalysts and as such their use in industry is rare. It is interesting, however, that that all formulations use platinum as the active component, and it may be a unique property of platinum that allows the selective formation of hydrogen cyanide. An outline of the process is shown below -

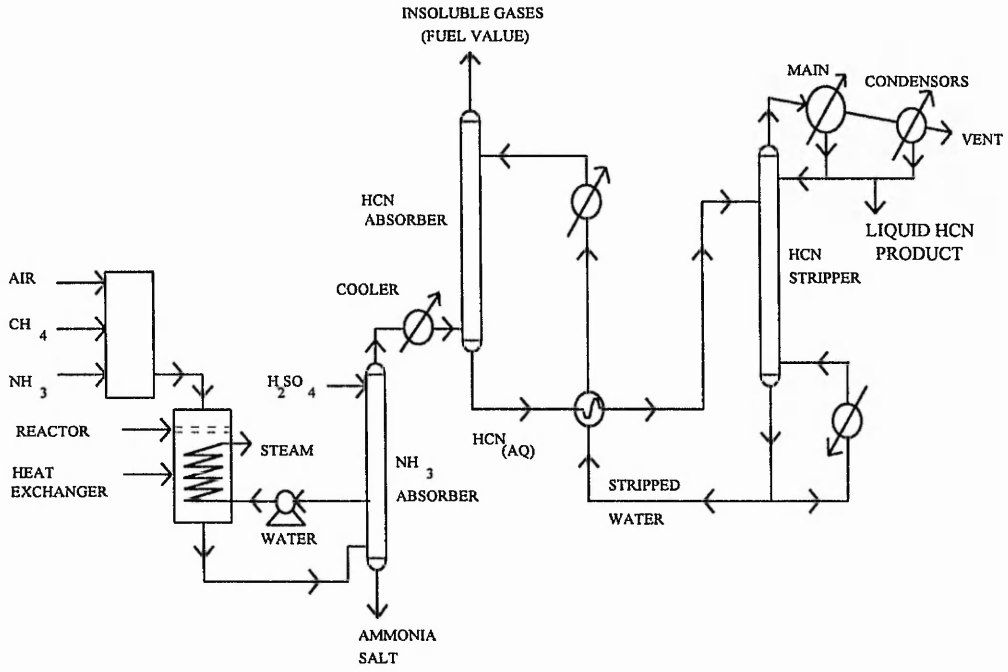

Figure 1.1: The Andrussow Process

The HCN production plant is commonly integrated into a process for HCN utilisation, such as a methyl methacrylate plant or a potassium cyanide plant, to minimise transport and storage.

At present the utilisation of hydrogen cyanide varies globally, but the production of methyl methacrylate is significant irrespective of region.

Further hydrogen cyanide is produced in the SOHIO process, where propene, steam, ammonia and air are passed over a bismuth molybdate or uranium antimonate catalyst at between 693 and 773K[3]. The major product (> 75 %) is acrylonitrile, but during this process, hydrogen cyanide is produced in considerable quantities (up to 0.1 lb. / lb. acrylonitrile). Once separated however, this material is normally sold and adds value to the process. As the European production figure for acrylonitrile is approximately 0.9 Mt., this indicates a significant level of hydrogen cyanide production (0.09 Mt.)

$$C_3H_6 + NH_3 + 1\,{}^1/_2\,O_2 \rightarrow CH_2{=}CHCN + 3\,H_2O$$

Equation 1.3: The Formation of Acrylonitrile From Propene, Air and Ammonia (The SOHIO Process).

Possible new routes to HCN have been investigated recently, including the use of microwave heating of the catalyst[4] and the use of a fuel cell reactor[5], although neither process is near large scale industrial application. An interesting factor in the future, however, seems to be the reluctance of suppliers to transport hydrogen cyanide. This is primarily due to the toxic risks associated with HCN and at some time small scale preparation of HCN from methane and ammonia may become more industrially feasible. These plant are unlikely to be based around Andrussow technology due to the complexity of the process, but based on new technology, such as microwave heating of the catalyst, or the scale down of the Degussa process.

1.2 Thermodynamics Of Hydrogen Cyanide Synthesis

The synthesis of HCN from methane and ammonia is highly endothermic, whereas the synthesis from air, methane and ammonia is highly exothermic. The two idealised equations (i.e. 100% selectivities) are shown below.

$$CH_4 + NH_3 \rightarrow HCN + 3\,H_2 \qquad \Delta H^{298} = 252\ kJ\ mol^{-1} \qquad (i)$$

$$CH_4 + NH_3 + 1\,{}^1/_2\,O_2 \rightarrow HCN + 3\,H_2O \qquad \Delta H^{298} = -473\ kJ\ mol^{-1} \qquad (ii)$$

Equation 1.4: The Thermodynamics of HCN Formation - (i) The Degussa Process (ii) The Andrussow Process.

The oxidative process is thermodynamically favourable in the range of 300-1600K, with a Gibbs free energy change in the range of -500 to -600 kJ mol^{-1}. The non oxidative process has a strikingly different thermodynamic behaviour, with a broad range of Gibbs energies exhibited over the same temperature range. Here the reaction is highly unfavourable at low temperatures, exhibited by a large +ve Gibbs free energy, until a temperature in excess of 1000K is attained[#]. Above 1000K, the reaction becomes more and more favourable until at 1500K, the equilibrium predicts almost total conversion of methane and ammonia to hydrogen cyanide and hydrogen. Figures 1.2 and 1.3 describe the thermodynamics of the $CH_4 + NH_3 \rightarrow HCN + 3\ H_2$ reaction.

Effect of Temperature On Methane and Ammonia Conversion For the Degussa Process

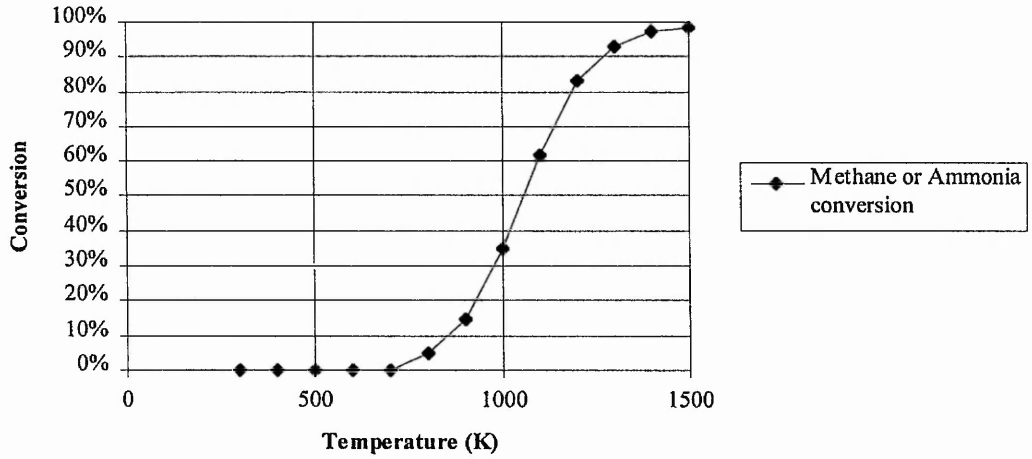

Figure 1.2: The Relationship Between Temperature and Conversion For the Degussa Process. The calculation is based only on the thermodynamics of the $CH_4 + NH_3 \rightarrow HCN + 3\ H_2$ reaction.

[#] All the thermodynamic calculations were performed on a PC running the IVTAN thermodynamics database. Published by CRC Press, Inc. (1993)

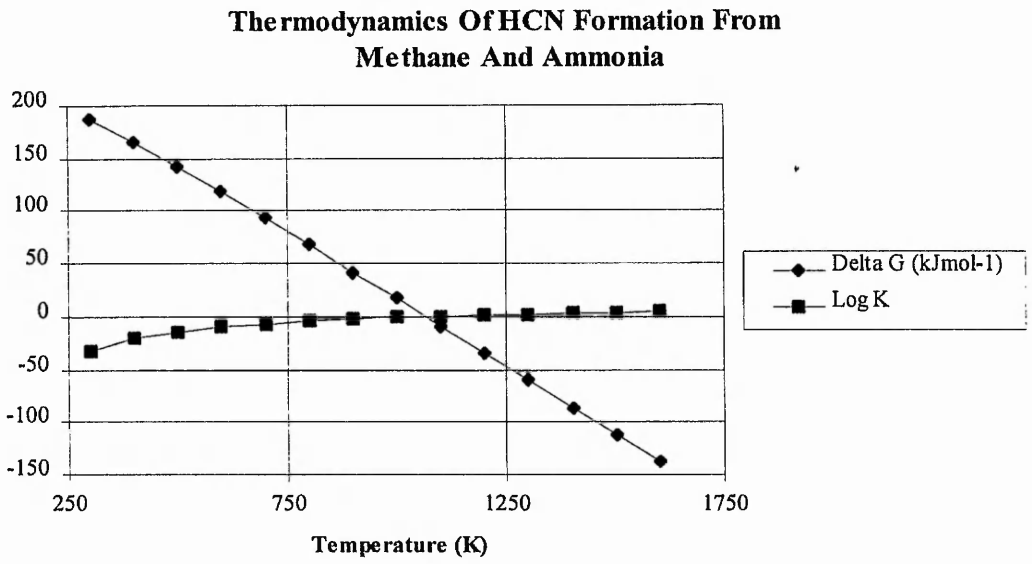

Where $K = \frac{[HCN][H_2]^3}{[CH_4][NH_3]}$ - The thermodynamic equilibrium as described by the Gibbs free energy equation.

Figure 1.3: Thermodynamics of the reaction between methane and ammonia - The Degussa process

The decomposition reaction of ammonia is also thermodynamically favourable at high temperature, and indicates that for high yields of HCN, the product distribution must be under kinetic control.

The reactions taking place in the Andrussow reactor are more complex, and there are a large number of possible products, most of which are even more thermodynamically favourable. Notable examples are the combustion products of methane and the hydrolysis reaction between hydrogen cyanide and water as shown in equation 1.5.

$CH_4 + {}^1/_2\ O_2 \rightarrow CO + 2\ H_2$	$\Delta H^{1300} = -23$	kJ mol^{-1}
	$\Delta G^{1300} = -278$	kJ mol^{-1}
$CH_4 + O_2 \rightarrow CO_2 + 2\ H_2$	$\Delta H^{1300} = -304$	kJmol^{-1}
	$\Delta G^{1300} = -448$	kJ mol^{-1}
$HCN + H_2O \rightarrow CO + NH_3$	$\Delta H^{1300} = -50$	kJ mol^{-1}
	$\Delta G^{1300} = -42$	kJ mol^{-1}
$2\ HCN + 2\ {}^1/_2\ O_2 \rightarrow 2\ CO_2 + N_2 + H_2O$	$\Delta H^{1300} = -1299$	kJ mol^{-1}
	$\Delta G^{1300} = -1164$	kJ mol^{-1}

Equation 1.5: Possible Side Reactions in the Andrussow Process

The process must therefore be under kinetic control if there is to be any significant hydrogen cyanide in the product stream.

1.3 Kinetics And Mechanism Of Hydrogen Cyanide Synthesis

1.3.1 Kinetics

Kinetic profiling of the elementary steps involved in Andrussow reaction is a formidable task. This is primarily due to the large number of possible reactions that may take place in this complex system. In the absence of oxygen, the reaction is much simplified.

1.3.1.1 In The Absence of Oxygen

Hasenberg and Schmidt investigated the mechanism and kinetics of the formation of hydrogen cyanide from methane and ammonia. The experiment was carried out exposing a foil of high purity platinum[6] or rhodium[7] to ammonia and methane at temperatures between 300 and 1500 K.

They showed that, in the absence of oxygen, two surface reactions were significant -

$$CH_4 + NH_3 \rightarrow HCN + 3\,H_2$$

$$NH_3 \rightarrow {}^1/_2\,N_2 + {}^3/_2\,H_2$$

Equation 1.6 : Significant Reactions In The Degussa Reaction

The observed rates were correlated semi-quantitatively over a fairly wide range of compositions and temperatures by the use of modified Langmuir Hinshelwood kinetic expressions.

$$r_{HCN} = k_{HCN}\theta_c(1-\theta_c)^n P_{NH_3}$$

$$= \frac{K_1 P_{CH_4} P_{NH_3}^{1/2}}{(1+K_2 P_{CH_4} / P_{NH_3}^{1/2})^{n+1}}$$

$$r_{H_2} = K_2(1-\theta_c)^n P_{NH_3}$$

$$= \frac{K_3 P_{NH_3}}{(1+K_2 P_{CH_4} / P_{NH_3}^{1/2})^n}$$

θ_C	=	Surface carbon species
n	=	Number of vacant sites required for NH_3 adsorption.
K_X	=	Groupings of temperature dependent rate coefficients and equilibrium coefficients.
$(1-\theta_C)^n$	=	Assumption of site blocking. n = 3 for platinum, n = 4 for rhodium.

Equation 1.7 : Langmuir Hinshelwood Kinetic Modelling For The Degussa Process

From this work the main conclusion was that kinetics of HCN synthesis for the two metals was very similar. The reported activation energies for the two metals (taken between 1100 and 1450 K) are as follows.

Activation energy for HCN on rhodium = 14.6 kJ mol^{-1}
Activation energy for HCN on platinum = 18.1 kJ mol^{-1}

Activation energy for ammonia decomposition on platinum = 18.9 kJ mol^{-1}
Activation energy for ammonia decomposition on rhodium = 18.9 kJ mol^{-1}

From the activation energies they measured, they conclude that the mechanism is the same on both metals. The methane dependence on r_{HCN} varies from first order at low P_{CH4} to negative third order at high P_{CH4}. The role of surface carbon has also been shown by this work. Exposure to methane at elevated temperatures results in multilayer carbon formation, and therefore deactivation, but exposure to a mixture of methane and ammonia yields a surface that has been shown by Auger spectroscopy to be covered with less than a monolayer of carbon. From kinetic rate measurements and TPD experiments, this carbon layer has been shown to inhibit ammonia decomposition, but the coverage of carbon itself, is controlled by the presence of ammonia.

$$\theta_c = \frac{KP_{CH_4} / P_{NH_3}^{0.5}}{1 + KP_{CH_4} / P_{NH_3}^{0.5}}$$

Equation 1.8: The Dependence of Surface Coverage on Methane and Ammonia Partial Pressures

Therefore, on an active surface, there is only a maximum of a monolayer of adsorbed carbon. Ammonia is responsible for regulating the build-up of carbon, and it is this that enables the reaction to proceed without massive carbon build-up. In summary, surface carbon is responsible for inhibition of ammonia decomposition but also promotes HCN formation by reacting with nitrogen containing surface intermediates.

1.3.1.2 In The Presence Of Oxygen

From a complex evaluation of kinetic behaviour in the three component system, (air, methane and ammonia), the following reactions have been identified as possibly significant in the Andrussow process[8-9].

1. $NH_3 \rightarrow {}^3/_2\ H_2 + {}^1/_2\ N_2$
2. $NH_3 + CH_4 \rightarrow HCN + 3\ H_2$
3. $NH_3 + 1\ {}^1/_4\ O_2 \rightarrow NO + 1\ {}^1/_2\ H_2O$
4. $NH_3 + 1\ {}^1/_2\ NO \rightarrow 1\ {}^1/_4\ N_2 + 1\ {}^1/_2\ H_2O$
5. ${}^1/_2\ O_2 + H_2 \rightarrow H_2O$
6. $CH_4 + 1\ {}^1/_2\ O_2 \rightarrow CO + 2\ H_2O$
7. $NO + H_2 \rightarrow {}^1/_2\ N_2 + H_2O$
8. $NO \rightarrow {}^1/_2\ N_2 + {}^1/_2\ O_2$
9. $NO + CO \rightarrow {}^1/_2\ N_2 + CO_2$
10. $CO + {}^1/_2\ O_2 \rightarrow CO_2$
11. $CH_4 + NO \rightarrow HCN + {}^1/_2\ H_2 + H_2O$
12. $CO + H_2O \rightarrow CO_2 + H_2$
13. $CH_4 + 3\ NO \rightarrow 1\ {}^1/_2\ N_2 + CO + 2\ H_2O$

Equation 1.9: Reactions Used in the Waletzco & Schmidt Kinetic Model (ref. 9) for HCN Synthesis From Air, Methane and Ammonia (1-13)

It is, however, apparent that the hydrolysis reaction between HCN and water is significant, and recently the kinetic model used by Waletzko and Schmidt has been modified to include this reaction[10] -

14. $HCN + H_2O \rightarrow CO + NH_3$

Kinetic evaluations of the above reaction indicate that the rate of hydrolysis is a function of temperature (T), and the gas phase concentrations of both HCN and water.

From the full kinetic model, the following has been concluded -

1. The major reaction for the formation of hydrogen cyanide appears to be the reaction between CH_4 and NH_3. This work also showed that oxygen reacts faster with NH_3 to form NO than with CH_4 to form CO, but under higher conversions, NO may react with CH_4 to form hydrogen cyanide.

2. Oxygen conversion is approaching completion very early in the gauze pack.

3. The other major conclusion from this work was that due to the high rates involved, diffusion limitations may have a significant influence on observed product distribution.

This work has been backed up by work carried out at atmospheric pressure by Suarez and Loffler[11]. They conclude that surface diffusion or surface reaction is indeed the rate limiting factor in this very fast reaction. Further work using a solid electrolyte cell reactor[12] by Kiratzis *et al.* used the distinctly unusual properties of a solid electrolyte cell reactor to investigate the role of oxygen in the HCN synthesis process. They report very similar kinetics of HCN synthesis agreeing to within 10% of the Schmidt and Walezco model. In this work, the reactor design, and the use of a platinum catalyst, enabled the reaction to proceed anaerobically (i.e. the Degussa process), with the addition of gaseous oxygen (i.e. a supported platinum catalyst for the Andrussow process) or in the presence of electrochemical oxygen (a novel reactor). Results show that there was no effect of oxygen, either in the gaseous form or in the electrochemical form, resulting in a linear relationship between $P_{CH4}*P_{NH3}$ and rate of HCN production for all three experiments.

1.3.2 Mechanistic Studies

1.3.2.1 Homogeneous Vs. Heterogeneous Reaction Mechanism

The reaction between oxygen, ammonia and methane is very exothermic and results in high adiabatic temperatures. The reaction is also very fast and there is some debate on whether the reaction is predominantly homogeneous or heterogeneous. As the rate of an homogeneous reaction is known to increase with pressure, Dietz[13] *et al.* investigated the effect of pressure on the product distribution in the Andrussow reaction using a lab scale reactor and pressures varying between atmospheric and 6.5 atmospheres. In this work, they noted that as the pressure increased, the selectivity decreased from 85% (from ammonia) to 76%. The reactor was kept at 1373 K but due to constant mass flow, the residence times were correspondingly longer for higher pressures. The conclusion from this work was that, due to the small change in selectivity with pressure, the reaction was predominantly heterogeneous in nature.

1.3.2.2 Model Studies

During the reaction between methane and ammonia over a platinum / rhodium catalyst, it is proposed that dehydrogenation of methane and ammonia are significant reaction steps. Although not detected in the products of reaction, methylamine could be a possible intermediate and has therefore been used by researchers in investigating the mechanism for HCN formation.

In work by Cordonier and Schmidt[14], methylamine was dosed onto clean single crystal surfaces of platinum and rhodium. After a methylamine exposure of $10*10^{-6}$ torr seconds (10 Langmuirs) at 300K, the surface was shown via Auger spectroscopy to be extensively covered with carbon and nitrogen containing species. Temperature Programmed Desorption (TPD) studies indicate that the methylamine dehydrogenates at 500 K on both Pt(111) and Rh(111). HCN desorbs slightly above this temperature and corresponds to a total removal of hydrogen from the surface. The remaining species (*surface*: Pt/Rh}----CN) is very stable on both metals, but more so on platinum, at 1100 K no evolution of any species is noted for Rh(111) but C_2N_2 is still desorbing from the surface of Pt(111) well above this temperature. Evidence was also obtained to show that there is a difference in the reactivity to dehydrogenation between Pt(111) and Rh(111)[15]. The H_xCN species from methylamine dehydrogenates at between 320 and 600 K on Pt(111) whereas for Rh(111), dehydrogenation occurs at between 300 and 460 K. Comparisons between the two metals for the decomposition pathway to N_2 and surface carbon species suggests that the major difference is their ability to cleave the C-N bond. Under low doses, the Rh(111) surface was capable of cleaving approximately 40% of the C-N bond whereas the Pt(111) surface showed no C-N bond cleavage activity. This indicates the increased stability of *surface*-CN on the Pt(111) surface over the rhodium surface, and may be responsible for the additional selectivity of Pt over Rh surfaces.

The proposed mechanism via a methylamine type species is backed up by recent work[16] by Jentz *et al.* who dosed a surface with hydrogen cyanide and observed the surface species by Fourier transform-infrared absorption spectroscopy (FT-IRAS). They found that HCN dissociatively adsorbs molecularly at 85 K but between 300 K and 450 K, IR bands consistent with aminomethylidyne were observed. The following mechanism is proposed -

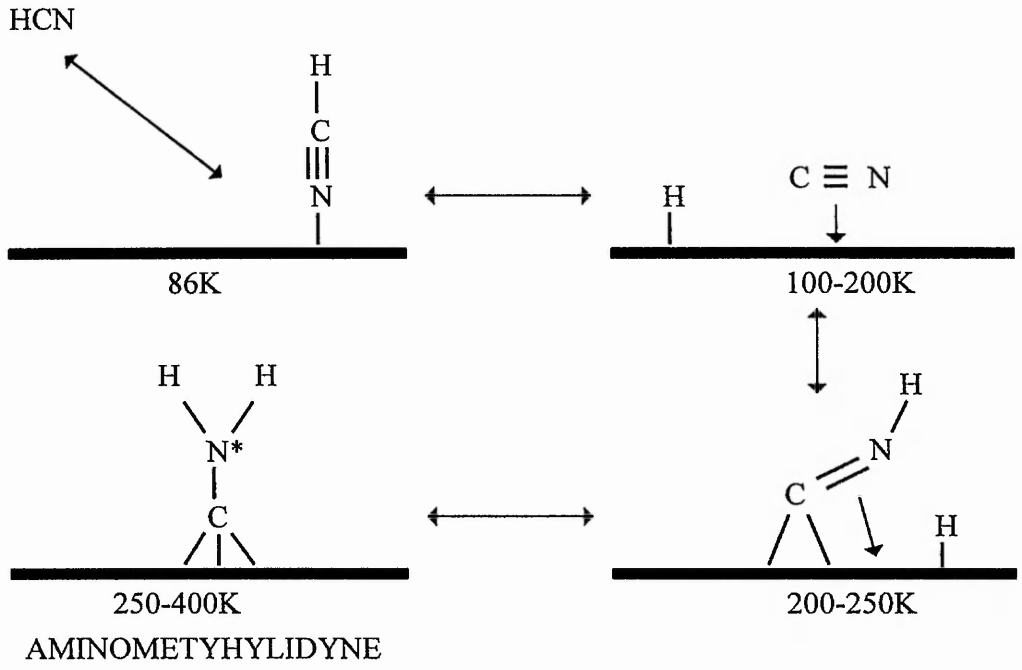

* The CN bond has some double bond character since the frequency of the observed C-N stretch is intermediate between that characteristic of a CN single and double bond.

Figure 1.4: Proposed Reaction Scheme For the Molecular Transformation Of HCN on Pt(111). From ref.16.

The oxidative dehydrogenation of methane to produce syngas over platinum and rhodium catalysts has been investigated[17]. In this work, monolith supported platinum and rhodium were tested for the following reaction -

$$CH_4 + {}^1/_2\, O_2 \rightarrow CO + 2\, H_2 \quad \Delta H = -35.7\ kJ\ mol^{-1}$$

Equation 1.10: The direct formation of syngas from methane and air.

The selectivity of the above reaction to CO and H_2 was shown to be strongly dependent on the catalytic metal used, and in comparing platinum with rhodium, rhodium was found to be significantly more active and selective than platinum. Under identical conditions, the following results were obtained by Schmdt *et al.*[18] -

	Conversion %	Selectivity to H_2 %	Selectivity to CO %
Platinum	67	78	94
Rhodium	80	90	96

Table 1.3: Selectivities and Conversions For Syngas Manufacture From Methane.

The superiority of the rhodium catalyst was attributed to be due to differences in stability of the *surface* --- OH bond. On rhodium, the OH bond is less stable, and therefore less water is produced. This result correlates with the results observed for HCN manufacture in that for high HCN yield, the activity of the catalyst towards water formation must be high. Consequently, a catalyst that is good at syngas manufacture is likely to be poor at HCN synthesis.

Hydrogen is produced by the dehydrogenation of both methane and ammonia, and efficient oxidation is vital to reduce oxygen levels to prevent oxidation of HCN. The mechanism and kinetics of the formation of water from hydrogen and oxygen has been investigated by Zum Mallen *et al.*[19] and Williams *et al.*[20]. From this work, they conclude that the activation energy for the formation of water from hydrogen and oxygen is significantly different on Rh and Pt. The proposed potential energy diagrams for the oxidation process are shown in figures 1.5 and 1.6. Their results indicate that the activation passes through significantly different profiles. For example, on rhodium, the activation energy for the formation of adsorbed hydroxyl (OH(ads)) from an adsorbed oxygen atom (O(ads)) and an adsorbed hydrogen atom (H(ads)) is large at 84 kJ mol^{-1}, whereas for platinum, the activation energy is much lower at 10 kJ mol^{-1}. The roles are, however, reversed when looking at the next stage in the process - the reaction between OH(ads) and H(ads) to form H2O(ads). Here the activation energy for platinum is high at 63 kJ mol^{-1}, whereas for rhodium, the activation energy is low at 33 kJ mol^{-1}. Assuming that the kinetics of the reaction between O(ads) (or OH(ads)) and H(ads) is the rate determining step, the greater activation energy for the rhodium-catalysed reaction, at 84 kJ mol^{-1} in comparison with the platinum-catalysed reaction at 63 kJ mol^{-1} indicates that platinum is likely to be superior to rhodium at the oxidation of hydrogen. As the oxidation of hydrogen is an essential stage in the oxidation of methane and ammonia, this will have an effect on the product distribution and may help to explain the observed product distributions.

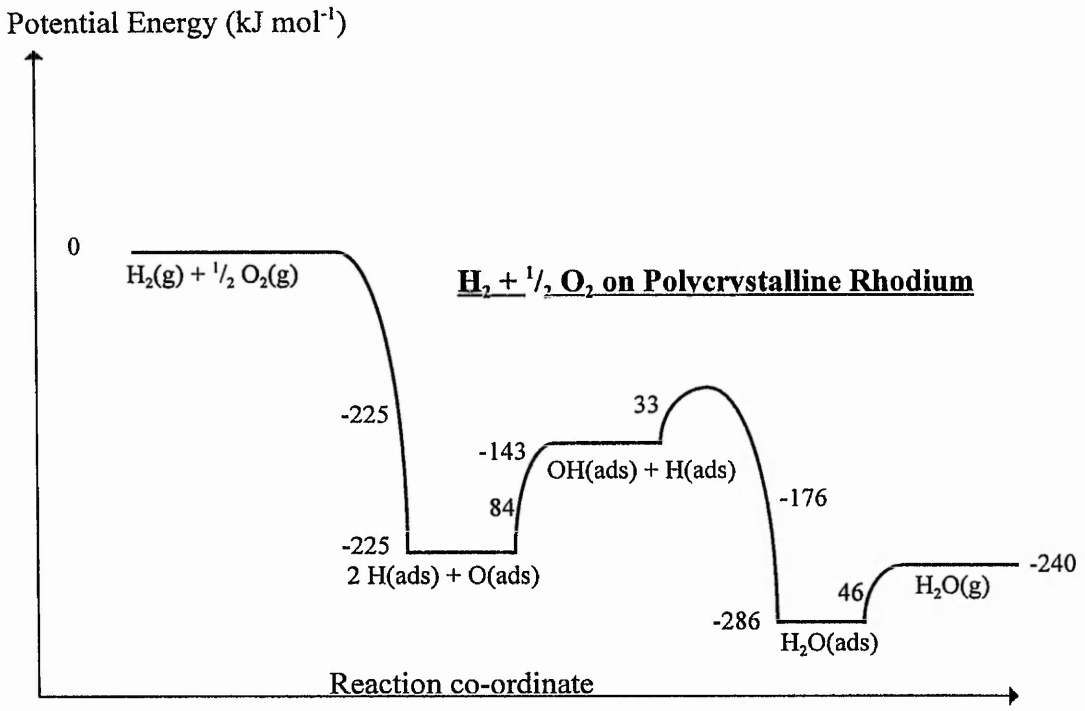

Figure 1.5: The Thermodynamics of Hydrogen Oxidation over Polycrystalline Rhodium.

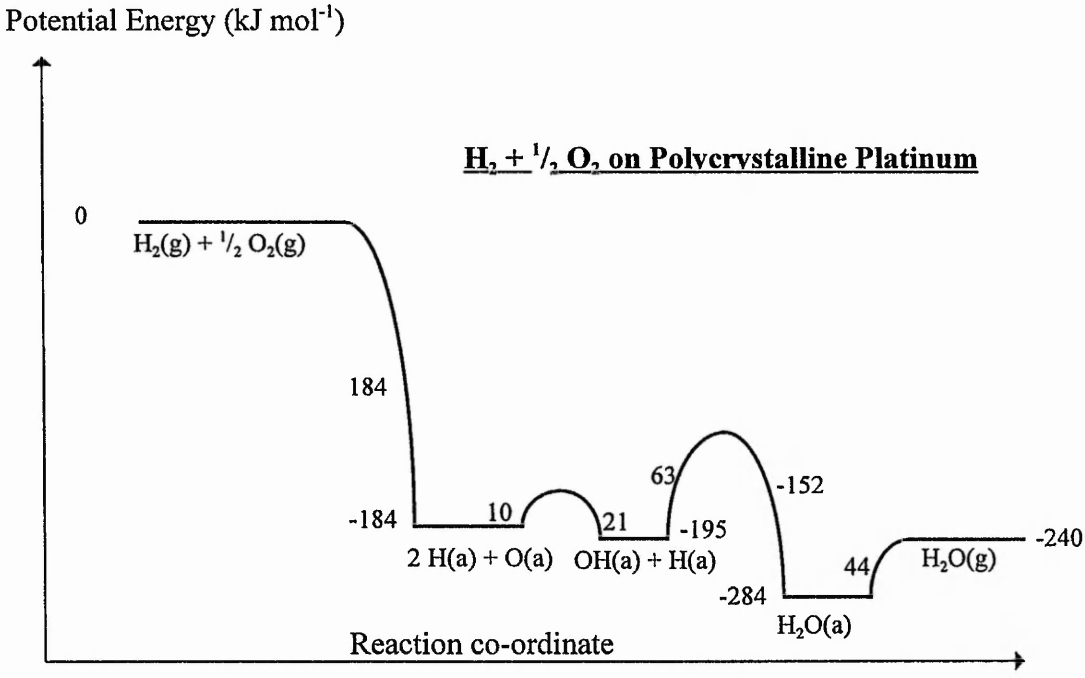

Figure 1.6: The Thermodynamics of Hydrogen Oxidation over Polycrystalline Platinum.

The conclusion of this work is that the mechanistic studies carried out both on single crystal surfaces and on polycrystalline surfaces indicates that rhodium is likely to be detrimental to HCN selectivity.

In summary -

1. The C-N bond is less stable on Rh than Pt.
2. H_2 is produced by the dehydrogenation of the feeds CH_4 and NH_3 and since H_2 oxidation has a lower activation energy on platinum than rhodium, the formation of water is likely to be faster on platinum than rhodium. As oxygen is consumed by the formation of water, and oxygen conversion is always essentially complete, by mass balance, any reduction in H_2O selectivity **must** result in an increase in the levels of carbon oxides and therefore a decrease in HCN selectivity.

1.4 The Catalyst In Hydrogen Cyanide Synthesis

1.4.1 General Properties of Platinum-Rhodium Alloy Catalysts

Platinum, platinum group metals, and their alloys have been utilised commercially in many oxidative roles, the most common being the three way exhaust catalyst where the catalyst performs the oxidation of CO, the oxidation of unburnt hydrocarbons and performs the reduction of NO_x by CO. The major advantage of platinum group metals over other metals is their ability to retain their metallic nature under highly oxidising conditions which would cause bulk oxidation of virtually all other metals. This is responsible for their high reactivity as metal surfaces are well known as being highly active catalysts in comparison with oxides, primarily due to their high surface free energy and thus ability to activate adsorbates.

1.4.2 The Role Of Rhodium

At present, the gauzes used in the Andrussow process have the same composition and structure as those used in ammonia oxidation[21] and usually contain 10% by weight of rhodium (17.4at% Rh). In the ammonia oxidation process, the benefits of rhodium addition are as follows -

- ***Increased Selectivity and Conversion*** - The addition of rhodium is reported to increase selectivity and conversion during ammonia oxidation[22].

- ***Physical Strengthening*** - The alloying of platinum-rhodium results in a much stronger gauze. This eases fabrication of the gauze and reduces the likelihood of tears forming in the gauze during use[23].
- ***Reducing Platinum Losses*** - The addition of rhodium reduces the losses of volatile platinum oxides, especially when operating under pressure. By contrast, precious metal losses in the Andrussow process are minimal[24-25].

Although there has been much published on the differences between rhodium and platinum surfaces under ultra high vacuum conditions, showing clear differences between the two metals, little has been published on the effect of rhodium loading on gauze catalysts.

Recent work has shown that the addition of rhodium to a monolith supported platinum catalyst is severely detrimental to selectivity[26]. In this work by Schmidt *et al.*, they report a significant decrease in yield of HCN, and a significant increase in both carbon monoxide and ammonia in the product stream when they increase the loading of rhodium in the monolith from 0 to 4%. Also seen was an increase in the hydrogen production and a decrease in water production from this catalyst. Apart from the sample without rhodium, the Pt:Rh weight ratio was kept constant at 4:1, indicating a constant level of 32atomic% rhodium. In varying the levels of platinum alone, there was little effect. The rhodium is thought to decrease the level of HCN production by suppressing the levels of water production, allowing more oxygen to react to form the undesirable products CO, CO_2 and N_2.

1.4.3 Surface Segregation Phenomena

Surfaces of Pt-Rh alloys are very labile and show distinct surface segregation phenomena and the surface composition is dependent on factors such as temperature and exposure to reactive gases such as oxygen and carbon monoxide[27-28]. There have been several studies of platinum-rhodium surface segregation properties under atomically clean conditions (UHV) and most experimental data points to a large Pt surface enrichment. Exceptions to the rule are invariably caused by the presence of significant impurities such as sulphur[29]. Most of these investigations have been based around well defined conditions i.e. single crystal studies but the results obtained from polycrystalline surfaces yield similar results.

Using low energy ion surface scattering (LEISS), it was found that Pt segregates to the surface of polycrystalline platinum-rhodium alloys[30]. This was also seen in the

temperature range of 800-1400 K on a (100) surface of a 60%Pt, 40% Rh single crystal. This conclusion is supported by similar work using Auger analysis[31].

Recently, work has been carried out using time of flight atom probe field ion microscopy (TOF-APFIM). The technique involves the use of an extremely high electrostatic field to remove surface atoms from the tip of a single crystal. The technique can selectively remove material layer by layer. In this work by Florencio[32] *et al.*, the atomically clean (100) and (111) surfaces of a 44.8at% Rh, 55.2at% Pt single crystal, annealed to 973K, were investigated. For each case the depth profile was taken for in excess of 10 surface layers. Results showed that there was a distinct non-monotonic depth profile showing significant surface segregation of platinum to the surface layer. From the results, it appears that the (100) surface showed a greater surface segregation than the (111) surface but the difference between the two results was within experimental error, quoted at ± 6%.

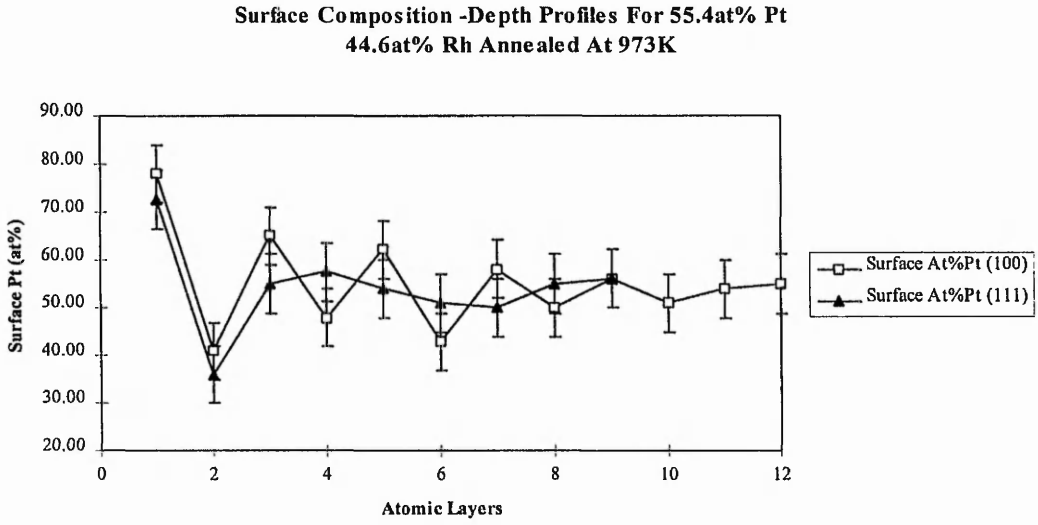

Figure 1.7: Segregation in Pt-Rh Alloys observed by TOF-APFIM (From Ref. 32).

The effect of temperature on the surface segregation of platinum has been investigated by Van Delft *et al.*[33] have used Auger spectroscopy to measure the dependence of temperature on the surface of a Pt62at% Rh38at% foil. In this work, a clean surface was annealed under vacuum to temperatures between 800 and 1500 K. They report that with increasing temperature from 800 to 1000 K, the surface composition changed from 80 to 89% Pt. Above this temperature, and up to 1500 K, the surface enrichment of platinum stayed approximately constant at 89% platinum. Also considered in this work is the effect of small quantities of contaminants on the

segregation phenomena. They report that small quantities of elements such as phosphorous, tin or carbon result in a different segregation trend. Here, the surface segregation of platinum is reduced by the presence of these elements, and a decrease in surface platinum is particularly evident at temperatures above 1300 K. By 1500 K, the surface exhibited a markedly different composition at ~ 80% Pt as opposed to 85+% for the clean sample.

Results from calculations of the heat of segregation indicate that the heat of segregation for platinum in platinum rhodium alloys under atomically clean conditions varies from 6 to 14 kJ mol^{-1}. As the differences between atomic diameter, the heat of mixing and the heats of sublimation are small, the typical models for surface segregation do not fully explain the origin of this segregation phenomena. The explanation proposed by Van Langenveld *et al*[34]. concentrates on the role of vibrational entropy on the surface composition. Platinum has a significantly higher surface vibrational entropy than rhodium 88 vs. 67 J mol^{-1} K^{-1} and it is proposed that it is this driving force that is the origin of the heat of segregation at high temperatures (under vacuum conditions).

1.4.4 Activation And Deactivation

The morphology of the catalyst has been well studied, or more accurately, its changes in morphology when under active service in both the oxidising atmosphere of the Ostwald process, and in the reducing, higher temperature process of HCN synthesis. In both processes, initially the catalytic gauze consists of clean smooth wires, but after a period of up to 60 hours use, the gauze becomes extensively faceted, with distinct pores and crystal planes. This reconstruction has been observed in many other platinum catalysed reactions, but the Ostwald and Andrussow processes have been studied in the greatest detail, due to their industrial importance.

Shown below are micrographs taken in a scanning electron microscope of -

i. An unused gauze
ii. The top of a used gauze taken from an industrial reactor after use.
iii. The bottom surface of a used gauze taken from an industrial reactor.

In these images the top side is the gas entry side, and the bottom is the gas exit side of the pack.

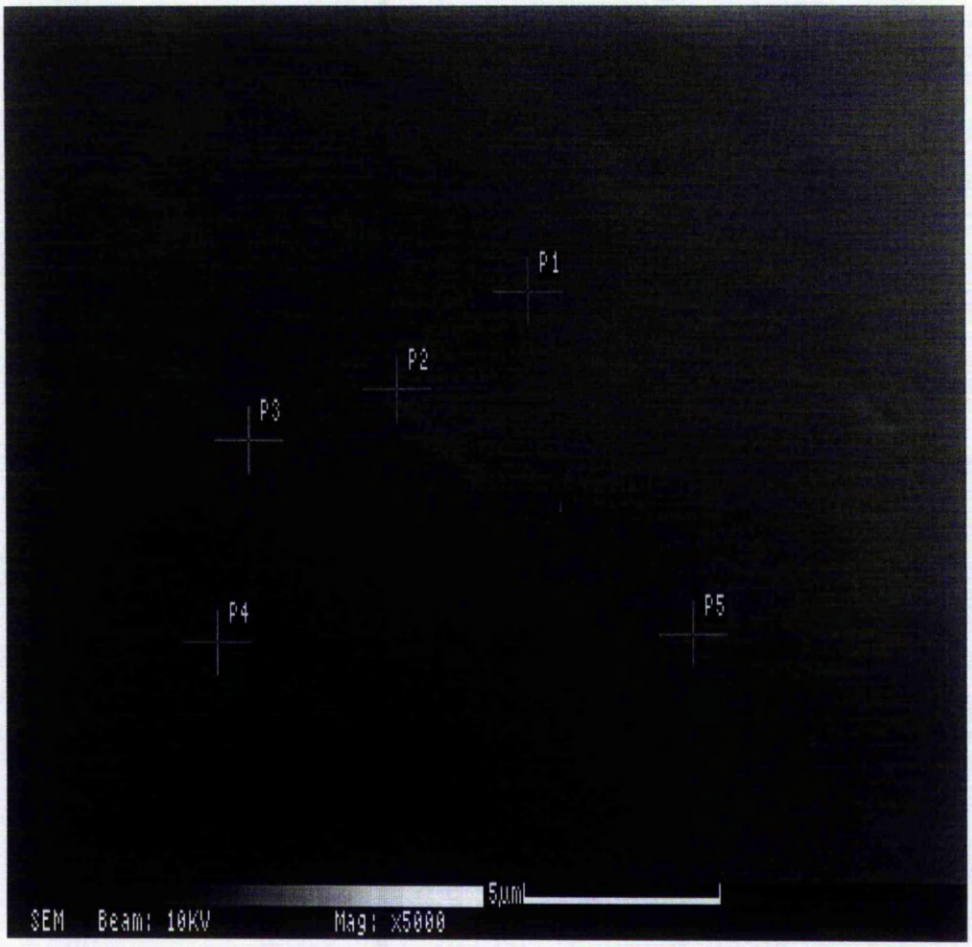

Figure 1.8: Unused Gauze Sample. Note the smooth appearance of the catalyst surface.

Figure 1.9: Top of a used catalyst gauze. Note the very regular facet formation.

Figure 1.10: The Bottom of a used gauze pack. Note the less well ordered nature of the features in comparison with the top surface. The magnification of this image is X2000. The dimensions of the image are 60 X 60 μm.

It is generally accepted that there is a 3-fold increase in surface area during the reconstruction process. The mechanism leading to the increase in surface area is currently under much debate with some researchers advocating a gas phase volatile metal oxide mechanism, whilst others attempting to describe the phenomenon by surface migration of an activated platinum species.

This reconstruction has been investigated by many researchers and results show that the morphology of the treated surface is strongly dependant on the gas it was exposed to[35-36]. processes occurs only in a reacting mixture of gases - either ammonia and air, or in the presence of all three reactants.

Faceting is the transformation of a planar single crystal surface into hill and valley structures as described in figure 1.8.

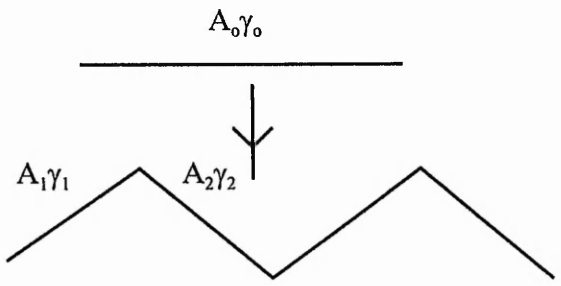

Figure 1.11 : Faceting Of A Single Crystal Plane

This physical process is generally believed to be driven by minimisation of surface free energy as described in equation 1.11.

$$\min \sum_i Ai\gamma i$$

γ_i is the surface tension of the *i*th crystallographic orientation.
A*i* is the surface area of the *i*th crystallographic orientation.

Equation 1.11 : The Summation of Free Energy In Relation To Faceting

For faceting to be thermodynamically favourable, the surface tension of some of the new crystallographic orientations must be less than that of the initial orientation to compensate for the increase in surface area.

Typically faceting may be classed in two categories, *thermal* and *catalytic*. Generally speaking, thermal faceting is slow when compared to catalytic faceting and is often observed only at higher temperatures. One further major difference between the two mechanisms is the observation that material is frequently removed simultaneously with catalytic faceting, resulting in etching of the surface.

On a macroscopic view, the originally smooth wires of the catalyst can be seen to be highly faceted and in some cases pores can run right the way through the catalyst wire diameter. This restructuring shows a distribution down the catalyst bed, with the uppermost layer of gauze showing a high level of crystallite order. Further down the bed the features, although still present, are less well defined i.e. have a lower degree of faceting[37-38]. Coincident with this major restructuring phenomena is an increase in selectivity to hydrogen cyanide[39].

Scanning tunnelling microscopy has been carried out on a sample of gauze used in the Andrussow process[40] in an attempt to assess whether nanoscale roughening significantly increases the surface area of the gauze. Results show that for the bottom layer of gauze (19 layers) taken from a pilot plant, the average surface area enhancement is around 15 %, although regions of area enhancement of up to 100 % have been seen. Regular steps in otherwise smooth crystal faces are common and give evidence for the formation of specific planes. Pits of approximately 2000 Å in diameter have been observed and are commonly located on grain boundaries. Material build-up is evident around the mouths of these pits. This work supports theories that the mechanism for facet formation is due to the removal of material from grain boundaries which then accumulates on certain crystallographic faces.

From previous work, the increase in selectivity (i.e. activation) of these catalysts is thought to be due to one or more of the following physical processes.

Change In Morphology

The catalyst undergoes an increase in effective diameter of around 20% and an increase of approximately 10 fold in surface area. This will change the mass transfer characteristic of the catalyst and may alone be sufficient to cause the large increase in selectivity[41].

Change In Surface Composition

Platinum-rhodium alloy surfaces are well known as being very labile and, for a given alloy composition, show different surface compositions for different crystal faces exposed - such as the (100) and (111) crystal faces[42]. During activation, the catalyst wires change from a smooth drawn wire to expose these regular crystallographic features, and this may cause a change in the selectivity. The surface composition will also be affected by the high temperatures of reaction. This change in Rh surface composition with use in the Andrussow reactor has been investigated via XPS[43]. Here results show that the unused catalyst gauze was enriched with rhodium but with use the surface concentration decreases. The reduction in Rh surface concentration was seen to be most significant in the first 24 hours of use. The results are as shown in table 1.4.

Sample	$Rh(3d_{5/2})/Pt(4f_{7/2})$ Peak Intensities
Unused	0.140
Used 24 hrs top layer	0.095
Used 24 hrs bottom layer	0.098
Used 6 months top layer	0.110
Used 6 months bottom layer	0.087

Table 1.4: XPS Results for Used and Unused Gauze (17.4at%Rh). From ref. 41. Results are corrected for cross sectional area.

In HCN manufacture, once the activation process is complete, the selectivity of the pack slowly decays and typically has a lifetime of several months. The activation process that occurs under Andrussow reaction conditions results in sufficient alloy migration that once used for several days, the migration of material locks the gauze layers together. Unlike the Ostwald process for ammonia oxidation, the precious metal losses associated with the Andrussow process are minimal, a factor which is primarily due to the net reducing conditions which preclude the formation of volatile oxides.

Under industrial conditions the activation process, observed as an increase in HCN selectivity, is complete after about 70 hours, after which, the selectivity slowly decreases until the economics of the process require the catalyst to be replaced. Once the pack has been removed from use, the precious metal is recycled. Figure 1.12 shows a typical activation-deactivation curve for an industrial reactor.

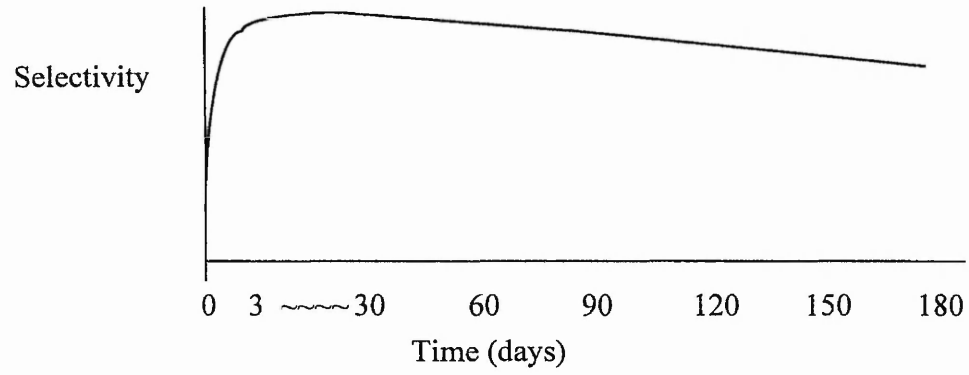

Figure 1.12 : Activation And Deactivation Of The Platinum Rhodium Gauze

The deactivation processes are, at present, not fully understood but is proposed that deactivation may be due to one or more of the following physical processes.

Foreign matter

Contamination of the gauze with foreign matter has been a cause of gauze failures. Contaminants, such as iron oxide, from corroded pipelines have a profound effect on catalyst activity and selectivity[44-45].

Excessive carbon build up

Severe carbon laydown causes a decrease in catalyst activity by a simple site blocking mechanism.

By-pass of reactants

Bypass of the reactants can occur if the gauze is damaged or not packed properly. A major cause of bypass is due to tears or cracks appearing in the gauze during plant trips or shutdowns, which result in rapid cooling and therefore contraction of the gauze[46].

1.4.5 Effect Of Morphology On Gauze Performance

There are reports in the literature about the effect of morphology on the selectivity of HCN synthesis catalysts. The correlation between crystallographic structure and selectivity was borne out by work carried out by Pan[47], who proposed

that catalysts with a face centred tetragonal (fct) structure have a higher selectivity than those with a face centred orthorhombic (fco) structure. This evidence strongly points to the fact that surface rearrangements have a strong effect on selectivity and a process which exposes the (100) plane of platinum rhodium crystal surfaces in preference to others may result in an increase in selectivity. An interesting feature of the used hydrogen cyanide catalyst is the presence of sulphur at the surface of a used catalyst, which presumably originated from sulphur in the natural gas feed. Work carried out by Harris at Cambridge[48] showed that the presence of sulphur can induce faceting of small platinum particles, the restructuring tending to expose predominantly (100) facets. The effect of sulphur addition to gauze has been observed by Schmidt & Luss, who added ~100 PPM H_2S to the feed gas of a laboratory Andrussow reactor[49]. During the activation process, and afterwards, they noted a higher than normal selectivity to hydrogen cyanide. Afterwards exposure to H_2S in the feed they observed that the gauze was perfectly crystalline, the exposed crystal faces attributed to (100) planes and contained many rectangular channels of approximately 3 μm width. A noticeable expansion of the wires had occurred over and above that found for 'typical' catalysts. Depth profiled Auger spectroscopy was performed on these samples. Results from this work showed that the presence of sulphur was limited to the surface, and that the presence of sulphur had caused a change in the morphology of the catalyst.

The general conclusions from the work to date is -

1. Rhodium has been shown to be detrimental to HCN selectivity using supported catalysts.
2. Polycrystalline Pt-Rh alloys show significant platinum surface segregation.
3. Catalyst morphology has a strong influence on selectivity possibly via exposing reactive crystal planes of varying rhodium levels and this may go some way to explain the activation phenomena.
4. Feed gas composition has an influence on catalyst morphology.

1.5 References

[1] G.J. Hutchings. S. Afr. J. Chem. **38** (2) 44-48 (1985).

[2] D.A. Hickman, M. Huff, L.D. Schmidt. Ind. Eng. Chem. Res. **32** (5) 809-817 (1993).

[3] C.A. Heaton (Ed.) 'An Introduction to Industrial Chemistry' Leonard Hill Publishers ISBN 0-249-44165-9. pp.358.

[4] J.K.S. Wan, T.A. Koch. Res. Chem. Intermed. **20** (1) 29-37 (1994).

[5] E.A. McKenna, A. Ornotheos, N. Kiratzis, M. Stoukides. Ind. Eng. Chem. Res. **32** 1904-1913 (1993).

[6] D.Hasenberg, L.D. Schmidt. J. Catal. **97** 156-168 (1986).

[7] D. Hasenberg, L.D. Schmidt. J. Catal. **91** 116-131 (1985).

8 D. Hasenberg, L.D. Schmidt. J. Catal. **104** 441-453 (1987).

[9] N. Waletzko, L.D. Schmidt. AIChE Journal **34** (7) 1146-1156 (1988).

[10] E.A. McKenna, A. Ornotheos, N. Kiratzis, M. Stoukides. Ind. Eng. Chem. Res. **32** 1904-1913 (1993).

[11] M.P. Saurez, D.G. Loffler. React. Kinet. Catal. Lett. **43** (1) 195-199 (1991).

[12] N. Kiratzis, M. Stoukides. J. Catal **132** 257-262 (1991).

[13] A.G. Dietz III, L.D. Schmidt. Catal. Lett. **33** 15-29 (1995).

[14] G.A. Cordonier, F. Schuth, L.D. Schmidt. Vacuum **41** (1-3) 278-281 (1990).

[15] S.Y. Hwang, A.C.F. Kong, L.D. Schmidt. J. Phys. Chem. **93** 8327-8333 (1989).

[16] D. Jentz, H. Celios, P. Mills, M. Trenary. Surface Science **341** pp. 1-8 (1995).

[17] D.A. Hickman, L.D. Schmidt. J. Catal. **136** 300-308 (1992).

[18] P.M. Torniainen, X. Chu, L.D. Schmidt. J. Catal. **146** 1-10 (1994).

[19] M.P. Zum Mallen, W.R. Williams, L.D. Schmidt. J. Phys. Chem. **97** 625-632 (1993).

[20] W.R. Williams, C.M. Marks, L.D. Schmidt. J. Phys, Chem. **96** 5922-5931 (1992).

[21] S. Axon. ICI Acrylics R&T. Personal communication. (1995).

[22] C.N. Satterfield 'Hetererogeneous Catalysis in Practice' McGraw-Hill, New York 214-221 (1980).

[23] S. Axon. ICI Acrylics R&T. Personal communication (1993).

[24] D.R. Anderson. J. Catal. **113** 475-489 (1988).

[25] R.W. McCabe, T. Pignett, L.D. Schmidt. J. Catal **21** 114-126 (1971).

[26] D.A. Hickman, M. Huff, L.D. Schmidt. Ind. Eng. Chem. Res. **32** (5) 809-817 (1993).

[27] M. Rubel, M. Pszonica, W. Palczewska. J. Mat. Sci. **20** 3639-3648 (1985).

[28] F.C.M.J.M. van Delft, B.E. Nieuwenhuys, J. Siera, R.M. Wolf. I.S.I.J. International. **29** 550-559 (1989).

[29] M. Ahmad, T.T. Tsong. Surface Science **149** L7-L12 (1985).

[30] F.L. Williams, G.C. Nelson. Appl. Surf. Sci. **3** 409 (1979).

[31] D.P. Holloway, F.L. Williams. Appl. Surf. Sci. **10** 1 (1982)

[32] J. Florencio, D.M. Ren, Tien T. Song. Surface Science **345** L29-L33 (1996).

[33] F.C.M.J.M. Van Delft, A.D. Van Langenveld, B.E. Niewenhuys. Surface Science **189-190** 1129-1134 (1987).

[34] A.D. Van Langenveld, J.W. Niementsverdriet. J. Vac. Sci. Tech. A **5** (4) 558-561 (1987).

[35] M. Flytzani-Stephanopoulos, S. Wong, L.D. Schmidt. J. Catal. **49** 51-82 (1977).

[36] A.G. Knapton. Pt. Met. Rev. **22** 131-137 (1978).

[37] G. Hutchings. S. Afr. J. Chem. **38** (2) 44-48 (1985).

[38] M.P. Saurez, D.G. Loffler. React. Kinet. Catal. Lett. **43** (1) 195-199 (1991).

[39] B.Y.K. Pan. J. Catal. **21** 27-38 (1971).

[40] B.A. Cowans, K.A. Jurman, W.N. Delgass, Y.Z. Li, R. Reifenberger, T.A. Koch. J. Catal. **125** 501-513 (1990).

[41] D.A. Hickman, L.D. Schmidt. J. Catal. **136** 300-308 (1992).

[42] J. Siera, F.C.M.J.M. van Delft, A.D. van Langeveld, B.E. Nieuwenhuys. Surface Science **264** 435-439 (1992).

[43] B.A. Cowans, K.A. Jurman, W.N. Delgass, Y.Z. Li, R. Reifenberger, T.A. Koch. J. Catal. **125** 501-513 (1990).

[44] B.Y.K. Pan. J. Catal. **21** 27-38 (1971).

[45] D.A. Hickman & L.D. Schmidt. Ind. Eng. Chem. Res. **30** 50-55 (1991).

[46] S. Axon. ICI Acrylics R&T. Personal communication. (1994).

[47] B.Y.K. Pan. J. Catal. 21 27-38 (1971).

[48] P.J.F. Harris. Nature. **323** pp. 792-794 (October) (1986).

[49] L.D. Schmidt, D. Luss. J. Catal. **22** 269-279 (1971).

2. Microreactor Design

2.1 Introduction

Evaluation of catalyst performance for the production of hydrogen cyanide was carried out on a laboratory scale reactor which was designed, constructed and commissioned in-house. The laboratory reactor was designed and built to mimic the industrial reactor, but on a vastly reduced scale.

For the microreactor the main design criteria were as follows -

- The ability to feed gaseous reactants in a controlled manner.
- The ability to monitor the composition of the feed-gas and product streams of the reactor.
- Destroy the HCN produced (zero HCN emissions).
- Allow easy recovery of the catalyst for subsequent characterisation.
- Operate in a safe manner

2.2 Microreactor Design

For this study, the reactor design is described in the following sections -

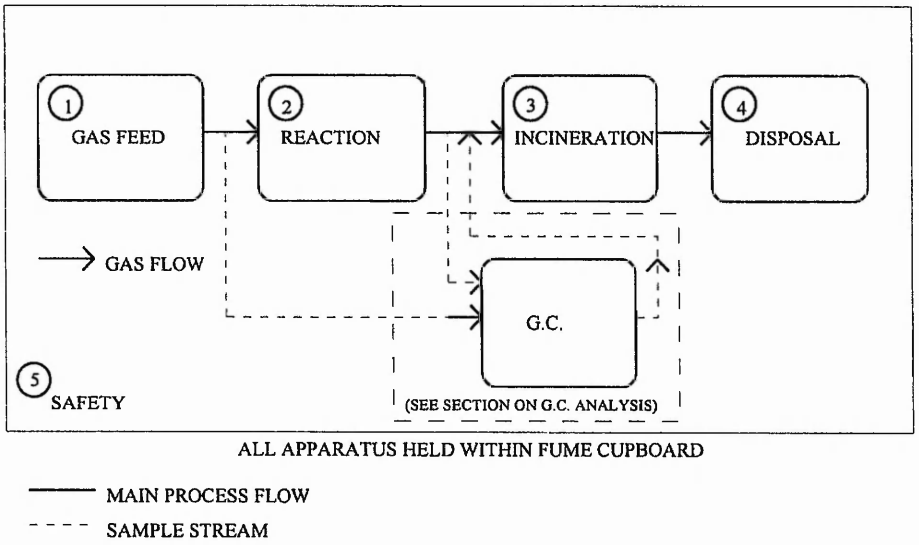

Figure 2.1: Major Aspects of the Laboratory Andrussow Apparatus

From figure 2.1, the apparatus has been considered in five sections. Each section is discussed in turn.

2.2.1 Gas Feed

The reactant feed gases used in the laboratory Andrussow reactor were methane, ammonia and air. The apparatus also required the controlled addition of nitrogen[a] and argon[b].

Air, methane, nitrogen and argon were taken from the common laboratory gas supply whereas the ammonia supply was a dedicated supply. Mass flow controllers were used for methane, air, argon and ammonia (Brooks 5070TR). The feed gas lines were of 316 stainless steel construction and $^1/_4$" external diameter. The flow of each gas could be stopped by a Nupro SS-4P-4T[c] plug valve. 2μ filters were fitted upstream from the mass flow controllers (SS-4F-2) and non return valves afterwards (SS-4C-1).

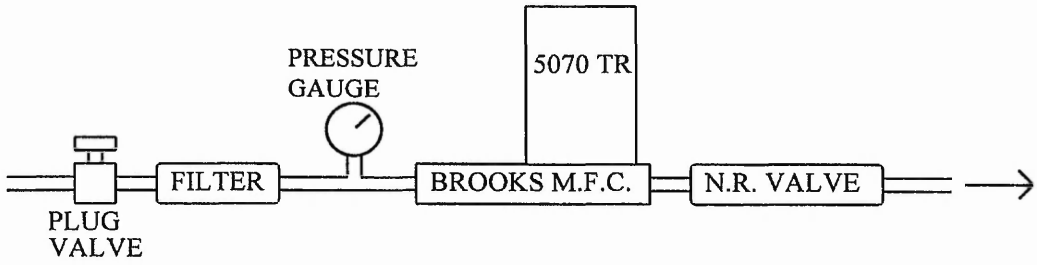

Figure 2.2: Feed gas handling system for methane, air and ammonia.

The gas flows from the mass flow controllers were then mixed at a cross piece equipped with a pressure gauge. A 3 way valve then directed the feed gas either to the reactor or to a 100 ml ground glass syringe for flow measurement. A ground glass syringe was used as ammonia was found to dissolve in the soap water solution used in wet film flowmeters.

---

[a] See safety section.

[b] See analysis section.

[c] All Viton seals were replaced with Buna seals as Viton is incompatible with ammonia.

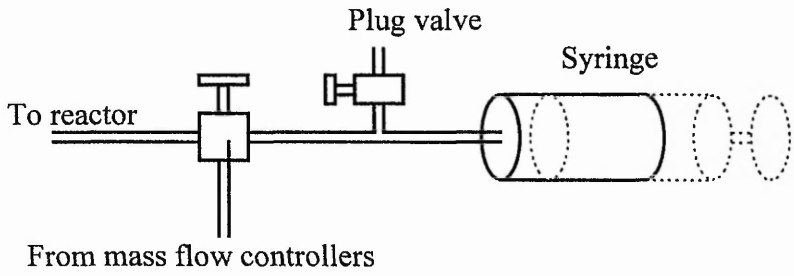

Figure 2.3: Bypass valve and syringe for checking mass flow controller output

To calculate the gas flow rate necessary for operation at a residence time of approximately 1 millisecond, typical of industrial reactors, the following factors were considered -

- Bed Volume.
- Temperature effects (PVT corrections).
- Molecularity changes
- Void fraction.

Bed Volume

Bed depth for 4 layers of unseparated gauze = 0.25 cm
Internal diameter of bed = 0.6 cm

Cross sectional area (C.S.A.) of inner tube $= \pi (0.6 / 2)^2$.
$= 0.28\ cm^2$.
Bed volume (C.S.A * bed depth) $= 0.28 * 0.25$
$= \underline{0.07\ cm^3}$.

Temperature Effects

During reaction under conditions typical of the Andrussow process, the temperature of the gas changes from ambient to a ca. 1325 K. Assuming an isothermal bed at 1325 K (T_2), and a feed gas temperature of 300 K (T_1), the effect of the change in temperature on the gas velocity through the bed, and therefore the contact time, was calculated via the ideal gas laws. The result of the calculation (T_2/T_1) indicated that the contact time would be decreased by a factor of 4.4 (1325/300) by the increase in temperature.

Molecularity Changes

The average molecularity change in the Andrussow reaction stream is small and estimates predicted a 10-13% increase in volume going from feed to products[1]. As the change in volume was small, the effect of change in molecularity was, therefore, ignored.

Voidage

The catalyst had a very high voidage, assumed to be greater than 95%. A correction for voidage was, therefore, not included in the calculation.

A combination of the factors illustrated above predicted that the residence time was approximately 4.4 times shorter than that predicted by the standard temperature and pressure (STP) gas flow rates.

Flow Rate Calculation

Flow (ml min^{-1}) = 60 x bed volume / (residence time in seconds * PVT correction)

= 60 x 0.07 / (0.001 x 4.4)

= 1024 ml min^{-1}

To operate at a residence time of millisecond, the required flowrate was, therefore, ca. 1000 ml min^{-1}. Typically, the feed gas composition was 74 % air (740 ml min^{-1}), 13 % ammonia (130 ml min^{-1}) and 13 % methane (130 ml min^{-1})

To provide a sample of the feed gas to the G.C. for analysis, a small flow of reactant gas was allowed to flow down a sample line just before the gases entered the reactor. The feed gas passed to a stream selection valve and passed either to the G.C. sample valve or bypassed the reactor and entered the incinerator furnace directly.

2.2.2 Reaction

The high temperatures of reaction and the reported sensitivity to iron contamination[2] precluded the use of steel tubing for the reactor. The reactor section was manufactured from high purity silica supplied by Heraeus Ltd. Connection of the reactor section to the steel lines was achieved by glass to metal seals and ball joints as shown in figure 2.4.

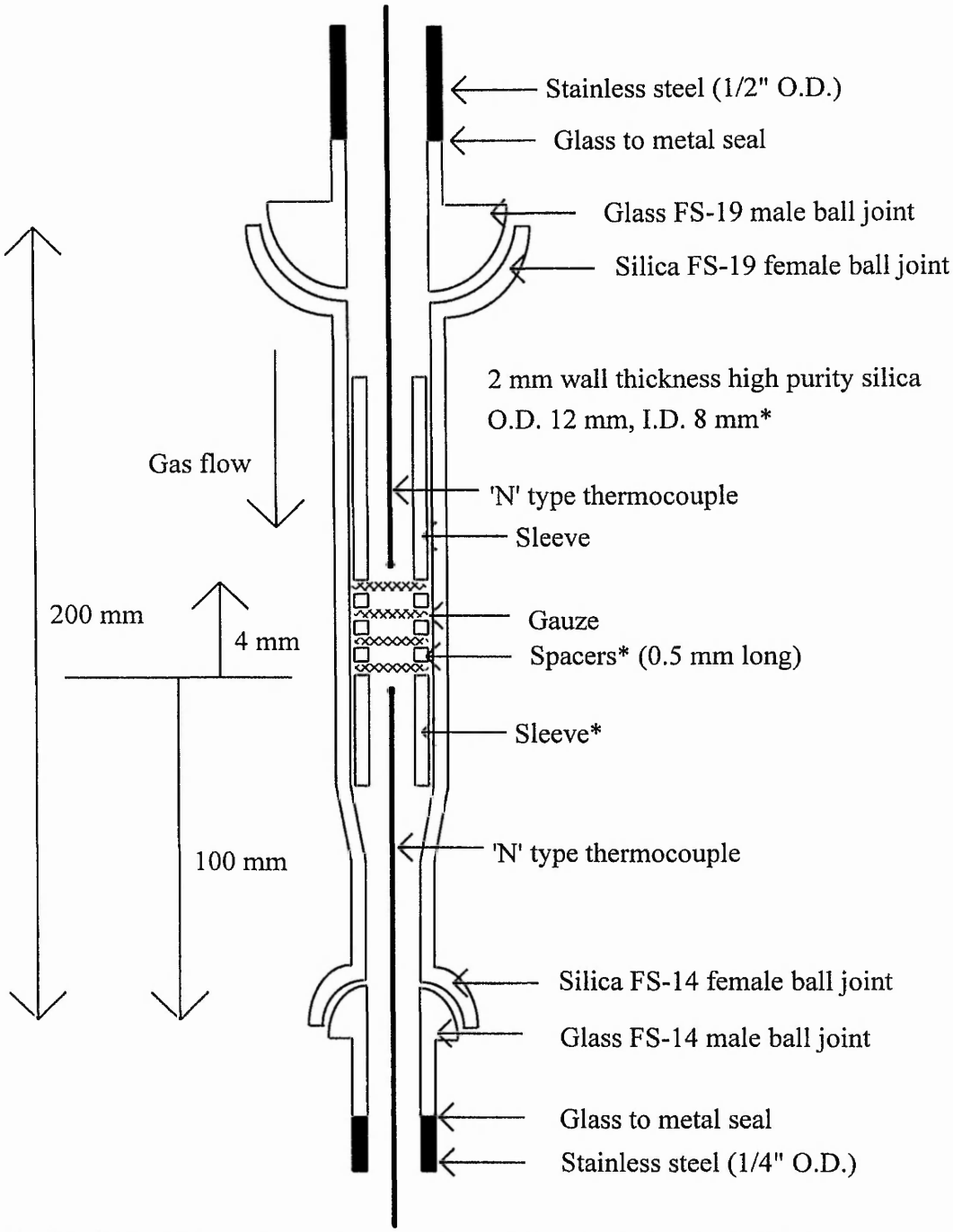

* The sleeve and spacers were manufactured from bore matched tubing to reduce bypass of reactants. This tubing was 8 mm O.D., I.D. 6 mm. The effective cross sectional area of the reactor is therefore 6 mm.

Figure 2.4: Close-up of the Silica Reactor

The reactor bed volume was typically 0.07 cm^3, a figure which was the volume of 4 layers of unseperated catalyst gauze. A main aim of the reactor design was to allow easy recovery of the catalyst, and in particular, be able to characterise the

individual gauze layers. To enable separation of the gauze samples which, if left in physical contact, often fuse together[3], the gauze layers were separated by 0.5 mm spacers, cut and ground accurately from bore matched tubing (8 mm O.D., 6 mm I.D.). These were ignored in the calculation of bed depths as the actual volume of catalyst remained the same.

A pressure gauge (0-4 bar gauge) was located in the feed line just before the reactor which was connected to the gas lines by Swagelok unions - directly to the metal portion of the glass to metal seals. In the case of the top section, a $^1/_4$" to $^1/_2$" union was used, whereas at the bottom, a $^1/_4$" union was used. In each case the gas line was connected to a T-piece allowing the gas tight fitting of a 300 mm Inconel sheathed $^1/_{16}$" N-type thermocouple[a] supplied by Minta Ltd. Measurement of the thermocouple output was via a dedicated electronic display (Jenko model 7001H). The ferrule used in fitting of the thermocouple was made of graphite as this allowed movement of the thermocouple to allow accurate placement of the tip. The ball joints were clamped together using spring loaded clamps.

The assembled reactor was then placed into a furnace of dimensions 18 cm high, 1.6 cm internal diameter. The furnace was set on a platform, and the reactor tube extended 1 cm below the bottom of the furnace as shown in figure 2.5.

Temperature control of the furnace was achieved a K-type thermocouple and Eurotherm 91e controller, the setting for which could be varied in the range 0-800°C. All gas lines containing product gas were heated using Isopad heating tape (KPG series) and electrically and thermally insulated using Dalfratex thermal insulation tape.

From the reactor, the product stream was split and most of the flow went direct to the incinerator. A carefully controlled sidestream passed through a 1/8" heated gas line to the stream selection valve, and was directed ether to the G.C. sample valve, or to the incinerator.

[a] The choice of an N-type thermocouple was recommended by Minta Ltd, as they provide a stability advantage over the more common K-type thermocouples, especially at high temperatures.

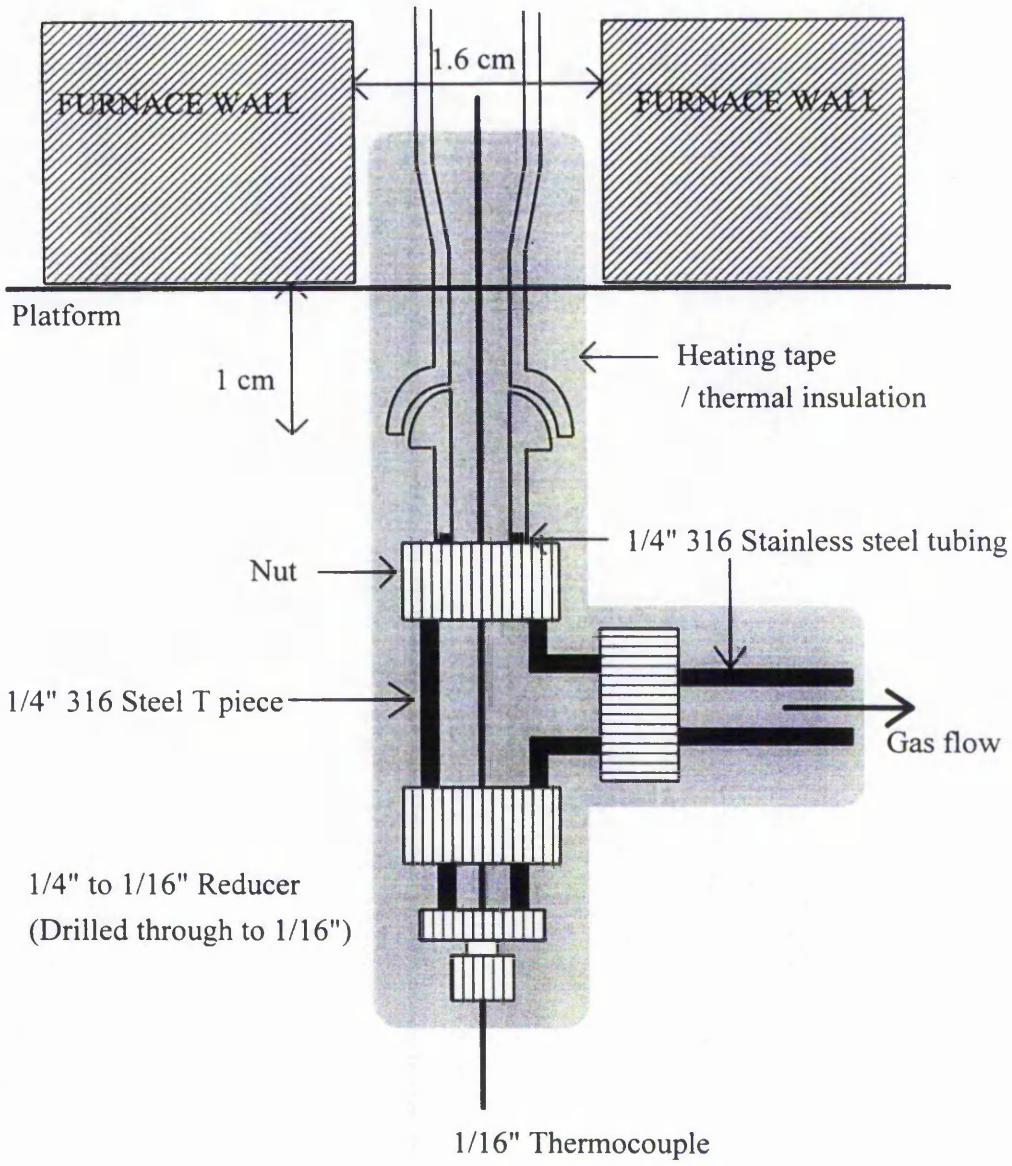

Figure 2.5: Thermocouple / Gas Flow Assembly

2.2.3 Incineration

HCN and CO are highly toxic, and therefore must not be discharged in large quantities into the fume cupboard. To dispose of the HCN, the product gases were incinerated. Incineration was achieved by adding excess oxygen to the reaction products, achieved by using a Charles Austen FS85 D/E diaphragm pump. The flow was controlled by a combined float rotameter (Rotameter Mfg. Series 1100) / flow control valve. The feed line, which joined the product line just before the incinerator, was fitted with a non return valve (Nupro SS-4C-1).

The flow rate of air to the incinerator was calculated using the total oxidation reaction of the feed gases i.e.

$$CH_4 + NH_3 + 3\,{}^3/_4\,O_2 \rightarrow CO_2 + NO_2 + 3\,{}^1/_2\,H_2O$$

Equation 2.1: The Total Combustion Reaction for Methane and Ammonia

The oxygen contained in the reaction feed was subtracted from this value and a 30% excess added to ensure total combustion (5 litres / min).

The incinerator catalyst was 2% platinum supported on chromia, supplied by ICI Katalco. The catalyst was held inside a $^1/_2$" stainless steel reactor by silica wool. The reactor tube was held vertically within a Carbolite MTF 12/25 B furnace at 800 K. The incinerator effluent was discharged high in the fume cupboard. The reactor tube was fabricated so that the exit was still within the heated zone to prevent condensation products re-entering the reaction zone. The incineration process resulted in large exotherm which was observed by a temperature rise within the furnace. The catalyst efficiency was periodically checked by placing a portable HCN detector (Neotronics model Neotox HCN Plus) by the exit of the incinerator. No HCN was ever detected in the effluent[a] .

2.2.4 Disposal

All equipment that could possibly contain HCN was kept within the fume cupboard. Due to the efficiency of the incinerator, levels of HCN discharge up the stack were minimal. There was, however, a significant discharge of carbon and nitrogen oxides. Assuming 100% selectivity to NO_X from ammonia, the total discharge from the reactor of NO_X could may have been 130 ml min^{-1} which was not considered excessive as the stack concentration of NO_X was calculated to be within safety guidelines.

[a] Low levels of HCN may have been present, but due to the interference of NO on the HCN monitor, could not be quantified.

2.2.5 Safety Systems

The gas handling system was designed with a number of safety features to stop the reactant feeds automatically and purge the apparatus with nitrogen in the event of a system failure. The system was set up to monitor the following -

1. Fume Cupboard - Low air flow

2. Emergency stop

3. Furnace Undertemperature
   The temperature of the Carbolite incinerator furnace was monitored so that if the operating temperature fell below 500°C, the apparatus would trip out. The temperature was measured by an independent K-type thermocouple and the trip mechanism was triggered by a Watlow series 140 alarm unit.

4. Mass Flow Controller Output
   The Dynamass mass flow controller control box was interfaced via an RS232 link to an IBM PC. The P.C. and Dynamass control unit were running communication software which enabled the computer to obtain real-time information about flow rates. During operation the flow rates were constantly monitored by the P.C. and if found to deviate form the set-point, the apparatus would trip. The apparatus was designed and built, and the software was written, in-house[a].

In each case, the trip situation resulted in the removal of the reactant feeds and the addition of a nitrogen purge. The gas handling system is outlined in figure 2.6. Under normal operating conditions the nitrogen solenoid valve was shut by applying + 12V to the terminals and the mass flow controllers functioned normally. In the event of a trip, power to the solenoid valve was removed, and a signal was sent to the mass flow controllers to close fully.

[a] With the help of Mr. B. Townley. Electronics Workshop, Department of Chemistry, Liverpool University.

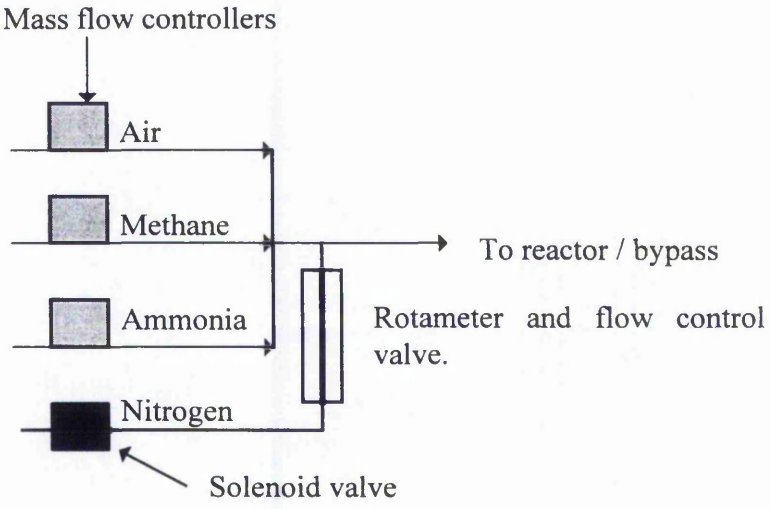

Figure 2.6: The Gas Handling System

During operation of the reactor, the portable HCN monitor was placed on the fume cupboard sash.

2.3 Analysis of Feed and Products

Analysis of the feed gas and products was performed by on-line gas chromatography. The gas chromatograph used was a Pye Unicam model 610. The G.C. was fitted with a six port gas sample valve, a 2 m Hayesep C G.C. column and a 2 m Molsieve 5A column. Detection of the separated components was achieved by a thermal conductivity detector (TCD). The TCD output was first amplified using an integral amplifier and then fed to a Spectra Physics SP4290 integrator. The sample valves were heated to 140°C via heating tape (Isopad KPG series) which was controlled by a Eurotherm 847 temperature controller and a K-type thermocouple placed at the centre of the sample valve. Figure 2.7 describes the flow of products through the sampling system.

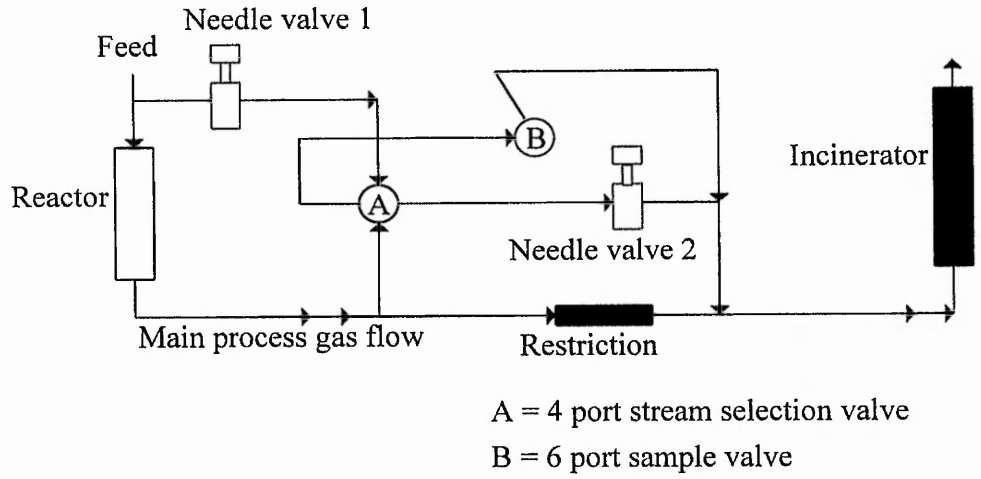

Figure 2.7: The Gas Handling System

Needle valves 1 and 2 were used to balance the gas flows and enabled a constant flow of feed and product gases to flow through the sample system irrespective of which stream was selected. During commissioning, the flows through the sample loop were set at ~ 10 ml min, achieved by the use of the needle valves and a section of crimped $^{1}/_{8}$" tubing. All tubing after the reactor was trace heated to 120 - 140°C.

2.3.1 Stream Selection

The stream to be analysed (either the feed or products) was selected via a heated 4 port valve as shown in figure 2.8.

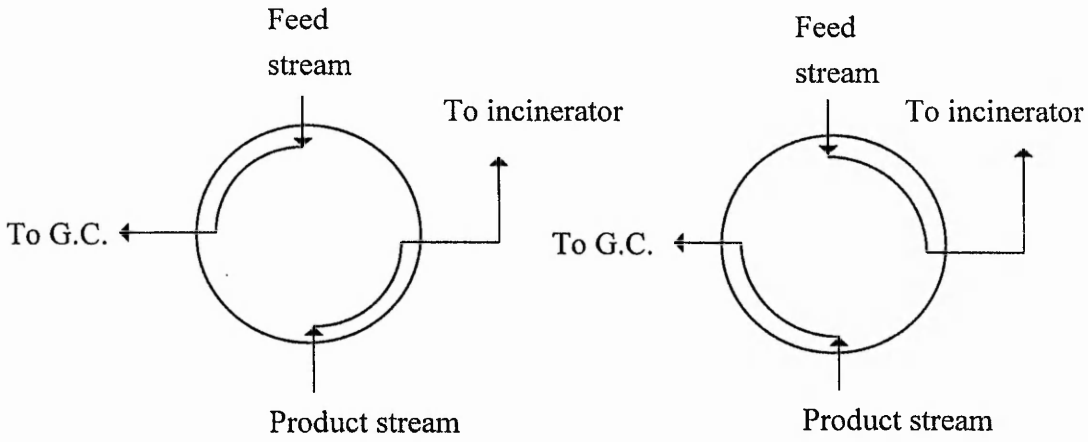

Figure 2.8: Stream selector valve operation

The switching system, therefore, maintained a constant flow of both feed and product streams irrespective of the selected stream.

2.3.2 Analytical Method

The G.C. utilised a pneumatic automated gas sample valve switching system. A $^1/_{16}$" six port Valco gas sampling valve with a 1 ml sample loop was controlled by the G.C. and used to inject samples of gas onto the first analytical column.

Once injected, the analysis was carried out over a combination of 2 columns. The column 1 was a Haysep C ($^1/_8$" external diameter X 2 m 80-100 mesh) at 60°C and separated polar components such as carbon dioxide, ammonia, water and hydrogen cyanide. Gases such as hydrogen, oxygen, argon, nitrogen and carbon monoxide were eluted quickly from the Hayesep C column and were unresolved. The unresolved gases were then passed onto the second column (Molsieve 5A X 2m 80-100 mesh), typically within 1.5 minutes of injection onto the Haysep column. The Molsieve 5 A column then eluted hydrogen, oxygen, nitrogen and methane before being switched out of series and isolated. A temperature ramp (to 120°C at 5°C min^{-1}) then increased the rate of elution of products off the Haysep column and NH_3, H_2O and HCN were eluted. Once elution of products from the Haysep C column was complete, the temperature of the G.C. oven returned to 60°C, and the Molsieve column was switched back into series. The final component eluted was carbon monoxide. A representative G.C. trace for product analysis is shown in appendix 1.

The timescale of elution of products from the Hayesep column was such that it was found impossible to perform a full determination of products, as CO_2 was passed onto the Molsieve column. To measure CO_2 concentration in the products, the analysis was performed using only the Haysep C column.

2.3.3 Calibration

2.3.3.1 Calibration of Carbon Monoxide, Methane and Ammonia

Calibration of the G.C. was complicated by the pressure effects of the incinerator and high flow rates. To calibrate, the G.C., the mass flow controllers were re-plumbed such that methane, ammonia and carbon monoxide were mixed with helium and passed into the reactant feed section. The analysis then proceeded as normal (the same analytical method was used for calibration and product determination).

The concentration of methane, ammonia and carbon monoxide was varied by changing the output of the relevant mass flow controller. Total flow was always 1000 ml min^{-1} (± 15 ml min^{-1}) and before analysis, the output from each mass flow controller was checked. Accuracy of blending was ± 1ml min^{-1} for NH_3, CH_4, and CO and ± 15 ml min^{-1} for helium.

The calibration curves for CO, CH_4 and NH_3 were found to be approximately linear over the ranges tested. The following figures are the slope of the calibration curve. The calibration curve for methane is shown in appendix 2.

Gas	Sensitivity Factor
CO	8,353,000
CO_2	10,153,000*
CH_4	8,963,000
NH_3	6,922,000

Table 2.1: Relative Sensitivity Factors For the Main Gases in Use

* The CO_2 calibration factor was calculated from a comparison of sensitivity factors with another calibrated G.C. (based at ICI Wilton).

2.3.3.2 Calibration For Hydrogen Cyanide

Due to the difficulties and hazards associated with HCN gas standard preparation, the concentration of HCN was determined by mass balance. Although mass balance calculations are common, the mass balance calculation for HCN was complicated by the high conversion and change in average atomicity of the products. The concentration of carbon in the products ($[C]_{PRODUCTS}$), was, therefore, not the same as in the feed ($[C]_{FEED}$). To calculate the concentration of carbon in the product stream, the expansion due to reaction must be known such that the concentration of carbon in the products can be calculated. The measurement of expansion was achieved by adding a small but accurately known concentration of argon (ca. 1%) to the feed gases and measuring the concentration of argon in the product stream. The addition of argon to the feed was achieved using a Brooks 5070 TR mass flow controller and a Brooks 0154 control box. The flow of argon was directed either to the reactant feed or to a calibrated 20 ml wet film flowmeter for flowrate measurement using a 3 way Whitey SS-41XS2 valve. To calculate the HCN mass balance the following equations were used -

Product Carbon Concentration (Calculated)

$$[C]_{FEED} * \frac{1}{EXPANSION} = [C]_{PRODUCTS}$$

Where $$EXPANSION = \frac{[Ar]_{FEED}}{[Ar]_{PRODUCTS}}$$

Hydrogen Cyanide Concentration (Calculated)

$$[HCN] = [C]PRODUCTS - [CO] - [CO_2] - [CH_4]$$

Equation 2.2: Mass Balance Calculation For HCN Product Concentration

The application of a 'corrected' mass balance, therefore, enabled an accurate concentration of HCN to be determined. To check the accuracy of the mass balance calculation, the Andrussow reactor was operated under various conditions which resulted in a range of selectivities. Figure 2.9 shows the plot of HCN G.C. counts vs. calculated concentration by mass balance.

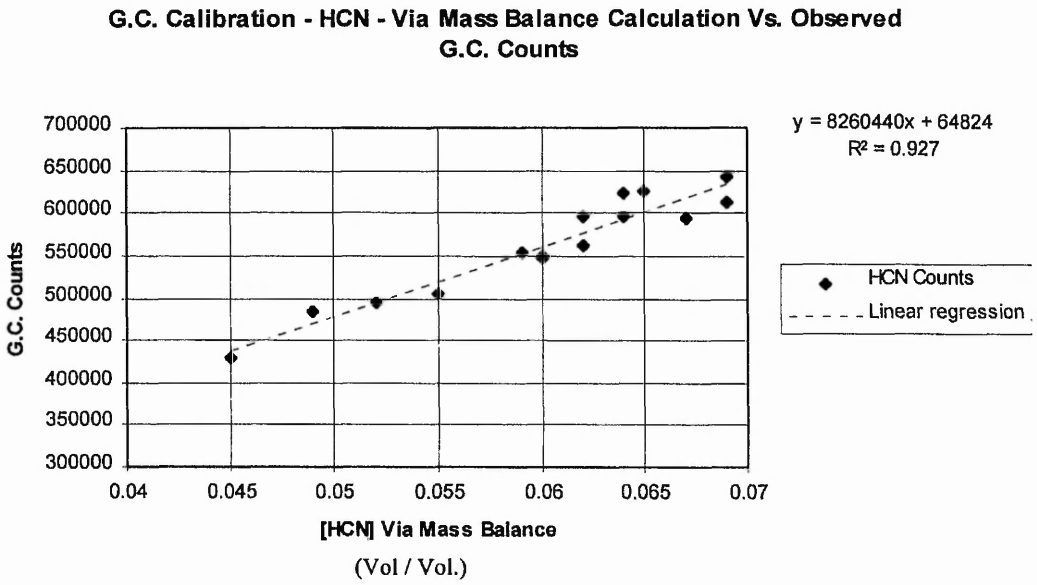

Figure 2.9: The Comparison Between Calculated [HCN] and the G.C. Counts for HCN.

The high correlation factor (R^2 = 0.927) and the low intercept (64,824) give strong evidence for the validity of the mass balance method. Over the range of HCN selectivities shown in figure 2.9, the expansion coefficient was seen to be dependent on HCN selectivity and was measured as 1.09 at high HCN selectivity and 1.15 at low HCN selectivity.

2.4 Experimental Methods

2.4.1 Catalyst Preparation

The samples of catalyst used were firstly cut into 8mm disks from a sheet of the required composition. The disks were then loaded into the reactor and the whole reactor rinsed firstly in acetone and then in water. The reactor tube was then lowered into a measuring cylinder containing ~ 50% by volume of concentrated nitric acid and placed in a sonic bath for 2 minutes. The nitric acid was then rinsed off the tube with distilled water. After a final rinse with acetone the reactor tube was placed into the furnace at 473 K and left overnight before use.

2.4.2 Reactor Operation

2.4.2.1 Start-Up

From being left overnight at 473K in a slow flow of nitrogen (~50 ml min^{-1}), the furnace nitrogen flow was then increased to 1000 ml min^{-1} using a needle valve / rotameter and stopped using the solenoid valve. This procedure was designed to prepare the valve setting to switch in ca. 1000 ml min^{-1} at shutdown. The 3 way valve was then set to bypass to allow flow measurement. The gas feed rates were then set to their target settings (± 1 ml min^{-1} for CH_4 and NH_3, ± 15 ml min^{-1} for air). All gas flows were then switched on and allowed to equilibrate. During the equilibration time the furnace setpoint was raised from 200 to 450°C. As the furnace reached 450°C, the flow was switched to the reactor which invariably resulted in light-off of the reaction observed as a yellow-orange glow from the catalyst.

2.4.2.2 Shutdown

At the end of the experiment the reactor was shut down by instantaneously removing the feed gases and replacing them with an equivalent flow of nitrogen. This effectively purged the lines of reactants and provided an inert environment in which the catalyst could cool down. The visible exotherm characteristic of HCN synthesis was seen to stay stable for ca. 1 second after switching the feed to nitrogen and then extinguish rapidly. The catalyst was, therefore, 'quenched' from the operating temperature to < 600°C within a very short timescale (<10 s). Coincident with the feed shutdown procedure the furnace setpoint was reduced from 450°C to either 200°C (overnight storage) or switched off for later catalyst removal.

2.5 Commissioning

During initial trials of the apparatus under HCN synthesis conditions, it was found impossible to operate the reactor under steady state conditions. Coincident to this lack of stability was the observation of a small but significantly increasing pressure (as seen by the pressure gauge just before the reactor). On disassembly, this was seen to be due to the presence of severe carbon laydown on the lower (exit side) thermocouple.

On closer inspection, the tip was found to be clean and intact but further down the thermocouple the Inconel sheath had been eroded away, exposing the inner insulation. The temperature observed by the thermocouple was, however, found to vary considerably from catalyst load to catalyst load. The variation in temperature was attributed to changes in the exact position of the thermocouple in the reactor. The recorded temperature was, therefore, considered unreliable and the thermocouple removed. Subsequent experiments proved much more successful, with no pressure build-up and no further carbon deposits were observed. The carbon build up and subsequent increase in pressure was therefore attributed to an interaction of the Inconel thermocouple sheath with the product gases.

From monitoring the feed gas composition over several days of operation, the stability of the feed gas system was found to be excellent, and as such the analysis of feed gas composition was not thought necessary and was not routinely carried out.

2.6 References

[1] S. Axon. Personal communication (1994).

[2] B.Y.K. Pan. J. Catal. **21** 27-38(1971).

[3] A.G. Knapton. Pt. Met. Rev. **22** 131-137 (1978).

3. Microreactor Studies - Results

3.1 Introduction

It is generally accepted that, under the reaction conditions of the Andrussow process, there is an increase in selectivity to hydrogen cyanide with time over the first few hours of use. To investigate the activation process, a series of gauze catalysts have been tested in a laboratory scale reactor for their activity and selectivity for hydrogen cyanide synthesis. Catalyst compositions, form, wire dimensions and supplier were as shown in table 3.1. All compositions are quoted as atomic%.

Composition (Pt%-Rh%)	Form	Wire Diameter (μm)	Supplier
83- 17	Woven	72	Johnson Matthey
83- 17	Knitted[a]	72	Johnson Matthey
86-14	Knitted[a]	72	Engelhard
91-9	Woven	72	PGP Industries
100%Pt	Woven	60	Goodfellow

Table 3.1: Table of Wire Properties and Suppliers

The activation of each of the above catalysts was established by measuring changes in ammonia and methane conversion and selectivity to hydrogen cyanide with time. Results of the activation studies are presented in section 3.2. The HCN synthesis reaction is known to be sensitive to temperature[1] and the effect of external heating on the catalytic properties of activated 83-17, 91-9 and 100%Pt catalysts was also investigated. Results from the effect of heat on selectivity and conversion are presented in section 3.3.

[a] The spatial density of the Pt-Rh wires in the knitted samples were similar to that for the woven samples.

3.2 Activation Studies

As discussed in chapter 2, the reactor was designed to use a 4 ply pack of catalyst gauze and operate with a contact time of around 1 millisecond. The total flow was, therefore, calculated to be 1000 ml min^{-1}. From preliminary studies the following reaction conditions were chosen as they gave conversions and selectivities comparable to industrial operation at > 90% methane conversion and ~ 50% selectivity from methane.

- Furnace temperature 450°C.
- Feed gas composition 13% ammonia, 13% methane, 74% air, resulting in a gas feed ratio of 1 : 1 : 1.13 (CH_4 : NH_3 : O_2)

A variety of catalyst bed configurations and catalyst compositions were tested for their performance in HCN synthesis. The catalyst performance was evaluated by measuring the concentration of methane, ammonia, carbon monoxide, carbon dioxide and hydrogen cyanide in the reaction products.

Note that due to the extremely long timescales involved with the activation experiments, the apparatus was typically operated for several days per experiment. Due to safety constraints, the apparatus could not be operated overnight and and as such a startup / shutdown procedure was performed several times per experiment. The effect of the shutdown / startup procedure can be seen in the results as a 'blip' in the selectivity / conversion data. For an example, refer to figure 3.1 where after 680 minutes a transient decrease in selectivity is noted. This was caused by the shutdown, storage and start-up, procedures as documented in chapter 2.

3.2.1 The Effect Of Catalyst Form And Of Number Of Layers

The 83-17 composition gauze was obtained in both woven and in knitted form. The difference in form enabled a comparison of the two gauze types to be carried out as differences in the mass transport properties of the two forms may have a significant effect on catalyst performance[2]. The activation profiles from the woven and knitted catalysts are shown in figures 3.1, and 3.2 respectively.

For the 83-17 catalyst the effect of increasing the residence time by 25% was investigated by the addition of an extra gauze layer. Figure 5.3 shows the resulting activation profile.

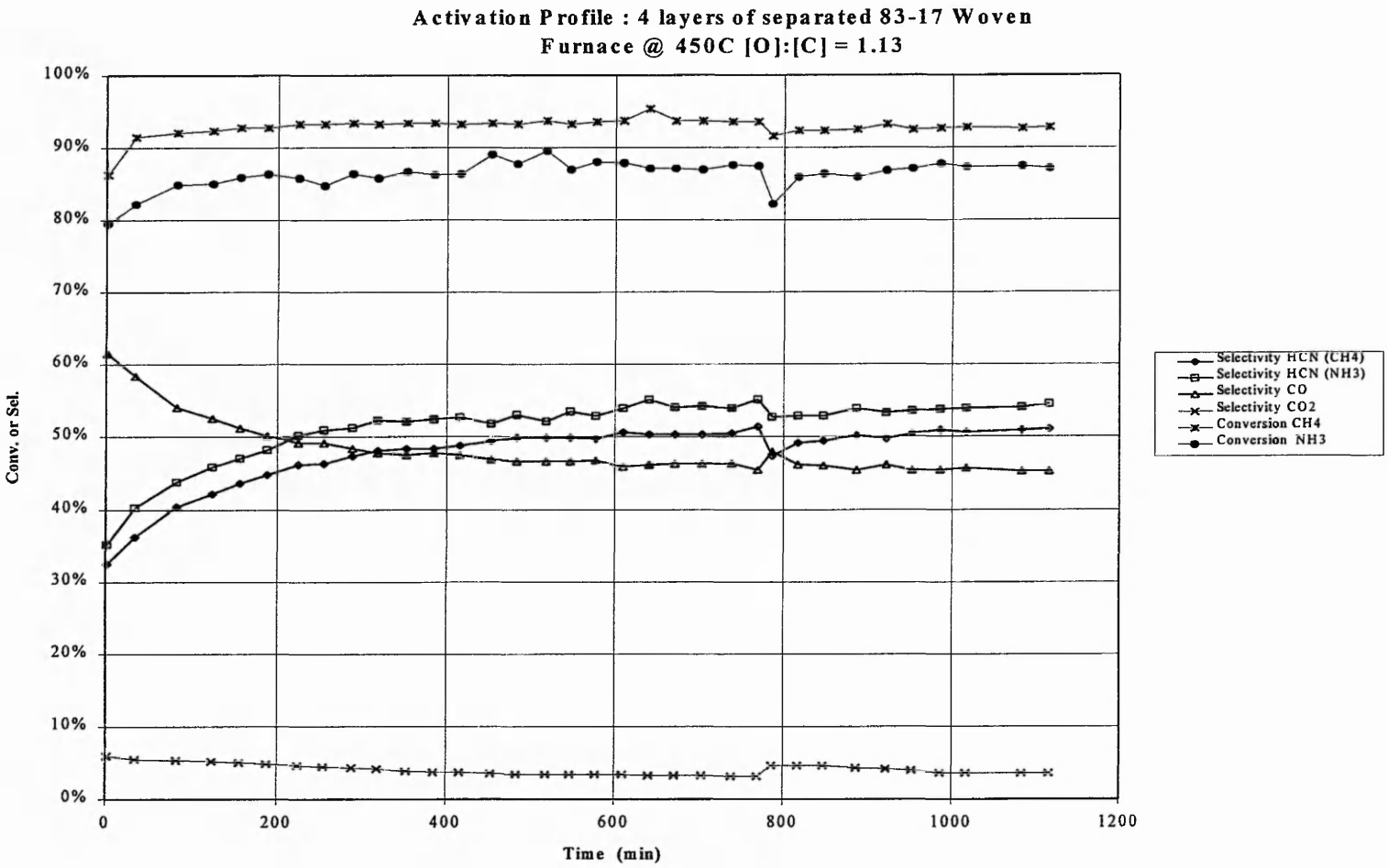

Figure 3.1: Activation Profile for 4 Layers of 83-17 Woven Catalyst

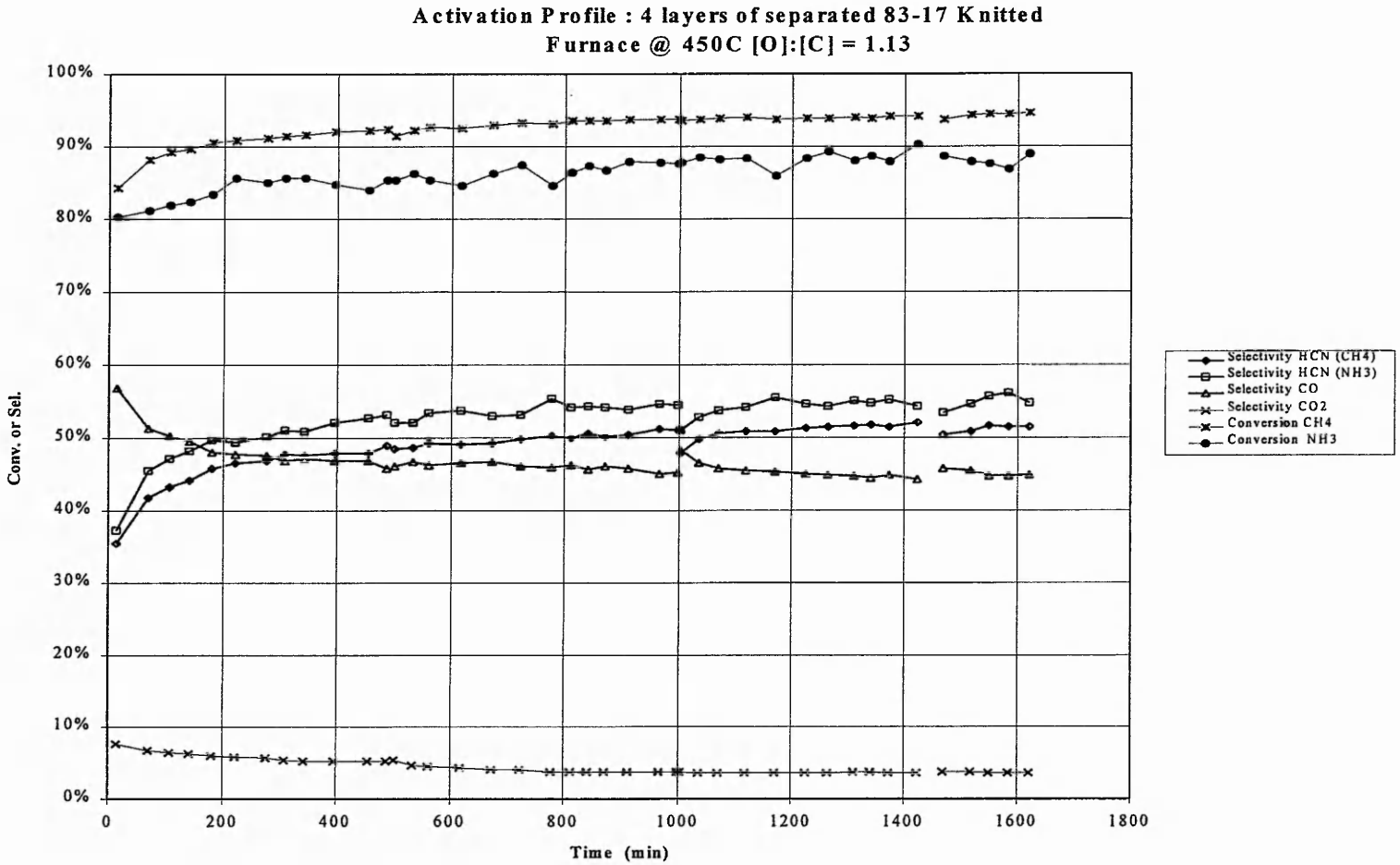

Figure 3.2: Activation Profile for 4 Layers of 83-17 Knitted Catalyst

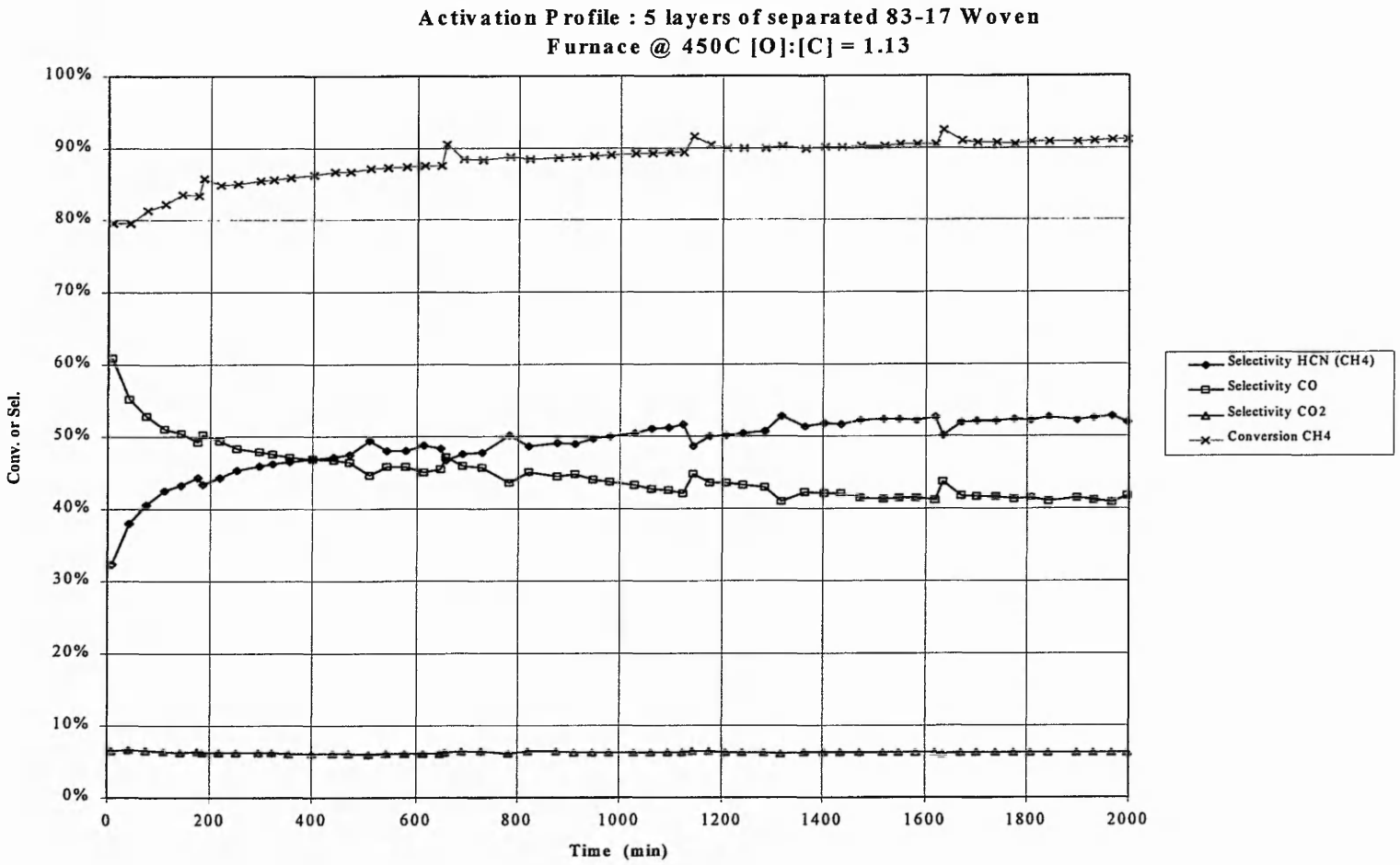

Figure 3.3: Activation Profile for 5 Layers of 83-17 Woven Catalyst

Figure 3.4 shows the change in selectivity to hydrogen cyanide from methane with respect to time for a 4 layered woven gauze pack (4-W), a 4 layered knitted gauze pack (4-K), and a 5 layered woven gauze pack (5-W). The results were taken from figures 3.1-3.3.

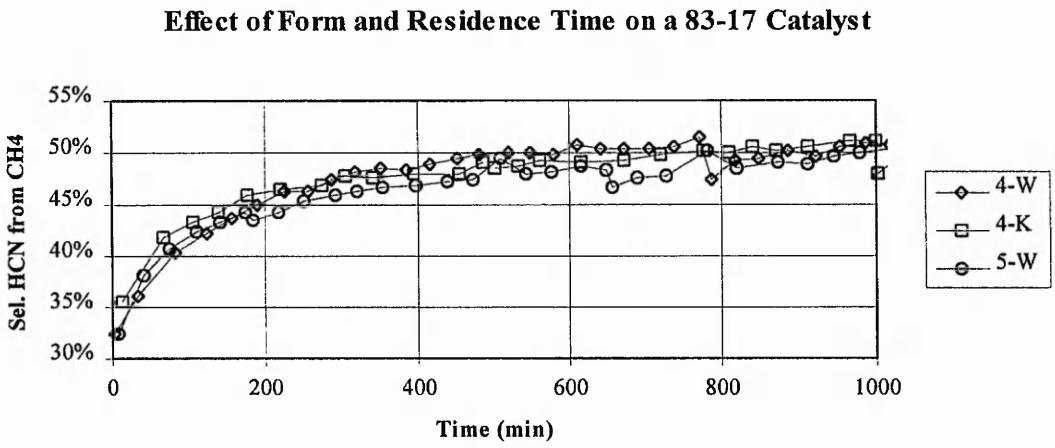

Figure 3.4 :The Effect of Form and Residence Time on HCN Selectivity

From figure 3.4, the activation profiles do not differ significantly, indicating that the catalysts were activating similarly. Table 3.2 summarises the catalytic performance of the three gauze packs.

Catalyst Gauze Pack	Conv. % CH_4 ±1%	Conv. % NH_3 ±2%	Sel. HCN from CH_4 ±1%	Sel. HCN from NH_3 ±2%	Yield HCN ±1%
83-17 x 4 layers knitted	94	88	51	55	48
83-17 x 4 layers woven	93	88	50	55	47
83-17 x 5 layers woven	92	N/A	51	N/A	47

Results shown, unless stated otherwise, are for analyses taken at 1000 min (~17 hours) of use.

Table 3.2: Summary of Results - 83-17 Knitted and Woven Catalysts

In all cases, the major unselective product was carbon monoxide, with low levels of carbon dioxide formation.

Effect of Number of Layers

This experiment showed that an increase of 25% in residence time did not significantly affect the observed HCN yields or selectivities. The results show that there was no significant change in ammonia or carbon monoxide concentration in the products which would be indicative of the HCN hydrolysis reaction ($HCN + H_2O \rightarrow CO + NH_3$). Similar results were obtained by Schmidt *et al.*[2], where the selectivity of the catalyst to HCN was studied using platinum coated foam monoliths. In that work, doubling the length of the monolith, and therefore residence time, only resulted in a decrease of ~ 10% in HCN yield. From these results the major conclusion is that, under the range of residence times under study, the effect of the HCN hydrolysis reaction is either insignificant or constant.

Effect of Catalyst Form

In considering the effect of form on HCN synthesis, the use of a knitted gauze, as opposed to a woven one, appeared to have little effect. This experiment was important to perform as a control experiment as later the performance of an 86-14 knitted gauze is compared to other compositions of woven construction. Since the Andrussow reaction has been shown to operate near mass transfer rates, the similarity in results for the woven and knitted 83-17 samples indicates that the difference between the two forms, in terms of mass transfer, is minimal.

Conclusion

As the activation process progressed, the hydrogen peak shape observed by the G.C. TCD detector changed from a clear double peak to a single peak plus shoulder, described by Villalobos[3] *et al.* as a decrease in the concentration of hydrogen in the product gases. Also noted in the G.C. traces during the activation process was an increase in the water peak area.

Since the mole fraction of oxygen in the feed was known accurately, and oxygen conversion was always approximately complete[a], a mass balance calculation was used to estimate the quantity of water and hydrogen produced by the reaction.

[a] Except for the platinum catalyst below 450°C.

concentration of oxygen in feed	=	concentration of CO in the products
(corrected for changes in	+	2x concentration of CO_2 in the products
volume due to reaction)	+	concentration of H_2O in the products

From the mass and heat balance calculation, shown in appendix 3, the activation process resulted in a decrease in ammonia decomposition, from 49% to 40%. The overall exotherm per mole of methane feed also changed slightly from -326 kJ mol^{-1} to -320 kJ mol^{-1}. The major difference in the heat balance was due to changes in the contribution to the overall heat of reaction for the endothermic HCN forming reaction (i) and the exothermic H_2O forming reaction (ii).

$$CH_4\,(g) + NH_3\,(g) \rightarrow HCN\,(g) + 3\,H_2\,(g) \qquad \Delta H_{298} = 252\ kJ\ mol^{-1} \qquad (i)$$

$$H_2\,(g) + {}^1/_2\,O_2\,(g) \rightarrow H_2O\,(g) \qquad \Delta H_{298} = -242\ kJ\ mol^{-1} \qquad (ii)$$

Under conditions of low HCN selectivity, the endothermic HCN forming reaction initially contributed 83 kJ per mole of methane feed, but as the reaction became more selective, this increased to 119 kJ per mole of methane feed. Coincidentally, the exotherm due to water formation increased from -396 kJ per mole of methane feed to -432 kJ per mole of methane feed, almost exactly balancing out the increase in the endothermic contribution for HCN synthesis.

The activation process was, therefore, shown to result in a decrease in -

- ammonia decomposition reaction(s)
- carbon monoxide forming reaction(s)
- hydrogen forming reaction(s)

And an increase in -

- HCN forming reaction(s)
- water forming reaction(s)
- methane conversion
- Ammonia conversion

3.2.2 The Influence Of Rhodium Concentration

Samples of 83-17, 86-14, 91-9 and 100%Pt were activated in the laboratory reactor under standard conditions described in section 3.2. The activation profiles for the 83-17, 86-14, 91-9 and 100%Pt samples are shown in figures 3.1, 3.5, 3.6 and 3.7 respectively.

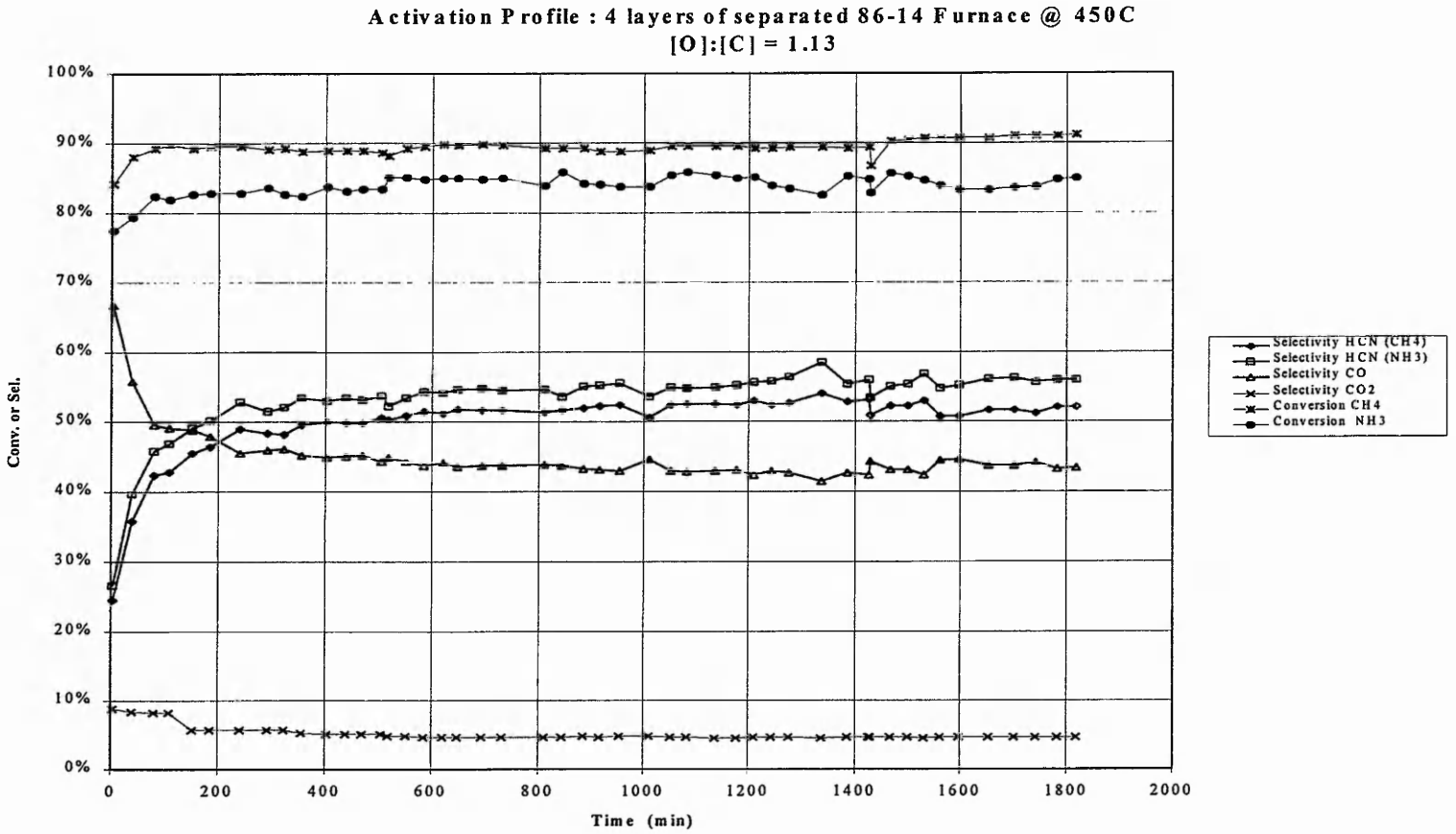

Figure 3.5: Activation Profile for 4 Layers of 86- 14 Woven Catalyst

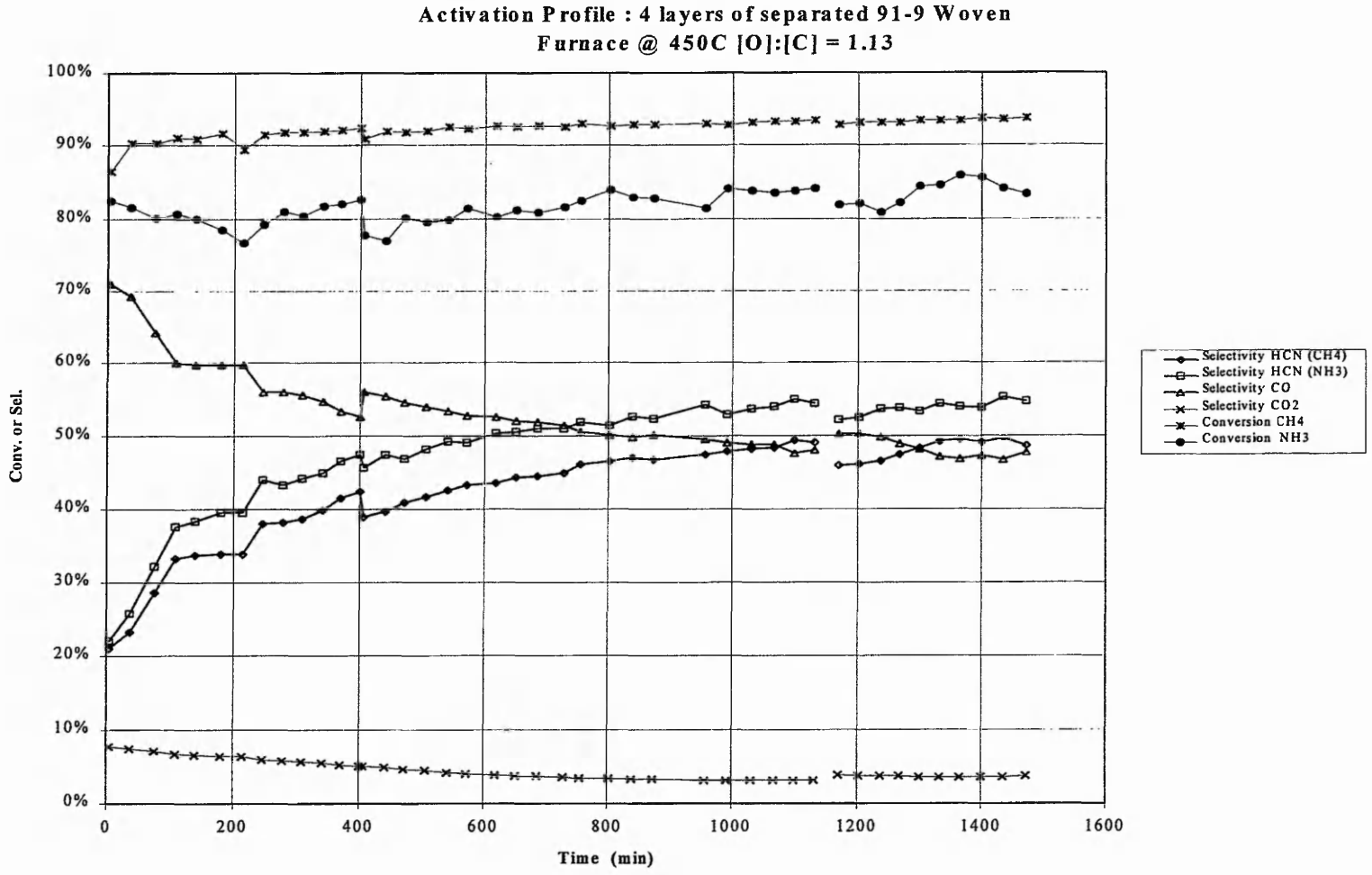

Figure 3.6: Activation Profile for 4 Layers of a 91at%Pt, 9at%Rh Woven Catalyst

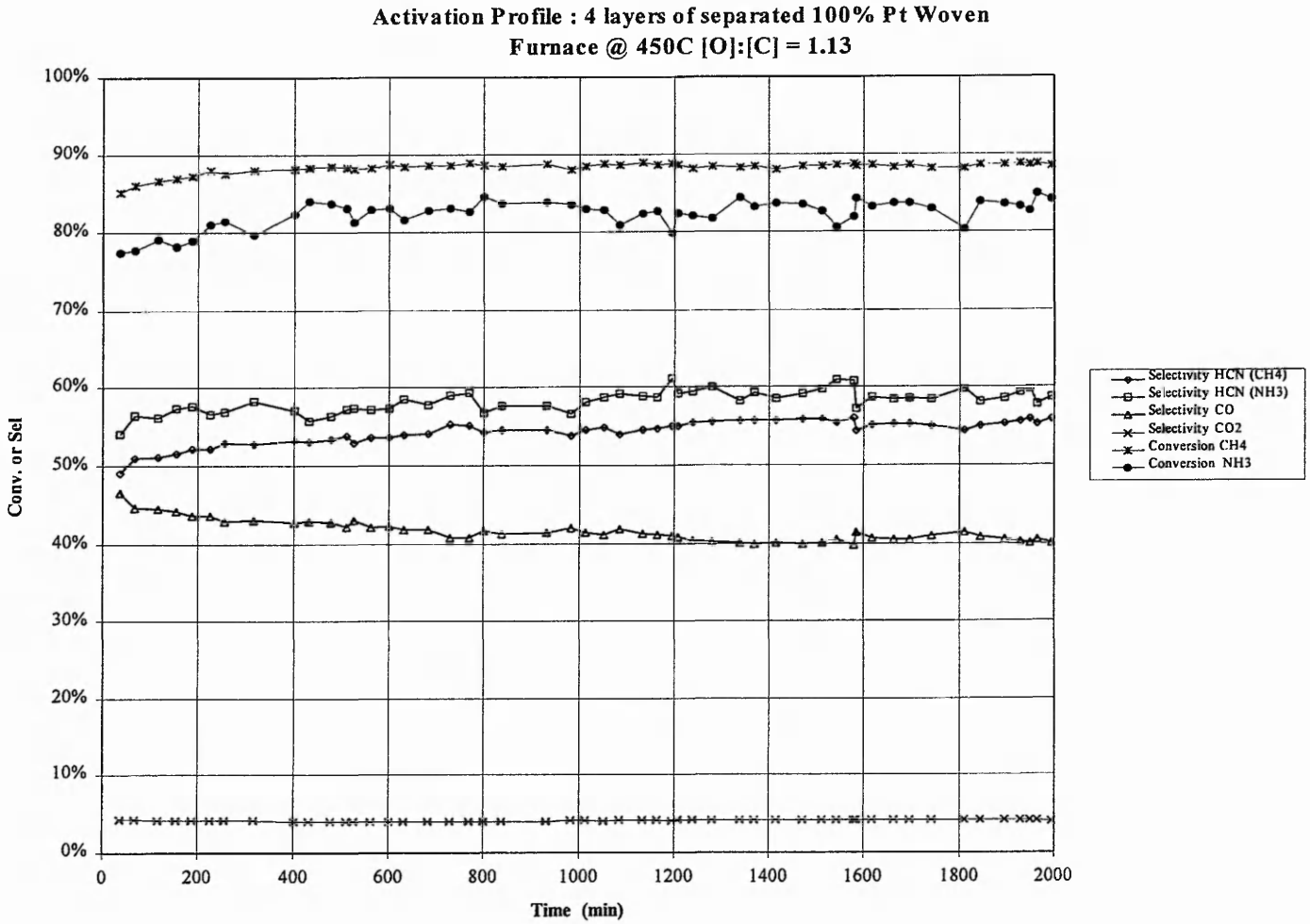

Figure 3.7: Activation Profile for 4 Layers of a 100%Pt Woven Catalyst

By comparing the activation results shown in figures 3.1, 3.5, 3.6 and 3.7 the activation experiments indicated that there was a significant difference between the activation properties of the catalysts. A plot of HCN selectivity vs. time of activation is shown in figure 3.8.

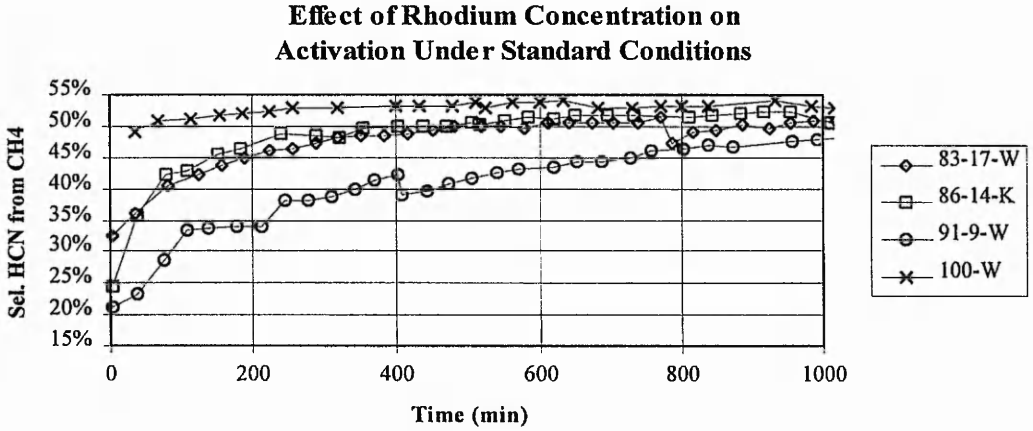

Figure 3.8: The Effect of Rhodium Concentration on Activation (Selectivity to HCN from Methane)

From figure 3.8, the 100%Pt sample showed a significantly higher selectivity than rhodium containing catalysts. The superior selectivity was especially apparent early in the activation process. Although not shown in the activation profiles, of note in the activation experiments was that, unlike the rhodium containing catalysts, the pure platinum catalyst did not exhibit total oxygen conversion. A summary of the activation results presented in figures 3.1, 3.5, 3.6 and 3.7 is shown in table 3.3.

Catalyst Gauze Sample	Conv.% CH_4 (±1%)	Conv.% NH_3 (± 2%)	Sel. HCN from CH_4 (±1%)	Sel. HCN from NH_3 (±2%)	Yield HCN (±1%)
83-17 Woven	94	88	51	55	48
86-14 Knitted	89	85	52	55	46
91-9 Woven	93	84	48	53	45
91-9 Woven[a]	94	86	49-50	55	47
100%Pt[b]	89	82	55	59	49

Results shown, unless stated otherwise, were for analyses taken at 1000 min (~17 hours) of use.

Table 3.3: The Effect of Rhodium Concentration on HCN Yield, Selectivity and Conversion

From table 3.3, it is apparent that rhodium enhances activity, resulting in complete oxygen conversions[b] and higher ammonia and methane conversions, but that rhodium has a detrimental effect on selectivity.

In considering the results shown in figure 3.8, it is clear that the selectivity to HCN after 100 minutes is only slightly higher than the beginning of the activation process but at all times showed high selectivity to HCN. This may be due to one of two possibilities, either the activation for pure platinum catalysts is significant but very fast, being essentially complete within a few minutes, or that pure platinum shows only marginal activation. The 83-17 sample and the 86-14 sample showed remarkable similarities in the activation profiles, reaching high selectivity (>50%) very quickly. The 91-9 sample, however, took much longer to reach high selectivity. As the composition of the 91-9 sample is intermediate between the 83-17 catalyst and the 100%Pt catalyst, the activation trend did not follow a simple pattern. The activation results, therefore, indicated that either the 91-9 catalyst was contaminated or the activation process exhibited a non-linear relationship to rhodium concentration.

[a] Value taken at 1450 min. This catalyst still showing signs of activation at >1500 min and was unusual behaviour unique to the 91at%Pt - 9at%Rh catalyst.

[b] Note that the pure platinum catalyst did not show complete oxygen conversion under these conditions. A small but constant level of oxygen was found in the product gases, estimated at 0.18%.

Once fully activated, the rhodium containing catalysts showed remarkably similar catalytic behaviour, with selectivities within ± 2% of each other but inferior to the pure platinum sample.

Examination of the gauzes after activation under standard conditions showed that there had been a significant amount of carbon laydown in use, primarily around the circumference of the catalyst, as shown in figure 3.9.

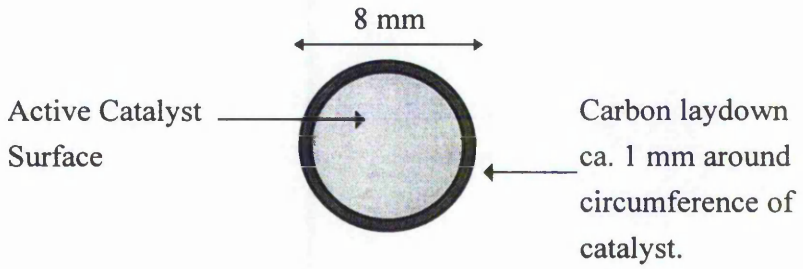

Figure 3.9: Diagram of a Used Catalyst Gauze Showing the Location of Carbon Laydown

The mechanism for carbon deposition was thought to be through the disproportionation of carbon monoxide - the Boudouard reaction which, as the thermodynamic calculations below illustrate, is only thermodynamically favourable for temperatures below 973 K.

$$2\ CO(g) \rightarrow C(s) + CO_2(g)$$

$\Delta G_{298} = -120$ kJ mol^{-1}

$\Delta G_{973} = 0.0$ kJ mol^{-1}

$\Delta G_{998} = 4.4$ kJ mol^{-1}

Since the carbon was found around the circumference of the catalyst, the distribution indicated that there was a temperature profile across the catalyst bed with the centre of the bed operating at a higher temperature than the extremities.

For rhodium containing catalysts, carbon laydown was restricted to the outer diameter of the gauze where the spacers prevent gas flow and the catalyst is in thermal contact with the silica reactor and sleeves. The pure platinum catalyst gauzes were, however, found to be heavily carburised within the inner area of the catalyst not shielded by spacers. The extent of carbon deposition became more and more prevalent down the pack (from gauze 1 → 4) as shown in figure 3.10.

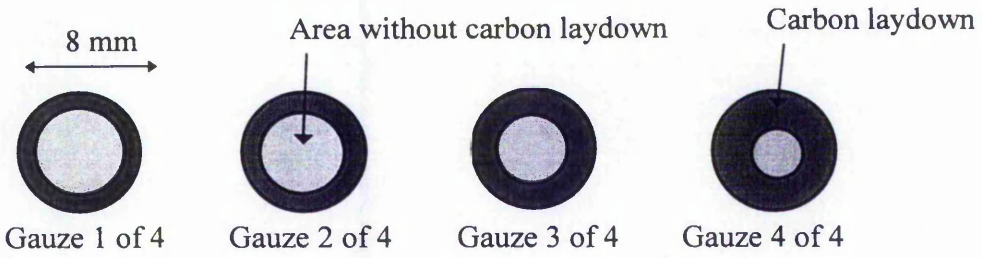

Figure 3.10: Diagram of Used Platinum Catalyst Gauzes Showing The Distribution of Carbon Laydown from Gauze 1-4.

As catalysts for the synthesis of HCN are deactivated by multilayers of carbon, the build up of carbon indicates that the breakthrough of oxygen observed when using pure platinum catalysts may be due to deactivation of the catalyst by carbon laydown. Since Boudouard carbon formation is only thermodynamically favourable below 973 K the pure platinum catalyst appeared to be operating at a lower temperature than the Pt-Rh catalysts. Due to problems with the downstream thermocouple, the true catalyst bed temperature could, however, not be measured.

3.3 Effect of Furnace Temperature

The effect of furnace temperature on the catalytic performance of the 83-17, 91-9 and 100%Pt catalysts was investigated. The catalysts were firstly activated using standard conditions as described in section 3.2 and then the furnace temperature ramped from 450 to 600°C (or 750°C) in 50°C steps whilst maintaining the feed gas composition and flow rate. Through HCN yield calculations and the measurement of methane and ammonia conversion, the selectivity to HCN from both methane and ammonia was calculated

Each value of selectivity and conversion was an average of several analyses taken over > 1hour. Figures 3.11 and 3.12 describe he effect of furnace temperature on the selectivity to HCN from methane and ammonia respectively.

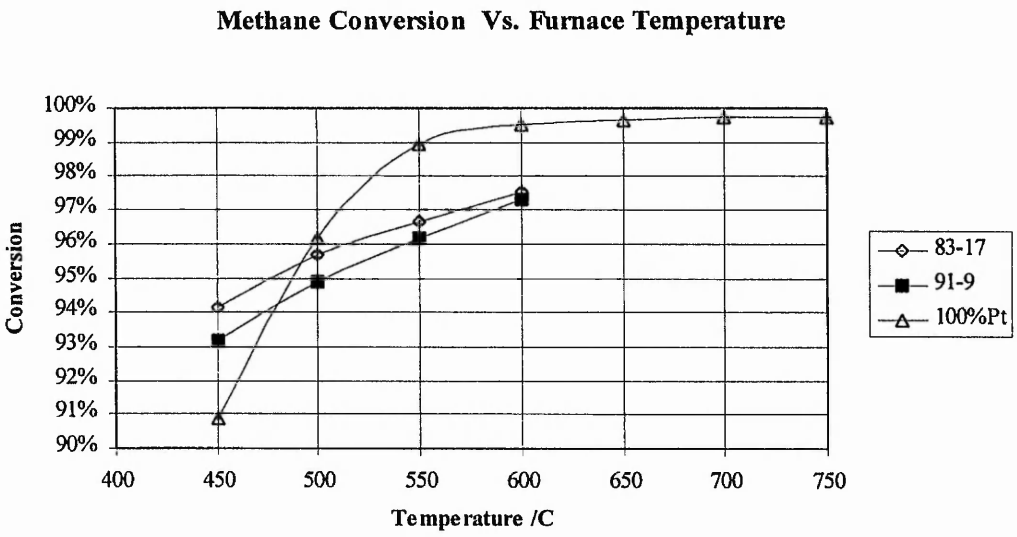

Figure 3.13: Methane Conversion

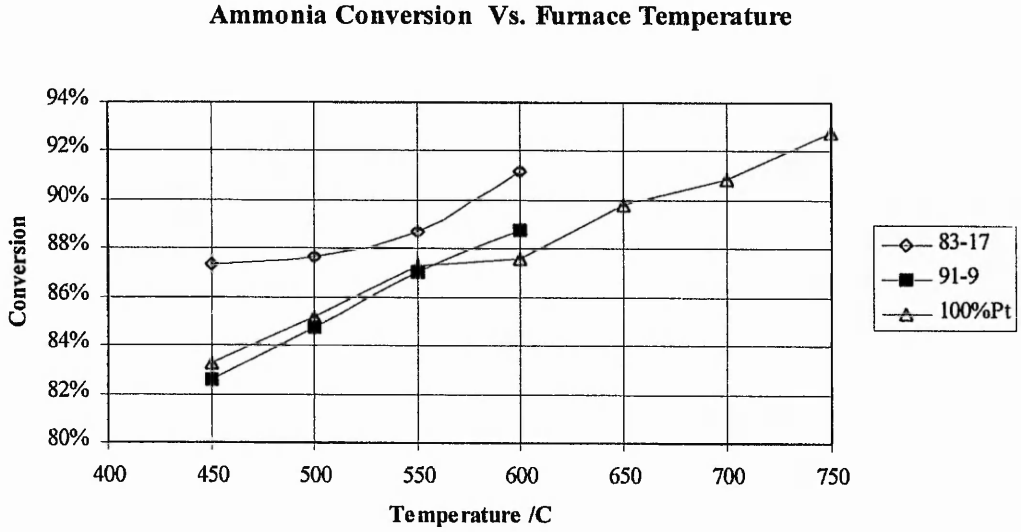

Figure 3.14:Ammonia Conversion

From figure 3.13 the platinum sample had low a methane conversion at 450°C in comparison with the rhodium containing catalysts. Methane conversion for the pure platinum catalyst was, however, affected by temperature to a greater degree than for the rhodium containing catalysts and by 500°C, methane conversion for the pure platinum catalyst was much higher than the rhodium containing catalysts. At 550°C the methane conversion was 99% for pure platinum, but was only 96-97% for the rhodium containing samples.

From figure 3.14, the general trend in ammonia conversion was similar to the trends observed for methane conversion, with the catalysts showing significant increases in ammonia conversion with applied temperature. The conversion of ammonia, was however, never greater than 93%. The 83-17 catalyst was seen to be the most active in the conversion of ammonia at 87%, with the 91-9 catalyst and the pure platinum catalyst showing much lower conversions at ~ 83%. This result in particular may reflect the fact that the 91-9 catalyst had not yet reached full activity as results from a fully activated catalyst, presented in section 3.2, showed ammonia conversions approaching 86%.

From the conversion and selectivity results, the effect of temperature on HCN yield was calculated. The yield Vs. temperature profiles for the 83-17, 91-9 and 100%Pt catalysts are shown in figure 3.15.

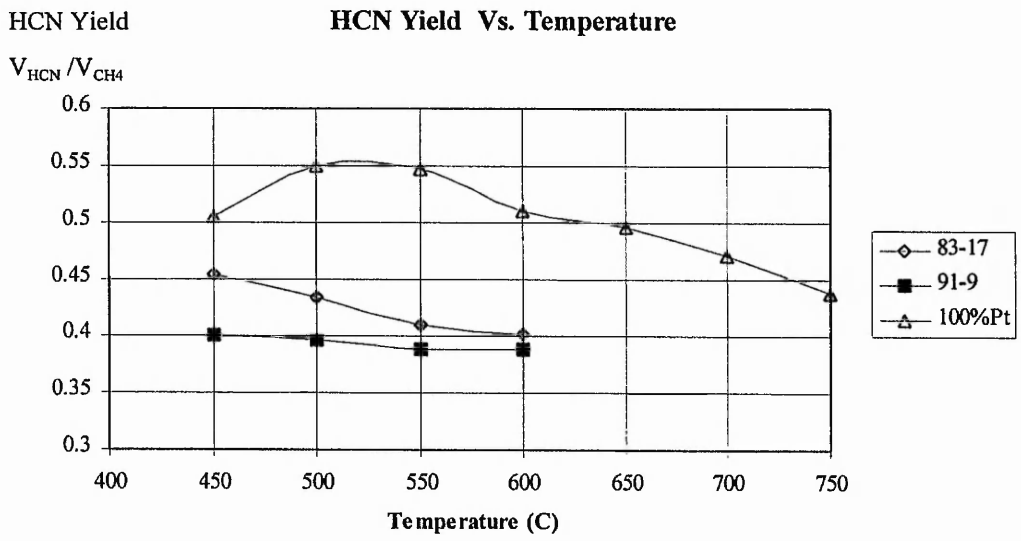

Figure 3.15: HCN Yield

Figure 3.15 shows that the pure platinum catalyst, operated under the correct temperature conditions is superior to the rhodium containing catalysts. The 83-17 catalyst outperformed the 91-9 catalyst, but this was probably due to the fact that the 91-9 catalyst was not fully activated.

3.4 References

[1] S.S. Bharadwaj. PhD Thesis. Faculty of the Graduate School, University of Minnesota. August 1995.

[2] D.A. Hickman, M. Huff, L.D. Schmidt. Ind. Eng. Chem. Res. **32** (5) 809-817 (1993).

[3] R. Villalobos, G.R. Nuss. ISA Transactions **4** 284-286 (1965).

4. Characterisation Introduction

4.1 Scanning Auger Microscopy (SAM)

4.1.1 Introduction

4.1.1.1 The Auger Process

When a specimen is irradiated with high energy electrons, a core electron may be ejected producing an excited state, for example a K-shell hole. The excited state is energetically unstable and must return to ground state. De-excitation may be achieved by the emission of an X-ray, and this is the physical basis of X-ray fluorescence. An alternative relaxation mechanism is the Auger radiationless process whereby an outer shell electron falls into the hole. The Auger process is spontaneous and liberates energy causing the emission of a second electron, leaving a doubly charged atom, as shown in figure 4.1.

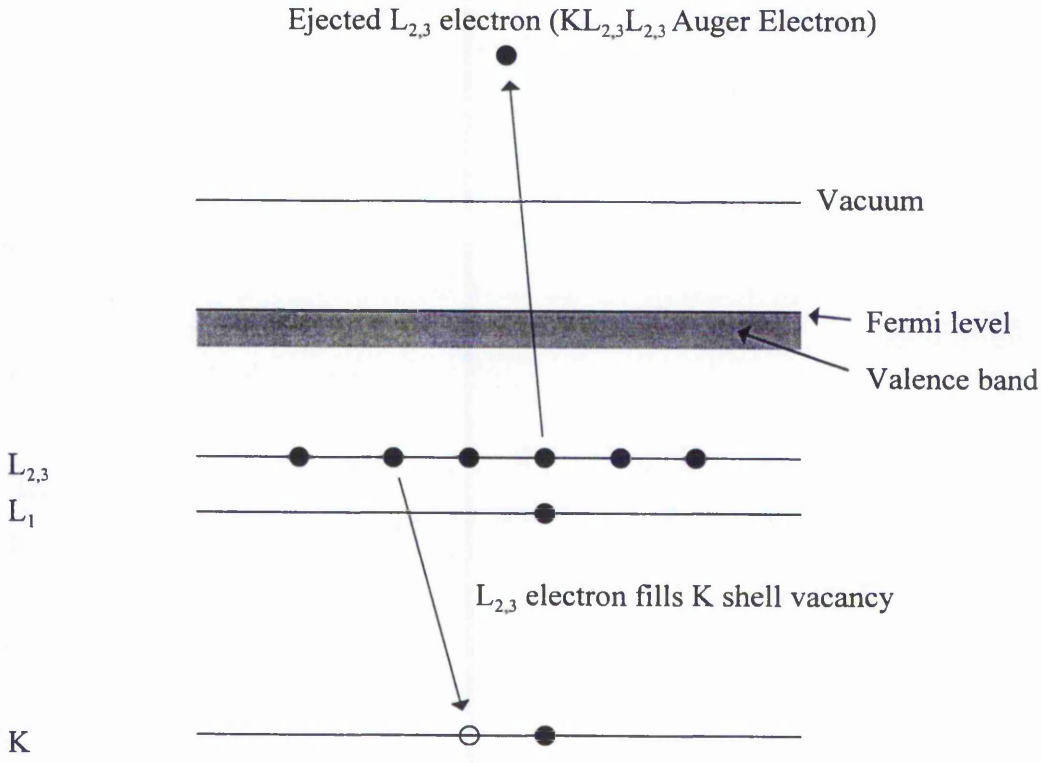

Figure 4.1 : Relaxation Of An Ionised Atom By the Emission Of a $KL_{2,3}L_{2,3}$ Auger Electron

Auger and background intensity that is more dependent on topography than chemical variations. To estimate near surface concentration of elements from Auger electron spectroscopy (AES) and Auger maps, a common procedure is to measure the peak intensity by measuring the count rate at the Auger peak (P) and subtract the value for the background (B) a few eV above the peak and normalise the peak height by dividing the peak intensity by the background intensity i.e. $(P-B)/B$[2]. The application of (P-B)/B correction has been shown to remove most of the effects due to changes in topography although the normalisation has not, however, met with total success[3]. There is a general acceptance that the use of a (P-B)/B ratios, as described above, is only valid for surfaces where the primary beam angle of incidence is near to normal[4] and has been shown to be highly sensitive to subsurface composition due to the effects of backscattering of the primary beam[5]. The backscatter factor contribution to the Auger yield, as shown in equation 4.2, is a function of the ionisation cross-section and the inelastic scattering energy spectrum[6]. Since the contribution due to backscattering changes with angle, surface composition and subsurface composition, backscattering has prevented the development of an analytical method for calculating surface ratios from the intensity of relative peaks, analogous to that used for quantitative X-ray photoelectron spectroscopy (XPS)[4].

Although there have been several attempts to quantify Auger spectroscopy without the use of calibration samples[7,8], the interpretation of results is usually carried out semi-quantitatively[5,9].

4.1.1.2 Surface Sensitivity of Auger Electron Spectroscopy

For an Auger electron to be detected, the electron must either originate from the surface layer or the electron must penetrate through the solid being analysed. The intensity of electrons emitted from a depth is given by a Beer-Lambert relationship[10] as shown by equation 4.3.

$$I = I_O e^{-d/\lambda Cos\theta}$$

Where I = the observed signal
I_O = the intensity at depth d
λ = the inelastic mean free path
d = the depth from which the electron was emitted
θ = the angle of trajectory through the solid from the normal

Equation 4.3: The Beer-Lambert Law Applied to the Extinction of Emitted Electrons

The inelastic mean free path is, according to definition, the distance normal to the surface at which the probability of an electron escaping without significant loss due to inelastic scattering drops to e^{-1} (36.8%) of its original value[11]. The inelastic mean free path (λ) has been investigated by Seah and Dench[12] and their results show that the probability of an electron escaping from the bulk of a solid is dependent on the depth below the surface at which it was emitted and on the energy of the electron. The Seah and Dench study also indicated that, within groups of materials i.e. organic substances, inorganic substances and metals, the inelastic mean free path is material independent. The inelastic mean free path was seen to pass through a minimum, at approximately 60 eV, as shown in figure 4.2.

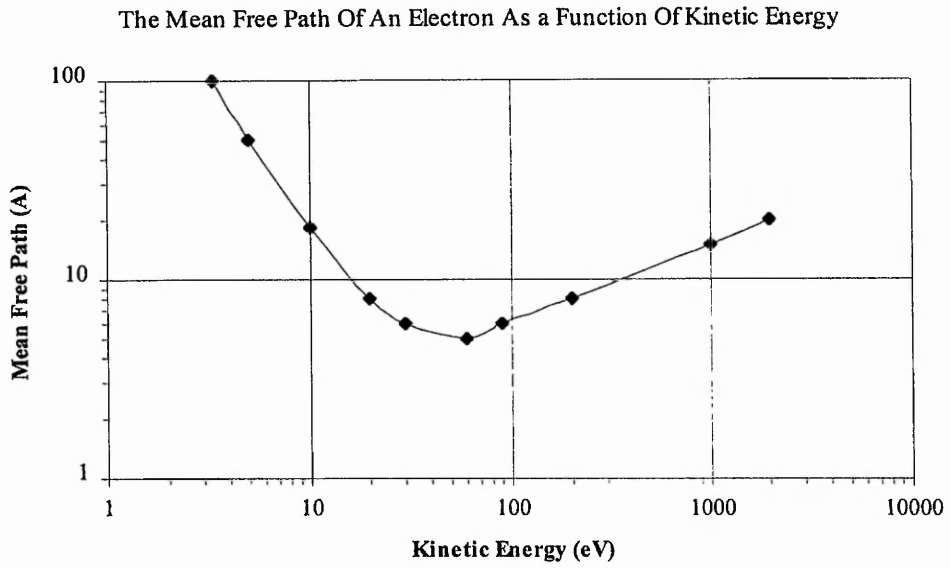

Figure 4.2: Inelastic Mean Free Path (λ) Variation With Respect to Electron Energy

In applying AES to platinum-rhodium alloys, the Auger electron energies shown in table 4.1 are of use as they are of high intensity and do not overlap each other. For reference, the inelastic mean free path for a 30 keV primary beam is also included. For the estimation of escape depth in monolayers, the thickness of 1 monolayer was assumed to be 2.5 Å.

Element	Auger Transition	Auger Electron Energy (eV)	Mean Free Path (Å)	Mean Free Path (monolayers)
Platinum	NOO	64	5	2
Carbon	KLL	270	8	3
Rhodium	MNN	302	9	3.5
Oxygen	KLL	510	11	4
Platinum	MNN	1,960	18	7
Primary Beam	N/A	30,000	75	30

Table 4.1: Auger Transitions of Interest in Pt-Rh Alloys

From knowing the inelastic mean free path, the layer-by-layer contribution to the total Auger yield can be calculated. The signal intensity for a monolayer below the surface (I_d) relative to the total intensity (I_0) was calculated by calculating the

intensity, at depth *d*, and subtracting the contribution due to the underlying substrate i.e. from depth *d+1*, as shown in equation 4.4.

$$I_i = (I_O e^{-d_i/\lambda}) - (I_O e^{-d_i+1/\lambda})$$

Equation 4.4 : Layer-By-Layer Contribution to the Auger Yield

The layer-by-layer contribution to the total Auger yield, obtained by solving equation 4.4 is shown in figure 4.3. The figure indicates that the contribution to the total observed Auger yield is insignificant for Auger electrons created more than 5 monolayers from the surface. Due to the high energy of the primary beam, and therefore large inelastic mean free path, attenuation of the primary beam over the first 5 monolayers is small at ca. 15%. Auger spectroscopy using a 30 keV primary beam can, therefore, be assumed to be essentially independent of the effects of primary beam attenuation.

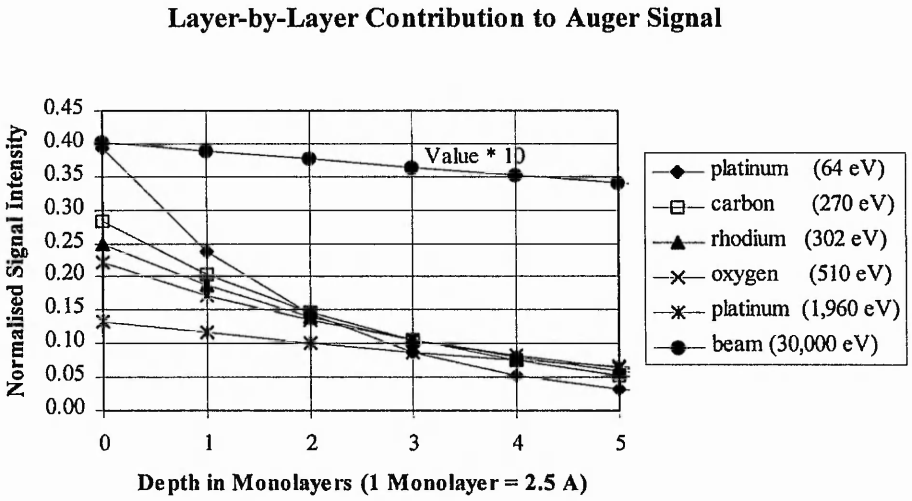

Figure 4.3: Attenuation of Primary and Auger Electrons With Depth

By examining the results shown in figure 4.3, the effect of changes in surface concentration on the observed Auger yield, and therefore observed near surface concentration, can be predicted. Although the assumption that segregation is limited only to the surface monolayer is not strictly true due to non-monotonic compositional variation in the near surface layers[13], the surface segregated substrate may be modelled using the following assumptions.

1. The Surface Monolayer may have any composition 0-100at%Rh.

2. The Bulk (excluding the surface monolayer) where the concentration of rhodium and platinum is assumed to be equal to the bulk value.

As the surface monolayer concentration is the only variable, limits exist for the model where the surface monolayer concentration is 0at%Rh (complete platinum surface segregation) and 100at%Rh (complete rhodium surface segregation). The surface sensitivity of the 302 eV Rh Auger peak is estimated at 25% (from figure 4.3), the calculation of Auger yields, and therefore observed Rh concentration at the near surface of a 17.4at%Rh alloy is as follows -

Rhodium 302 eV Peak		Surface Contribution		Bulk Contribution		
Pt surface	=	(25% * 0.000)	+	(75% * 0.174)	=	13%
Uniform surface / bulk	=	(25% * 0.174)	+	(75% * 0.174)	=	17.4%
Rh surface	=	(25% * 1.000)	+	(75% * 0.174)	=	38%

The model, therefore, suggests that a variation of rhodium surface concentration from 0% to 100% in an alloy containing 17.4at%Rh will result in a change in the observed Rh concentration from 13 to 38at%. For the platinum 1960 eV Auger peak the calculated change in observed near surface concentration is significantly less than the case for rhodium due to the low surface sensitivity of the analysis. Calculations indicate that a change of 100at% in the monolayer concentration from 0 to 100at%Pt would result in a change in the observed near surface concentration of 13at% (from 72at% to 85at%). Also shown below is the calculation for the 64 eV platinum Auger peak which, due to the short inelastic mean free path of the 64 eV electron, is highly surface sensitive.

Platinum 1960 eV Peak		Surf. Contribution		Bulk Contribution		
All Rh surface	=	(13.4% * 0.000)	+	(86.6% * 0.826)	=	72%
Uniform surface / bulk	=	(13.4% * 0.826)	+	(86.6% * 0.826)	=	82.6%
All Pt surface	=	(13.4% * 1.000)	+	(86.6% * 0.826)	=	85%

Platinum 64 eV Peak		Surf. Contribution		Bulk Contribution		
All Rh surface	=	(40% * 0.0)	+	(60% * 0.826)	=	50%
Uniform surface / bulk	=	(40% * 0.826)	+	(60% * 0.826)	=	82.6%
All Pt surface	=	(40% * 1.0)	+	(60% * 0.826)	=	94%

4.1.1.3 Background Effects And Quantification of Auger Spectra

Auger spectra for platinum and rhodium and carbon are shown in figure 4.4[14]. Although the distribution of the background for platinum and rhodium with respect to energy is similar, the exact shape of the background is shown, from these spectra, to be material dependent.

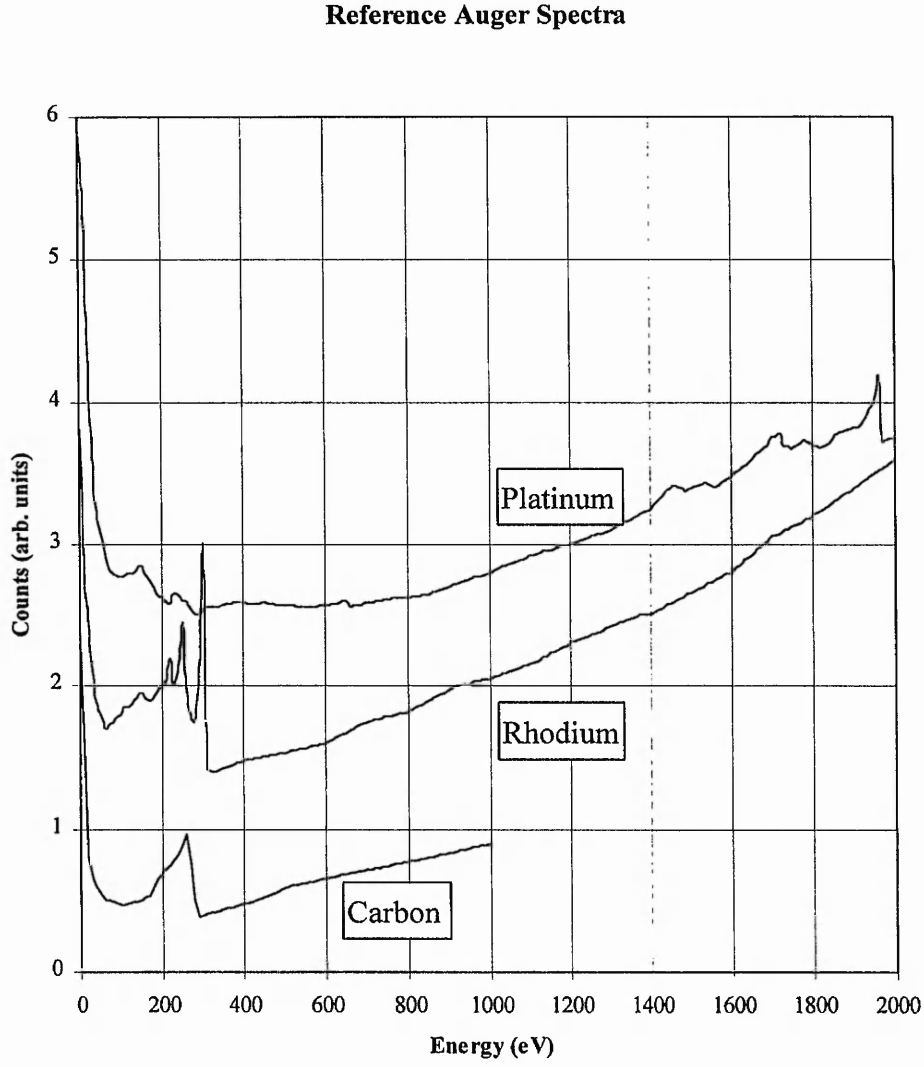

Figure 4.4 : Reference Auger Spectra for Platinum, Rhodium and Carbon

The non-equal contribution to the background with respect to energy, as shown in figure 4.4 is illustrated by comparing count rates, at points along the energy spectrum, for platinum and rhodium. From the platinum reference spectrum, the

background at 312 eV was found to be 68% of the background at 1980 eV. For rhodium, the background at 312 eV was found to be only 39% of the background at 1980 eV. The background intensity distribution for a platinum-rhodium alloy would, therefore, be a function of the composition, and as the concentration of rhodium increases, there would be a decrease in the background at 312 eV in comparison with the background at 1980 eV. The shift in background distribution has serious implications in attempts to quantify concentration measurements from Auger spectra by using ((P-B)/B) normalisation as changes in the background intensity (B) will have an effect on the background normalised peak intensity ((P-B)/B). For a Pt-Rh alloy a decrease in the background intensity in the rhodium 302 eV region of the Auger spectrum with increasing rhodium concentration would, therefore, result in a non-linear ((P-B)/B) Vs. concentration relationship. Furthermore, due to the possibility of differences in absolute background contribution[15], the background distribution with composition is difficult to predict. The use of calibration standards is, therefore, necessary to quantify AES on platinum-rhodium alloys. For high platinum concentration platinum-rhodium alloys such as a 83at%Pt-13at%Rh alloy, however, the background distribution is likely to be dominated by the background distribution for platinum.

As illustrated in figure 4.4, there is also a large difference in the background distribution between carbon and platinum[a]. For carbon the background at 312 eV was 46% of the background at 1000 eV, whilst for platinum, the background at 312 eV was 95% of the background at 1000 eV. Since, in the absence of Auger peaks, the background intensity at greater than 300 eV increases with kinetic energy, the background intensity for carbon at 312 eV would, therefore, be less than 46% of the value at 1980 eV. The presence of carbon at the near surface of a platinum-rhodium alloy would, therefore, cause a decrease in the background intensity at 312 eV relative to the background at 1980 eV. The relatively small contribution by carbon to the background intensity at 312 eV in comparison with the intensity at ~ 1000 eV and above is interesting as the presence of carbon will affect the background intensity at ca. 312 eV and ca. 1980 eV differently, and may result in a lesser reduction in the rhodium (302 eV) (P-B)/B peak than the platinum (1960 eV) peak.

Any attempt at quantifying AES of platinum-rhodium alloys may be further complicated by the possibility of carbon being either in the form of an overlayer (i) or within the bulk of the sample (ii) -

---

[a] Unfortunately the spectrum was only available in the energy range 0-1000 preventing a direct comparison with platinum or rhodium.

(i) The Presence of Carbon as an Overlayer

Consider the analysis of a homogeneous solid substrate, for example a homogeneous 83at% platinum 17at% rhodium alloy, covered with a layer of carbon 2 monolayers (5 Å) thick, as shown in figure 4.5.

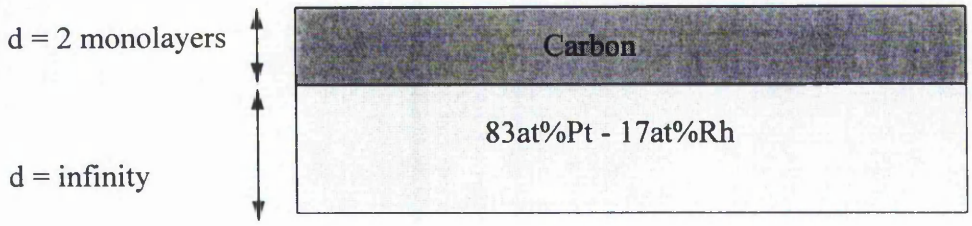

Figure 4.5 : Model of a Homogeneous Platinum Rhodium Alloy Covered With a Carbon Overlayer.

The interaction of a 30 keV SAM primary source and the subsequent secondary electrons with the sample would have the following effects.

1. The primary beam would not be attenuated significantly by the carbon overlayer due to the high energy, and therefore penetration depth. The intensity of high energy electrons capable of causing core excitation, and therefore Auger electron emission intensity at the platinum-rhodium surface would be unaffected by the presence of the overlayer.

2. The Auger and background electrons emitted from the surface of the platinum-rhodium alloy would be attenuated significantly by the presence of the carbon overlayer (Beer-Lambert attenuation).

3. The interaction of the primary beam with the carbon overlayer would result in both a carbon Auger peak and a contribution to the background intensity.

Since the presence of a 2 monolayer thick layer would not attenuate the primary beam significantly, there are therefore, two factors to consider -

1. Attenuation of secondary electrons

From the results of Seah and Dench, the inelastic mean free path of a 312 eV electron is approximately 3.5 monolayers, whilst the inelastic mean free path for a 1980 eV electron is approximately 7 monolayers. Assuming an overlayer thickness of 2 monolayers, the model indicates that 312 eV electrons emitted from and normal to the alloy surface would have a probability of escaping of $e^{-(2/3.5)} = 56\%$. At 1980 eV, the probability of escape from below a 2 monolayer thick overlayer would be $e^{-(2/7)} = 75\%$.

2. Contribution to the background

Although an overlayer of carbon would attenuate the emerging Auger and background electrons, for a reduction in the platinum and rhodium (P-B)/B value the overlayer must contribute to the background intensity. As the background intensity for carbon at 312 eV relative to the value at 1980 eV is significantly less than the corresponding value for platinum or platinum-rhodium alloys, there would be a change in the background distribution. Since the Pt and Rh Auger peaks are superimposed onto the background, by which the peak intensity is normalised ((P-B)/B), an estimation of overlayer thickness by measuring a decrease in either the Rh or Pt ((P-B)/B) with increasing carbon coverage may, therefore, contain serious errors due to the change in background distribution.

(ii) The Effect of Carbon Within the Bulk of the Alloy

Assuming an homogeneous bulk and surface composition, the presence of carbon within a platinum rhodium alloy would result in the following -

1. A reduction in the near surface of the concentration of the alloy components and, therefore, a reduction in the Auger electron peak intensities of platinum and rhodium.

2. The emission of carbon, rhodium and platinum Auger electrons and a contribution to the background from carbon, rhodium and platinum.

Although the presence of carbon would not attenuate the emerging electrons as in case (i), the presence of carbon would result in a carbon Auger peak and a contribution to the background intensity. The background contribution for carbon,

however, indicates that the decrease in the observed (P-B)/B value for platinum and rhodium would not be in direct relationship with the carbon concentration but would be a function of the difference between the background distribution of the alloy and carbon.

The presence of carbon either as an overlayer or within the bulk would, therefore, result in a change in the background distribution although the precise background distribution for cases (i) and (ii) may differ slightly due to the attenuation term in (i) but not in (ii). The calibration of AES for the analysis of platinum-rhodium alloys in the presence of carbon is, therefore, difficult and the exact location of carbon may influence the background intensity. Quantitative analysis of Pt-Rh-C samples, therefore, requires the use of Pt-Rh-C calibration standards, and as such is considered beyond the scope of this work.

4.1.2 Experimental

4.1.2.1 The Vacuum Generators Scanning Auger Microscope

The Auger spectra and maps were obtained on a model 220 Vacuum Generators scanning Auger microscope, fitted with a field emission tip (FET) source, operating at 30 keV, and a 200 mm hemispherical sector analyser (HSA) operating at a constant retard ratio (CRR) of 4. The FET, optic column, analysis and pre-treatment chambers were pumped by a combination of rotary-backed diffusion and ion pumps. The base pressure in the FET, analysis and preparation chambers was always better than 10^{-10} 10^{-8} and 10^{-8} mbar respectively. Instrument control was via an IBM compatible computer, running the IBM OS/2 operating system and V.G. Eclipse V1.7 software.

To achieve sample admission to the SAM, samples were mounted on stubs and admitted into the instrument via a fast entry lock and pre-treatment chamber. Analysis was performed with the sample mounted on a stage allowing x,y,z and θ movement. A diagram of the main features of the SAM is shown in figure 4.6.

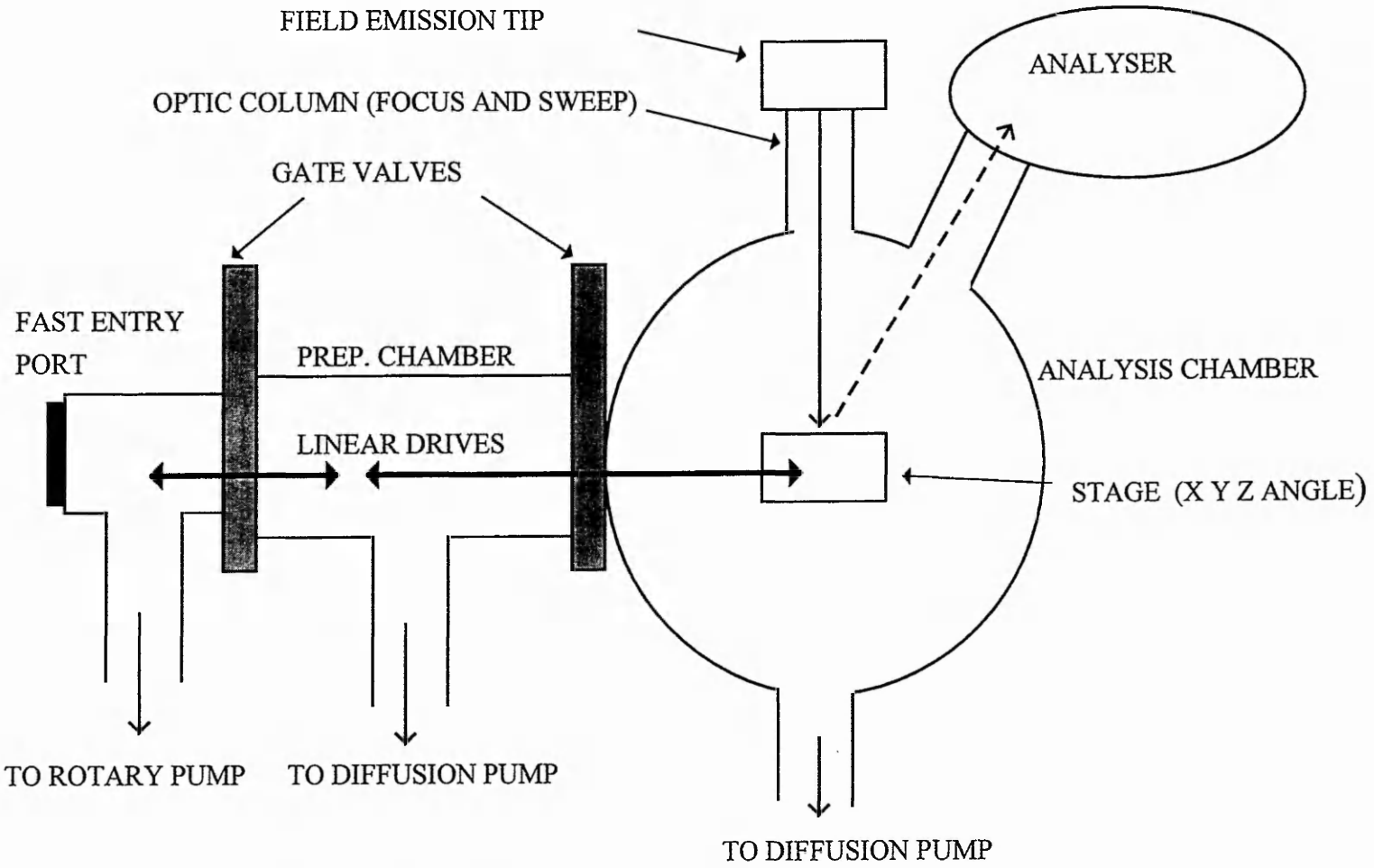

Figure 4.6: Diagram of the Scanning Auger Microscope

The SAM was operated for (i) point analyses and (ii) Auger maps. Time of acquisition varied from 2-5 minutes for point analyses and up to 20 minutes per element for Auger maps. During repeated mapping of the same area (for C, O, Rh and Pt) the stage drift was checked using the background Auger image, as this was found to be virtually equivalent to the SEM image.

(i) Point Analysis

For point analyses, the SEM image was captured via the computer data station and displayed on the computer display. Points of interest were then located on the image by locating a cross on the precise location of interest. The analysis was performed either as a single region from 20-2200 eV or in the following regions -

20-270 eV	platinum 64 eV, carbon 270 eV and rhodium 302 eV Auger peaks.
450-550 eV	oxygen 510 eV Auger peak.
1800-2200 eV	platinum 1960 eV Auger peak (+other platinum peaks).

The step size was either 1 eV for the scans performed from 20-2200 eV otherwise a step size of 0.2 eV was used. The dwell time was always 100 ms per step and typically two scans were performed per region.

(ii) Auger Maps

For the generation of Auger maps, the SEM image was first captured as described above. A wide area scan (20-2200 eV) was then performed to accurately quantify suitable peak and background values for the peaks of interest. The mapping process was carried out either as an array of either 256*256 (65,536) pixels or 128*128 (15,876) pixels. The dwell time used was typically 100 ms per pixel (50 ms measuring the peak count rate and 50 ms measuring the background count rate).

4.1.2.2 Data Analysis

Point Analyses

Data analysis was carried out by firstly converting the file from V.G. Eclipse format to an ASCII file[a] and then importing the file into the Grams[b] software package for data manipulation.

---

[a] Written by D. Batchelor IRC For Surface Science, Liverpool University.

[b] Grams386. Published by Galactic Industries Corporation.

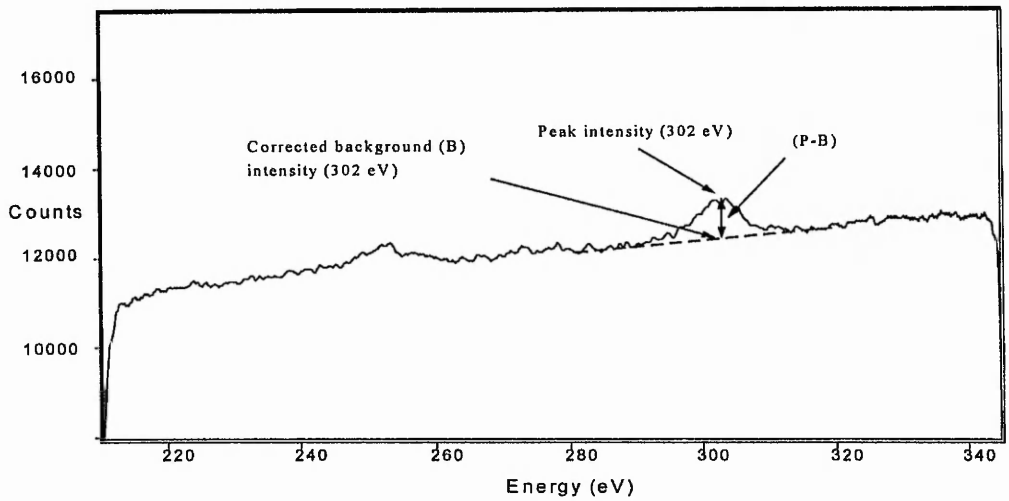

Figure 4.7: Example Spectrum Showing Peak and Background Assignments

Normally, the estimation of near surface concentration was achieved by a standard (P-B)/B intensity where P was the peak Auger count rate and B was the background intensity a few eV above the Auger peak. As seen in figure 4.7, the background intensity for the region at around 200-350 eV is sloping, an attribute that was found to be highly sensitive to instrumental effects. For rhodium, the background intensity (B) was calculated by averaging background intensities at 292 and 312 eV (10 eV either side of the peak).

Auger Mapping

Since the Eclipse Auger mapping software did not allow for multiple background measurement, the use of a 'corrected' 302 eV background value for rhodium was not possible. For all elements, a (P-B)/B normalisation was used where P was the Auger peak intensity and B was the background intensity a few eV above the Auger peak.

4.1.2.3 Instrument Calibration

In general, AES analyses accurate to within ± 5% are extremely difficult, even impossible without standards of a composition very similar to that of the unknown[16]. The use of calibration standards is, therefore, necessary if there is to be any attempt at estimating near surface composition. The use of Pt-Rh standards is, however, complicated by surface segregation[17] requiring the sample to be sputtered before use. The application of sputtering to prepare surfaces for analysis is, however,

complicated by artefacts caused by the sputtering process such as differential sputtering[18] which may result in inaccuracies in the calibration procedure. Sputter yield studies performed on the pure metals[19] have, however, indicated that the sputter yields for platinum and rhodium are similar and the results predict that the exposed near surface composition would be similar to the bulk composition.

Calibration Procedure

To carry out the calibration, a sample of 82.6at%Pt-17.4at%Rh alloy was firstly admitted to the preparation chamber and sputtered with 10 keV Ar^+ ions (80 μA over 1 cm^2) for 25 minutes before admission of the sample into the analysis chamber.

The Pt and Rh sensitivity factors are defined as the (P-B)/B value divided by the bulk concentration, as shown below.

$$\frac{\frac{(P-B)}{B}}{bulk\ concentration} = sensitivity\ factor.$$

The results of the AES point analyses of the sputtered surface are shown in table 4.1

Point Analysis	Carbon	Rhodium	Oxygen	Platinum
P1	0.06	0.14	trace	0.21
P2	0.02	0.10	trace	0.20
P3	0.08	0.10	trace	0.22
P4	0.11	0.12	trace	0.22
P5	0.12	0.09	trace	0.20
P6	0.13	0.08	trace	0.20
P7	0.15	0.07	trace	0.19
Average	0.10 ± 0.05	0.10 ± 0.02	trace	0.21 ±0.01

Table 4.1: SAM Results for Sputtered Unused 83-17 Gauze. Surface concentrations are expressed as peak - background / background intensities.

The platinum near surface concentration for the 83-17 sample, measured as (P-B)/B, was 0.21 ± 0.01. The rhodium near surface concentration was measured as 0.10 ± 0.02. The sputtered sample exhibited significant carbon Auger peaks and indicated that carbon may have been present within the bulk of the sample, however, the possibility that adsorption of carbon containing species from the residual gas within the pre-treatment and analysis chambers cannot be excluded.

Samples of real catalyst almost universally exhibited a carbon Auger peak and the use of these calibration figures may, to some extent, correct for the error associated with the presence of carbon although the results obtained must be considered semi-quantitative.

By dividing the observed rhodium and platinum near surface concentration ((P-B)/B) by the respective bulk concentration, as discussed earlier, the sensitivity factors were estimated -

Observed Rh near surface concentration (Rh 302 eV (P-B)/B)		=	0.10± 0.02	
Bulk Rh Concentration		=	0.174	
Sensitivity factor	0.10 / 0.174	=	0.57	± 0.11

Observed Pt near surface concentration (Pt 1980 eV (P-B)/B)		=	0.21± 0.01	
Bulk Rh Concentration		=	0.826	
Sensitivity factor	0.21/ 0.826	=	0.25	± 0.01

4.1.2.4 Sample Pre-treatment

Initial attempts to characterise samples of unused catalyst and a sample of used platinum-rhodium catalyst taken from an industrial reactor were dominated by a large carbon Auger peak which required extensive Ar^+ ion sputtering (10 keV Ar^+ ions, 80 μA over 1 cm^2, for 10 minutes) to reveal significant platinum or rhodium Auger peaks. As sputtering of samples, using the conditions specified above, is generally accepted to remove many monolayers from the surface[20], and that any surface segregation would only be likely for the first monolayers or so[21], sputtering of the sample was not considered conducive to obtaining a representative sample of an active catalyst surface.

In an attempt to remove the carbon overlayer without the need for sputtering of the surface, a sample of catalyst, removed from the industrial reactor, was heated to

200° C in oxygen overnight before admission, whilst still hot, into the fast entry lock of the Auger spectrometer. As the temperature of the furnace was kept to less than < 0.3 of the melting point of either platinum or rhodium, the temperature was considered too low to enable surface or bulk diffusion to occur significantly[22].

From results presented in chapters 5-7 the oxygen pre-treatment method was seen to be capable of removing much of the carbon from the surface of the catalyst, allowing characterisation the underlying platinum and rhodium, but also left some surface carbon. Furthermore, as samples of catalyst gauze in some cases were found to exhibit little or no surface oxygen, the pre-treatment was shown to cause little or no surface oxidation of the samples.

4.2 X-Ray Photoelectron Spectroscopy

4.2.1 Introduction

When a specimen is irradiated with an X-ray source, a core electron may be ejected as a photoelectron as indicated by figure 4.8.

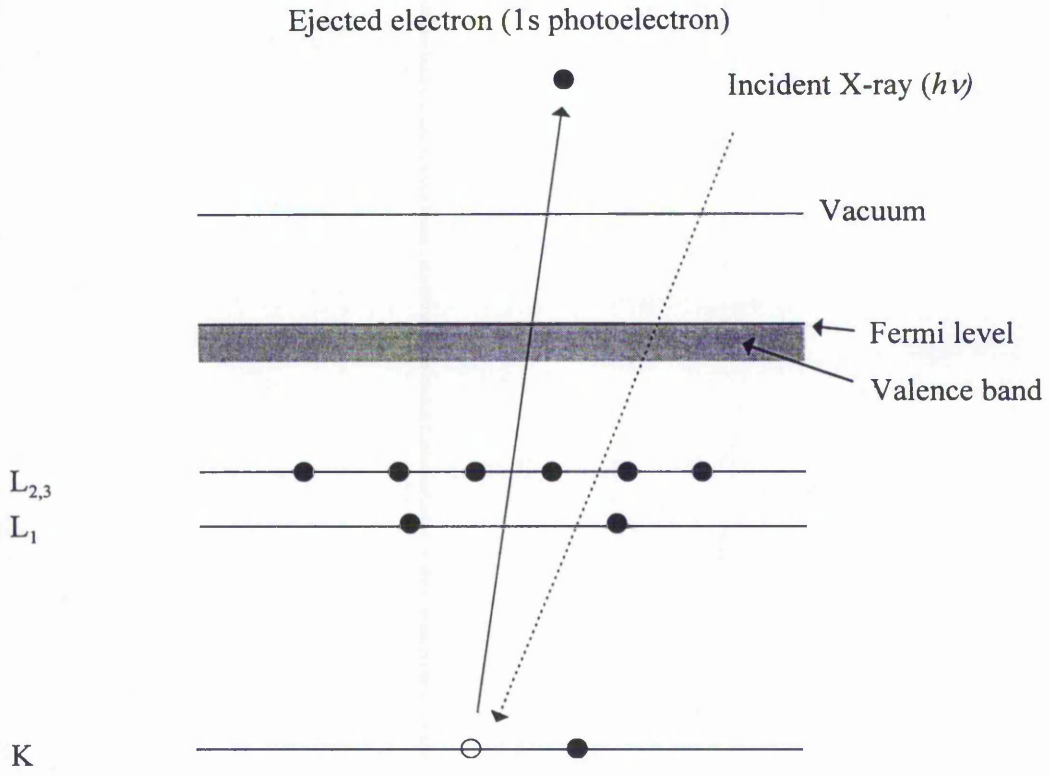

Figure 4.8: The X-Ray Photoelectron Process

The kinetic energy of the electron is determined by the energy of the incident X-ray and the binding energy of the orbital from which the electron originated. Commonly used X-ray sources include Al K_α ($h\nu$ = 1486.3 eV) and Mg K_α ($h\nu$ = 1253.6 eV) produced by the interaction of high energy electrons with aluminium or magnesium. Equation 4.5, the Einstein equation, describes the relationship between incident photon energy, the binding energy and the kinetic energy of the emitted electron.

$$E_K = h\nu - E_B + \phi$$

Where E_K = Kinetic energy of the emitted photoelectron
$h\nu$ = Incident photon energy
E_B = Electron binding energy
ϕ = Spectrometer workfunction

Equation 4.5 : XPS Photoelectron Energy Calculation - The Einstein Equation

Although the penetration of X-rays through the sample may extend significantly into the bulk, the escape depth for the photoelectrons produced within the bulk is determined by the kinetic energy as discussed in section 4.1.1.2. The technique is therefore surface sensitive, with the true surface sensitivity governed by the photoelectron energy. A major advantage of X-ray photoelectron spectroscopy over other surface spectroscopies, such as AES, is the ease with which quantitative analyses may be performed [23].

4.2.2 Experimental

X-ray photoelectron spectroscopy were recorded using a Vacuum Generators ESCA3 instrument. The X-ray source used was the Al (K_α $h\nu$ = 1486.3 eV). During analysis, the pressure in the analysis chamber was always less than 10^{-6} mbar. Samples were attached onto the sample holder by a single Pt-Rh wire as shown in figure 4.9. Note that due to the form of the catalyst samples, i.e. a mesh, a contribution from the sample holder to the XPS spectrum was unavoidable, and this prevented the estimation of either carbon or oxygen near surface concentrations. The analysis, therefore, concentrated on the measurement of platinum to rhodium elemental ratios.

Instrument control and data analysis was via an IBM compatible computer, running MSDOS operating system and Spectra 6 software[a]. The acquisition time for the narrow spectra from 475-575 eV binding energy was 1-2 hours per sample.

[a] Published by Ron Unwin Associates

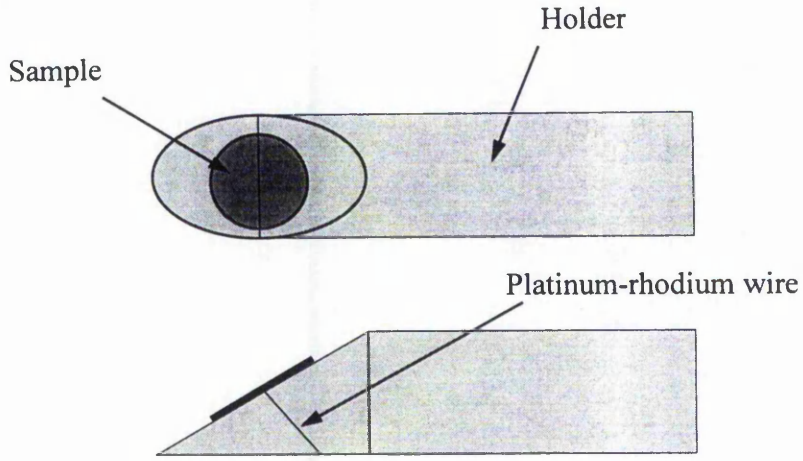

Figure 4.9 : Attachment of the Sample to the Holder

The sample was admitted to the analysis chamber via a sample admission / pre-treatment chamber coupled with gate valves and a linear drive.

For the investigation of platinum rhodium alloys the Rh 3p $^3/_2$ and Pt 4p $^3/_2$ XPS peaks were used as they have similar binding energies at around 500 eV, and therefore similar photoelectron energies (1000 eV), resulting in equivalent escape depths (14Å). Cross sectional areas for the Rh and Pt XPS peaks were taken from a table of calculated cross sectional areas by Schofield[24]. Complexities arose, however, in the use of these peaks as the Rh 3p $^3/_2$ peak overlapped with the Pt 4p $^3/_2$ peak and it was found necessary to separate the Pt 4p $^3/_2$ peak from the O 1s peak via a peak-fit routine. A sample XPS spectrum is shown in figure 4.10.

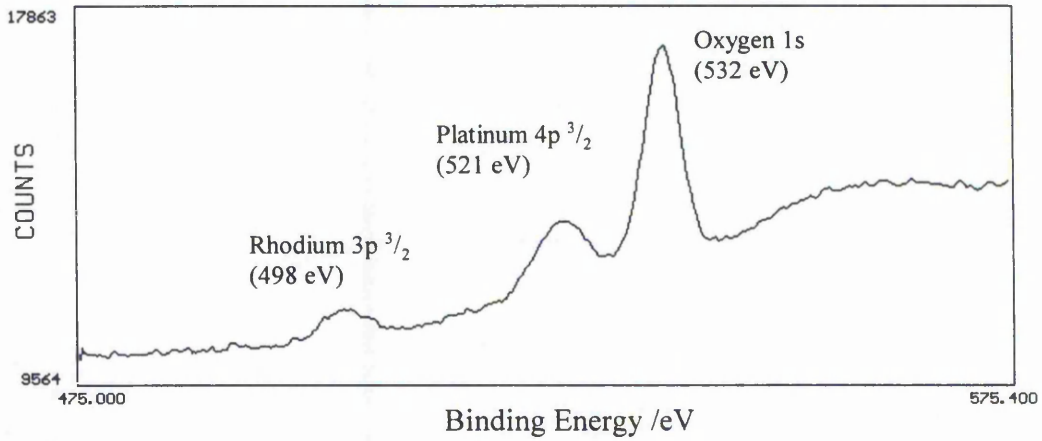

Figure 4.10: Example XPS Spectra Showing Rh, Pt and O peaks

An example peak-fit for platinum and oxygen is shown in figure 4.11. A good degree of fit is seen by the close correlation of the theoretical and experimental values (the dotted and solid lines), and indicated in the lower section of the figure.

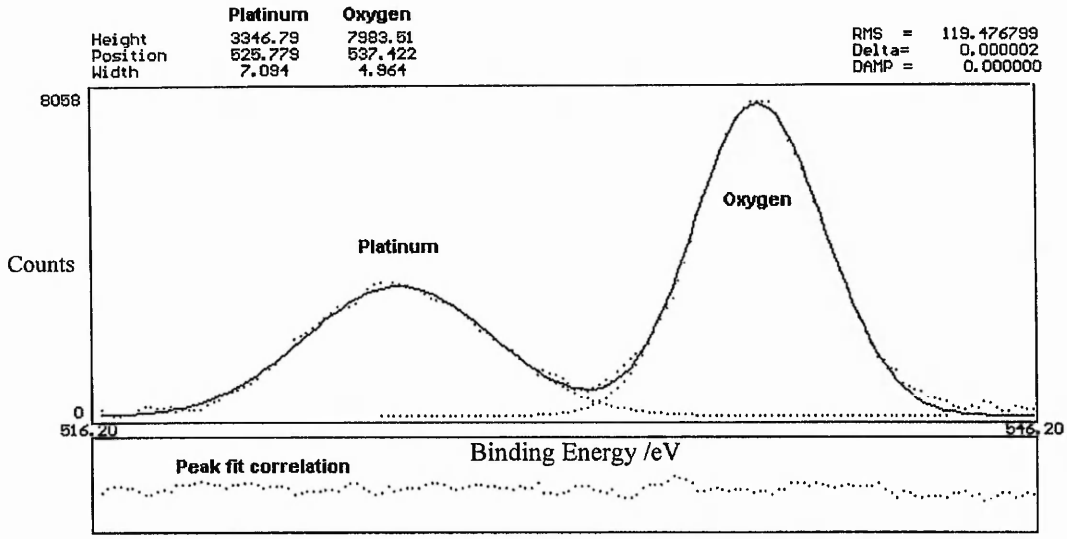

Figure 4.11: Example XPS Spectra Pt - O Peak Fit

The method of data analysis, using results taken from the characterisation of an unused 17.4at%Rh 82.6at%Pt catalyst sample (from chapter 5), is shown below.

Example XPS Surface Concentration Calculation

Peak area : Rh 3p $^{3}/_{2}$ (498 eV binding energy) = 366
Peak area : Pt 4p $^{3}/_{2}$ (521 eV binding energy) = 1007

As can be seen from Schofields table of cross sectional areas[26], the Rh 3p $^{1}/_{2}$ XPS peak overlaps the Pt 4p $^{3}/_{2}$ peak at 521 eV binding energy. From knowing the relative intensities of the Rh 3p $^{3}/_{2}$ and Rh 3p $^{1}/_{2}$ XPS peaks, as shown below, the Rh 3p $^{1}/_{2}$ peak area was calculated and subtracted from the Pt 4p $^{3}/_{2}$ peak area.

Rh 3p $^{3}/_{2}$ cross sectional area (at a primary X-Ray energy of 1486.3 eV) = 7.21
Rh 3p $^{1}/_{2}$ cross sectional area (at a primary X-Ray energy of 1486.3 eV) = 3.64
Pt 4p $^{3}/_{2}$ cross sectional area (at a primary X-Ray energy of 1486.3 eV) = 5.74

To correct for peak overlap -

Pt 4p $^3/_2$ (corrected) = Pt 4p $^3/_2$ (observed) - (Rh 3p $^3/_2$ * (3.64 / 7.21))
= 1007 - (366 * (3.64 / 7.21))
= 822

The corrected Pt 4p and Rh 3p $^3/_2$ peak areas were then normalised by dividing the peak areas by the relevant cross sectional areas to give the normalised peak areas.

Normalised peak area for Rh = 366 / 7.21 = 50.8
Normalised area peak for Pt = 822 / 5.74 = 143.2

The normalised peak areas were then used to calculate the near surface concentration of rhodium by dividing the normalised area for rhodium by the sum of the normalised platinum and rhodium peak areas i.e.

$$Rhat\% = \frac{Normalised\ counts\ for\ rhodium}{Normalised\ counts\ for\ (rhodium+platinum)}$$

$$Rhat\% = \frac{50.8}{50.8+143.2} = 26at\%$$

As discussed in section 4.2, the XPS analysis was estimated to have a surface sensitivity of 18% i.e. a change in the surface monolayer composition of 100% (from 0 to 100% Rh) would increase the observed Rh concentration by 18at%. By calculating and subtracting the bulk contribution from the concentration, observed by XPS, the surface monolayer contribution to the observed concentration could be calculated.

Bulk contribution = bulk sensitivity * bulk concentration
= 82% * 17.4%
= 14.3at%

Surface monolayer contribution = 26% - 14.3% = 11.7at% ± 1at%[a]

[a] The error associated with the analysis was estimated by calculating the standard deviation of repeated measurements of the Rh 3p $^3/_2$ peak area.

Surface monolayer rhodium concentration = 11.7% / 18%
(surface contribution / sensitivity) = 66% ± 6at%Rh

Surface monolayer platinum concentration = 34% ± 6at%Pt
(By balance)

The technique of XPS, therefore, allowed an estimation of the surface concentration of platinum and rhodium which was independent of the presence of other near surface elements such as oxygen and carbon.

4.3 Secondary Ion Mass Spectroscopy

4.3.1 Introduction

Secondary ion mass spectroscopy, (SIMS), is the mass spectroscopy of atomic or molecular particles which are ejected from a surface when bombarded with energetic primary ions such as Ar^+ or Cs^+.

When an energetic ion hits a surface, the ion will lose energy to the surface atoms although some energy may be lost in electronic (inelastic) excitation processes[25]. Due to the large cross section for elastic energy transfer, an incident ion will set many target atoms in motion either directly or via collisions of primary knock-on atoms with other target ions[25]. Such an event is commonly known as a 'collision cascade' which may be interpreted as a series of billiard ball type interactions. If the energy transferred from either the primary ion or from a cascade type interaction exceeds a certain limit, the struck atom may be displaced permanently from its original site, leaving a vacancy behind. The displaced atom which will then either strike another atom in series, or if the outward momentum and energy exceed the surface potential barrier, the particle may be 'sputtered' from the surface[26].

A computer simulation study on copper has been carried out by Ishitani and Shimizu[27] where 4 keV Ar^+ ions were assumed to strike a copper surface at normal incidence. Their results indicated that the travel of most of the displaced atoms within the solid was of the order of 1 nm and only very few atoms travelled for more than 3 nm before coming to rest. The results, therefore, indicate that the mean depth of origin of sputtered samples was less than 1 nm. Assuming a monolayer thickness of 2.5 Å, the majority of sputtered particles originate from the first 4 monolayers.

Ionisation of secondary particles may occur as the particle leaves the surface and the electronic state of the surface has a strong effect on the ionisation probability of the desorbing species[28]. The probability of ionisation (to a negative or positive ion) shows a dependency on the ionisation potential and electron affinity of the particle, but the electronic state of the matrix is the major influence[29]. Care has therefore to be exercised when evaluating SIMS results and there are significant difficulties in quantification of SIMS results. The SIMS yield is given in equation 4.6.

$$i_s^M = i_p Y R^+ \theta_M \eta$$

Where i_s^M = the secondary ion current of an element or species M.
i_p = the primary particle flux.
Y = the sputter rate for M.
R^+ = the ionisation probability of positive secondary ions.
θ_M = the fractional coverage of M.
η = the transmission of the analysis instrument.

Equation 4.6: SIMS Yield Equation

If the primary current density impinging on the surface is high, the surface may be eroded away at a significant rate, resulting in a technique that is amenable to depth profiling, but not to analysis of the original surface. This type of SIMS analysis is termed dynamic SIMS (DSIMS) and is commonly used in the analysis of fairly thick overlayers (in the μm range) used in the electronic device manufacture industry[30]. The surface specific variant of the SIMS process - static SIMS (SSIMS) is dependent on the ion dose to the surface being sufficiently low at the end of an analysis that the surface is essentially undamaged by the sputtering process[31]. The surface sensitivity of SSIMS is, therefore, dependent only on the sputter escape depth which is typically < 1 nm giving the technique good surface sensitivity.

4.3.2 Experimental

The SIMS results were obtained using a Physical Electronics PHI 7200 ToF SIMS instrument as described elsewhere[32]. The apparatus used an 8 keV Cs^+ primary ion beam extracted from a tungsten heated frit-type ion source. The beam diameter was ~ 100 μm in spectroscopy mode, and ~ 50 μm in depth profiling mode. The ion gun produced primary ion pulses with a duration of approximately 1 ns at the sample surface. Secondary ion mass analysis was achieved via a time of flight (ToF) detector.

For the depth profile characterisation of platinum-rhodium alloys, the Rh : Pt M^+ ion peak area ratio was measured with respect to ion dose. The analysis was normally continued for sufficient time such that the observed Rh : Pt ion ratio was constant. This was done so that the ion ratio at the end of the analysis could be assumed to be representative of the bulk composition of the sample, allowing calibration of the analysis. For example, in the characterisation of a 17.4at%Rh alloy, if the final Rh : Pt ion ratio was found to be 10 : 1, and at the beginning of the analysis the Rh : Pt ion was found to be 20 : 1, the elemental ratio at beginning of the analysis, i.e. the surface, was assumed to be twice that found in the bulk.

For the estimation of trace components, such as iron, calibration would have been virtually impossible. Here the analysis was carried out comparatively from sample to sample, by comparing values obtained by dividing the ion yield for the specific element by the total ion yield.

Static SIMS Operation

Firstly, a *spectroscopy* mode was used which utilised a static ~ 100 μm diameter beam and collected information about the sample in this area. This technique was used to survey the sample as the technique gave spectra of high mass range in high resolution.

Dynamic SIMS Operation

The instrument was used in *depth-profiling* or dynamic SIMS mode. The experiment consisted of a series of quasi-static SIMS experiments performed one after another on the same 50 μm diameter point on the sample. In depth profiling mode the spectrum was recorded continuously and the depth profiling arose from sample damage during spectrum acquisition.

Due to the destructive nature of SIMS, in each case a fresh portion of the gauze was used for any subsequent analysis.

4.4 References

[1] I.R. Barkshire, J.M. Walton, M. Prutton. Surface and Interface Analysis **20** 583-588 (1993)

[2] E. Paparazzo, L. Moretto, C. D'Amato, A. Palmieri. Surface And Interface Analysis **23** 69-76 (1995).

[3] M.A. Baker, P. Tsakiropoulos. Surface And Interface Analysis **20** 589-594 (1993).

[4] L. Frank, M.M. El Gomati. Czechoslovak Journal of Physics **44** (3) 173-193 (1994).

[5] M.M. El Gomati. Vacuum **38** (4-5) 337-340 (1988).

[6] C.L. Lee, K.Y. Kong, H. Gong, C.K. Ong. Surface And Interface Analysis **24** 15-22 (1996).

[7] I.G. Batirev, A.N. Karanov, J.A. Leiro, M. Heionen, J. Juhanoja. Surface and Interface Analysis **23** 50-54 (1995).

[8] S. Mroczkowski, D. Lichtman. Surface Science **127** 119-134 (1983).

[9] C.G.H. Walker, D.C. Peacock, M. Prutton, M.M. El Gomati, Surface And Interface Analysis **11** 266-278 (1988).

[10] J.F. Watts. 'An Introduction to Surface Analysis by Electron Spectroscopy' Royal Microscopical Society Microscopy Handbooks Vol. **22** 3-9 (1990).

[11] A. Jablonski. Surface And Interface Analysis. **21** 758-763 (1994).

[12] M.P. Seah, W.A. Dench. Surface and Interface Analysis **1** 2-11 (1979).

[13] A.D. van Langenveld, J.W. Niemantsverdriet. J. Vac. Sci. Technol. A **5** (4) 558-561 (1987).

[14] Adapted from V.G. Scientific Auger Handbook. First Edition. Pub. V.G. Scientific Ltd. East Grinstead, England. (1989)

[15] Practical Surface Analysis by Auger and X-Ray Photoelectron Spectroscopy. D. Briggs, M.P. Seah. (Ed.) Pub. John Wiley & Sons. Chichester pp. 183-187. (1983).

[16] Practical Surface Analysis Volume 2 - Ion and Neutral Spectroscopy (second edition). D. Briggs, M.P. Seah. (Ed.) Pub. John Wiley & Sons. Chichester pp. 194 (1992).

[17] F.C.M.J.M. van Delft, B.E. Nieuwenhuys, J. Siera, R.M. Wolf. I.S.I.J. International. **29** 550-559 (1989).

[18] Practical Surface Analysis by Auger and X-Ray Photoelectron Spectroscopy. D. Briggs, M.P. Seah. (Ed.) Pub. John Wiley & Sons. Chichester. pp. 213 (1983)

[19] V.G. Scientific Auger Handbook. First Edition. Pub. V.G. Scientific Ltd. East Grinstead, England. (1989)

[20] P.C. Zalm. Surface And Interface Analysis **11** 1-24 (1988).

[21] P.A. Dowben, A. Miller. Surface Segregation Phenomena. CRC Press pp. 408-409 and references within. (1990).

[22] C.N. Satterfield. Heterogeneous Catalysis In Industrial Practice. 2nd Ed. McGraw-Hill Inc. pp.113 (1991)

[23] C. R. Brundle, C. A. Evans Jr., S. Wilson. Encyclopaedia of Materials Characterisation p 282-299, Butterworth - Heinemann (1990).

[24] J.H. Schofield. J. Electron Spectroscopy. **8** 129 (1976).

[25] D. Briggs, M.P. Seah. (Ed.). Practical Surface Analyis Second Edition. Volume 2 - Ion and Neutral Spectroscopy. Pub. John Wiley & Sons. Chichester pp. 106 (1992).

[26] R. Behrisch (Ed.) Topics in Applied Physics **47**. Sputtering by Particle Bambardment 1. Physical Sputtering of Single Element Solids. Springer-Verlag pp. 5 (1981)

[27] T. Ishitani, R. Shimizu. Phys. Lett. **46A** 487 (1974).

[28] D. Briggs, M.P. Seah. (Ed.). Practical Surface Analyis Second Edition. Volume 2 - Ion and Neutral Spectroscopy. Pub. John Wiley & Sons. Chichester pp. 178 (1992).

[29] L.C. Feldman, J.W. Mayer. Fundamentals of Surface And Thin Film Analysis. Pub. North-Holland. pp. 86 (1986).

[30] D. Briggs, M.P. Seah. (Ed.). Practical Surface Analyis Second Edition. Volume 2 - Ion and Neutral Spectroscopy. Pub. John Wiley & Sons. Chichester pp. 229-301 (1992).

[31] D. Briggs, M.P. Seah. (Ed.). Practical Surface Analyis Second Edition. Volume 2 - Ion and Neutral Spectroscopy. Pub. John Wiley & Sons. Chichester pp. 303-307 (1992).

[32] S. Reichlmaier, J.S. Hammond, M.J. Hearn, D. Briggs. Surface and Interface Analysis **21** 739-746 (1994).

5. Characterisation - Unused Gauze

5.1 Introduction

Samples of unused catalyst gauze of composition 83at%Pt - 17at%Rh (83-17) and 91at%Pt - 9at%Rh (91-9) were characterised using a range of techniques. Scanning electron microscopy (SEM) was used to image the catalyst surface whilst the analytical techniques of Auger electron spectroscopy (AES), X-Ray photoelectron spectroscopy (XPS) and time of flight secondary ion mass spectroscopy (ToFSIMS) were used to investigate the near surface composition.

5.2 Scanning Electron Microscopy / Scanning Auger Microscopy

A sample from an unused catalyst gauze was admitted to the scanning electron microscope (SEM) and imaged. Figure 5.1 shows a representative SEM image of a catalyst of knitted construction. Figure 5.1 also shows that, apart from draw marks along the length of the wire, the surface of the unused catalyst was smooth.

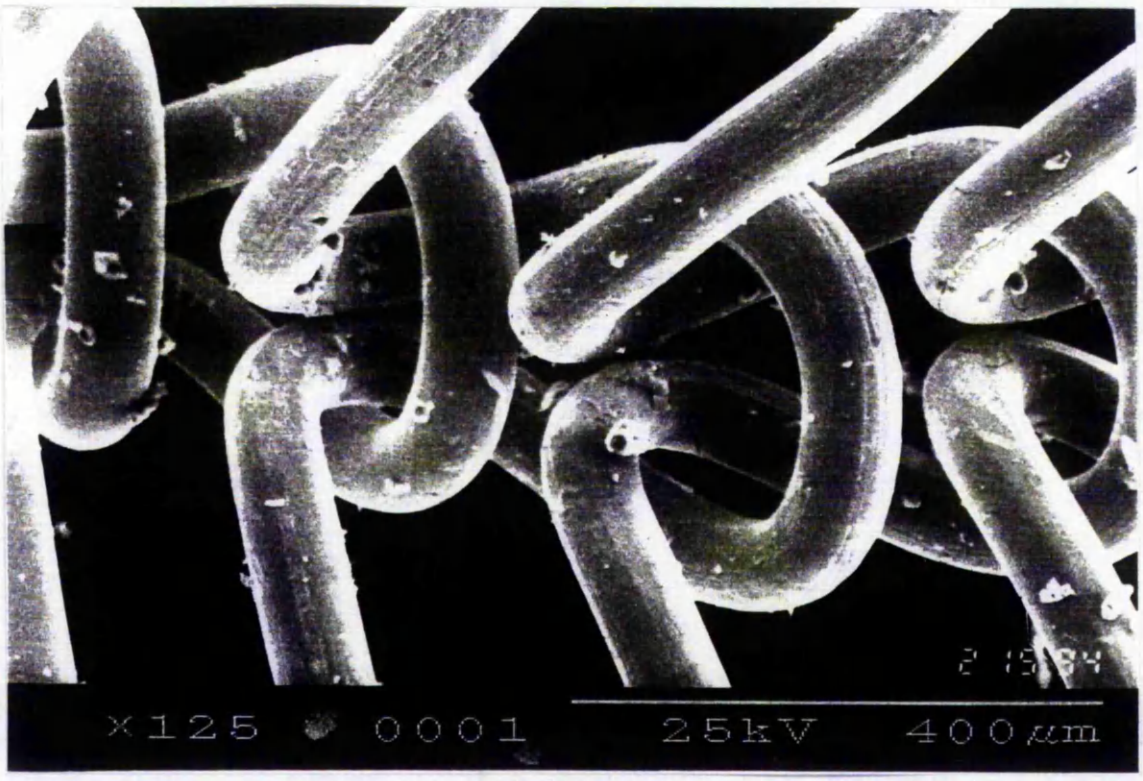

Figure 5.1 : SEM Image of an Unused Catalyst Gauze

Attempts to characterise unused catalyst samples resulted in Auger spectra which were dominated by the carbon 270 eV Auger peak. The large carbon Auger peak was, however, much reduced after the surface had been sputtered with 10 keV argon ions (80 μA over 1 cm^2) for 25 minutes. Since this argon sputtering process is known to remove many monolayers from the surface, this treatment was considered inappropriate for studying surface composition. The samples of catalyst were, therefore, pre-treated in oxygen as described in section 4.4 in an attempt to obtain a more representative surface.

After oxygen pre-treatment, samples of 83-17 and 91-9 catalyst were placed in the SAM and imaged by SEM. Figure 5.2 is an SEM image of an unused 83-17 catalyst.

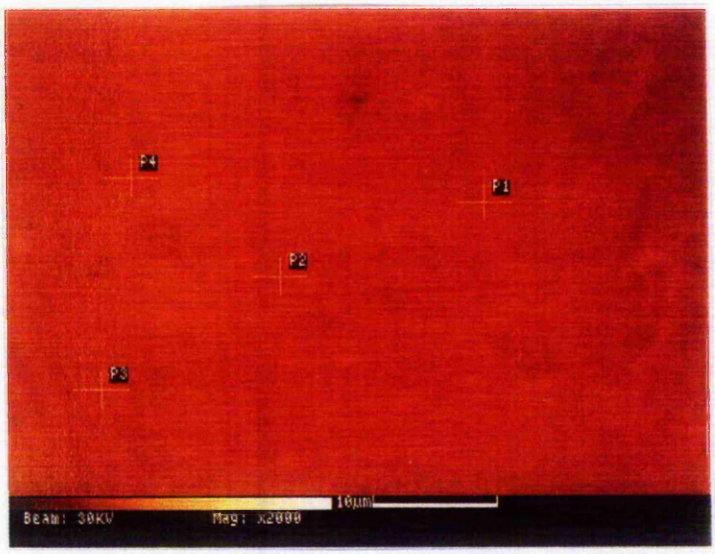

Figure 5.2 : High Magnification SEM Image of an Unused Catalyst Gauze

The unused 83-17 and 91-9 catalyst samples were characterised by point mode Auger electron spectroscopy. As discussed in section 4.1, the near surface concentrations of carbon, rhodium, oxygen and platinum were interpreted by measuring the peak and background intensities and performing a P-B/B calculation. The results of the characterisation process for the unused 83-17 and 91-9 catalysts are shown in table 5.1.

Unused 83-17				
Point Analysis	Carbon (P-B)/B	Rhodium (P-B)/B	Oxygen (P-B)/B	Platinum (P-B)/B
P1	0.05	0.18	0.13	0.20
P2	0.10	0.13	0.16	0.18
P3	0.10	0.19	0.12	0.17
P4	0.07	0.17	0.07	0.18
P5	0.09	0.17	0.09	0.18
Average	0.08 ± 0.02	0.17 ± 0.02	0.11 ± 0.04	0.18 ± 0.01
Unused 91-9				
P1	0.09	0.09	0.12	0.17
P2	0.06	0.12	0.10	0.20
P3	0.11	0.16	0.05	0.23
P4	0.10	0.16	0.07	0.23
Average	0.09 ± 0.02	0.13 ± 0.03	0.09 ± 0.03	0.20 ± 0.03

Table 5.1 : SAM Characterisation of Unused 83-17 and 91-9 Gauze.

From the results shown in table 5.1, both the unused 83-17 and the unused 91-9 catalysts exhibited significant carbon, rhodium, oxygen and platinum (P-B)/B values. No other elements were detected in the Auger spectra.

The average carbon (P-B)/B for the 83-17 an 91-9 samples was similar, at 0.08 and 0.09 respectively, although there was a significant degree of scatter. The oxygen (P-B)/B was also similar for the 83-17 and 91-9 catalysts, measured at 0.11 and 0.09 for respectively. The rhodium (P-B)/B for the 83-17 catalyst was 0.17 ± 0.02 whilst the corresponding value for the 91-9 catalyst was 0.13 ± 0.03. From calibration of the Auger microscope, as discussed in section 4.1, the near surface concentration of rhodium was, therefore, measured at 0.17/0.57 = 30 ± 4 %Rh and 0.13/0.57 = 23 ± 5 %Rh for the 83-17 and 91-9 catalysts respectively. The platinum (P-B)/B for the 83-17 and 91-9 catalysts was measured at 0.18 ± 0.01 and 0.20 ± 0.03 respectively. By

comparison with the calibration sample, the near surface concentration of platinum was calculated to be 0.18/0.25 = 72 ± 4 at%Pt and 80at ± 8 at%Pt for the 83-17 and 91-9 catalysts respectively.

The concentration of platinum at the near surface of both the 83-17 and 91-9 catalysts was less than the bulk concentration whilst the rhodium concentration at the near surface of the catalysts was greater than the bulk concentration. The surface of the unused catalysts was, therefore, significantly enriched with rhodium.

As discussed in section 4.1, the observed concentration of an element, measured by AES, can be considered as comprising contributions from the surface monolayer and the bulk (not including the surface monolayer). From a knowledge of the escape depth for the 302 eV rhodium Auger electron, the monolayer contribution to the Auger intensity, as discussed in section 4.1, was estimated to be 25%. Equation 5.1 was used to calculate the surface monolayer concentration of rhodium, the results for which are shown in table 5.2. This approach could not be applied to the 1960 eV platinum peak as the surface sensitivity, at 13%, was loo low.

$$\%Rh = \frac{observed\ composition\ by\ AES - (0.75 * bulk\ composition)}{0.25}$$

Equation 5.1 : The Calculation of Rhodium Surface Monolayer Composition From AES

From equation 5.1, the surface monolayer composition of rhodium was calculated. The results are shown in table 5.2.

Sample	Near Surface Composition		Surface Monolayer Composition
	at%Rh	at%Pt	at%Rh
83-17	30 ± 5	72 ± 8	56 ± 28
91-9	23 ± 5	80 ± 8	55 ± 28

Table 5.2 : Calculated Near Surface and Surface Monolayer Composition

Although the error associated with the estimation of surface monolayer concentration is large, analysis of the surface by AES showed the surface to be significantly enriched with rhodium. Within experimental error, the surface composition of the two surfaces was found to be the same at ca. 55 at%Rh.

5.3 X-Ray Photoelectron Spectroscopy

Samples of unused 83-17 and 91-9 catalyst were characterised by XPS. The experimental and data analysis methods used are discussed in section 4.2.

The characterisation by XPS concentrated on obtaining the Pt 4f $^{3}/_{2}$, O 1s and Rh 3p XPS peaks and representative spectra from unused 83-17 and 91-9 catalyst samples are shown in figure 5.3.

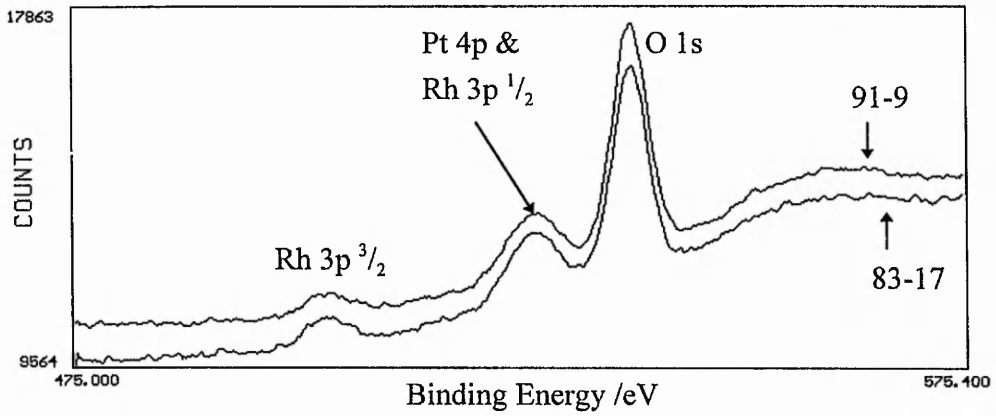

Figure 5.3 : XPS - Unused 83-17 Catalyst.

Using the method described in section 4.2, the near surface concentration of rhodium was calculated to be 27 ± 2 %Rh and 21 ± 2 %Rh for the 83-17 and 91-9 catalysts respectively.

As discussed in section 4.2, XPS was estimated to have a surface monolayer sensitivity of 18%. A subtraction of the bulk contribution from the observed near surface concentration, observed by XPS, allowed an estimation of the contribution due to the surface monolayer and therefore surface monolayer rhodium concentration. Equation 5.2, which is similar in form to equation 5.1, describes the method used to calculate the surface monolayer rhodium concentration.

$$\%Rh = \frac{observed\ Rh\ concentration - (0.82 * bulk\ composition)}{0.18}$$

Equation 5.2 : The Calculation of Surface Monolayer Composition From XPS

From equation 5.2, the surface monolayer concentration for the 83-17 and 91-9 catalysts was calculated and given in table 5.3.

Sample	Near Surface Composition		Surface Monolayer Concentration	
	at%Rh	at%Pt	at%Rh	at%Pt
83-17	26 ± 2	74 ± 2	66 ± 10	34 ± 10
91-9	18 ± 2	82 ± 2	58 ± 10	42 ± 10

Table 5.3: Near Surface Composition and Surface Monolayer Composition Observed by XPS for the Unused 83-17 and 91-9 Catalysts.

XPS, thus again, demonstrates that the near surface composition of both the 83-17 and 91-9 catalysts was significantly enriched in rhodium. In comparing the surface monolayer concentration, calculated at 66 % and 58 %Rh for the 83-17 and 91-9 samples respectively, the results indicated that the two surfaces had very similar composition despite the difference in bulk composition.

5.4 Time of Flight Secondary Ion Mass Spectroscopy (ToFSIMS)

5.4.1 Static Secondary Ion Mass Spectroscopy

Samples of unused 83-17 and 91-9 catalyst gauze were investigated by static secondary ion mass spectroscopy as discussed in section 4.3. Representative positive ion mass spectra obtained from an 83-17 catalyst sample are shown in figures 5.4 (a and b) and 5.5 (a, b, c and d). From the high mass range spectrum shown in figure 5.4a, the complexity of the information gained by ToFSIMS is immediately apparent. By selecting certain ranges in the spectrum, the intensity of defined masses becomes more apparent, and these are shown in figures 5.4b, 5.5a, 5.5b, 5.5c and 5.5d. The masses of most interest in these spectra are at m/z = 103 (Rh^+) and at m/z 194, 195, 196 and 198 (Pt^+). The other major components in the spectra originate from the caesium ion source m/z = 137 (Cs^+), and from clusters such as Pt_2^+ but the majority of detected ions originated from organic and inorganic contaminants at the surface of the catalyst.

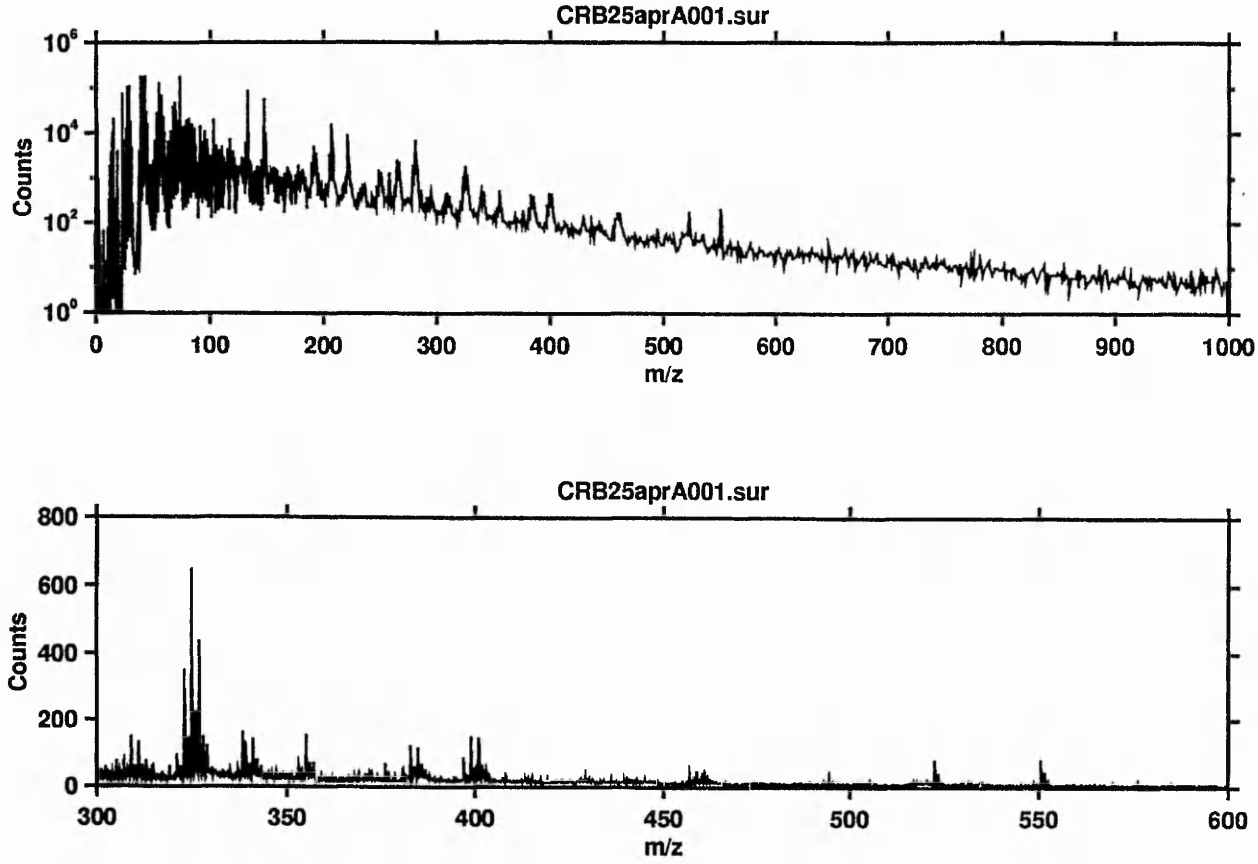

Figure 5.4 : ToFSIMS Mass Spectra - Unused 83-17 Catalyst Gauze

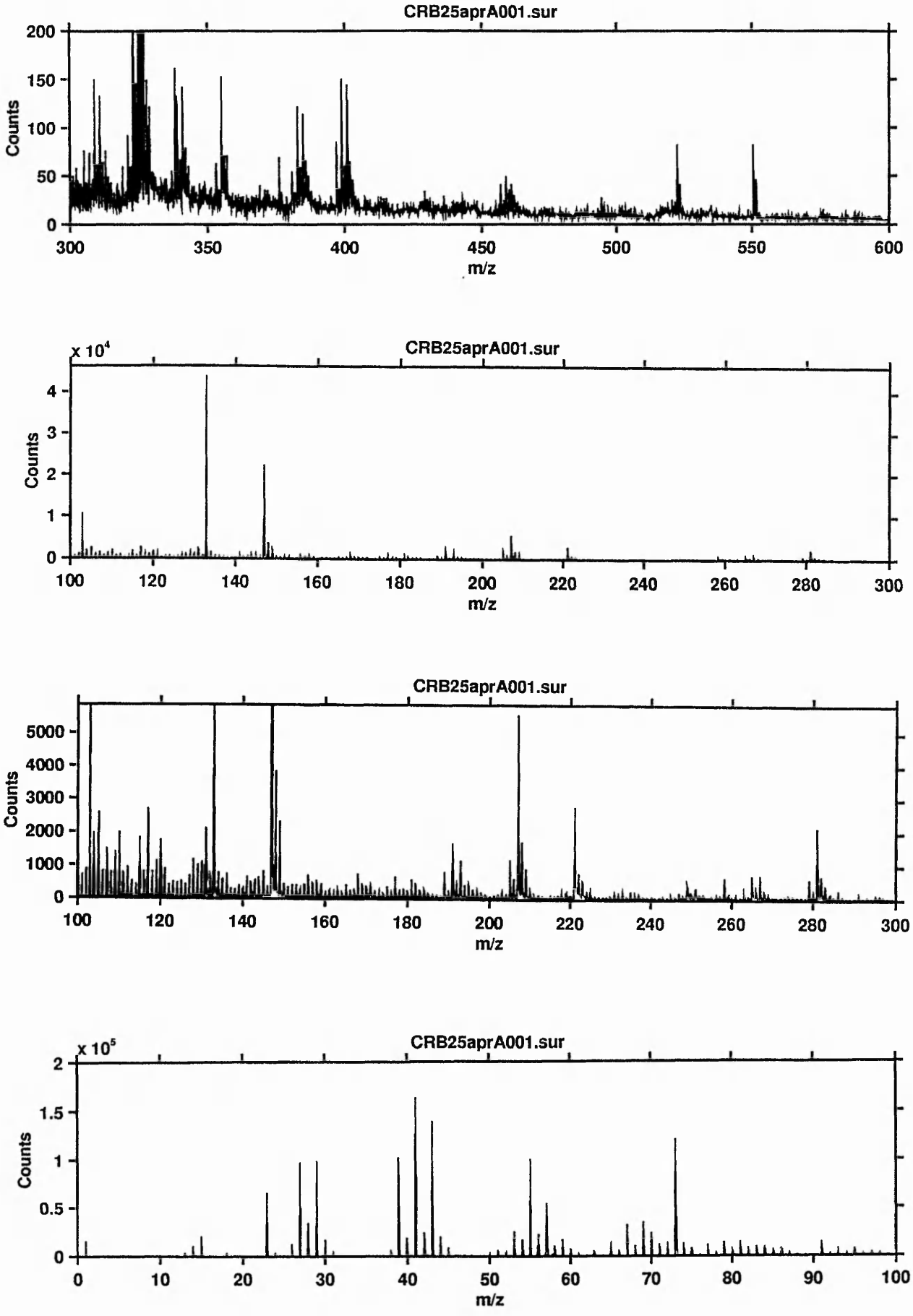

Figure 5.5 : ToFSIMS Mass Spectra - Unused 83-17 Catalyst Gauze

From the high mass resolution mass spectra for both positive and negative ions, obtained from a 50 x 50 μm area of unused catalyst gauze, both the 83-17 and the 91-9 samples showed the presence of polydimethylsiloxane (PDMS). Due to the common use of this material in furniture polishes, and the extremely high sensitivity of SIMS to PDMS, this is a commonly observed contaminant[1]. Also seen were B, Na, Mg, Al, Si, K, Ca, Cr, Fe, Cu, Cl, P (as PO_2, PO_3), and S (as SO_2, SO_3 and SO_4). The technique of SIMS is highly sensitive to these species, and the ion yields are highly dependant on both the oxidation state of the species and the matrix from which they originated[2]. Even semi-quantitative analysis of these species is considered beyond the scope of this work, and the concentrations may not be significant. The coverage of these contaminants was fairly thin or patchy, however, as platinum and rhodium were clearly observable in the positive ion (M^+) spectrum.

The total ion dose of 8 keV Cs^+ ions used to obtain the spectra was, in each analysis, $3.4x10^{12}$ ions cm^{-2}. Assuming the sputter yield for platinum and rhodium was 10 atoms per incident ion[3], the total number of atoms removed from the surface was $3.4x10^{13}$ cm^{-2}. Since the surface density of atoms at the surface of a solid is approximately $1x10^{15}$ cm^{-2}, approximately 4% of a monolayer was removed from the surface during the analysis, indicating that the analysis was representative of the original surface.

5.4.2 Dynamic Secondary Ion Mass Spectroscopy

Depth profiling or 'dynamic' SIMS was performed on the 83-17 catalyst. In particular, attention was paid to the relative positive ion yield (M^+) for platinum and rhodium with respect to total ion dose to give an ion ratio Vs. depth profile. Due to the possible importance of iron in the catalyst activation process[4], the relative abundance of trace levels of many contaminants such as iron and other base metal contaminants at the near surface was also investigated during the depth profiling process. Figure 5.6 shows the Rh^+ : Pt^+ ion yield ratio with exposure to incident ion dosage for the unused 83-17catalyst.

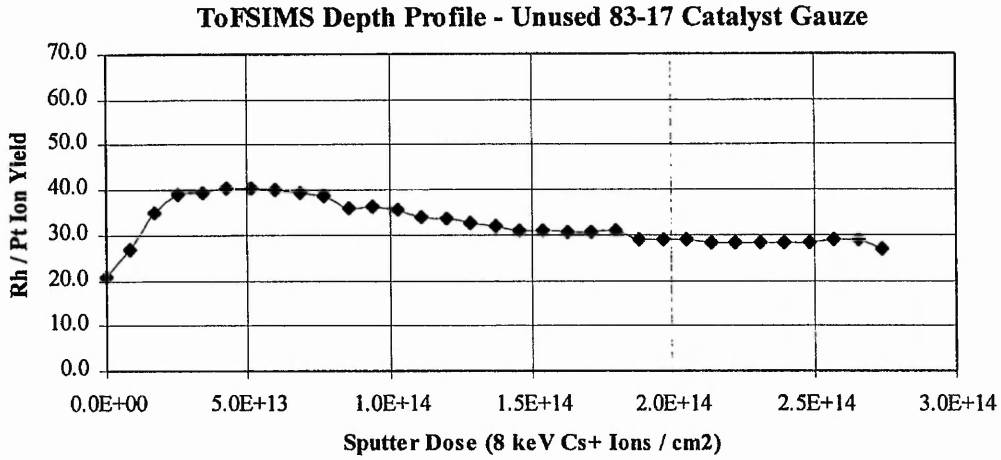

Figure 5.6: ToFSIMS Depth Profile - Unused 83-17 Pt-Rh Gauze.

The 83-17 sample was found to exhibit a peak in Rh^+ : Pt^+ ion ratio at 40:1 after a sputter dose of $2.5x10^{13}$. After the peak in the Rh^+ : Pt^+ ion ratio, the ratio was then seen to decline to a steady state value of 28 ± 2. Assuming a surface monolayer concentration of $1x10^{15}$ atoms / cm^2 and a sputter yield of 10 atoms per incident ion[3], the analysis was calculated to have removed ca. 2.75 monolayers from the surface of the catalyst after a sputter dose of $3 X 10^{14}$.

Assuming that the steady state Rh^+ : Pt^+ ratio after an ion dose of > $2x10^{14}$ was representative of the bulk Rh : Pt atomic ratio of the sample, the relative ion yield for rhodium (M^+) Vs. platinum (M^+) was calculated from the bulk atomic ratio and the observed M^+ ion ratio, as shown below.

Observed steady-state Rh : Pt Ion yield = 28

Atomic ratio (Rh : Pt) = 0.21 : 1

$$\text{Relative sensitivity } \left(\frac{Rh/Pt\ Ion\ Yield}{Bulk[Rh/Pt]}\right) = \frac{28}{0.21} = 133$$

From the above calculations, the probability of detecting a sputtered rhodium atom as Rh^+ was found to be 133 times greater than the probability for the same process for platinum. The ratio of sensitivity to rhodium vs. sensitivity to platinum was therefore 133 : 1. From the ToFSIMS depth profile, the peak Rh : Pt ion ratio was 40 : 1, indicating that the elemental ratio of Rh : Pt reached a maximum of 40/133 : 1 (0.3 : 1), equivalent to a concentration of 23 % Rh..

From figure 5.6, the Rh^+ : Pt^+ ion ratio was seen to proceed through a maximum after the removal of approximately 0.5 monolayers from the surface. The result, therefore, indicated that the surface monolayer may have been platinum-rich in comparison with the underlying layer, however, the influence of a matrix effect such as preferential sputtering of platinum cannot be excluded. As the region of greatest interest, i.e. the first monolayer or so, overlapped with the region where the possibility of preferential sputtering effects was likely to be most significant, quantification of the initial stages of the sputter depth profile was not possible. In comparison with the Rh : Pt ion ratio representative of the bulk composition (>2 monolayers removed) the analysis did, however, again indicate a higher Rh : Pt ratio at the near surface region.

Although the quantification of he SIMS depth profiles is difficult due to the influence of matrix factors, sample to sample comparisons, where the chemical composition of the samples is similar, is of use as the matrix factors would be approximately equal in both samples. The results obtained from the unused catalyst samples are, therefore, compared with results from activated catalyst samples and discussed in chapter 8.

5.4.3 Trace Component Characterisation

As the technique of ToFSIMS, as discussed in section 4.3, is highly sensitive to the presence of many elements, the samples of unused gauze were characterised by measuring the ion yield for the elements as shown in table 5.4. The results shown were obtained after an ion dose of $5x10^{13}$ ions cm^2 and therefore representative of the first few monolayers. The normalised ion ratio was obtained by dividing the specific ion yields by the global ion yield, including several ions not listed in the table, such as caesium (originating from the primary ion source) and organic fragments.

Element	Ion Yield 83-17 Pt-Rh	Ion Yield 91-9 Pt-Rh	Normalised Ion Ratio 87-13 : 91:9
Rh	$4.0x10^4$	$7.0x10^3$	0.6
Pt	$1.0x10^3$	$1.0x10^2$	1.0
Cr	$1.5x10^4$	$1.0x10^2$	15.0
Fe	$5.0x10^4$	$1.5x10^3$	3.3
Ca	$7.0x10^4$	$4.0x10^3$	1.8
Cu	$1.8x10^4$	$1.8x10^2$	10.0
Al	$2.5x10^4$	$1.2x10^3$	2.1
Na	$4.0x10^4$	$8.0x10^2$	5.0
K	$5.5x10^4$	$3.0x10^3$	1.8
Global Ion Yield	$1.0x10^6$	$1.0x10^5$	N/A

Table 5.4: SIMS Ion Ratios - Trace elements

By comparing the normalised ion ratio for various elements shown in table 5.4, the 83-17 catalyst appeared to contain a greater concentration of base metal contaminants than the 91-9 catalyst. This observation was in line with claims by the manufacturers[5], that the 91-9 catalyst was of higher purity than the 83-17 catalyst.

5.5 Conclusion

The range of characterisation techniques applied to the samples of unused 83-17 and 91-9 catalyst gauze shows that significant enrichment of the near surface region occurs. A summary of the platinum and rhodium concentrations is shown in table 5.5.

Analysis	IMFP (monolayers)	Near Surface Concentration				Surface Monolayer Concentration			
		at%Pt		at%Rh		at%Pt		at%Rh	
		83-17	**91-9**	**83-17**	**91-9**	**83-17**	**91-1**	**83-17**	**91-9**
Pt AES	7.0	72 ± 4	80 ± 12						
Rh AES	3.5			27 ± 7	21 ± 7			44 ± 28	60 ± 28
XPS	5.0	74 ± 2	82 ± 2	26 ± 2	18 ± 2	34 ± 10	42 ± 10	66 ± 10	58 ± 10
SIMS	N/A	<83		>17					

Table 5.5 : Characterisation Results - Unused Gauze

The techniques applied to the characterisation of the unused gauze are, therefore, in general agreement. The study of atomically clean single crystal surfaces of platinum-rhodium alloy after annealing at elevated temperatures of 800 to 1500 K have shown that the alloy surface is normally platinum enriched[6]. The presence of oxygen at the surface has, however, been shown to markedly increase the surface concentration of rhodium to an extent that the surface may become strongly enriched with rhodium[7]. This is presumably due to the fact hat rhodium has a higher oxygen affinity than platinum. Observation of an oxygen Auger peak and a high rhodium concentration at the surface of the unused catalyst gauze shows that the catalyst surface was oxidised. Carbon has, however, been shown to cause an increase in the near surface concentration of rhodium in platinum-rhodium alloys under UHV conditions[8]. Auger spectra of the unused catalysts exhibited a significant carbon Auger peak, and as such, the presence of carbon may have been a factor in rhodium surface segregation of unused catalysts. The surface segregation of rhodium was, therefore, likely to have been caused by a combination of exposure to an oxidising environment and the presence of carbon.

5.6 References

[1] I.W. Fletcher ICI Surface Science Team. Personal communication (1996)

[2] P. Williams in Practical Surface Analysis Second Edition. Volume 2 - Ion and Neutral Spectroscopy. D. Briggs, M.P. Seah. (Ed.) Pub. John Wiley & Sons. Chichester. pp. 198 (1992).

[3] H.H. Anderson, H.L. Bay in Topics in Applied Physics Vol. 47. Sputtering by Particle Bombardment 1. R. Behrisch (Ed.) Springer-Verlag (Pub) Berlin. pp. 186 (1981)

[4] B.Y.K. Pan. J. Catal. **21** 27-38 (1971).

[5] S. Frank. ICI Acrylics RT&E. Personal communication. (1996).

[6] F.L. Williams, G.C. Nelson. Appl. Surf. Sci. **3** 409 (1979).

[7] M. Rubel, M. Pszonica, W. Palczewska. J. Mat. Sci. **20** 3639-3648 (1985).

[8] F.C.M.J.M. van Delft, A.D. van Langeveld, B.E. Nieuwenhuys. Surface Science **189/190** 1129-1134 (1987).

6. Characterisation - Industrial Samples

6.1 Introduction

A sample of 83at%Pt - 17at%Rh catalyst was supplied by ICI Acrylics, which was representative of samples taken from a 4m diameter industrial reactor gauze, removed from a reactor due to declining catalytic performance. The catalyst sample was part of a multilayer gauze bed which had, through use, become fused into a solid mass, and as such, only the 'top' and 'bottom' surfaces were exposed and therefore amenable to characterisation. In chapter 6, the terms 'top' and 'bottom' refer to the exposed sides of the sample where 'top' was the gas entry side of the catalyst and 'bottom' was the gas exit side of the catalyst.

As the surface concentration of platinum, rhodium and carbon are factors which are likely to affect the performance of the catalyst, the catalyst was characterised by scanning Auger microscopy (SAM) and X-Ray photoelectron spectroscopy (XPS). Due to the high degree of spatial resolution afforded by the scanning Auger microscope, a combination of point analyses and Auger mapping was applied to the catalyst sample to determine whether the surface was homogeneous within the spatial resolution of the instrument (ca. 0.5 μm).

6.2 Scanning Auger Microscopy

6.2.1 Bottom Surface of the Gauze Pack

An SEM image of the bottom surface of the catalyst pack (gas exit side), is shown in figure 6.1. The elemental composition of the near surface was investigated via the use of point-mode Auger electron spectroscopy. The precise locations of the point analyses were as indicated in figure 6.2.

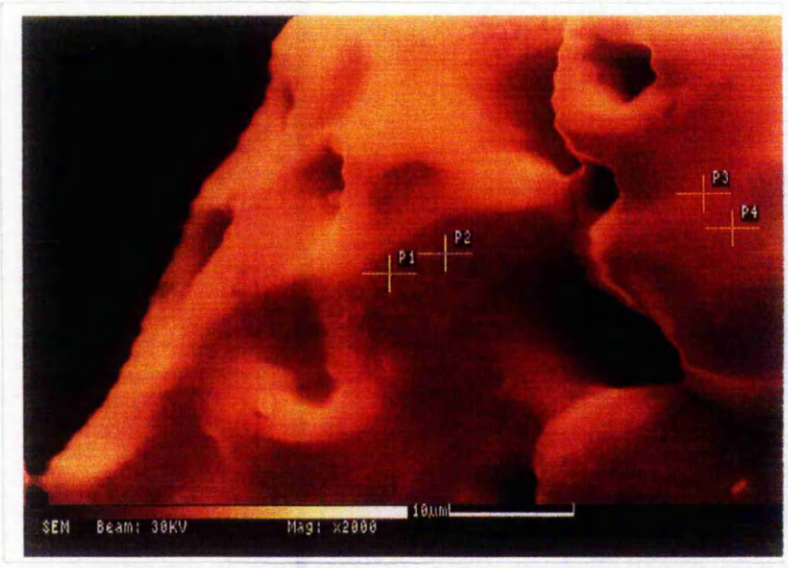

*Figure 6.1: SEM of the Bottom of a Used Industrial Gauze 60*60 µm (X2000).*

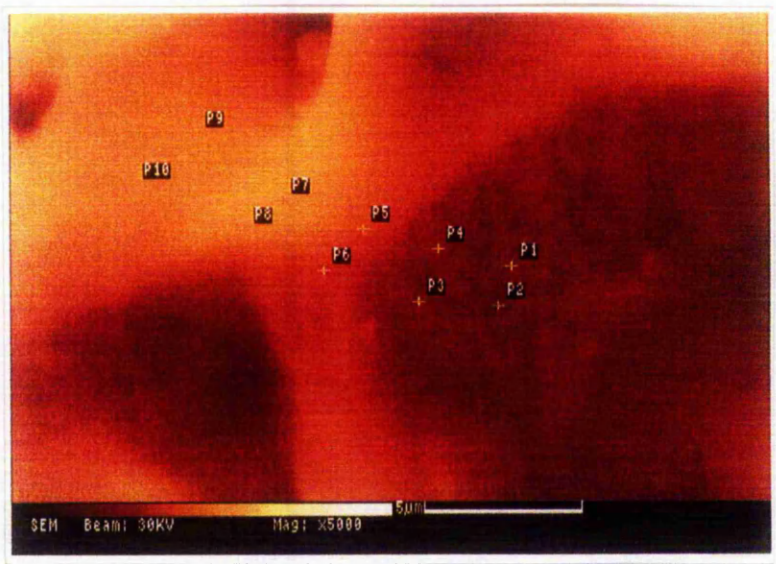

Figure 6.2: Close-up SEM of the Bottom of a Used Industrial Gauze 24*24 µm (X5000).

Figures 6.3-6.5 show the Auger spectra in the regions 250-350 eV, 450-550 eV and 1800 to 2200 eV respectively for point analyses P1 - 10, located as shown in figure 6.2.

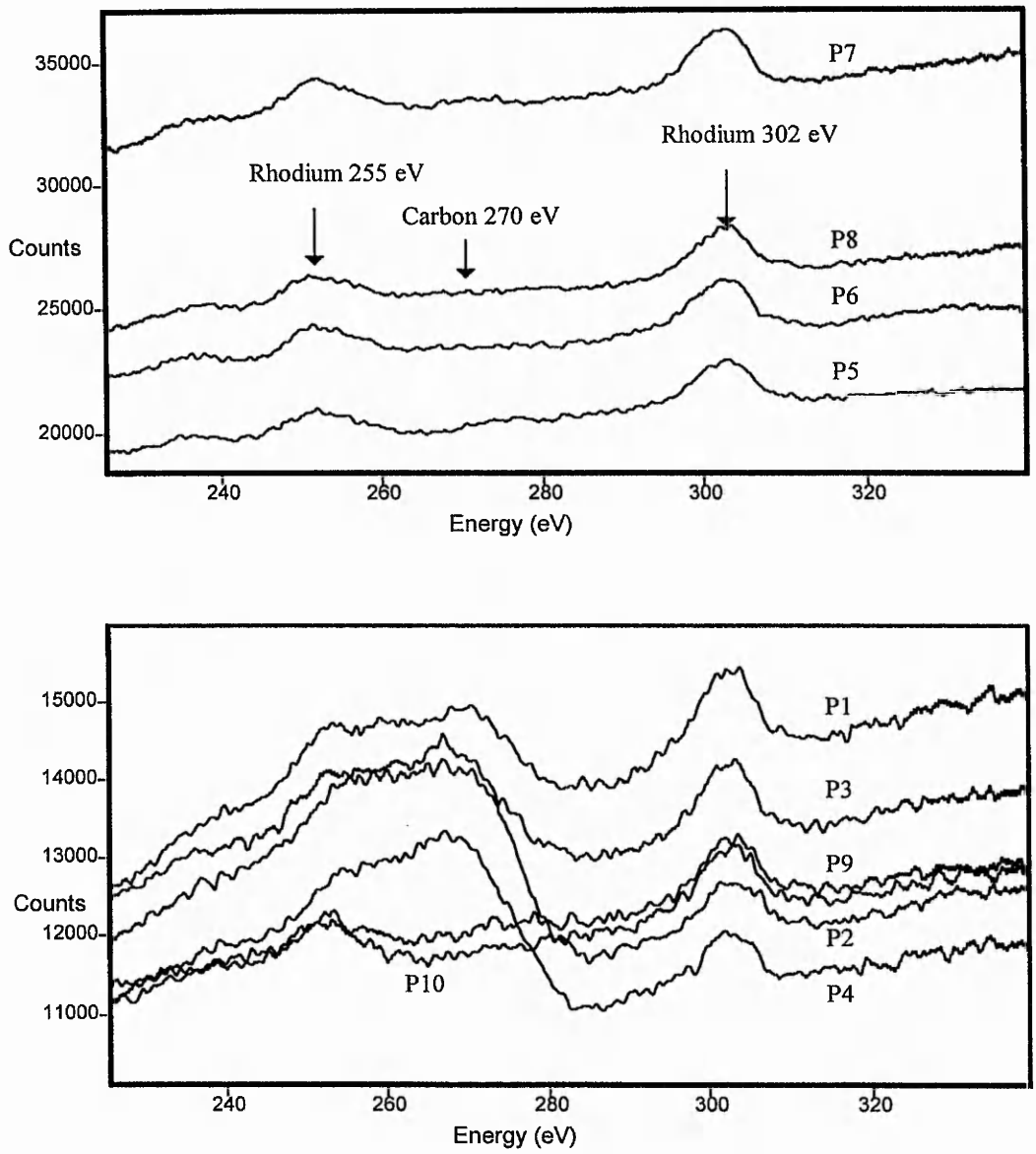

Figure 6.3: Point Analyses P1-10, Carbon and Rhodium Auger Region.

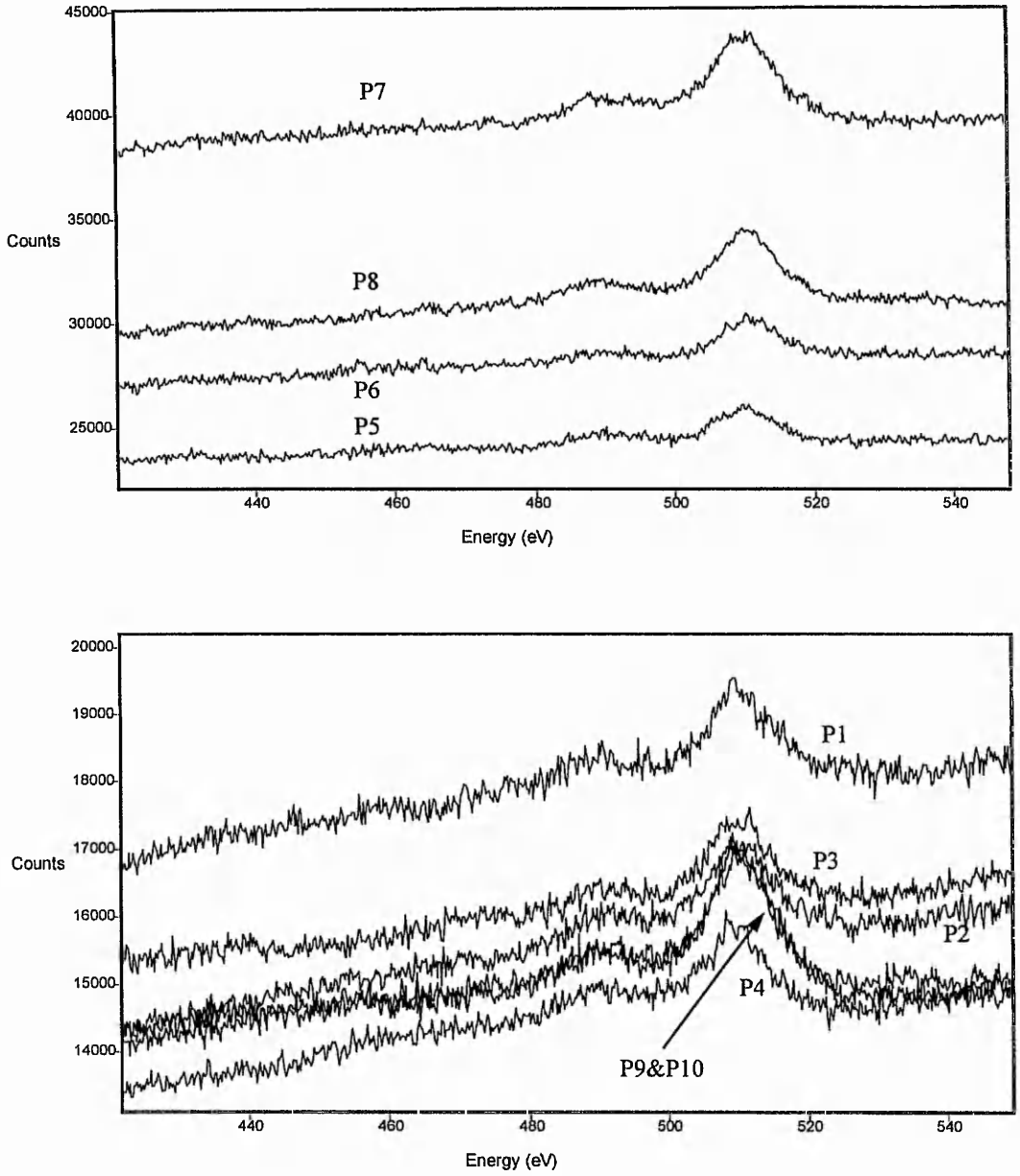

Figure 6.4 : Point Analyses P1-10, Oxygen Auger Region.

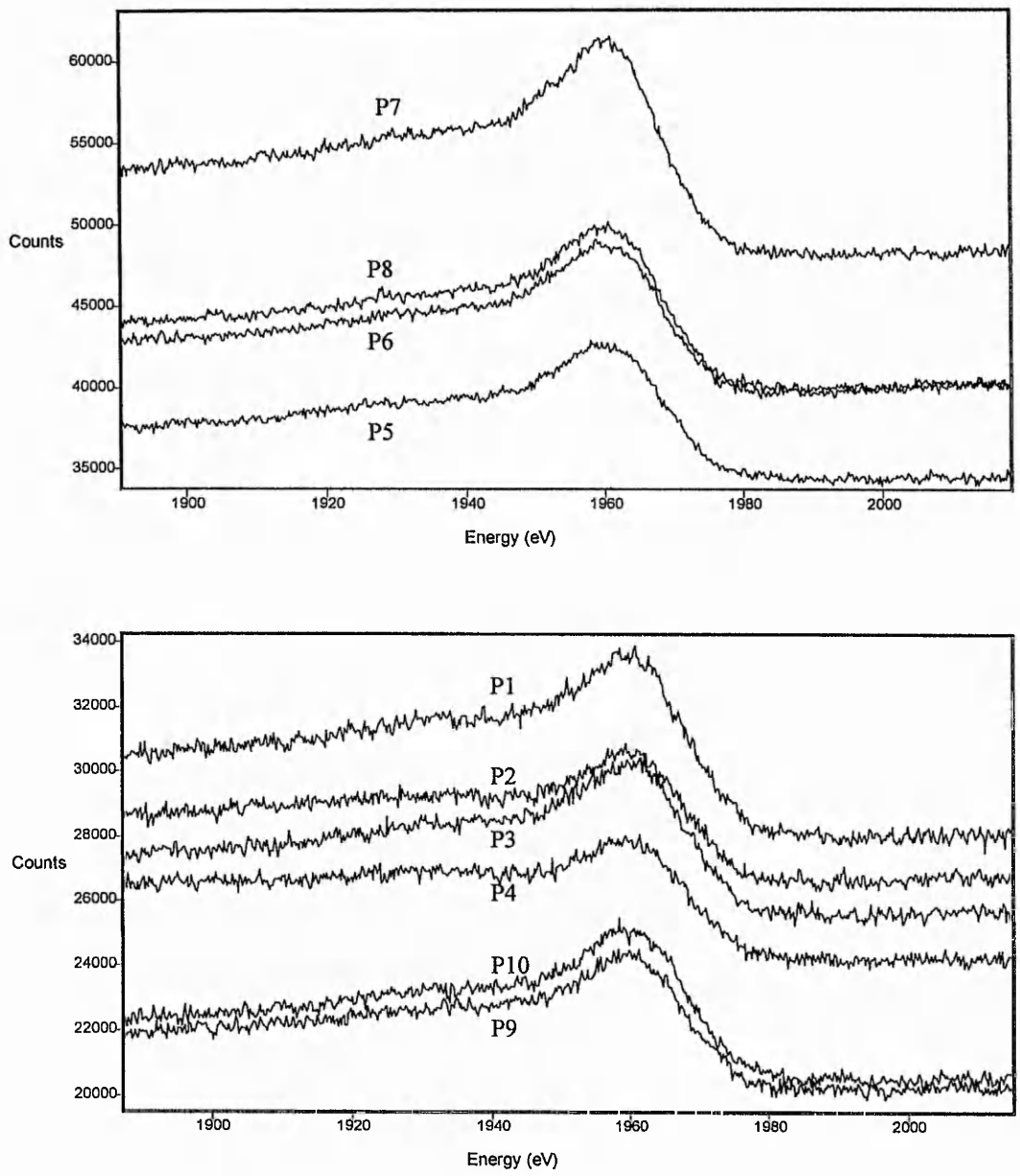

Figure 6.5 : Point Analyses P1-10, Platinum Auger Region.

As discussed in section 4.1, (P-B)/B normalisation can be used to measure near surface elemental concentration[1]. Table 6.1 shows the normalised peak intensities i.e. (P-B)/B for carbon, rhodium, oxygen and platinum for point analyses P1-P10. Note that in the absence of a carbon Auger peak, as exhibited by point analysis P5, there was a slightly higher background (B) at 286 eV than the peak (P) at 270 eV which resulted in the slightly negative carbon (P-B)/B values.

Point Analysis	C (P-B)/B	Rh (P-B)/B	O (P-B)/B	Pt (P-B)/B
P1	0.08	0.08	0.07	0.19
P2	0.23	0.06	0.07	0.14
P3	0.08	0.08	0.06	0.18
P4	0.19	0.06	0.10	0.14
P5	-0.03	0.09	0.07	0.21
P6	-0.02	0.09	0.06	0.21
P7	-0.01	0.07	0.11	0.27
P8	-0.01	0.08	0.10	0.23
P9	-0.02	0.07	0.16	0.19
P10	-0.03	0.07	0.12	0.21

Table 6.1: Point Analyses of the Bottom of a Used Industrial Gauze Pack (P1-10). Auger peak intensities are represented by (P-B)/B values.

The results in table 6.1 show that there was significant variation in the normalised Auger intensity (P-B)/B for carbon, rhodium, oxygen and platinum between point analyses. In particular, the variation in carbon Auger intensity was large, and whilst some points (P5-P10) exhibited little or no carbon Auger peak intensity, other point analyses (P1-P4) exhibited a large carbon Auger intensity. From a statistical analysis of the results shown in table 6.1, the conclusion was that there was an inverse relationship between the surface concentration of carbon and the near surface concentration of platinum (correlation coefficient = - 0.82) and rhodium (correlation coefficient = - 0.64). A decrease in oxygen (P-B)/B with increasing carbon (P-B)/B was also observed (correlation coefficient = - 0.32) indicating the possibility of an inverse relationship, but that the degree of scatter was large.

6.2.1.1 The Near Surface Concentration of Platinum And Rhodium

The average (P-B)/B values for rhodium and platinum in areas of little or no carbon i.e. with a (P-B)/B of 0.05 or less, were 0.078 and 0.22 respectively. By comparison with the calibration standards the near surface concentration of rhodium and platinum was, therefore, measured at (0.078/0.57) = 14at%Rh and (0.22/0.25) = 88at%Pt respectively. The rhodium near surface concentration was, therefore, less than the bulk concentration whilst the observed platinum near surface concentration

was greater than the bulk concentration. The carbon free surface was, therefore, shown to be platinum enriched.

As discussed in section 4.1, rhodium and platinum AES signals were estimated to have surface sensitivities of 25% and 13% respectively. From a subtraction of the contribution due to the bulk sensitivity, as discussed in section 4.1, the surface monolayer concentrations of platinum and rhodium were estimated to be ca. 120 %Pt and 3%Rh respectively. The statistical error associated with the monolayer concentration was, however, estimated at ± 15at% for Rh and ± 25at% for Pt.

6.2.1.2 The Distribution of Carbon at the Near Surface

To investigate the relationship between the near surface concentration, as measured by (P-B)/B ratios, the plots of platinum (P-B)/B Vs. carbon (P-B)/B and rhodium (P-B)/B Vs. carbon (P-B)/B were generated, and are shown in figures 6.6 and 6.7 respectively.

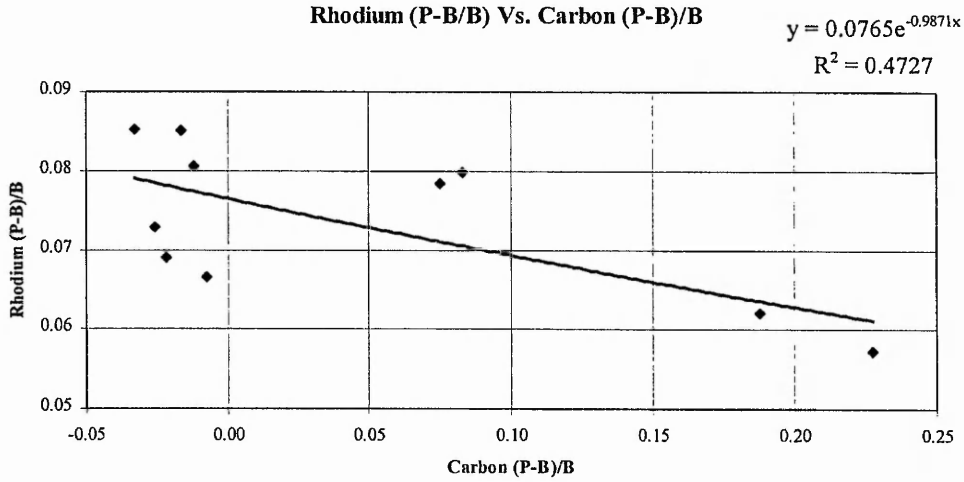

Figure 6.6: Rhodium Vs. Carbon Auger Intensity.

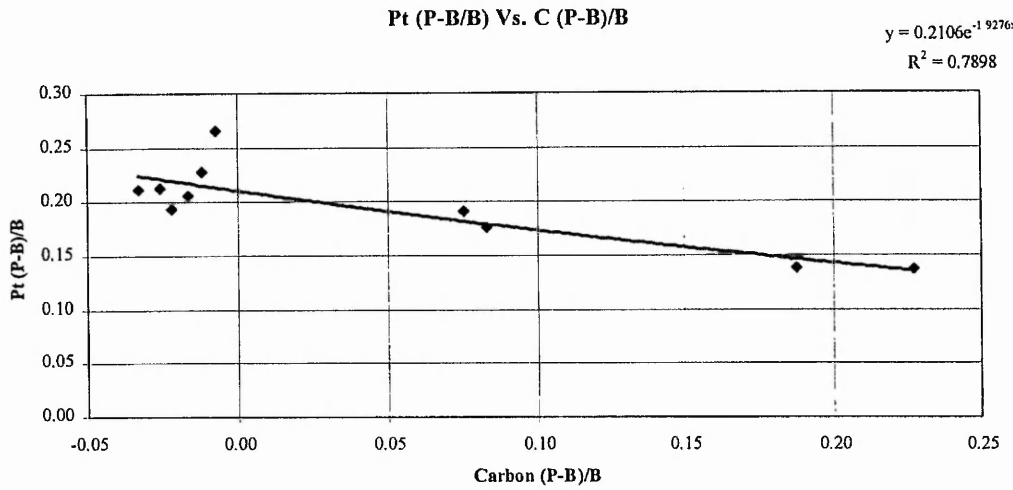

Figure 6.7: Platinum Vs. Carbon Auger Intensity.

The plots shown in figures 6.6 and 6.7, show that, coincident with an increase in carbon Auger intensity from a (P-B)/B of value of -0.03 to a (P-B)/B of 0.23, there was a significant decrease in both the platinum and rhodium (P-B)/B Auger intensities. For rhodium the (P-B)/B value fell by 20% from 0.078 to 0.062 whilst the platinum (P-B)/B value fell from 0.22 to 0.14, a decrease of 37%. The greater reduction in the platinum (P-B)/B value than the Rh (P-B)/B value is, at first examination, somewhat surprising as the inelastic mean free path of the 1960 eV platinum Auger electrons was significantly greater than the inelastic mean free path for the rhodium 302 eV Auger electrons.

The presence of carbon did, however, cause a large change in the background distribution with respect to energy, exemplified by comparing the background distribution for point analyses P4 (high carbon) and P5 (no carbon). For point analysis P4 the background intensity at 286 eV was 45% of the background at 1980 eV, whereas for point analysis P5 the background at 286 eV was 60% of the background at 1980 eV. The presence of carbon, therefore, caused a large change in background distribution. As discussed in section 4.1, a change in background distribution is of major importance in the estimation of overlayer thickness as the quantitative influence of an overlayer on the absolute background intensity cannot be determined by point analyses alone.

In an attempt to determine whether the absolute background intensity was affected by the presence of a layer of carbon, the area shown in figure 6.2 was characterised by SAM. For the mapping process the secondary electron analyser was

firstly tuned to 312 eV to map the rhodium background intensity and then to 1980 eV to map the platinum background intensity. The results are shown in figures 6.8 and 6.9 respectively. Note that the images are in false colour, and are such that the lighter the colour, the higher the count rate (or intensity). The intensity scale has been altered from image to image and as such is only qualitative in nature. Refer to the accompanying text for a fuller description where necessary. The corresponding area, imaged by SEM, is shown in figure 6.2.

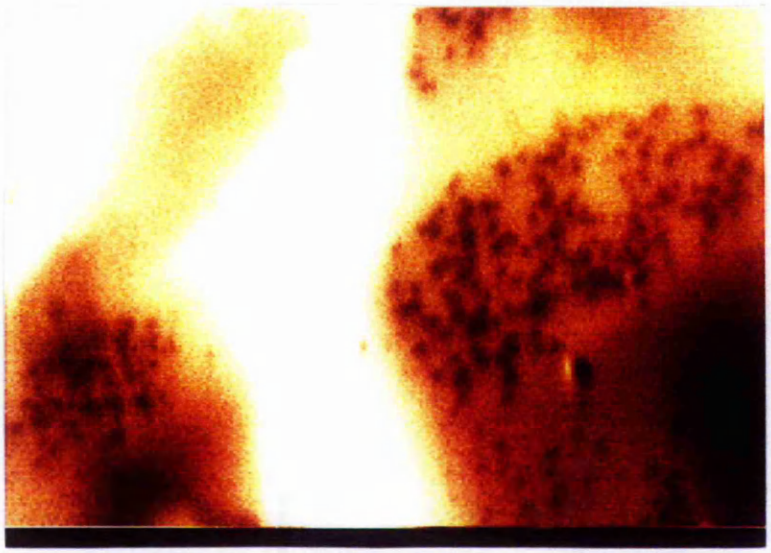

Figure 6.8: Background Map for Rhodium - 312 eV 24*24 μm (X5000).

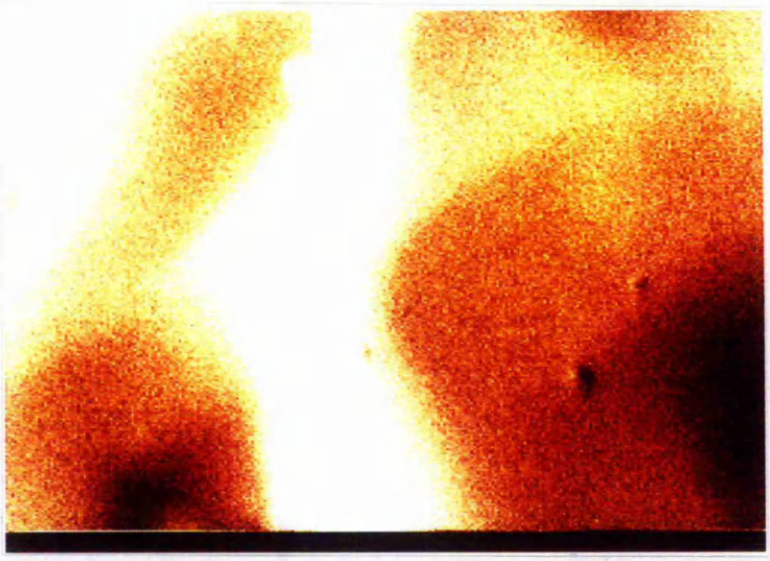

Figure 6.9: Background Map for Platinum - 1980 eV 24*24 μm (X5000).

From figures 6.8 and 6.9, the following features are immediately apparent -

1. The overall spatial distribution of background intensity for both the 312 eV and 1980 eV maps was similar to the SEM image (fig. 6.2). The difference in contrast between the SEM image and the background images is attributable to a decreased dynamic range used to generate the background images.
2. In the 312 eV map (figure 6.8), the areas of high carbon concentration, as measured by the point analyses P1-P10 were associated with a decrease in the background intensity, seen as dark spots in the image of diameter ca. 0.5 μm.
3. In the 1980 eV map (figure 6.9), the variation in concentration of carbon, as measured in point analyses P1-P10, had no effect on the background intensity - resulting in a background intensity distribution that was similar to the SEM image.

The difference in background distribution is exemplified clearly by examining the area of the image just to the right of the centre of the image. In the 312 eV map, several areas of the surface of approximately 0.5 μm diameter exhibited a decreased intensity which was associated with a high carbon Auger intensity. In the 1980 eV map, the same region appeared as an area of constant background intensity. The analysis by SAM, therefore, agreed with the results of the point analyses which indicated that the presence of carbon was associated with a decrease in background intensity at 312 eV relative to the background at 1980 eV. Since the background intensity at 1980 eV was shown to be independent of the presence of carbon, the 1980 eV background provided a suitable method for normalising the intensities of the Rh (302 eV), O (510 eV) and Pt (1960 eV) Auger peaks. Although not common practice, the use of a high energy background normalisation technique has been reported elsewhere[2] where it was proposed that the background intensity at 2 keV was less susceptible to the local chemical environment than at lower energies. The high energy normalisation process is, however, prone to inaccuracies in sample-to-sample comparisons due to the difficulty in maintaining a constant analyser transmission function.

The rhodium peak intensity was, therefore, normalised by the background at 1980 eV i.e. $(P-B)/B_{1980}$. Figure 6.10 shows a plot of the 302 eV rhodium Auger peak intensity, normalised by the background at 1980 eV, vs. the carbon (P-B)/B.

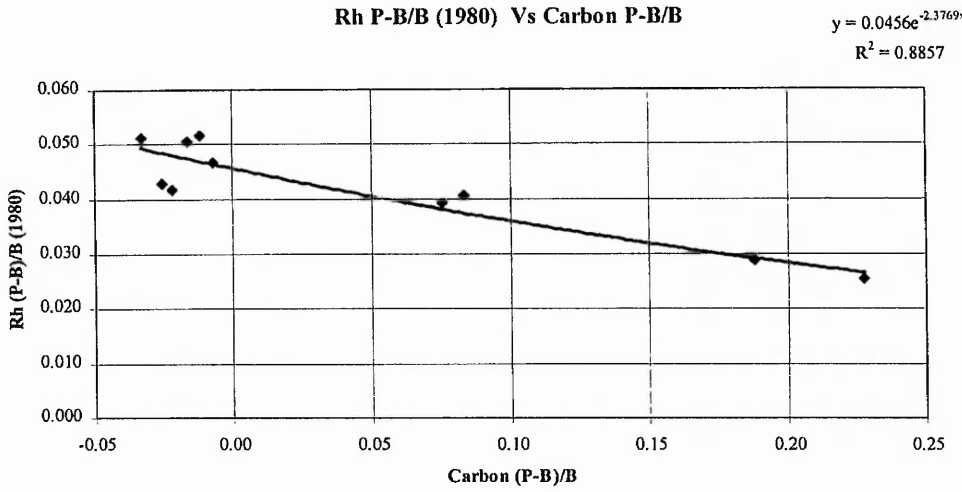

Figure 6.10 : Rhodium P-B intensity normalised by the 1980 eV background Vs. Carbon Auger Intensity

In comparison with the standard normalisation process ((P-B)/B) where the correlation factor (R^2) value for rhodium was 0.47, the R^2 value for $(P\text{-}B)/B_{1980}$, at 0.89 was significantly higher, although this may have been due to an improvement in statistics caused by the higher overall count rate at 1980 eV in comparison with the count rate at 312 eV. More important, however, was the change in slope in changing from a 312 eV background normalisation process to a normalisation performed at 1980 eV. For example, in going from a carbon free surface ((P-B)/B= -0.03) to a surface exhibiting a high carbon Auger peak ((P-B)/B = 0.23), the standard normalisation process for rhodium (P-B)/B yielded a change in normalised intensity from 0.078 to 0.062 (0.062 / 0.078 = 80%), whilst the normalisation process using the 1980 eV background ($(P\text{-}B)/B_{1980}$) yielded a change in normalised intensity from 0.049 to 0.027 (0.027 / 0.049 = 55%). The difference in results obtained by the two normalisation methods, therefore, indicates that extreme care must be exercised in the analysis of surfaces by the use of (P-B)/B normalisation methods and is best performed by normalisation using a background intensity that has been proven to be independent of changes in surface composition.

The observation of a range of carbon concentration at the near surface of the catalyst, and the effect on the 1980 eV normalised Pt and Rh peaks was interesting as the result could be used to identify the precise location of the carbon. Consider the models shown in figure 6.11.

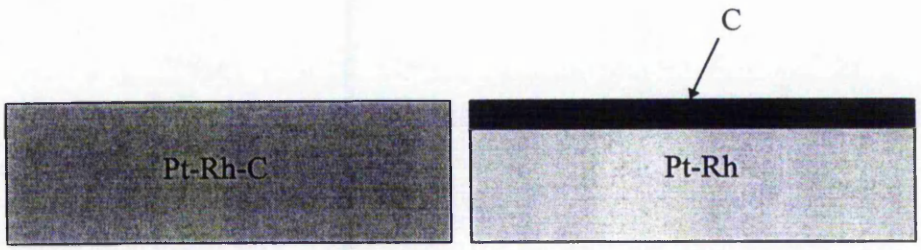

Model 1 : Carbon within the bulk Model 2 : Carbon Overlayer

Figure 6.11 : Surface Models - Carbon In The Bulk And Carbon As An Overlayer

From figure 6.11, model 1 proposes that carbon was within the bulk of the alloy. Any increase in carbon concentration would, therefore, decrease the near surface concentrations of both platinum and rhodium. Assuming that carbon did not promote the surface segregation of either component, the decrease in Rh Auger intensity would be precisely the same as the decrease in the Pt Auger intensity. Where I_O = the observed peak intensity ((P-B)/B) of the clean surface and I = the observed peak intensity ((P-B)/B) of the carbon covered surface, the bulk carbon model predicts -

$$\frac{\frac{I}{I_O}(Rh)}{\frac{I}{Io}(Pt)} = 1 \qquad \text{(i)}$$

Model 2 proposes that carbon was in the form of an overlayer sitting on top of the alloy. Any increase in the thickness of the carbon overlayer (from zero) would attenuate the platinum and rhodium Auger electrons according to the Beer-Lambert relationship. As the escape depth for the 302 eV rhodium Auger electrons is less than half the escape depth of the 1960 eV platinum Auger electrons, the rhodium Auger electrons would be attenuated to a greater degree than the platinum Auger electrons. The change in normalised peak intensity ratio with carbon concentration would, therefore, be a function of the thickness of the overlayer. Where I and I_O are as described for model 1, d = the overlayer thickness and $\lambda_{(Rh\ or\ Pt)}$ = the escape depth (in monolayers) for Rh or Pt, the ratio of the Pt and Rh Auger peaks can be predicted thus -

$$\frac{\frac{I}{I_O}(Rh)}{\frac{I}{Io}(Pt)} = \frac{e^{-(d/\lambda_{Rh})}}{e^{-(d/\lambda_{Pt})}} \leq 1 \qquad \text{(ii)}$$

The exponential decay and R^2 values for the platinum (P-B)/B and rhodium (P-B)/B_{1980} Vs. carbon (P-B)/B were found to be as follows -

$Rhodium_{1980}$ Vs. carbon	-	exponential decay = $0.0456e^{-2.3769}$	$R^2 = 0.89$.
Platinum Vs. carbon	-	exponential decay = $0.21e^{-1.9276}$	$R^2 = 0.79$.

The standard deviation from the line of best fit (the exponential decay line) was calculated and the results indicated an accuracy of ± 0.02 for Pt and ± 0.01 for Rh. By substituting the carbon (P-B)/B values equivalent to a clean surface (-0.03) and an area of high carbon (0.23), the exponential decay equations predict the following-

Platinum -	$I_O = 0.22$	± 0.02	$I = 0.14$	± 0.02
Rhodium -	$I_O = 0.049$	± 0.01	$I = 0.026$	± 0.01

The value of I/I_O for rhodium was, therefore, 0.53 ± 0.02 whilst the corresponding value for platinum was 0.64 ± 0.04. Since the decrease in the 1980 eV normalised Rh Auger intensity was significantly greater than the corresponding decrease in Pt Auger intensity, model 1 failed to explain the results and is therefore inaccurate. In the presence of carbon, model 2 predicts a value of ≤ 1 which was in agreement with the results. Model 2, therefore, provided a better model of the near surface structure and indicated that carbon was located at the surface rather than within the bulk the alloy.

Assuming model 2 accurately described the near surface structure the thickness of the overlayer could be calculated by measuring the decrease in both the Pt (P-B)/B and Rh (P-B)/B_{1980} Auger intensities and the application of the Beer-Lambert relationship (equation 6.1) -

$$\frac{I}{I_O} = e^{-(d/\lambda)}$$

Where I = the observed (P-B)/B_{1980} value in the presence of carbon
I_o = the observed (P-B)/B_{1980} for the carbon free clean surface
d = the thickness of the overlayer (in monolayers)
λ = the escape depth.

Equation 6.1 : Calculation of Monolayer Thickness By The Beer-Lambert Equation

As discussed earlier, the platinum (P-B)/B value was reduced from 0.22 to 0.14 by the presence of carbon. The corresponding decrease in rhodium (P-B)/B_{1980} value was from 0.049 to 0.026. The following calculations show the calculated overlayer thickness by application of equation 6.1. In the estimation of overlayer thickness, 1 monolayer is assumed to be equivalent to 0.25 nm.

For platinum $\frac{0.14}{0.22} = e^{-(d/7)}$ $d = 3.2$ monolayers (0.8 nm).

For rhodium $\frac{0.026}{0.049} = e^{-(d/3.5)}$ $d = 2.2$ monolayers (0.6 nm).

Use of the Beer-Lambert equation, therefore, indicated that the thickness of overlayer of carbon was in excess of a monolayer. The difference in calculated thickness by measuring the changes in Rh and Pt Auger peak intensities, at 3.2 for platinum AES and 2.2 for rhodium AES was, however, large. Although the difference may have been due to experimental error, there are other possible explanations, such as an error in the estimation of inelastic mean free path. The possibility that the presence of a carbon overlayer caused a change in the near surface rhodium concentration cannot, however, be excluded as the presence of carbon has been shown to cause the surface segregation of rhodium in platinum-rhodium alloys[3]. Assuming that the thickness measurement obtained by platinum AES was accurate, the Beer-Lambert model predicts that the change in the 302 eV Rh peak intensity (I / I_o) due to the presence of a 3.2 monolayer thick carbon overlayer would be $e^{-(3.2/3.5)} = 0.4$. Since the change in normalised Rh peak intensity (I / I_o) was 0.55, the results, although inconclusive, indicate that the alloy under the carbon overlayer may have been rhodium enriched by a factor of (0.55 / 0.4) 1.4 in comparison with the surrounding (carbon-free) surface. Since the concentration of rhodium at the carbon free surface was 14at%Rh, the results indicate that the near surface rhodium concentration may have been ca. 19at%Rh.

6.2.1.3 Spatial Distribution At The Near Surface

The spatial distribution of carbon, rhodium, oxygen and platinum was investigated by measuring the secondary electron intensities at the relevant peak and background energies. Figures 6.12 and 6.13 show the spatial distribution of the carbon peak (270 eV), and background (286 eV) intensities, whilst figure 6.14 shows the background normalised peak intensity distribution or (P-B)/B 'map'.

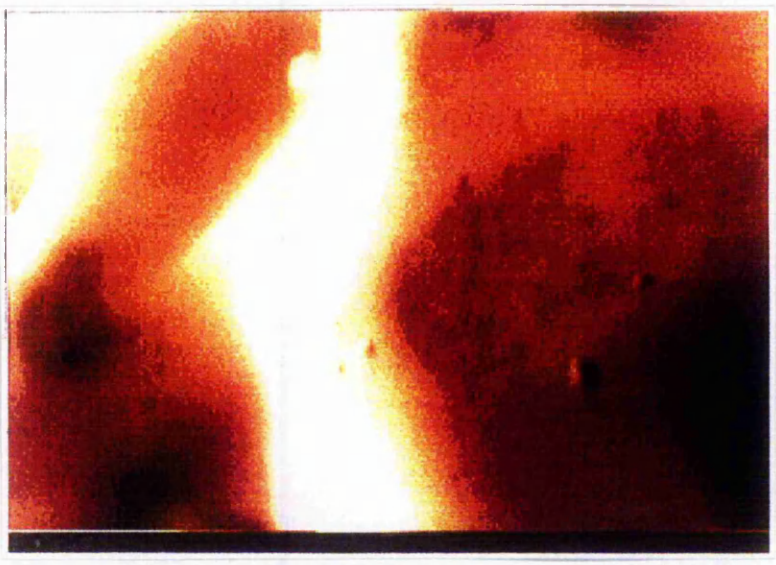

*Figure 6.12: Peak Map For Carbon 24*24 μm (X5000).*

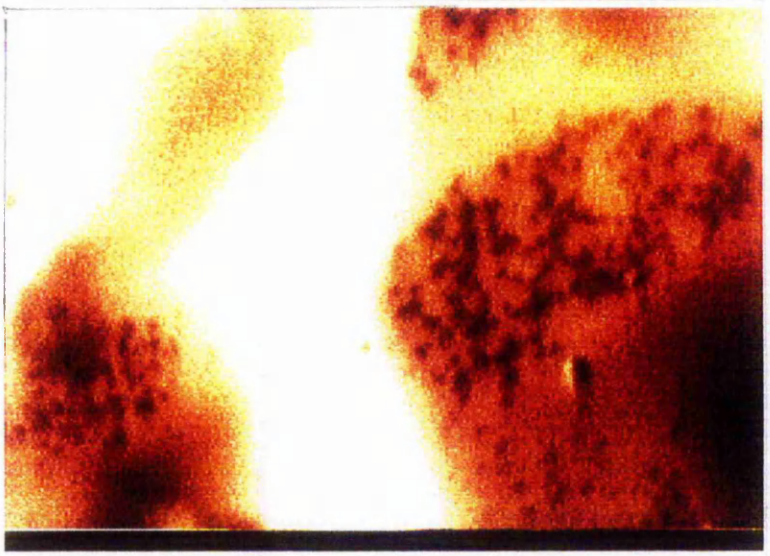

*Figure 6.13: Background Map For Carbon 24*24 μm (X5000).*

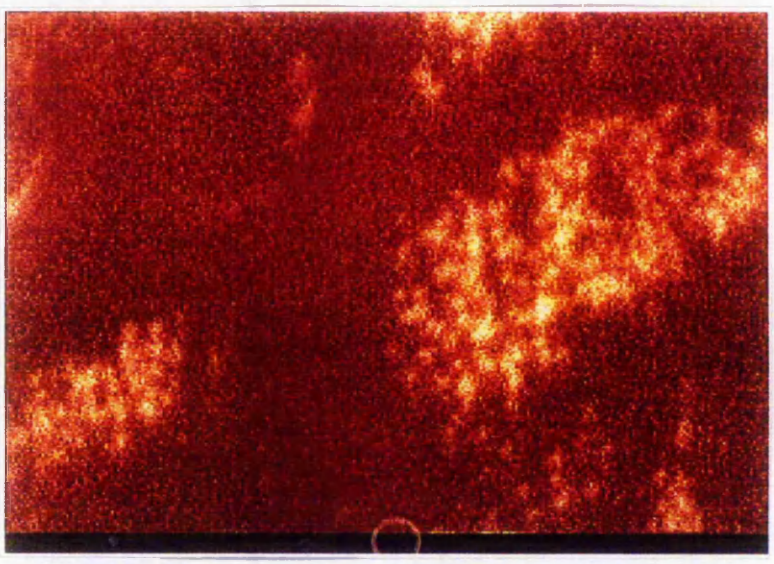

Figure 6.14: Carbon (P-B)/B Map 24*24 μm (X5000).

From an examination of the carbon peak intensity map (figure 6.12) a large variation in absolute peak intensities is clearly evident. Due to a close correlation with the SEM image (figure 6.2), the distribution of intensity was attributed to the topography of the sample. The background map (figure 6.13), although very similar to the peak map, contained significant differences seen as areas of decreased intensity of approximately 0.5 μm in diameter. The (P-B)/B map is shown in figure 6.14, and clearly indicates an inhomogeneous distribution of carbon at the surface of the catalyst. By comparing the carbon peak and background maps with the carbon (P-B)/B map a surprising feature is that, in comparison with carbon free areas, the presence of carbon did not result in an increase in the count rate at 270 eV but caused a decrease in the background at 286 eV. The changes in (P-B)/B value were, therefore, caused by changes in the background intensity. The role of the decrease in background intensity on changes in the carbon (P-B)/B value is shown clearly by comparing the Auger maps generated by normalisation at 286 eV (figure 6.14) and at 1980 eV (figure 6.15).

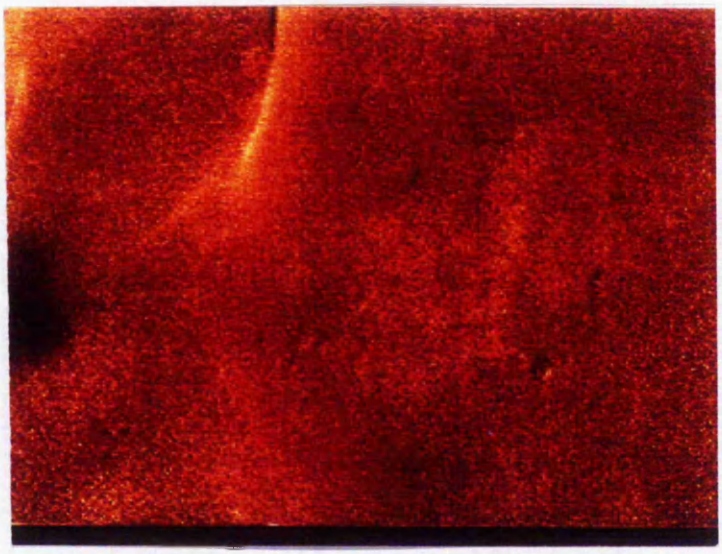

Figure 6.15: Carbon (P-B)/B_{1980} Map 24*24 μm (X5000).

By comparing the Auger maps for carbon generated by the (P-B)/B and (P-B)/B_{1980} methods, the (P-B)/B normalisation method was shown to produce an image with greater contrast. The greater contrast in the C (P-B)/B map relative to the C (P-B)/B_{1980} map was attributable to the decrease in background observed at 286 eV in areas of high P-B intensity, effectively increasing the (P-B)/B value by decreasing the denominator (B) in the (P-B)/B calculation. Since the high energy background (B_{1980}) did not alter with changes in carbon concentration, background factors did not contribute to the contrast in the 1980 eV normalised image and the resulting image shows only slight variations in (P-B)/B_{1980} value where large variations in the (P-B)/B value were observed.

The combination of the point analyses (AES) and intensity mapping (SAM), therefore, clearly identified that most of the alloy surface was carbon free, but that there was a significant area of the catalyst surface that was covered with a multilayer thickness of carbon. A proposed model of the surface is shown in figure 6.16.

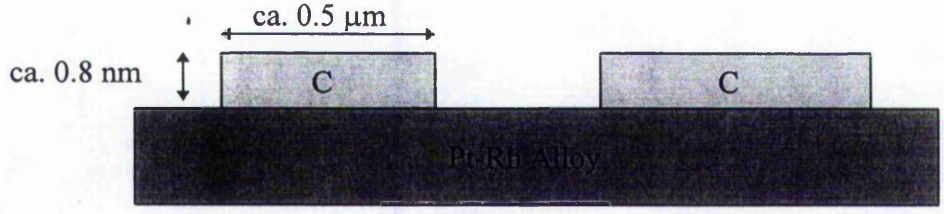

Figure 6.16 : Proposed Model of the Carbon Overlayer.

The results from mapping the surface at 302 eV (the rhodium peak) is shown in figure 6.17. The 312 eV map (the rhodium background) is discussed earlier and shown in figure 6.8.

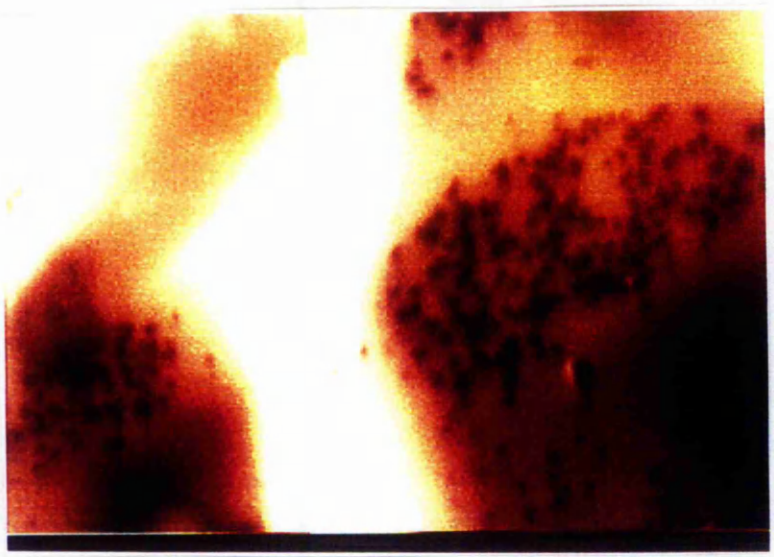

*Figure 6.17: Peak Map for Rhodium 24*24 μm.*

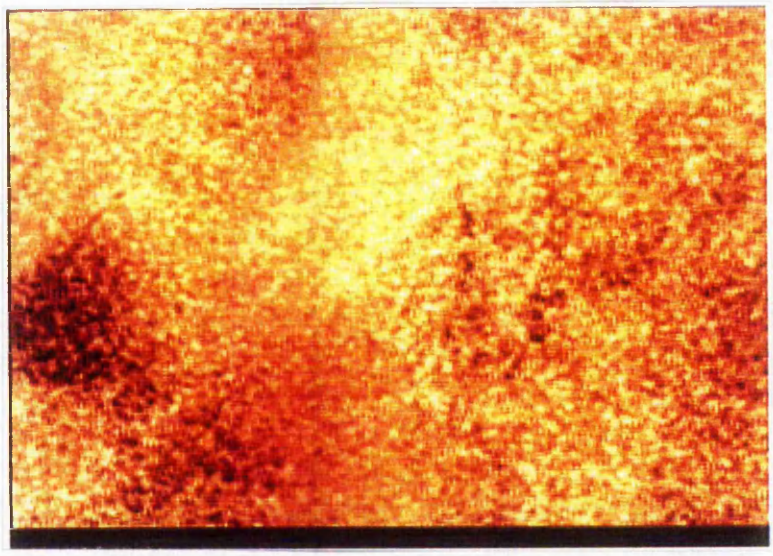

*Figure 6.18: (P-B)/B Map for Rhodium 24*24 μm (X5000)*

From the rhodium peak and background Auger maps, shown in figures 6.17 and 6.8, areas of high carbon, as imaged in figure 6.13, appeared as areas of low rhodium peak (P) and background (B) count rate. From the rhodium (302 eV) (P-B)/B image (figure 6.18), areas of high carbon result were shown to decrease the overall (P-B)/B value for Rh, but as seen in the analysis by point analyses, the decrease was small and there was a large degree of scatter in the results. As discussed in section 6.1.2.2, the smaller than expected decrease in the (P-B)/B value was caused by a decrease in the background intensity at ca. 300 eV caused by the presence of carbon. As the high energy background intensity (1980 eV) was shown to be unaffected by the presence

of carbon, and therefore provided a better method of background normalisation, the P_{302}-B_{312}/B_{1980} map was created and is shown in figure 6.19.

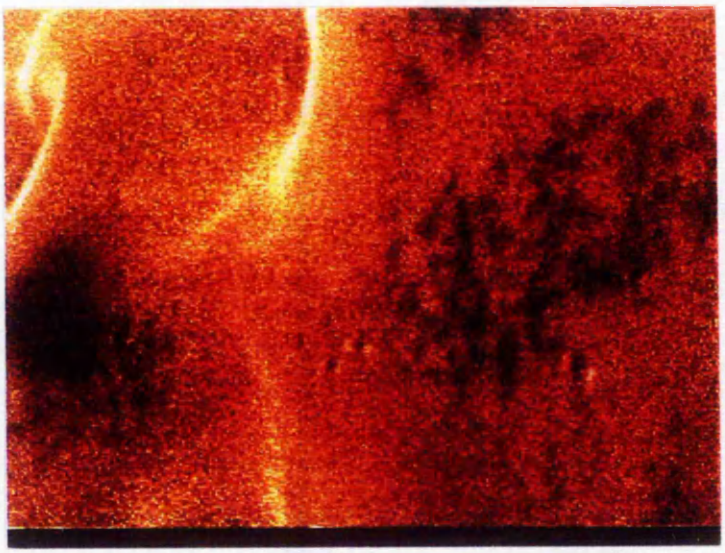

Figure 6.19: (P-B)/B_{1980} Map for Rhodium 24*24 μm (X5000)

By comparing figures 6.18 and 6.19, the choice of normalisation method was shown to have a large effect on the resulting map. The major difference between the images was that the high energy normalised map showed a much larger decrease in normalised rhodium intensity in areas of high carbon than the map generated by the standard method. The decreases observed by point analyses and the mapping procedure were, therefore, in agreement, and provided evidence that the normalisation process carried out at 1980 eV gave a better representation of the true changes in Auger peak intensity than the normalisation process carried out at a few eV above the peak i.e. at 312 eV.

In considering areas not covered in carbon, there was an apparent enrichment of rhodium just above and to the left of the centre of the image. The observation may have been due to a region of higher than average rhodium concentration, but due to the high SEM image contrast, the result may have been an artefact caused by the high primary beam angle of incidence (θ). The dependence of (P-B)/B with θ is clearly described by Batchelor *et al*[4] who studied the effect of θ on the (P-B)/B ratio of the Cu 914 eV, Si 1610 eV and W 1730 eV Auger peaks obtained from pure elemental standards. Their results indicated that for $\theta < 60°$ the (P-B)/B values were more or less constant but for $\theta > 60°$ there was a rapid increase in the observed (P-B)/B values.

The measurement process was repeated with energies representative of the peak and background intensities for oxygen and figures (6.20, 6.21 and 6.22) show the peak, background and (P-B)/B maps for oxygen.

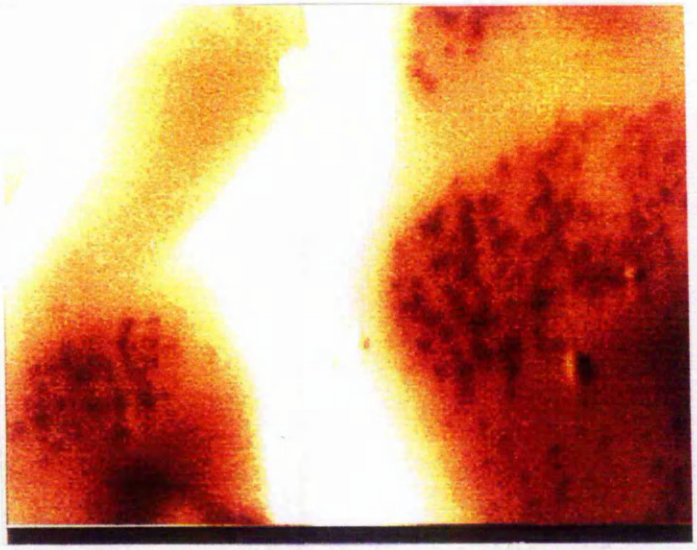

Figure 6.20: Peak Map for Oxygen 24*24 μm (X5000).

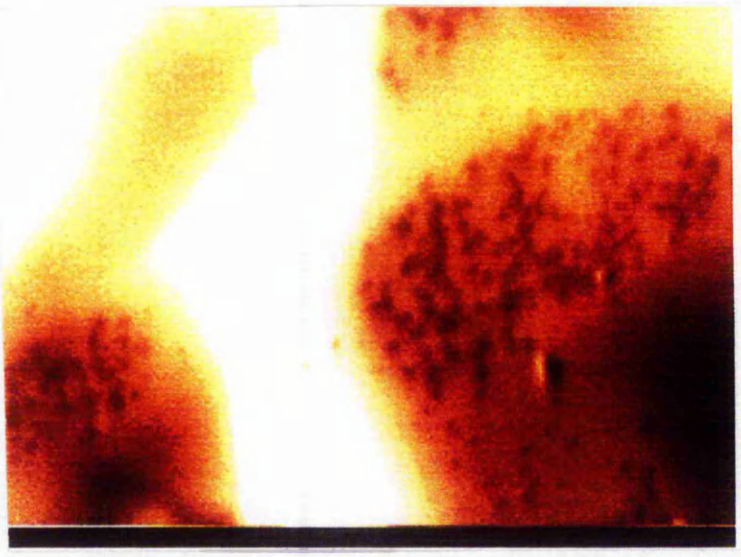

Figure 6.21: Background Map for Oxygen 24*24 μm (X5000).

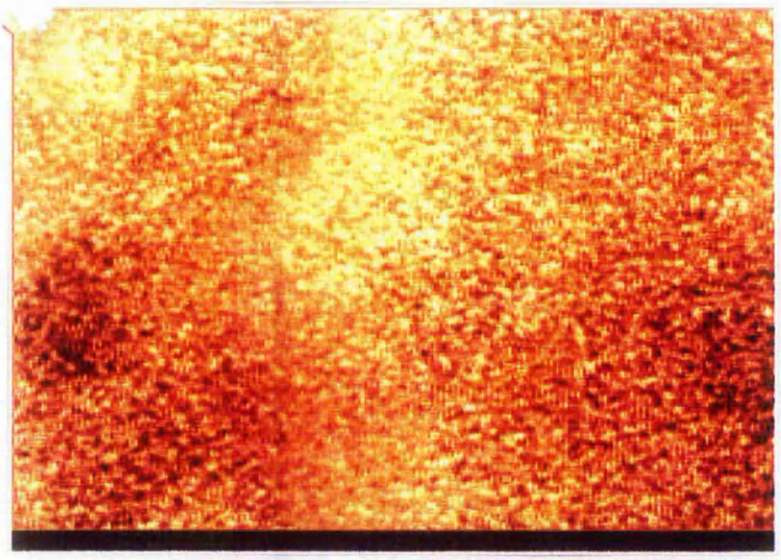

*Figure 6.22: (P-B)/B Map for Oxygen 24*24 μm (X5000).*

The oxygen peak and background images were very similar to the rhodium peak and background images in that both the peak and background count rates were reduced by the presence of carbon. The distribution of oxygen, measured by (P-B)/B, is shown in figure 6.22, and in areas not covered with carbon, the apparent spatial distribution closely matched the SEM image. The similarity of the result with the SEM image provided evidence, as seen for the rhodium image, that a breakdown of the topographical correction performed by (P-B)/B or $(P-B)/B_{1980}$ may have occurred. As discussed for the Rh (P-B)/B map, a better representation of the decrease in peak intensity was provided by a normalisation process carried out via use of the background at 1980 eV. Figure 6.23 shows the high energy background normalised map i.e. $(P-B)/B_{1980}$.

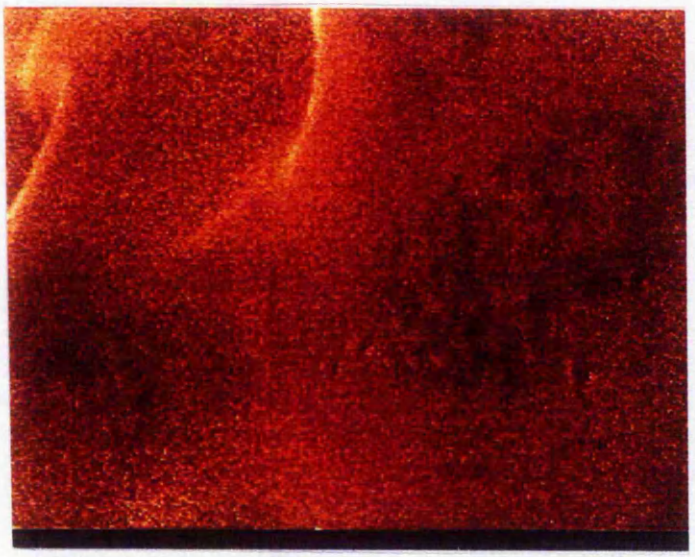

*Figure 6.23: $(P-B)/B_{1980}$ Map for Oxygen 24*24 μm (X5000)*

As seen in the case for rhodium, the use of a normalisation process at 1980 eV rather than at a few eV above the oxygen Auger peak (530 eV) resulted in a map that exhibited a larger decrease in intensity in regions of high carbon.

As discussed earlier, and shown in figure 6.9, the platinum background map was found to be very similar to the SEM image. Figure 6.24 shows the peak map for platinum, from which, the presence of carbon can be seen to cause a decrease in the peak intensity.

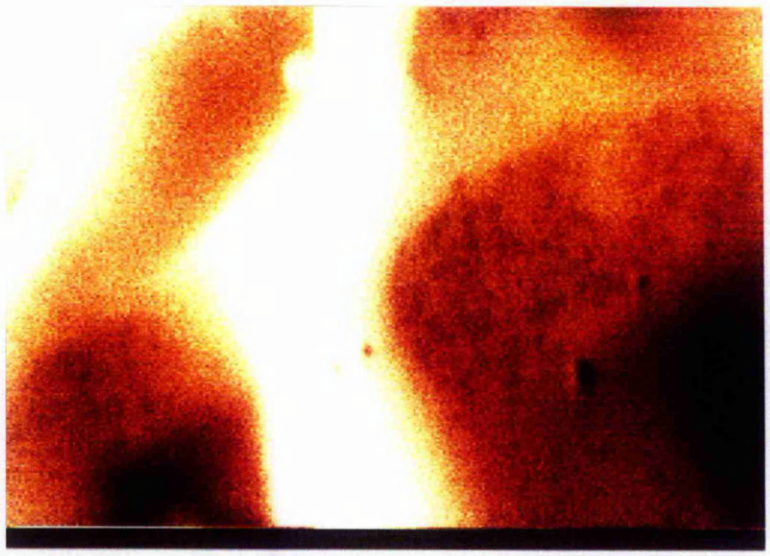

Figure 6.24: Peak Map for Platinum 24*24 μm.

Since the background intensity, from figure 6.9, was shown to be unaffected by the presence of carbon, whilst the peak intensity was seen to be decreased by the presence of carbon, the resulting (P-B)/B values were unaffected by changes in background. The (P-B)/B map, is shown in figure 6.25.

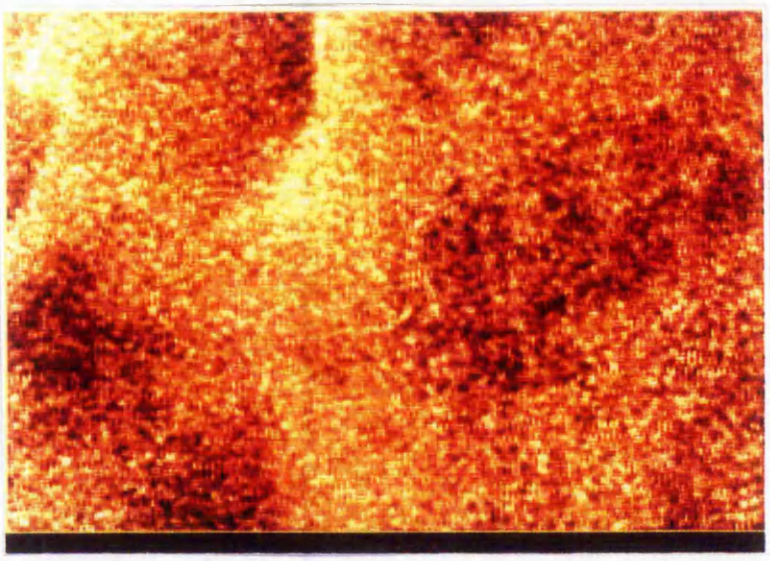

Figure 6.25: (P-B)/B Map for Platinum 24*24 μm.

Although the Pt (P-B)/B map (figure 6.25) clearly imaged the effect of the presence of carbon, similarity to the SEM image indicated that there were residual topographic effects contained within the result.

6.2.2 Top Layer of Gauze

An SEM image of the top layer of the catalyst sample (gas inlet side) is shown in figure 6.26. The SEM image was representative of the 'top' surface of the catalyst sample and revealed that the surface was highly faceted.

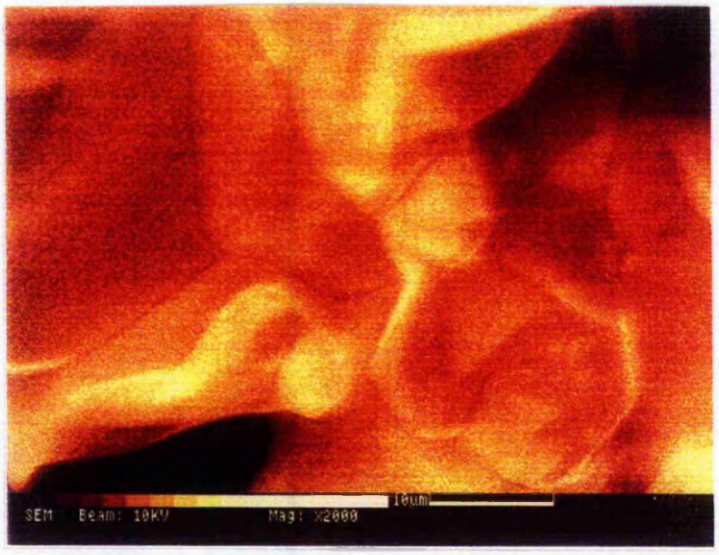

Figure 6.26: SEM of the Top of a Used Industrial Gauze. 60*60 μm (X2000).

Figure 6.27 shows a close-up SEM of the surface of the catalyst, the area of which was investigated by point-mode Auger electron spectroscopy.

Figure 6.27: Close-up SEM of the Top of a Used Industrial Gauze. 24*24 μm (X5000)

The Auger spectra obtained for point analyses P1-P6 are shown in figures 6.28-6.30. Although the point analyses P1-P6 were performed within the area of the surface shown in figure 6.27, unfortunately, the image indicating the exact location of the point analyses was lost due to a technical fault.

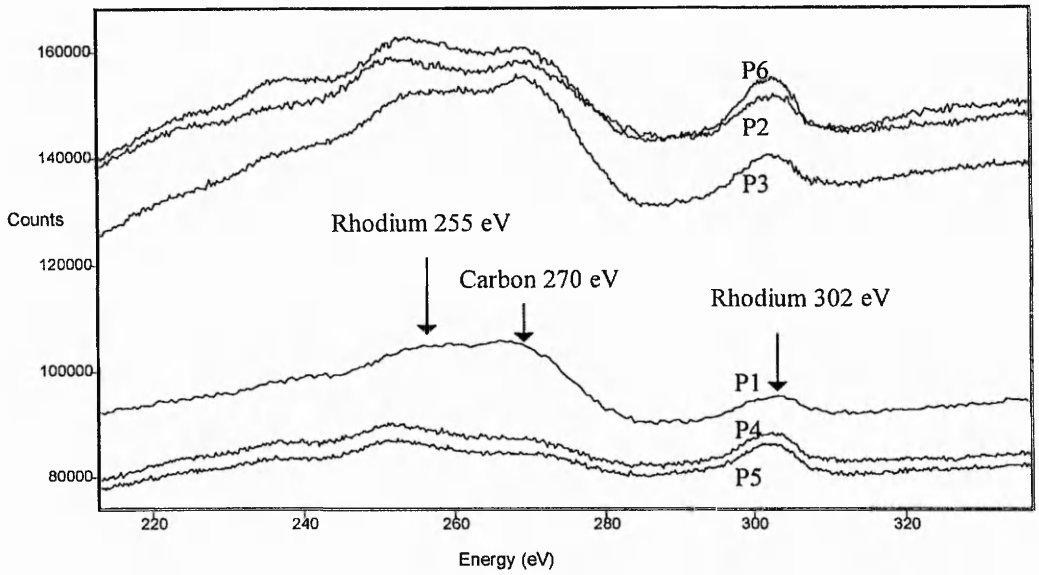

Figure 6.28: Point Analyses P1-6 Carbon And Rhodium Auger Region.

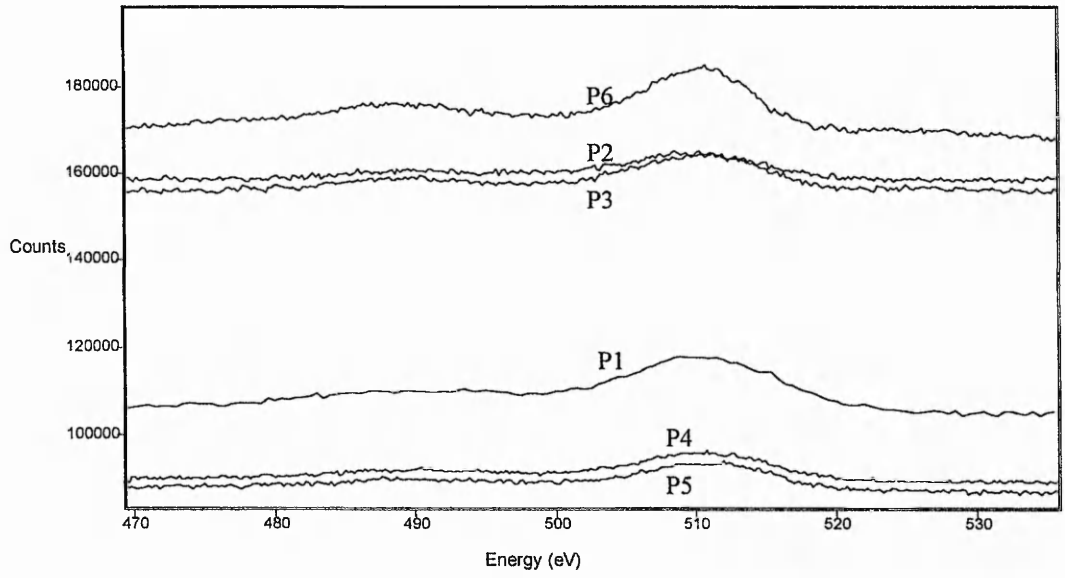

Figure 6.29: Point Analyses P1-6 Oxygen Auger Region.

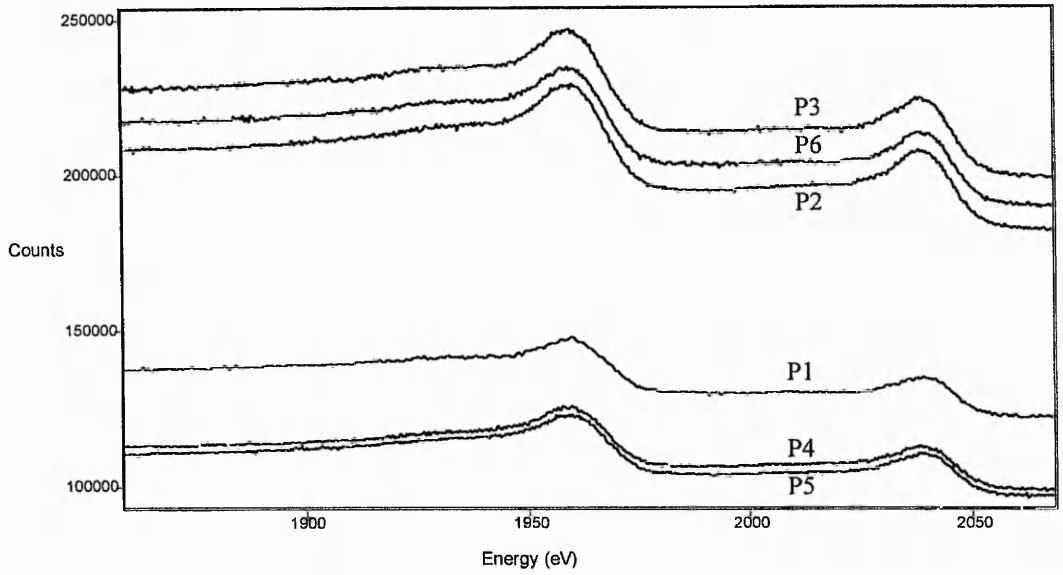

Figure 6.30: Point Analyses P1-6 Platinum Auger Region.

The (P-B)/B values for carbon, rhodium, oxygen and platinum for point analyses P1-P6 are shown in table 6.2.

Point Analysis	C (P-B)/B	Rh (P-B)/B	O (P-B)/B	Pt (P-B)/B
P1	0.17	0.04	0.12	0.14
P2	0.18	0.05	0.05	0.14
P3	0.12	0.07	0.04	0.16
P4	0.06	0.06	0.07	0.18
P5	0.05	0.07	0.07	0.18
P6	0.10	0.06	0.10	0.15

Table 6.2: Point Analyses of the Top of a Used Industrial Gauze Pack (P1-6). Auger peak intensities are represented by (P-B)/B values.

The results shown in table 6.2 indicate that large variations in surface concentration was observed. From a statistical analysis of the results, increases in carbon (P-B)/B were associated with decreases in the rhodium, oxygen and platinum (P-B)/B values. The correlation factors were - 0.75 for rhodium, - 0.6 for oxygen and - 0.3 for platinum.

6.2.2.1 *The Near Surface Concentration of Platinum And Rhodium*

The results of point analyses P1-P6 are shown in figures 6.31 and 6.32 in the form of plots of platinum (P-B)/B vs. carbon (P-B)/B and rhodium (P-B)/B vs. carbon (P-B)/B.

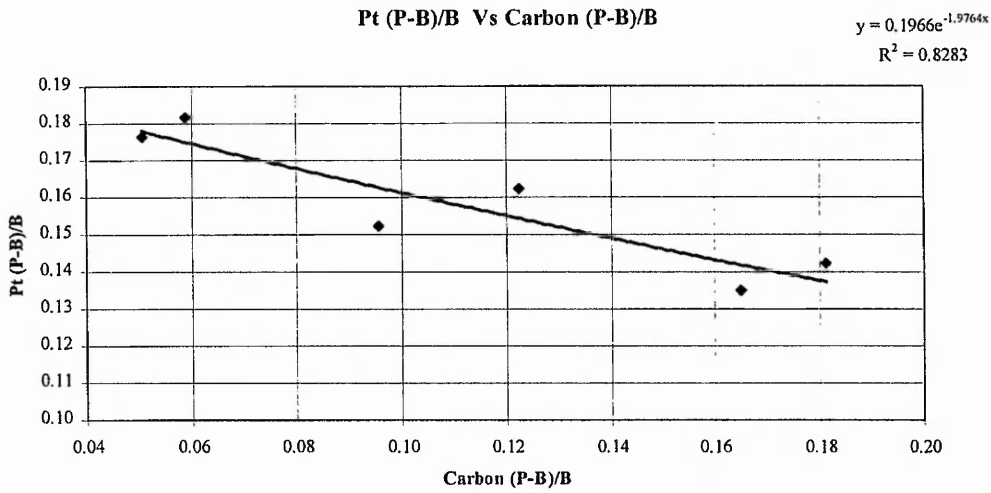

Figure 6.31 : Platinum Vs. Carbon Auger Intensity.

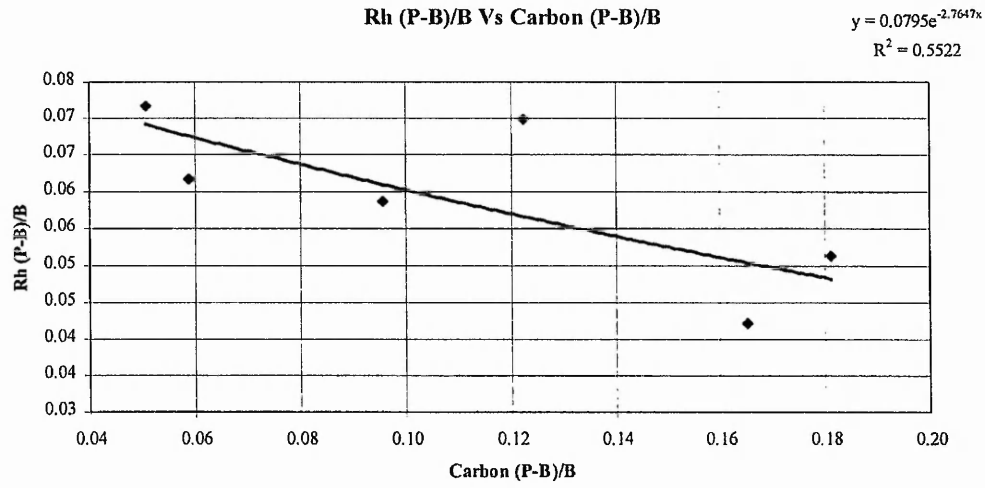

Figure 6.32 : Rhodium Vs. Carbon Auger Intensity.

From the plots shown in figures 6.31 and 6.32, the minimum carbon (P-B)/B value observed was 0.05 which was associated with a platinum (P-B)/B value of 0.18 and a rhodium (P-B)/B value of 0.07. By comparing the Pt and Rh (P-B)/B

values with the calibration standards, the near surface concentrations of platinum an rhodium were, therefore, measured at 72 at%Pt and 12 at%Rh respectively. The observed concentrations of platinum and rhodium were, therefore, lower than the bulk concentrations but a significant carbon Auger peak was always observed. From the results obtained from the 'bottom' surface of the catalyst, shown in section 6.2.1, the carbon (P-B)/B value in the absence of a carbon Auger peak was measured at -0.03. By extrapolating the relationship between the Rh and Pt (P-B)/B values with the carbon (P-B)/B to a carbon (P-B)/B value of -0.03, the influence of carbon on both the Rh and Pt (P-B)/B values was removed from the results. For a carbon (P-B)/B value of -0.03, the extrapolation calculation predicted a Pt (P-B)/B value of 0.21 whilst the corresponding value for rhodium was 0.075. The results obtained by extrapolation, therefore, indicated that the near surface composition under the carbon layer was approximately 83at%Pt, 13at%Rh. The result must, however, be treated with caution due to the large degree of scatter within the results.

6.2.2.2 The Distribution of Carbon at the Near Surface

From the results obtained from the 'top' surface of the catalyst, a decrease in both the Pt and Rh (P-B)/B values was observed with increasing carbon (P-B)/B value. The plot of platinum (P-B)/B Vs carbon (P-B)/B (figure 6.32) showed that in the presence of a high carbon concentration, i.e. exhibiting a carbon (P-B)/B value of 0.18, the Pt (P-B)/B value was 0.14. From the discussion in section 6.2.2.1, extrapolation of the relationship between the Pt (P-B)/B value and the C (P-B)/B value predicted that the Pt (P-B)/B value at the carbon free surface would be 0.21. The decrease in the platinum peak intensity (I/I_o), due to the presence of carbon, was, therefore, 0.14/0.21 = 0.67.

The plot of rhodium (P-B)/B_{1980} Vs carbon (P-B)/B is shown in figure 6.33.

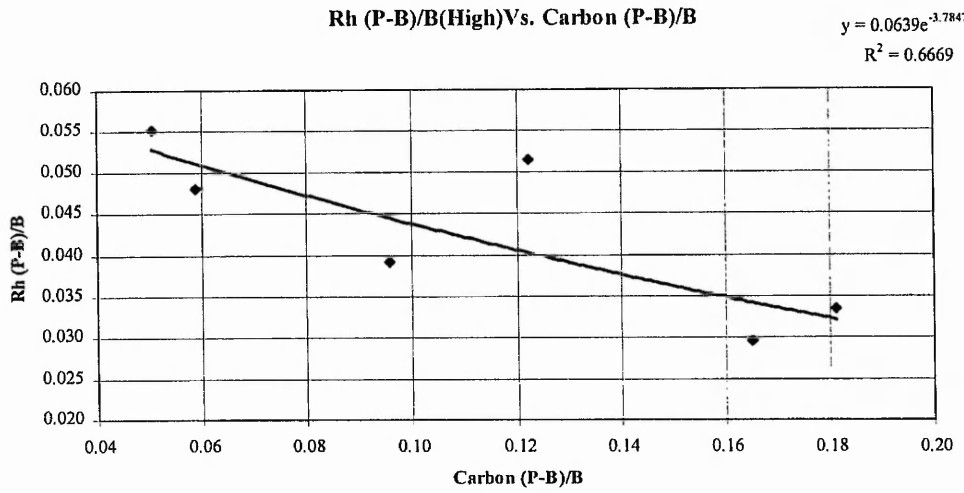

Figure 6.33 : Rhodium P-B intensity normalised by the 1980 eV background Vs. Carbon Auger Intensity

Figure 6.33 shows that, coincident with an increase in the carbon concentration from a (P-B)/B value of 0.05 to 0.18, the Rh (P-B)/B_{1980} value decreased from 0.053 to 0.032 (0.052/0.032 = 60%). Extrapolation of the results to a carbon (P-B)/B value typical of a carbon free surface (-0.03), however, predicted that the Rh (P-B)/B_{1980} value in the absence of carbon would have been 0.072. The calculated change in Rh (P-B)/B_{1980} intensity (I/I_o) in going from a carbon free surface to one exhibiting a carbon (P-B)/B of 0.18 was, therefore, 0.032/0.072 = 0.44.

The decrease in the Rh (P-B)/B_{1980} value in the presence of carbon was, therefore, larger than the decrease in Pt (P-B)/B value. As discussed in section 6.2.1.2 a greater decrease in the Rh (P-B)/B_{1980} value than the Pt (P-B)/B value indicates that the carbon present was in the form of a surface layer. From the decrease in Pt (P-B)/B and the application of the Beer-Lambert equation, as discussed in section 6.2.1.2, the maximum thickness of the carbon overlayer was calculated at 2.9 monolayers. From the decrease in Rh (P-B)/B_{1980} the thickness of the carbon overlayer was calculated at 2.8 monolayers. Although the calculated results for overlayer thickness are in excellent agreement, the poor correlation observed for the exponential decay curves indicates that the agreement may, in fact, be rather fortuitous.

6.2.2.3 *Spatial Distribution At The Near Surface*

SEM images of the 'top' surface of the catalyst, shown in figures 6.26 and 6.27, indicated that the surface of the catalyst was extremely rough. Figures 6.34 to 6.35 show the spatial distribution of the platinum background intensity (1980 eV) for the area of the catalyst shown in figure 6.27. The difference between the images shown in figures 6.34 and 6.35 is due to a change in the false colour intensity scale whereby the scale used to generate image 6.35 was $^1/_4$ that used to generate image 6.34. The contrast in image 6.35 is, therefore, 4 times greater than in image 6.34.

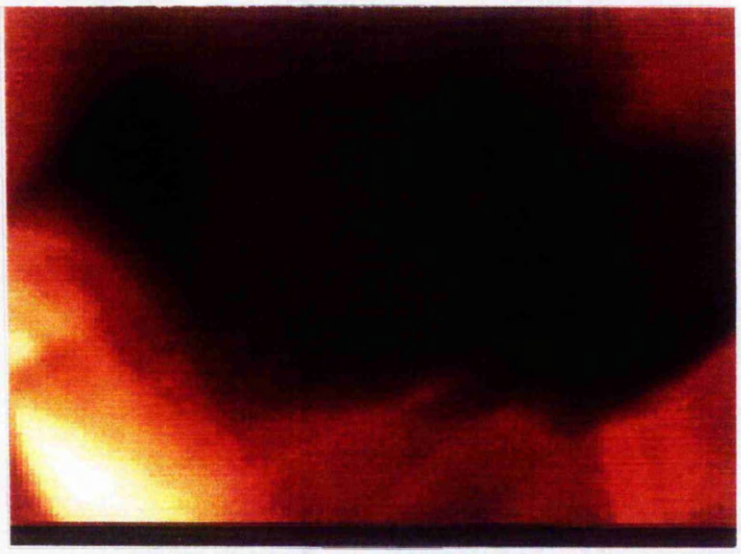

Figure 6.34: Background Map for Platinum - 1980 eV 24*24 μm (X5000).

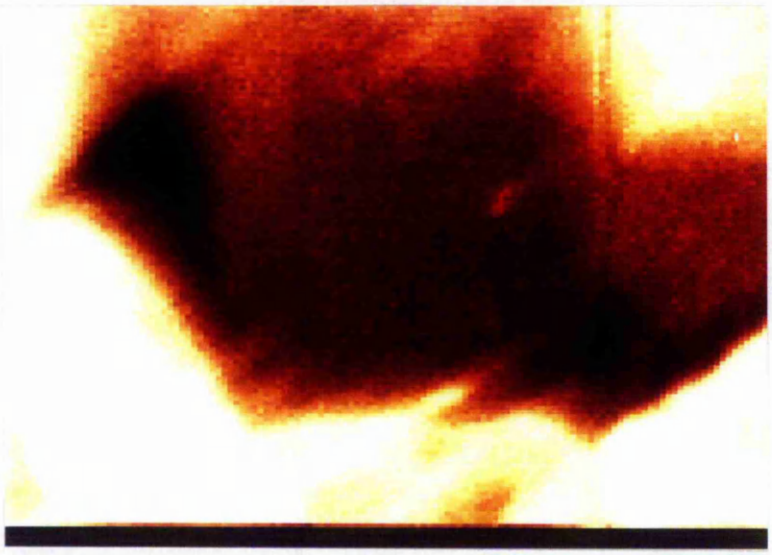

Figure 6.35: Contrast Enhanced (X4) Background Map for Platinum - 1980 eV 24*24 μm (X5000).

Figures 6.34 to 6.35 show that the spatial distribution of background intensity was large, and indicated that there was a large variation in the angle of incidence of the primary beam. The large variation in background intensity has important implications in the interpretation of Auger maps as large changes in angle of incidence will, to some degree, result in SAM images that contain residual topographic features.

The (P-B)/B map for carbon is shown in figure 6.36.

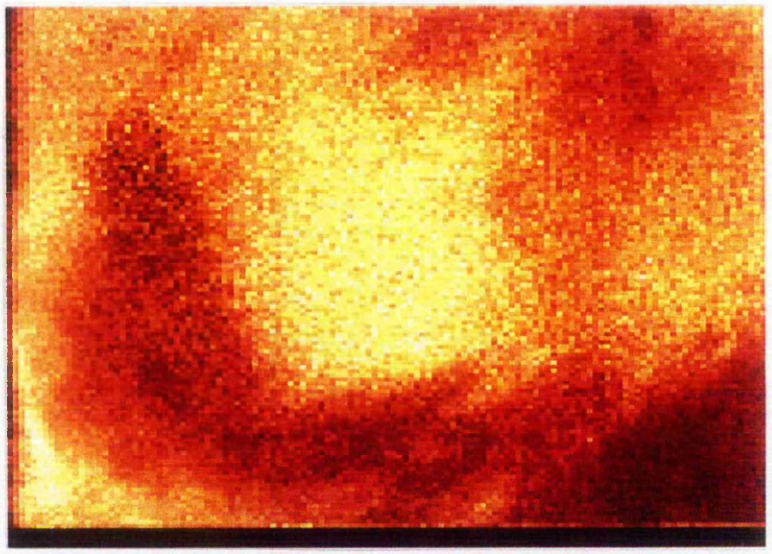

Figure 6.36: (P-B)/B Map For Carbon 24*24 μm (X5000).

Figure 6.36 indicates that there was an apparent distribution of carbon at the near surface of the catalyst. By comparing the (P-B)/B map for carbon with the SEM image (figure 6.27) a correlation was observed which indicated that the result may have been affected by topographic effects.

From the comparison of (P-B)/B images and $(P-B)/B_{1980}$ images obtained from the 'bottom' surface of the catalyst pack (section 6.2.1), the use of $(P-B)/B_{1980}$ normalisation was proven to provide a better method for generating SAM images for rhodium and oxygen than (P-B)/B normalisation. The $(P-B)/B_{1980}$ normalisation process was, therefore, used to generate $(P-B)/B_{1980}$ images for rhodium and oxygen. The results of the $(P-B)/B_{1980}$ maps for rhodium, oxygen and platinum are shown in figures 6.37 to 6.39. Due to the large degree of scatter within the experimental results it was found necessary to perform a smoothing routine on the images, achieved by calculating a pixel value that was an average of the pixel and the pixels immediately surrounding it i.e. in a 3 X 3 array.

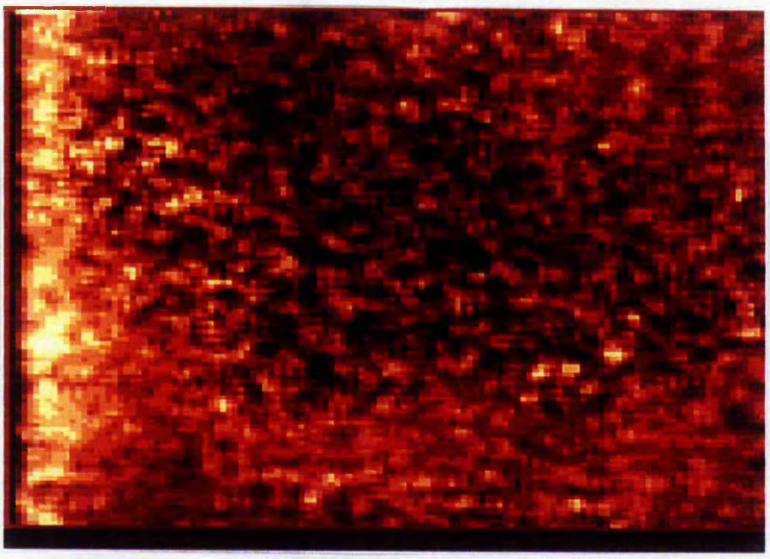

*Figure 6.37: (P-B)/B_{1890} Map For Rhodium 24*24 μm (X5000).*

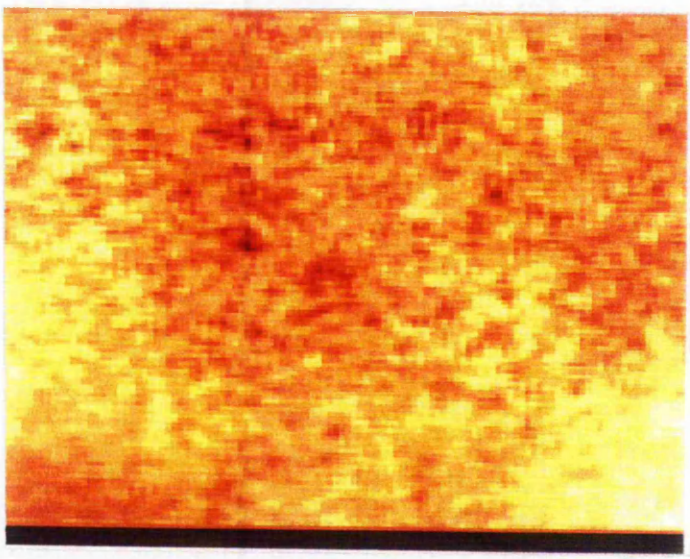

*Figure 6.38: (P-B)/B_{1980} Map For Oxygen 24*24 μm (X5000).*

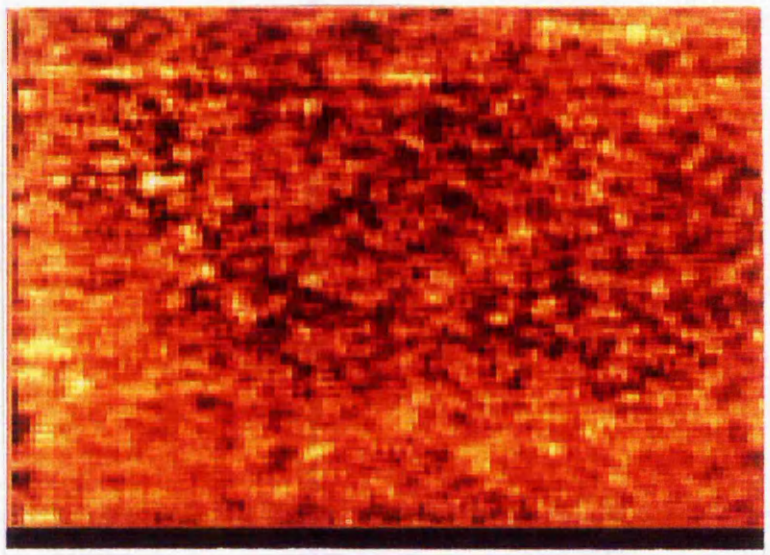

Figure 6.39: (P-B)/B Map For Platinum 24*24 μm (X5000).

From the (P-B)/B and $(P-B)/B_{1980}$ images shown in figures 6.36 to 6.39, there was an apparent spatial distribution of carbon, rhodium, oxygen and platinum. Although the presence of a high carbon (P-B)/B intensity was possibly associated with decreases in the rhodium, oxygen and platinum $(P-B)/B_{1980}$ maps, scatter in the results was large.

6.3 XPS

The 'top' and 'bottom' surfaces of the sample of 83-17 catalyst removed from the an industrial reactor were characterised by XPS. The source used was Al K_α ($h\nu$=1486.3 eV). The resulting XPS spectra of the 'top' and 'bottom' surfaces showing the Rh 3p, Pt 4p and O 1s XPS peaks are shown in figure 6.40.

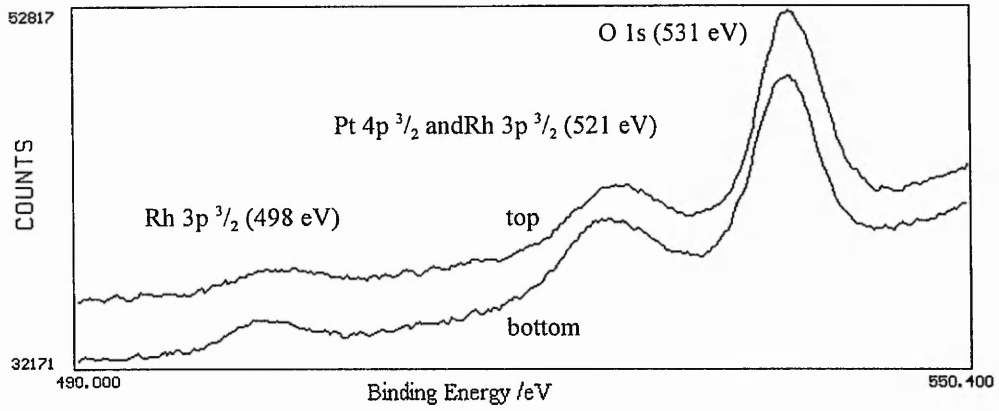

Figure 6.40 : XPS Spectra - Top and Bottom Surfaces of the Used Gauze

From an interpretation of the relative Rh : Pt XPS peak areas, as discussed in section 4.2, the rhodium concentration at the near surface of the top and bottom surfaces of the catalyst was measured at 17.6 and 17.8 %Rh respectively. The XPS results, therefore, indicated that the near surface concentration of rhodium at the near surface of both the top and bottom surfaces of the catalyst were within experimental error of the bulk composition. The error associated with the analysis was estimated by repeated measurement of the Rh 3p $^3/_2$ peak area and was approximately 2 %. The kinetic energy of the Pt and Rh photoelectrons was ca. 1000 eV (1486.3 - 500). As discussed in section 4.2, the surface sensitivity of 1000 eV photoelectrons is approximately 18% indicating that the analysis by XPS is sufficiently surface sensitive to detect changes in near surface composition. The near surface composition of the 'top' and 'bottom' surfaces were, therefore, shown to be within experimental error of the bulk composition.

6.4 Conclusions

From SEM imaging of the surface of the catalyst, the 'top' surface was seen to be much more highly faceted than the 'bottom' surface. Extensive faceting of the gauze, and in particular the 'top' surface is well known but caused significant problems in the quantitative characterisation of the gauze by SAM.

SAM imaging of the 'bottom' surface clearly identified localised changes in surface composition which were easy to image due to the relatively smooth topography of the surface. Imaging of the 'top' surface was an extremely difficult process as the rough topography of the sample often caused difficulty in obtaining a satisfactory secondary electron intensity due to 'shadowing' of the detector.

From imaging of the 'bottom' surface of the catalyst, the use of a $(P-B)/B_{1980}$ normalisation process rather than (P-B)/B yielded results which more accurately modelled the effects of changes in near surface composition, and in particular the effect of carbon on the Rh 302 eV (P-B)/B value, but neither of these normalisation techniques completely removed topographic effects. As both the 'bottom' and 'top' surfaces of the catalyst sample were macroscopically and microscopically very rough, failure of the normalisation processes to suppress the topographic effects completely was unsurprising and such effects are reported elsewhere[5].

The surface composition for both the 'top' and 'bottom' surfaces was measured by AES and XPS and were in agreement that there was no difference in Pt : Rh elemental ratio between the 'bottom' and 'top' surfaces. The results were, however, in disagreement in the measurement of the absolute near surface composition where the analysis by XPS indicated a significantly higher rhodium concentration than the analysis by AES. Although it is difficult to be certain as to the reason behind the observation, the difference in results may be due to the analytical method used. The analysis by AES measured a concentration and, therefore, the observed concentration would have been reduced by the presence of carbon and oxygen. The analysis by XPS measured the Pt : Rh elemental ratio rather than a concentration and, due to the almost identical inelastic mean free path of the platinum and rhodium photoelectrons, the observed Pt : Rh elemental ratio would not have been affected by the presence of any other element whether within the bulk of the alloy or in the form of an overlayer.

6.5 References

[1] C.G.H. Walker, D.C. Peacock, M. Prutton, M.M. El Gomati. Surface And Interface Analysis **11** 266-278 (1988).

[2] S. Michler, H.E. Bishop. Surface and Interface Analysis **17** 315-319 (1991).

[3] M. Ahmad, T.T. Tsong. Surface Science **149** L7-L12 (1985).

[4] D.R. Batchelor, H.E. Bishop, J.A. Venables. Surface And Interface Analysis **14** 709-716 (1989).

[5] L. Frank, M.M. El Gomati. Czechoslovak Journal of Physics **44** (3)173-193 (1994).

7. Characterisation - Laboratory Samples

7.1 Introduction

From the catalytic results shown in chapter 3, the activation behaviour of the different 83at%Pt - 17at%Rh, 91at%Pt - 9at%Rh and 100%Pt samples, under standard conditions, varied significantly. In an attempt to explain the activation process, and in particular the effect of rhodium on the catalytic behaviour of the catalysts, samples of fresh catalyst gauze were activated for a specific length of time and then removed from the reactor for characterisation. By reference to the activation results shown in chapter 3, it was decided to characterise the catalysts early in the activation process (after 1 hour), mid way through the activation process (after 8 hours), and after the catalyst was fully activated (after >30 hours of activation).

The samples were characterised by scanning electron microscopy (SEM) to investigate the effect of activation on the morphology, and in more detail, the effect of rhodium concentration on the changing morphology of the catalyst. Scanning Auger microscopy (SAM) and X-Ray photoelectron spectroscopy (XPS) were used to investigate the near surface concentration of platinum and rhodium whilst time of flight secondary ion mass spectroscopy (ToFSIMS) was used to characterise the depth distribution of rhodium. Due to the very high sensitivity of ToFSIMS to the presence of catalyst poisons such as iron, ToFSIMS was also performed on selected samples to provide a sample-to-sample comparison.

Of the range of techniques mentioned above, not all were applied to all samples. Table 7.1 shows whether a technique was applied to a gauze catalyst sample.

Sample	SEM	SAM	XPS	ToFSIMS
83-17 Activated for 1 hour	✓	✓	✓	no
91-9 Activated for 1 hour	✓	✓	✓	no
Pure Pt Activated for 1 hour	✓	✓	no	no
83-17 Activated for 8 hours	no	no	✓	no
91-9 Activated for 8 hour	no	no	✓	no
83-17 Fully activated	✓	✓	✓	✓
91-9 Fully activated	✓	✓	✓	✓
Pure Pt Fully activated	✓	✓	no	no

Table 7.1 : Results Index Table

7.2 One Hour Activation

7.2.1 Scanning Electron Microscopy / Scanning Auger Microscopy

The samples of 83-17, 91-9 and 100% platinum catalyst gauze activated for 1 hour were placed in the V.G. SAM and characterised by SEM. SEM images of the top layers of the 83at%Pt - 17at%Rh, 91at%Pt - 9at%Rh and 100%Pt catalyst packs are shown in figures 7.1, 7.2 and 7.3.

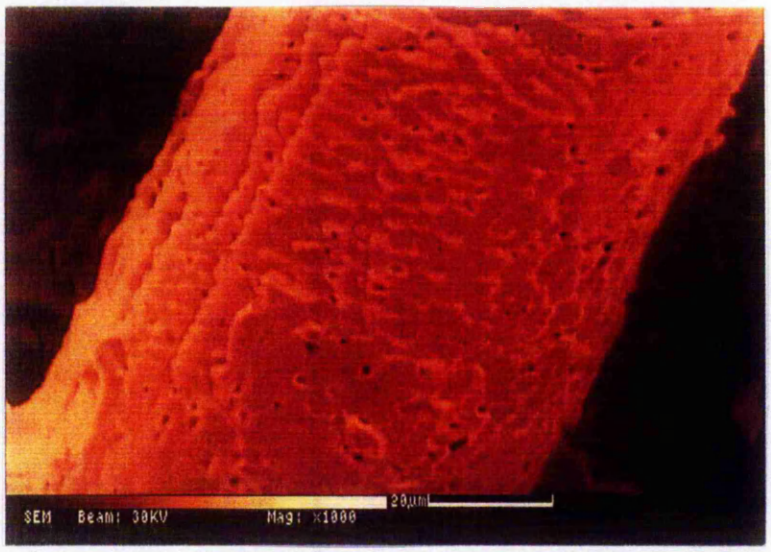

*Figure 7.1: SEM of the Top Layer of Gauze in a Separated 83-17 Pack After 1 Hour of HCN Synthesis. 120*120 µm.*

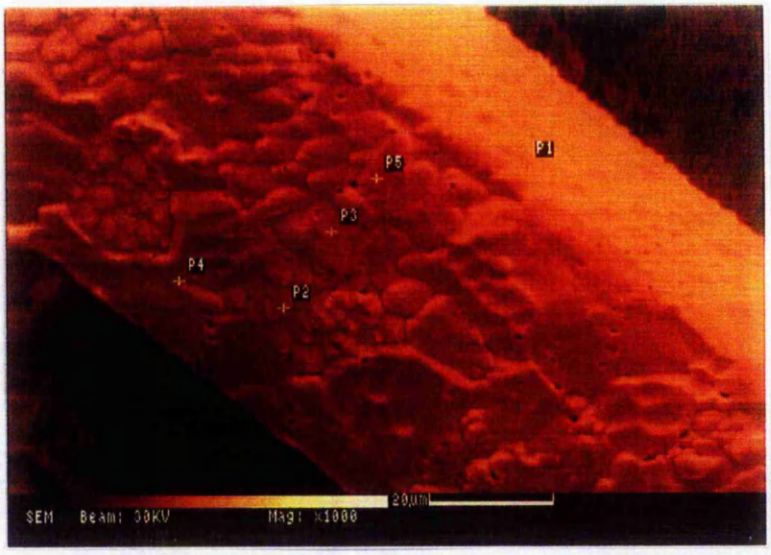

*Figure 7.2: SEM of the Top Layer of Gauze in a Separated 91-9 Pack After 1 Hour of HCN Synthesis. 120*120 µm.*

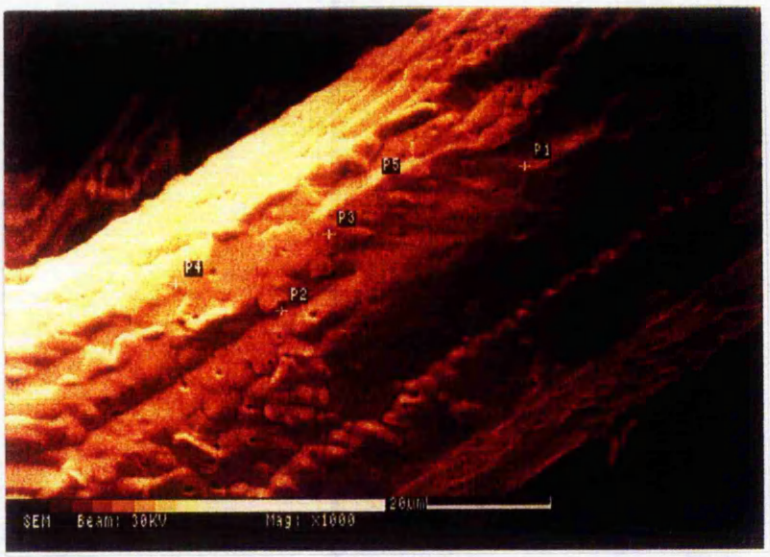

*Figure 7.3: SEM of the Top Layer of Gauze in a Separated 100% Pt Pack After 1 Hour of HCN Synthesis. 120*120 µm.*

No differences in morphology can be seen in the SEM images, shown in figures 7.1-7.3, so after 1 hour of HCN synthesis the morphology seemed to be independent of the rhodium content.

After characterisation by SEM, the samples of 83-17, 91-9 and 100 % Pt gauze were characterised by point-mode AES. As discussed in section 4.1, the near surface concentration of carbon, rhodium, oxygen and platinum, was estimated by measuring the background normalised peak intensity i.e. (P-B)/B ratio from the resulting Auger spectra. Some (P-B)/B ratios for carbon, rhodium, oxygen and platinum obtained from the 83-17 catalyst, the 91-9 catalyst and the pure platinum catalyst are shown in tables 7.2 to 7.4 respectively. Note that, although the point analyses were performed within the area of the catalyst shown in figures 7.1 to 7.3, the point analyses were not necessarily performed as indicated by the point markers.

Point Analysis	C (P-B)/B	Rh (P-B)/B	O (P-B)/B	Pt (P-B)/B
P1	0.05	0.10	trace	0.20
P2	0.06	0.10	trace	0.25
P3	0.06	0.17	trace	0.20
P4	0.07	0.13	trace	0.21
Average	0.06 ± 0.01	0.13 ± 0.03	N/A	0.22 ± 0.02

Table 7.2: SAM Results - 1 Hour Activated 83at%Pt-17at%Rh

Point Analysis	C (P-B)/B	Rh (P-B)/B	O (P-B)/B	Pt (P-B)/B
P1	0.06	0.05	nil	0.24
P2	0.09	0.07	nil	0.26
P3	0.09	0.06	nil	0.21
P4	0.05	0.07	nil	0.26
P5	0.05	0.05	nil	0.20
P6	0.05	0.04	nil	0.19
P7	0.07	0.06	nil	0.21
P8	0.09	0.06	nil	0.20
P9	0.06	0.06	nil	0.19
Average	0.07 ± 0.02	0.06 ± 0.01	N/A	0.22 ± 0.03

Table 7.3 : SAM Results - 1 Hour Activated 91at%Pt-9at%Rh

Point Analysis	C (P-B)/B	Rh (P-B)/B	O (P-B)/B	Pt (P-B)/B
P1	0.07	nil	trace	0.25
P2	0.08	nil	trace	0.25
P3	0.12	nil	trace	0.23
P4	0.09	nil	trace	0.25
P5	0.12	nil	trace	0.26
P6	0.07	nil	trace	0.22
Average	0.09 ± 0.02	N/A	N/A	0.24 ± 0.01

Table 7.4: SAM Results - 1 Hour Activated 100% Platinum

From the results for the 83-17 catalyst (table 7.2), the average Rh (P-B)/B was 0.13 ± 0.03. From calibration of the Auger microscope, as discussed in section 4.1, the near surface concentration of rhodium was, therefore, measured at 0.13/0.57 = 23 ± 5 %Rh. From the analogous calibration for platinum the near surface concentration of platinum was measured at 0.22/0.25 = 88 ± 8 %. The absolute concentration of carbon at the near surface of the catalyst samples is difficult to ascertain due to the difficulties in obtaining a suitable standard. Characterisation of the sample of industrial catalyst, however, showed that for multilayer carbon deposition the carbon (P-B)/B value was in excess of 0.1. The carbon concentration was, therefore, approximately one monolayer.

Although the total near surface concentration of platinum and rhodium was greater than 100%, this observation may be explained by a combination of experimental error and differences in surface sensitivity of the analysis. Calculations shown in section 4.1 show that the surface monolayer contribution to the rhodium Auger intensity was ca. 25% whilst the corresponding figure for the platinum Auger intensity was only 13%. Surface segregation of rhodium would, therefore, increase the rhodium Auger (P-B)/B value quicker than the corresponding decrease in platinum Auger (P-B)/B which may, therefore, result in an apparent surface concentration of > 100%.

For the 91-9 catalyst, the near surface concentration of rhodium was measured at 11 ± 2 % whilst the platinum surface concentration was measured at 88 ± 12 %. For the pure platinum sample, AES showed only the presence of platinum, carbon and oxygen at the near surface. The platinum near surface concentration was measured at 96 ± 4 %.

For the 83-17 and 91-9 samples, the results obtained by point mode AES, therefore, showed that after 1 hour of use, the rhodium concentration at the near surface was greater than the bulk concentration.

7.2.2 X-Ray Photoelectron Spectroscopy

Samples of both 83-17 and 91-9 catalysts were activated under standard conditions and removed from the reactor after 1 hour of HCN synthesis. XPS was performed on the top layer of the gauze pack. The resulting XPS spectra are shown in figure 7.4.

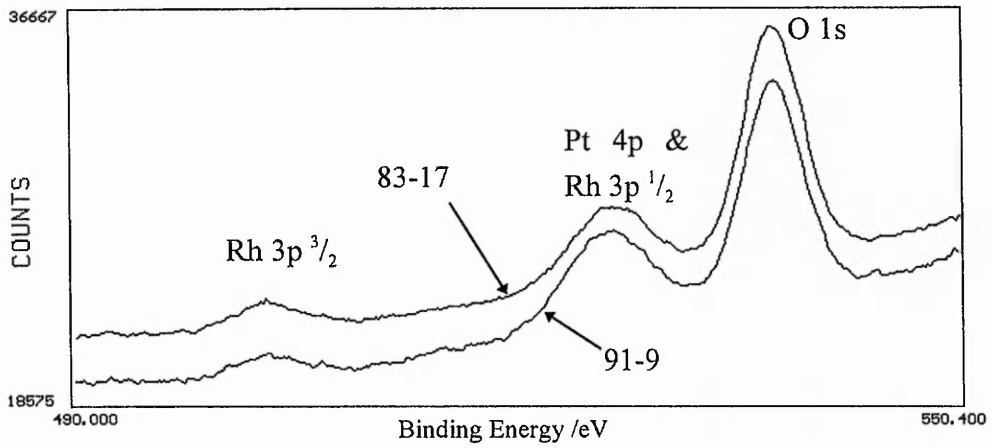

Figure 7.4 : XPS Spectra of the Top Layer of Gauze - 83-17 and 91-9 Samples after 1 hour activation

From an analysis of the relative Rh : Pt XPS peak areas, as discussed in section 4.2, the rhodium concentration at the near surface of the 83-17 and 91-9 catalysts was measured at 17 ± 2 and 11 ± 2 %Rh respectively. The XPS results, therefore, indicated that the near surface concentration of rhodium of the 83-17 catalyst was within experimental error of the bulk composition whilst the concentration of rhodium at the near surface of the 91-9 catalyst was greater than the bulk composition.

The X-Ray radiation used in the experiment was Al Kα ($h\nu$=1486.3 eV). Since the Rh 3p $^3/_2$ and Pt 4p $^3/_2$ levels have binding energies of 498 and 521 eV respectively, the photoelectrons produced from the Rh 3p $^3/_2$ and Pt 4p $^1/_2$ orbitals had a kinetic energy of ca. 1000 eV. From the discussion of the effect of inelastic mean free path on the surface sensitivity of secondary electron techniques, presented

in chapter 4, the contribution to the total signal by the bulk of the sample was estimated at 82% of the total intensity. The remaining of the signal 18%, therefore, originated from the surface monolayer. By assuming the concentration of rhodium below the surface monolayer was equivalent to the bulk concentration, the contribution due to the surface monolayer, and therefore the surface monolayer composition, could be calculated. The surface monolayer Rh concentrations for the 83-17 catalyst is shown below. The error associated with the estimation of surface monlayer concentration was calculated by dividing the standard error of the concentration by the surface sensitivity of the analysis and was ca. ± 10% Rh.

Observed Rh concentration	=	17	%
Observed Rh concentration attributable	=	82% * 17.4	%
to the bulk composition	=	14.3	%
Signal attributable to the surface	=	17-14.3	%
	=	2.7	%

Surface Monolayer concentration

(signal attributable to the surface / surface sensitivity) = 2.7 / 0.18

= <u>15 ± 10 %Rh</u>

The corresponding calculation for the 91-9 catalyst indicated a surface monolayer concentration of 20 ± 10%Rh.

7.3 8 Hour Activation

7.3.1 X-Ray Photoelectron Spectroscopy

Samples of 83-17 and 91-9 catalyst were activated for 8 hours under standard conditions. The top layers of gauze were subsequently characterised by XPS. The XPS spectra obtained from the 83-17 and 91-9 catalysts are shown in figure 7.5.

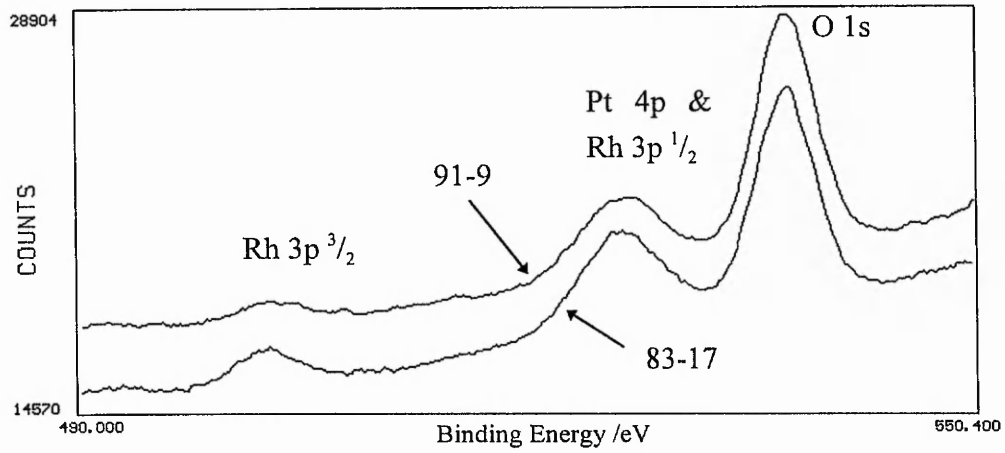

Figure 7.5 : XPS Spectra of the Top Layer of Gauze - 83-17 and 91-9 Samples after 8 hours activation

From interpretation of the relative Rh : Pt XPS peak areas, as discussed in section 4.2, the rhodium concentration at the near surface of the 83-17 and 91-9 catalysts after 8 hours of HCN synthesis was measured at 16 ± 2 and 11 ± 2 %Rh respectively. With reference to the calculation shown in section 7.2.2. the surface monolayer concentration for the 83-17 and 91-9 catalysts was, therefore, measured at 10 ± 10%Rh and 20 ± 10%Rh. Although the error associated with the analysis was large, the result indicated that the surface monolayer Rh concentration of the 83-17 catalyst may have been lower than the surface monolayer Rh concentration of the 91-9 catalyst.

7.4 Fully Activated

Catalyst beds of composition 83-17, 91-9 and 100% Pt were activated for > 30 hours and then removed from the reactor. The samples of catalyst gauze were then characterised by SEM / SAM, XPS and time of flight secondary ion mass spectroscopy (ToFSIMS). The aims of the study were as detailed below -

1. Examine the morphology and near surface composition through a fully activated catalyst bed via SEM / SAM (section 7.4.1).
2. Measure the rhodium and platinum concentration at the near surface of fully activated 83-17 and 91-9 catalysts via SAM (section 7.4.1.2).
3. Examine the spatial distribution of carbon, rhodium, oxygen and platinum at the near surface of an activated catalyst via SAM (section 7.4.1).
4. Measure the rhodium and platinum concentration at the near surface of fully activated 83-17 and 91-9 catalysts via XPS (section 7.4.2).
5. Compare the relative concentration of trace components in the 83-17 and 91-9 catalysts via ToFSIMS (section 7.4.3).
6. Measure the distribution of rhodium concentration with depth via ToFSIMS (section 7.4.3).

7.4.1 Scanning Electron Microscopy / Scanning Auger Microscopy

SEM imaging of the individual layers in the gauze pack was carried out on a fully activated 4 layer thick 91 %Pt - 9 %Rh gauze pack. The resulting SEM images are shown in figures 7.6 to 7.9.

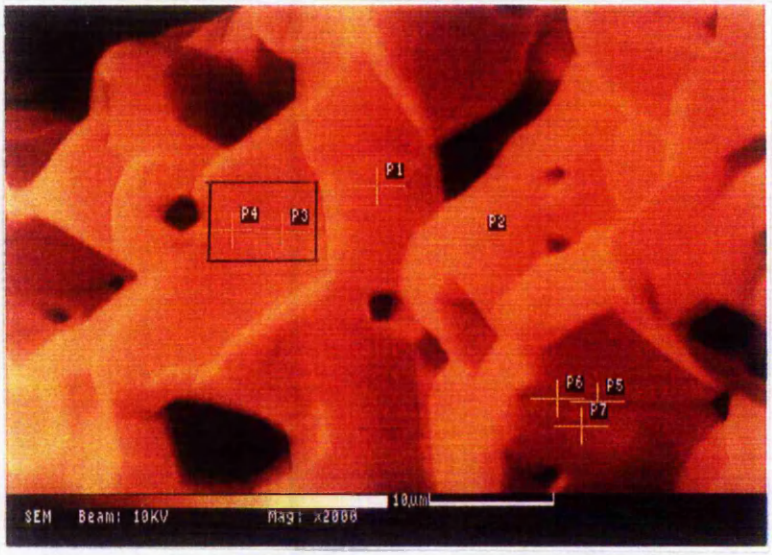

Figure 7.6 : Top Layer of Gauze Taken From a Fully Activated 91-9 Gauze Pack

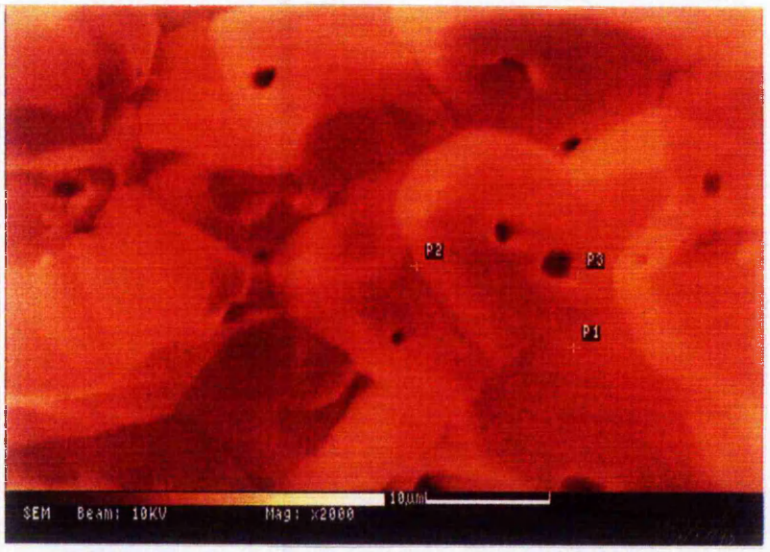

Figure 7.7 : Second Layer of Gauze Taken From a Fully Activated 91-9 Gauze Pack

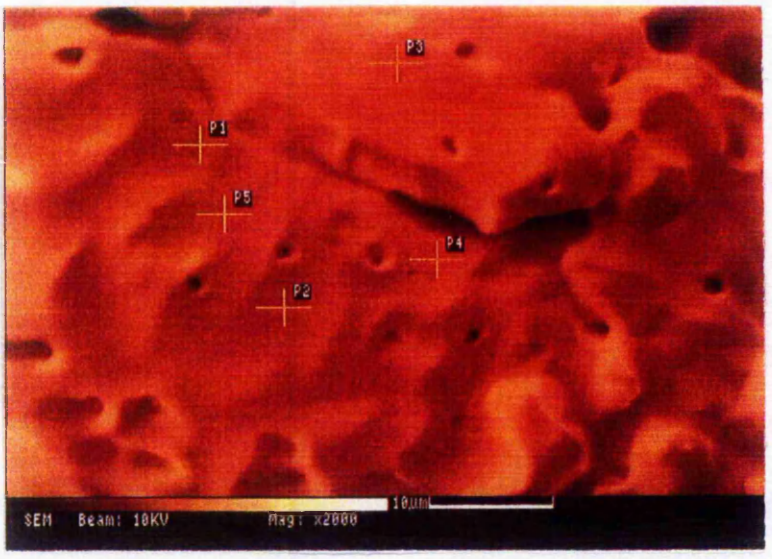

Figure 7.8 : Third Layer of Gauze Taken From a Fully Activated 91-9 Gauze Pack

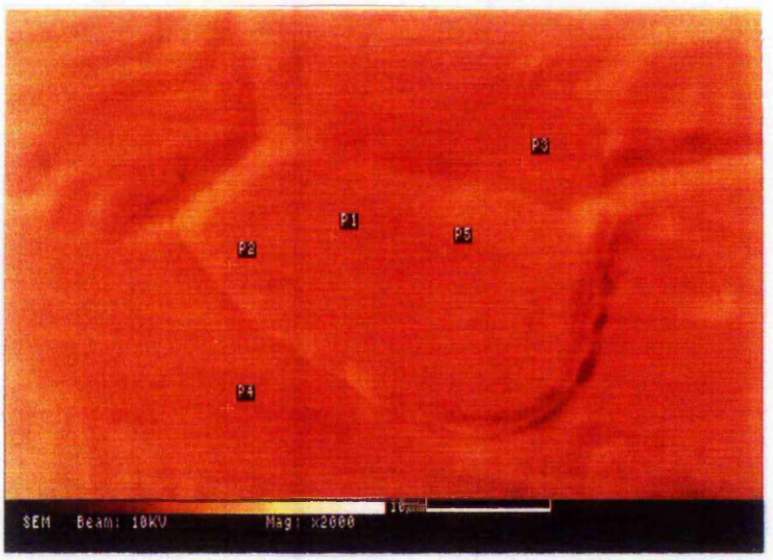

Figure 7.9 : Fourth Layer of Gauze Taken From a Fully Activated 91-9 Gauze Pack

By comparing the SEM image of the top layer (figure 7.6) with SEM images of the subsequent layers of the activated catalyst pack (figures 7.7 to 7.9), the images showed that the top layer of gauze had the greatest degree of regular facet formation and that the bottom gauze had the least degree of regular facet formation. There was, therefore, a change in morphology through the bed. Also apparent from the SEM images was the massive scale of reconstruction at the top layer, seen as a series of pores of up to 5 µm in diameter, which appeared to proceed deep into the bulk of the

catalyst wire. Although the presence of pores was observed at the surface of the second and third gauze samples, the pores were much smaller and the morphology was less regular. The bottom layer of the gauze was only slightly reconstructed. SEM imaging of the 4 gauze layers from an activated 83-17 catalyst pack and an activated 100%Pt catalyst pack revealed a very similar distribution of morphology. The morphology of the activated catalyst gauze was, therefore, typical of activated catalyst samples as presented in chapter 6 and published elsewhere[1], and showed that both the degree of reconstruction and rate of reconstruction was greatest at the gas entry side of the pack.

To investigate the distribution of rhodium concentration with position in the activated catalyst pack, the areas of the 91-9 catalyst gauze shown in figures 7.6 to 7.9 were characterised by point mode Auger electron spectroscopy. The (P-B)/B ratios, are shown in tables 7.5 to 7.8 respectively.

Point Analysis	C (P-B)/B	Rh (P-B)/B	O (P-B)/B	Pt (P-B)/B
P1	0.22	0.05	trace	0.18
P2	0.21	0.05	trace	0.17
P3	0.17	0.04	trace	0.17
P4	0.14	0.06	trace	0.19
P5	0.11	0.07	trace	0.24
P6	0.12	0.08	trace	0.25
P7	0.14	0.07	trace	0.21
Ave.	0.16 ± 0.04	0.06 ± 0.01	N/A	0.20 ± 0.03

Table 7.5: SAM Results - Fully Activated 91-9 Gauze 1 of 4.

Point Analysis	C (P-B)/B	Rh (P-B)/B	O (P-B)/B	Pt (P-B)/B
P1	0.20	0.05	trace	0.18
P2	0.21	0.05	trace	0.17
P3	0.23	0.06	trace	0.20
P4	0.23	0.08	trace	0.18
Ave.	0.21 ± 0.01	0.06 ± 0.01	N/A	0.18 ± 0.01

Table 7.6: SAM Results - Fully Activated 91-9 Gauze 2 of 4.

Point Analysis	C (P-B)/B	Rh (P-B)/B	O (P-B)/B	Pt (P-B)/B
P1	0.10	0.04	trace	0.21
P2	0.12	0.04	trace	0.16
P3	0.09	0.08	trace	0.24
P4	0.11	0.04	trace	0.16
P5	0.11	0.07	trace	0.22
Ave.	0.11 ± 0.01	0.05 ± 0.02	N/A	0.20 ± 0.04

Table 7.7: SAM Results - Fully Activated 91-9 Gauze 3 of 4.

Point Analysis	C (P-B)/B	Rh (P-B)/B	O (P-B)/B	Pt (P-B)/B
P1	0.12	0.04	trace	0.19
P2	0.12	0.04	trace	0.23
P3	0.24	0.03	trace	0.27
P4	0.19	0.05	trace	0.19
P5	0.14	0.06	trace	0.23
Ave.	0.16 ± 0.05	0.04 ± 0.01	N/A	0.22 ± 0.03

Table 7.8: SAM Results - Fully Activated 91-9 Gauze 4 of 4.

The distribution of the carbon, rhodium and platinum (P-B)/B values (from tables 7.5 to 7.8) with the position in the activated 91-9 catalyst pack are shown in figure 7.10. Note that the (P-B)/B values used to generate figure 7.10 were obtained by averaging the values of the relevant point analyses.

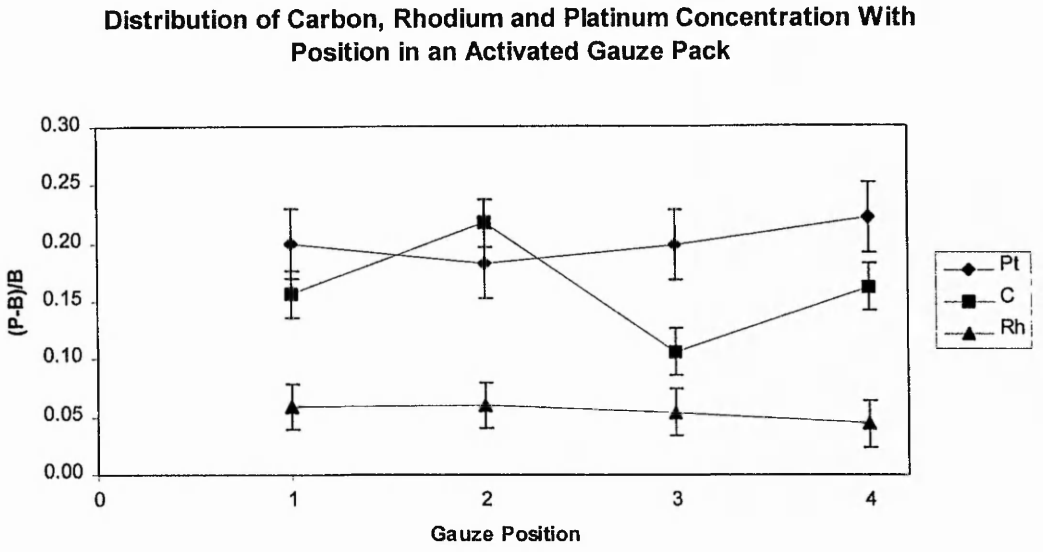

Figure 7.10 : Distribution of Near Surface Concentration With Position in a 91-9 Activated Gauze Pack. The concentration of C, Rh and Pt is expressed by (P-B)/B values.

There was, apparently, no systematic distribution of either rhodium or platinum near surface concentration through the pack. The presence of a significant amount of carbon at the near surface, estimated to vary from sub-monolayer to 2 layers thick[a], may have prevented the measurement of any true variation in near surface concentration with position in the pack. The equal distribution of rhodium and platinum near surface concentration through the gauze bed is, however, similar to the results obtained from an activated 83-17 gauze pack which had been removed from an industrial reactor, the details for which are presented in chapter 6.

From an average value of the Rh (P-B)/B values for gauze layers 1-4 of the 91-9 catalyst, the rhodium near surface concentration was measured at 9.5 ± 3 % whilst the platinum near surface concentration was measured at 80 ± 11 %. Point analyses from the top layer of a fully activated 83-17 catalyst were also obtained by choosing random locations from the corresponding SEM image. The results of interpreting the resulting Auger spectra are shown in table 7.9. Unfortunately, due to a technical fault, the Auger spectra were only obtained from 0 to 600 eV, and as such, no information was obtained about the platinum near surface concentration.

[a] Estimation of carbon layer thickness was achieved by comparison with the results presented in section 6.2.1.2.

Point Analysis	C (P-B)/B	Rh (P-B)/B	O (P-B)/B
P1	0.03	0.09	0.067
P2	0.02	0.07	0.061
P3	0.02	0.08	0.067
P4	0.02	0.08	0.075
P5	0.03	0.09	0.078
P6	0.01	0.10	0.067
P7	0.03	0.06	0.078
Ave.	0.02 ± 0.01	0.08 ± 0.01	0.07 ± 0.01

Table 7.9: SAM Results - Fully Activated 83-17 Catalyst Gauze 1 of 4.

From the results shown in table 7.9 the Rh (P-B)/B was found to be 0.08 ± 0.01. By comparison of the average Rh (P-B)/B value with the calibration standard, the near surface concentration of rhodium was, therefore measured at 14 ± 2 %, a little below the bulk concentration.

To investigate the spatial distribution of composition at the near surface of an activated catalyst sample, the area shown in figure 7.7 was characterised by SAM. The second layer of the 91-9 catalyst pack was chosen in preference to the top layer of the pack as the second layer had undergone less reconstruction, and as such, the SAM images were less likely to be dominated by topographic effects[2]. The (P-B)/B maps obtained for carbon, rhodium, oxygen and platinum are shown in figures 7.11-7.14.

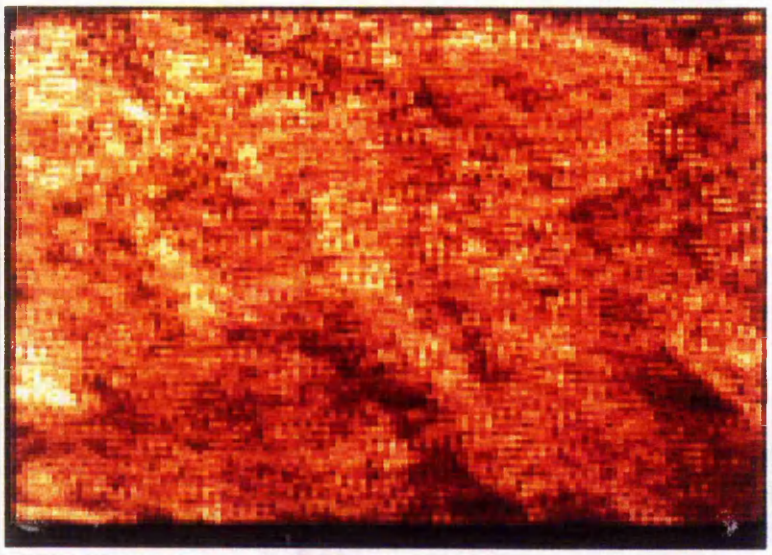

*Figure 7.11 : (P-B)/B Map for Carbon 60*60 μm (X2000)*

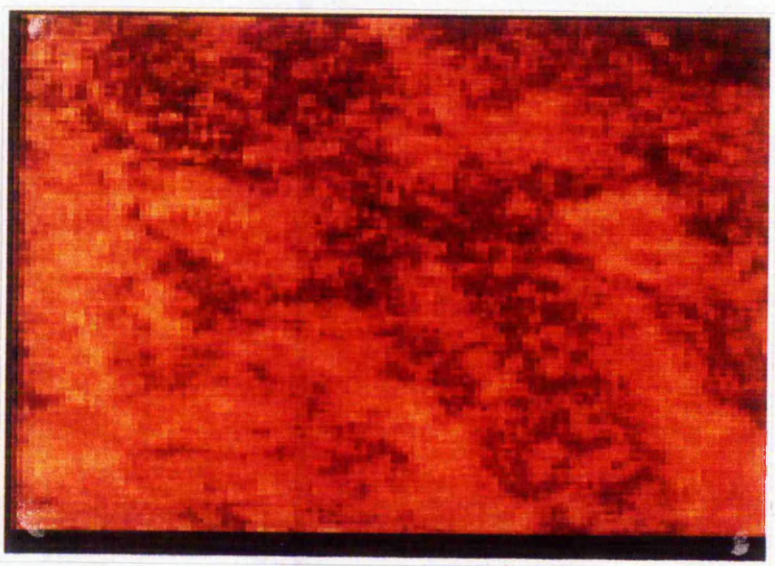

*Figure 7.12 : (P-B)/B Map for Rhodium 60*60 μm (X2000)*

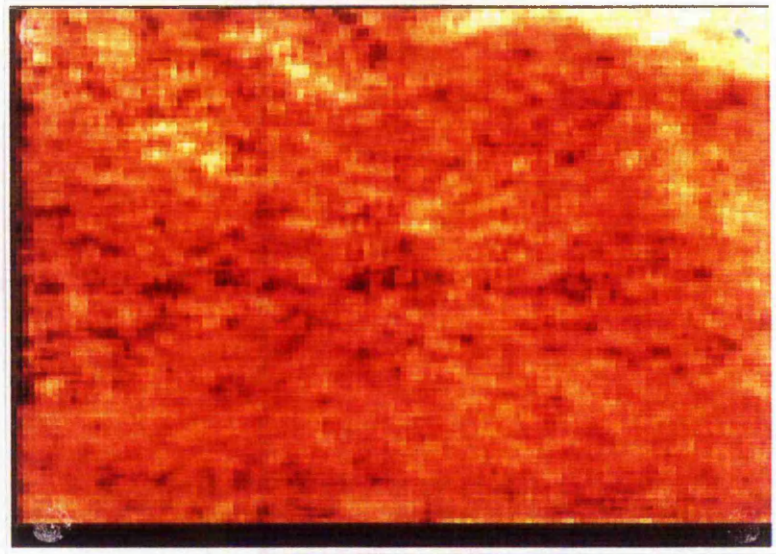

*Figure 7.13 : (P-B)/B Map for Oxygen 60*60 μm (X2000)*

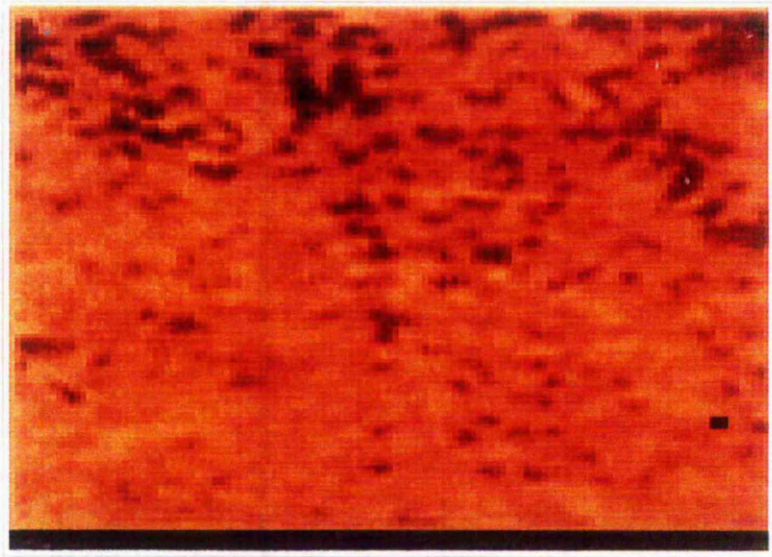

*Figure 7.14 : (P-B)/B Map for Platinum 60*60 μm (X2000)*

From the (P-B)/B images for carbon and rhodium, there were variations in the spatial distribution of (P-B)/B intensity. By comparing the rhodium (P-B)/B image with the carbon (P-B)/B image, a negative correlation was observed i.e. areas of high carbon (P-B)/B were associated with a low rhodium (P-B)/B intensity and visa versa.

The dynamic ranges used to generate the false colour in figures 7.11 and 7.12 were, however, such that a small change in surface composition would appear as a large change in intensity in the image. Since the variation in intensity of the image

was small, the absolute variation in both the C and Rh (P-B)/B intensities was small. The observation of a narrow distribution of both C and Rh (P-B)/B intensities was, however, in agreement with the results obtained by point analysis of the same area of catalyst surface, the results for which are shown in table 7.6.

The Auger (P-B)/B images for oxygen and platinum are shown in figures 7.13 and 7.14. Both the oxygen and platinum (P-B)/B images indicated that the surface was mainly homogeneous but there were distinct areas of non-uniform composition. In particular the region at the top right of the image appeared to be enriched with oxygen and depleted in platinum and rhodium. As for the C and Rh images, the dynamic ranges used to create the 'maps' were small indicating only small changes in (P-B)/B value with location at the surface.

The oxygen and platinum (P-B)/B images indicated that, although areas of the surface appeared to be of non uniform near surface composition, since the dynamic range used to generate the images was small, the absolute variation in (P-B)/B was small and the apparent spatial distribution of near surface concentration may have been due to artefacts of the imaging process due to effects such as changes in angle of incidence[2].

7.4.2 X-Ray Photoelectron Spectroscopy

Samples of fully activated catalyst gauze were characterised by XPS. In each case the sample characterised was the top layer of gauze. The resulting XPS spectra are shown in figure 7.15.

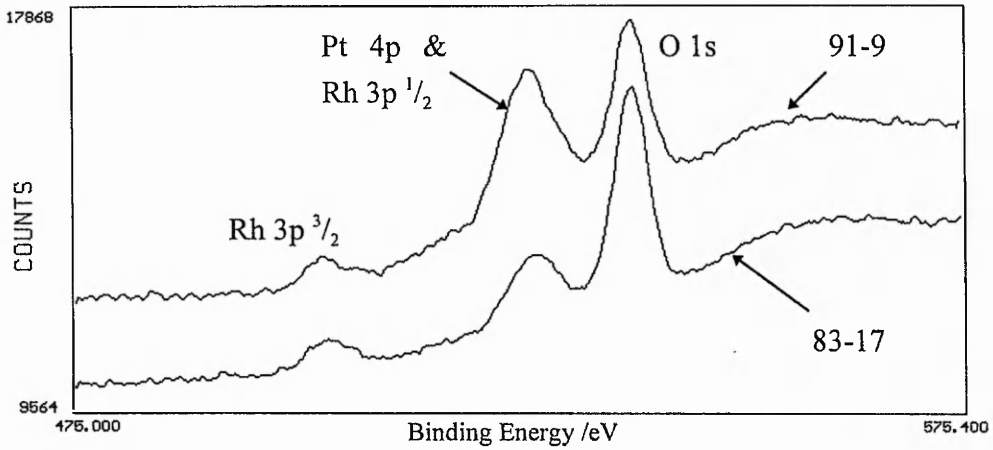

Figure 7.15 : XPS Spectra - Fully Activated 83-17 and 91-9 Catalysts

The peak areas of the Rh 3p $^3/_2$ and Pt 4p XPS peaks, shown in figure 7.15, were measured and the results interpreted according to the method discussed in section 4.2. The results indicated that the near surface concentration of rhodium at the near surface of the 83-17 and 91-9 catalysts was 15.0 ± 2 %Rh and 7.6 ± 2%Rh respectively. Although the deviation of the observed concentration from the bulk concentration was near to the level of experimental error, the results, therefore, indicated that the near surface of both the 83-17 and 91-9 samples may have been platinum enriched.

As discussed in section 7.2.2, the Rh surface monolayer concentration for the 83-17 and 91-9 catalysts was calculated from the near surface concentration. The results of the calculation showed that the surface monolayer Rh concentration for the 87-13 and 91-9 catalysts was 4 ± 10 %Rh and 1 ± 10 %Rh respectively.

7.4.3 Time of Flight Secondary Ion Mass Spectroscopy

7.4.3.1 Static Secondary Ion Mass Spectroscopy

To obtain information about the surface of the activated catalyst samples, the top (gauze 1 of 4) and bottom (gauze 4 of 4) gauze layers of composition 83-17 and 91-9 were admitted into the ToFSIMS instrument. The analysis was performed using a primary source of 8 keV Cs^+ ions which impacted with the surface of the sample in a 100 μm diameter spot size. The total ion dose for the analysis was $3.4*10^{12}$ ions cm^{-2}. Assuming a sputter yield of 10, the analysis, therefore, removed approximately $3.4*10^{13}$ atoms cm^{-2} from the surface of the sample[3]. Assuming a surface density of $1*10^{15}$ atoms cm^{-2}, the analysis removed approximately 3 % of a monolayer in the process of the analysis, indicating that the results were characteristic of the original surface. Since the escape depth of sputtered atoms was approximately 1 nm or 4 monolayers[4] (0.25 nm = 1 monolayer), the surface sensitivity of the analysis by SIMS was, therefore, not dependent on the amount of material removed but on the escape depth of the sputtered atoms. The static SIMS experiment, therefore, provided information about the composition of the first few monolayers of the catalyst surface.

From the study of the 'top' layer of gauze of the 83-17 and 91-9 catalysts Na, Si, Cu, Cl, NCO, F, NO_x and SO_x were detected. A difference between the 83-17 and 91-9 catalysts was that Mg was detected at the surface of the 91-9 catalyst whilst Cu was detected at the surface of the 83-17 catalyst. As these elements did not appear in the Auger spectra of similar samples of gauze, the concentration of these elements was, however, small and may not have been significant. The intensity of Cl containing species was the greatest at the bottom surface where PtCl and RhCl, were evident as well as mixed chloro / cyano species such as $[PtClCN]^-$ (m/z = 256). Also seen at the surface of the samples were several Rh and Pt species such as amines, alkyls and cyano species which have been proposed to be intermediates in the HCN forming reaction[5-6]. A difference between the results obtained from the bottom gauze layer of the 83-17 and 91-9 samples was a greater intensity of Cl containing fragments at the surface of the 91-9 catalyst. For both the 83-17 and 91-9 catalysts, the analysis by static SIMS identified the presence of iron but the intensity of the Fe^+ peak was much reduced in comparison with the intensity observed from the unused catalysts (from results presented in chapter 5). Although the decrease in Fe^+ ion yield may be due to oxidation state effects[7] caused by the reducing environment of HCN synthesis, the possibility of a decrease in iron concentration with use cannot be excluded.

7.4.3.2 Dynamic Secondary Ion Mass Spectroscopy

Dynamic SIMS was performed on activated 91-9 and 83-17 catalysts. The analytical method concentrated on measuring the relative positive ion yield for platinum and rhodium. The results of measuring the Rh / Pt ion ratio with time of sputtering for the 83-17 and 91-9 catalysts are shown in figure 7.16.

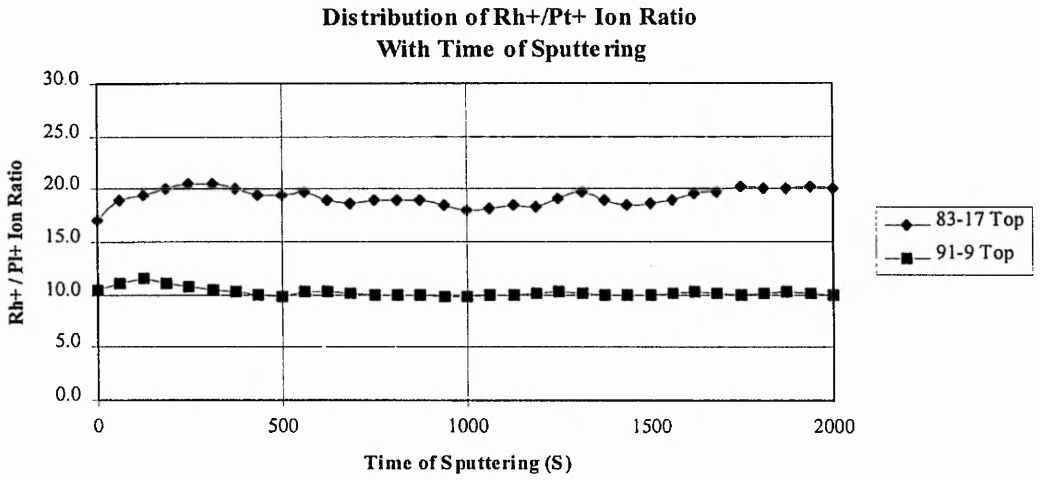

Figure 7.16 : Distribution of Rh^+ / Pt^+ Ion Ratio With Time of Sputtering

From the profiles shown in figure 7.16, the Rh:Pt ion ratio was approximately constant throughout the analysis. Of particular interest is the observation that the Rh:Pt M^+ ion ratio for the 83-17 catalyst, at 20:1, was approximately twice that seen for the 91-9 catalyst, where the Rh:Pt M^+ ion ratio was 10:1. Since the bulk atomic ratio (Pt:Rh) for the 83-17 and 91-9 catalysts was 4.9:1 and 10.1:1 respectively, the M^+ ion ratio was, therefore, in direct relationship with the bulk atomic ratio. Assuming the Rh:Pt ion yield observed at the end of both the 83-17 and 91-9 analyses was representative of the bulk composition, the relative ion yield for rhodium (Rh^+) vs. platinum (Pt^+) could be calculated. The results of the calculation are shown below.

Calculated Rh : Pt Ion Yield - 83-17 Sample

Observed steady-state Rh : Pt Ion yield	=	20
Bulk Rh concentration	=	0.174
Bulk Pt concentration	=	0.826
Atomic ratio (Rh : Pt)	=	0.174 : 0.825
	=	0.21 : 1

$$\text{Relative sensitivity } \left(\frac{Rh/Pt\ Ion\ Yield}{Bulk[Rh/Pt]}\right) = \frac{20}{0.21} = 95$$

The corresponding calculation for the 91-9 catalyst resulted in a relative sensitivity of 100. From the above calculations, the probability of detecting a sputtered rhodium atom as Rh^+ was found to be, on average, ((95+100)/2) 98 times greater than the probability for the same process for platinum. From the relative sensitivity, the Rh : Pt ratio could be estimated as shown below-

$$\text{Atomic ratio Rh:Pt} = \frac{Observed\ Rh/Pt\ SIMS\ Ratio}{Sensitivity}$$

The total ion dose for each experiment was $2.75*10^{14}$ Cs^+ ions. Assuming a surface monolayer concentration of $1*10^{15}$ atoms / cm^2 and a sputter yield of 10 atoms per incident ion, the removed ca. 2.75 monolayers from the surface of the catalyst. The results from estimating depth of analysis from the ion dose and the concentration of rhodium by relative SIMS ion ratios are shown in figure 7.17.

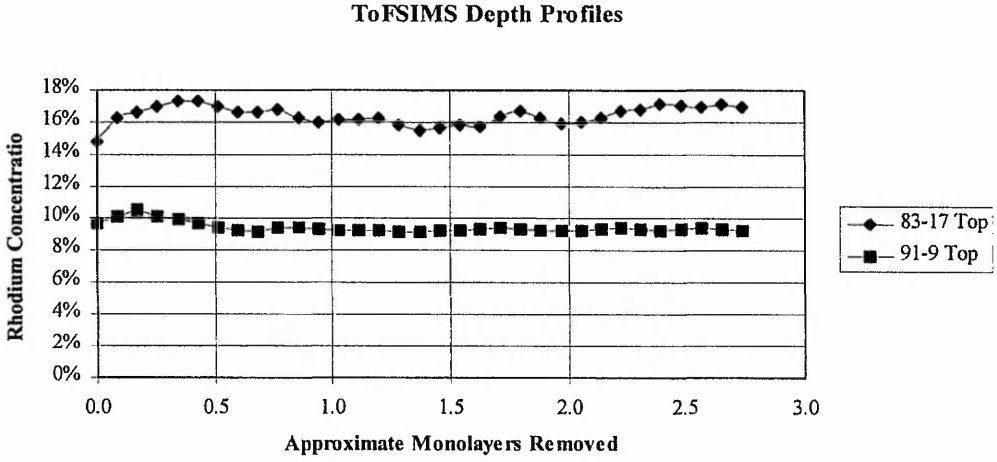

Figure 7.17 : ToFSIMS Depth Profiles - Activated 83-17 and 91-9 Catalysts

From figure 7.17, the Rh distribution of rhodium concentration with depth for both the 83-17 and 91-9 catalysts was seen to be approximately constant. Since the calibration technique relied on the Rh:Pt ratio after the removal of > 2.5 monolayers of material, the analysis indicated that there was, within the surface sensitivity of the ToFSIMS experiment, no inhomogenaety of rhodium concentration with depth.

The general shape of the ToFSIMS depth profiles obtained from the activated gauze sample are further discussed in chapter 8 where the results shown above are compared with the results obtained from the unused catalyst material.

7.5 Conclusions

From the study of the activation process by SEM, AES, XPS and ToFSIMS, the following points were of note.

1. The SEM images of the 83-17, 91-9 and 100%Pt samples after 1 hour HCN synthesis were similar, indicating that the concentration of rhodium had no effect on either the rate of reconstruction or the morphology of the resulting catalyst.

2. The SAM and XPS results were in general agreement in that the activation process resulted in a decrease in the near surface rhodium concentration.

3. The results obtained by XPS for the 83-17 and 91-9 catalysts showed that, despite the 83-17 catalyst having a higher bulk rhodium concentration than the 91-9 catalyst, the surface composition of the catalysts were within experimental error of each other. Figure 7.18 shows how the surface monolayer composition changed with activation time. The graph includes the result obtained from the characterisation of unused catalysts (time=0), the details of which are presented in chapter 5.

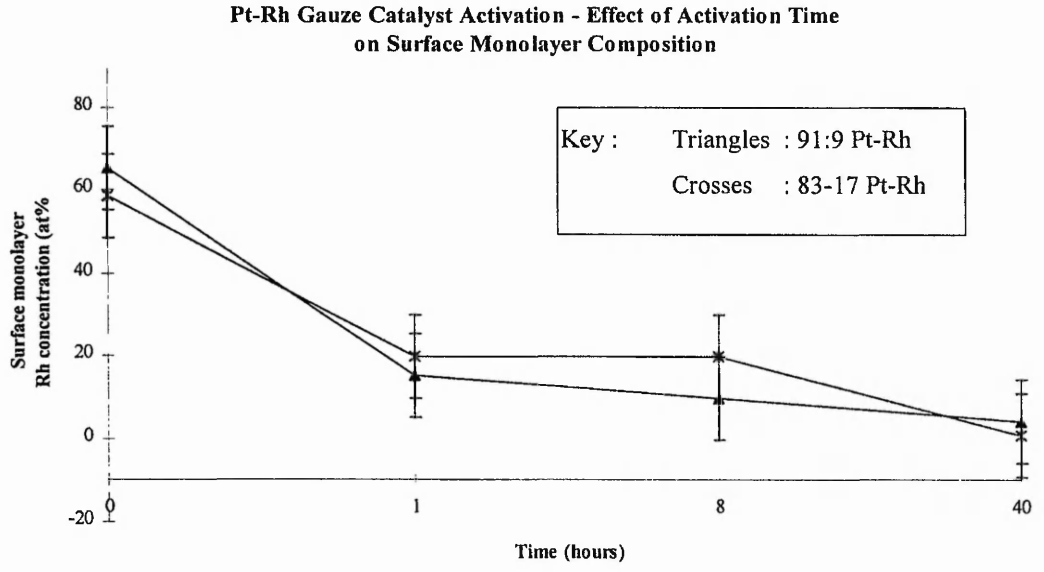

Figure 7.18 : The Effect of Activation Time on Surface Monolayer Composition

4. The SAM imaging process performed on the activated 91-9 catalyst indicated that there was no significant spatial distribution of either platinum or rhodium

near surface concentration. The imaging process was, however, hampered by the extremely rough topography of the sample under study and the presence of a large amount of carbon, both of which may have prevented the observation of any spatial distribution of either platinum or rhodium concentration.

5. The results obtained by ToFSIMS on samples of fully actvated 83-17 and 91-9 catalyst showed that there was no apparent change in the distribution of rhodium with depth.

7.6 References

[1] L.D. Schmidt, D. Luss. J. Catal. **22** 269-279 (1971).

[2] D.R. Batchelor, H.E. Bishop, J.A. Venables. Surface And Interface Analysis **14** 709-716 (1988).

[3] H.H. Anderson, H.L. Bay in Topics in Applied Physics Vol. 47. Sputtering by Particle Bombardment 1. R. Behrisch (Ed.) Springer-Verlag (Pub) Berlin. pp. 186 (1981)

[4] T. Ishitani, R. Shimizu. Phys. Lett. **46A** 487 (1974).

[5] M.L. Wagner, L.D. Schmidt. J. Phys Chem. **99** 805-815 (1995).

[6] D. Jentz, H. Celios, P. Mills, M. Trenary. Surface Science **341** 1-8 (1995).

[7] L.C. Feldman, J.W. Mayer. Fundamentals of Surface And Thin Film Analysis. Pub. North-Holland. pp. 86 (1986).

8. Conclusions

8.1 Effect of Rhodium on Peak Selectivity And Activity

Steady state microreactor studies of a range of fully activated catalysts of composition 0-17.4 at% Rh showed that the catalytic properties of platinum-rhodium alloy gauze catalysts are affected by the presence of rhodium. Under optimum temperature conditions, the pure platinum catalyst exhibited a peak in HCN selectivity from methane at 57%, some 8% higher than any value obtained from the rhodium containing catalysts. Selectivity to HCN from ammonia for the pure platinum catalyst, at 64%, was 12% superior to the platinum-rhodium catalysts where the maximum selectivity was 52%. Methane conversion for the pure platinum catalyst, at a preheat temperature of 550°C, was 99%, which was 3% superior to the conversion for platinum rhodium catalysts. For the pure platinum catalyst, an increase in the furnace temperature from 500°C to 550°C resulted in a decrease in selectivity from methane from 57% to 55%. Methane conversion, however, increased from 96 to 99%, maintaining the HCN yield at 55%, some 10% higher than any value observed for rhodium containing catalysts.

The peak in HCN selectivity from methane and ammonia for the pure platinum catalyst was observed at a preheat temperature of 500°C, corresponding to the lowest temperature at which complete conversion occurred, indicating the possibility of a link between oxygen conversion and selectivity for platinum catalysts. Oxygen conversion for rhodium containing catalysts was, however, always complete under the range of conditions investigated, indicating that the inclusion of rhodium in the catalyst results in a more active catalyst. Higher activity for rhodium containing catalysts is also reported in ammonia oxidation where the addition of rhodium results in a gain in both ammonia conversion and NO_x selectivity[1], and may be due to rhodium having a higher oxygen affinity than platinum.

Under the standard activation conditions used in the laboratory, as discussed in chapter 3, i.e. 4 layers of separated gauze, $CH_4 : NH_3 : O_2 = 1:1:113$, pure platinum catalysts have a much higher *initial* selectivity than rhodium containing catalysts. Selectivity to HCN, after > 30 hours of HCN synthesis was, however, only slightly higher than the initial selectivity. The rhodium containing catalysts exhibited low initial selectivity to HCN, but after the activation period of up to 30 hours, almost matched the selectivity exhibited by the pure platinum catalyst. The 83-17 activated significantly quicker than the 91-9 catalyst. Figure 8.1 shows how the selectivity to HCN changed with time for the 83-17, 91-9 and 100%Pt catalysts. Also included in

figure 8.1 is how the surface monolayer rhodium concentration, measured by XPS, changed with activation time for the top layer of gauze of the 83-17 and 91-9 catalysts.

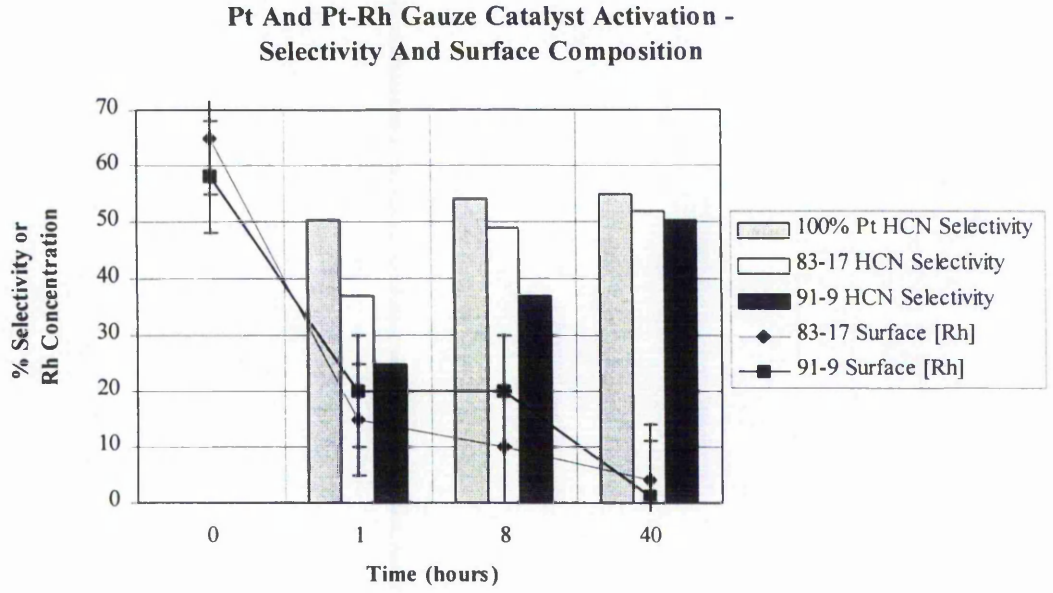

Figure 8.1 : Selectivity And Surface Composition Vs. Activation Time

From figure 8.1, the trend in rhodium surface monolayer concentration with time of activation was from a surface that was enriched with rhodium to a surface that was rhodium depleted. After 40 hours of use, the surface monolayer concentration of rhodium for the 83-17 and 91-9 catalysts was 4 ± 10 and 1 ± 10 at% respectively (i.e. within experimental error of eachother). SEM images taken after 1 hour were very similar showing that the differences in selectivity cannot be ascribed to the catalyst morphology on the micron (1 micron = 10^{-6} m) scale. The possibility of a difference between the samples on the nanometer scale, and thus reactivity, cannot, however, be ignored. Although inconclusive, the combination of selectivity and surface monolayer composition results, therefore, indicate the possibiility of an inverse corellation between surface rhodium cancentration and HCN selectivity.

Dynamic secondary ion mass spectroscopy (dynamic ToFSIMS) was performed on used and unused 83-17 catalyst. The initial ion yields observed during SIMS may, however, be affected by factors such as sputter induced changes in surface composition which may lead to a false indication of changes in composition. Such effects are grouped under the term 'pre-equilibrium factors'. The effects of any pre-equilibrium factors would, however, be similar for like samples. As stated in

chapters 5 and 7, without an exhaustive investigation the best way to evaluate dynamic SIMS depth profiles is to compare like samples. Figure 8.2, therefore, shows a comparison of the ToFSIMS depth profiles obtained from unused and fully activated 83-17 catalyst.

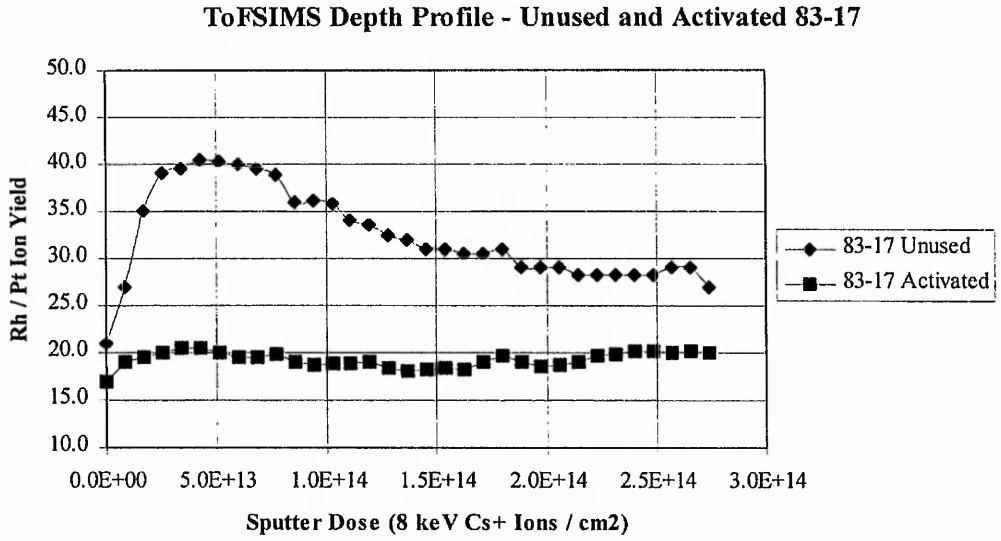

Figure 8.2 : ToFSIMS Depth Profiles - Unused and Activated 83-17

Since the Rh:Pt ion ratio for the unused catalyst was greater than for the activated sample, the results obtained by ToFSIMS of the 83-17 catalyst, therefore, showed an excess of rhodium at the near surface of the unused catalyst in comparison with the used catalyst. The results agree with the results obtained from XPS and SAM in that the near surface concentration of rhodium decreases with use. The reason behind the low initial Rh : Pt ion ratio at the beginning of the depth profile for the unused 83-17 catalyst is, however, unknown but may have been due to contamination of the surface in catalyst preparation and subsequent handling.

The study by microreactor and surface science techniques has, therefore, shown that the addition of rhodium to the gauze is *detrimental* to HCN selectivity. The detrimental effect of high surface rhodium concentrations after gauze fabrication is, however, *reduced* by the activation process which results in a large decrease in surface monolayer rhodium concentration. The addition of rhodium to gauze catalysts is predominantly to increase its strength and it is doubtful that pure platinum gauze catalysts would have the necessary mechanical strength.

Surface segregation in Pt-Rh alloys has been extensively studied and the overwhelming body of evidence points to rhodium surface segregation under oxidising conditions[2] and where the presence of other components such as carbon[3] and sulphur[4] have been detected at the surface. The atomically clean surface under UHV conditions is, however, invariably seen to be platinum enriched[5-6], with published heats of segregation ranging between 6 and 15 kJ mol^{-1} at 1100K. The driving force behind surface segregation of platinum is thought to be the difference in surface vibrational entropy between platinum and rhodium[7] which equals 11 J mol^{-1} K^{-1}. Figure 8.2 shows the bulk-surface isotherm for surface segregation in a platinum-rhodium alloy at 1100K assuming a heat of platinum surface segregation of (i) 6 kJ mol^{-1} and (ii) 15 kJ mol^{-1}.

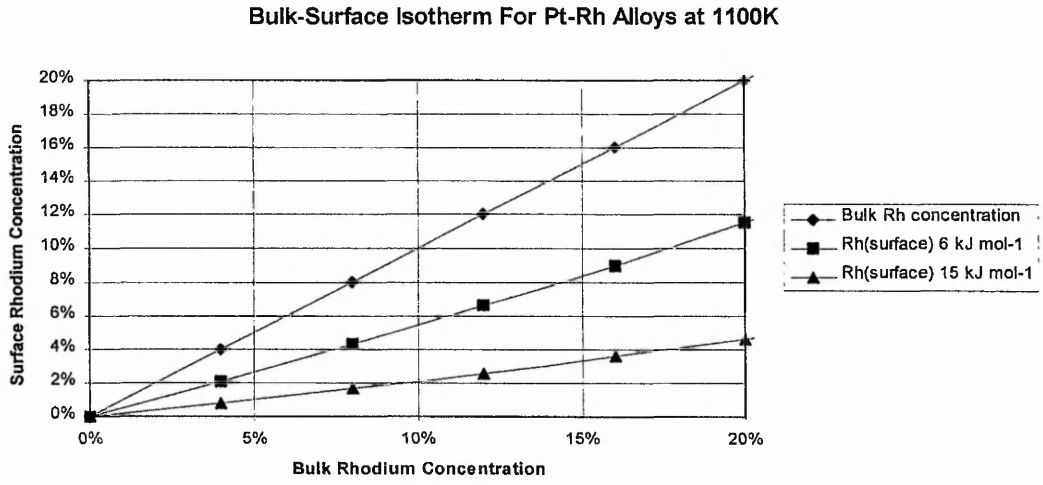

Figure 8.3 : Bulk-Surface Isotherm For Pt-Rh Alloys

For a clean surface of an 83-17 alloy, the published heats of segregation, therefore, predict that the surface monolayer would be between 4 and 10% Rh. For the 91-9 surface the theory predicts a rhodium concentration of between 2 and 5%. After extensive activation under HCN synthesis conditions, the surface monolayer Rh concentration for the top layers of the 83-17 and 91-9 catalysts were found to be 4 ± 10 %Rh and 1 ± 10 %Rh respectively. The rhodium surface monolayer concentrations for the top layers of gauze, measured by XPS, were, therefore, within experimental error of literature values published for atomically clean equilibrated surfaces. In the presence of an oxidising atmosphere, the gauze surface would be rhodium rich. The rhodium concentration at the near surface of fully activated catalysts was below the bulk concentration irrespective of position in the pack. All

the surfaces within the pack were, therefore, exposed to a reducing environment, caused by the fuel rich feed gas.

At a temperature of $\geq {}^{1}/_{2}$ the melting point, bulk-surface diffusion occurs readily in most metals. Since the melting point of platinum and rhodium is less than 2300 K equilibration of the bulk-surface equilibration occurs readily at $\geq$ 1150 K. Most surface segregation measurements are made after < 1 hour of annealing[5], which is considered sufficient to bring the surface into thermodynamic equilibrium. Since the Pt-Rh catalysts reacting under HCN synthesis conditions were operating at > 1150 K and required many hours of activation to reach an equilibrium surface composition the activation results were, therefore, different to that expected for pure alloys. Although surface composition may, to some degree, be controlled by changes in the crystal faces exposed[8], the effect is small and unlikely to have been significant. SAM of the unused 83-17 and 91-9 catalysts showed that oxygen was removed from the surface after 1 hour of HCN synthesis, an observation that was correlated with a rapid decrease in rhodium near-surface concentration. The combination of AES and XPS, therefore, showed that in the preparation of the gauze, surface oxidation had occurred and was the cause of a high rhodium surface concentration. As carbon is present at the surface and is known to promote the surface segregation in platinum-rhodium alloys, the role of carbon in the activation process cannot, however be ignored.

A decrease in the concentration of rhodium would result in a decrease in the equilibrium surface monolayer concentration of rhodium. The catalyst may, therefore, have a superior selectivity to HCN.

8.2 Deactivation

SAM studies of the industrial catalyst gauze showed the presence of areas of carbon formation of up to 3 monolayers thick. Possible explanations for carbon laydown include poor mixing or distribution of the feed gases, but a further possibility is the use of unrefined natural gas which contains higher hydrocarbons. which are proposed to promote carbon laydown[9].

8.3 Future Work

8.3.1 Effect of Rhhodium Concentration on Activation and Peak Selectivity

Although the work presented here adds to knowledge on the activation behaviour of Pt-Rh alloys, the unexplained behaviour undoubtedly requires further attention and the acquisition of a larger variety of Pt-Rh samples, complete with elemental analyses of trace component impurities, may give a better understanding as to the role of contaminants such as iron.

Rhodium is added as an alloying agent to strengthen the catalyst and undoubtedly reduces the selectivity to HCN. The mechanical strength of pure platinum is, however, such that pure platinum catalysts may disintegrate during use if not carefully supported from below. A possibility of increasing the selectivity to HCN is by utilising the selectivity of the pure platinum catalyst with the strength of a platinum-rhodium catalyst in a mixed bed whereby the pure platinum catalyst sits on top of the platinum-rhodium catalyst. Restructuring associated with catalyst activation would result in the layers fusing together. The platinum-rhodium catalyst would, therefore, form an intimate support for the pure platinum layer. A further possibility is to use gauze catalysts with a reduced rhodium concentration - for example 2.5, 5 and 7.5 at%Rh which, provided the mechanical strength is sufficient, may prove a viable alternative to catalysts with 9-17 at%Rh.

8.3.2 Catalyst Oxidation

Fully activated catalysts exhibit a platinum rich surface which may be oxidised to form a rhodium rich surface. By characterising the oxidised catalyst and then returning the catalyst to HCN synthesis conditions, information about the effect of catalyst oxidation on activation may be gained. A rapid recovery to high HCN

selectivity and low surface rhodium concentration would indicate that the initial activation process was governed by the presence of a 'contaminant' which had been removed by the activation process. A slow recovery to high HCN selectivity, equivalent to the original activation profile, would indicate that the activation process was governed by an intrinsic property of the catalyst.

8.3.3 Pre-Reduction

A high surface concentration of rhodium has a detrimental effect on HCN synthesis selectivity. Off line reduction of catalysts by H_2 at a temperature sufficient to allow diffusion of platinum to the surface would result in a catalyst that has a low rhodium surface concentration. The pre-treated catalyst may than exhibit a high initial selectivity, effectively bypassing the activation process.

Characterisation

Characterisation of platinum-rhodium catalysts by XPS using Al K_α *(hV=1486.3)* resulted in an electron energy of ca. 1000 eV, and thus a monolayer surface sensitivity of 18%. A monochromated X-ray source may, however, be tuned to an energy (600 eV) such that the kinetic energy of the emerging photoelectrons would be ca. 100 eV, and as such, perform a much more surface sensitive experiment. This would result in a large decrease in the standard error associated with the analysis. An alternative technique to measure the surface composition is ion scattering spectroscopy (ISS) as the technique is uniquely surface sensitive.

8.4 References

[1] C.N. Satterfield '*Heterogeneous Catalysis in Practice*' McGraw-Hill, New York pp. 214-221 (1980).

[2] J.P. Contour, G. Mouvier, M. Hoogewys, C. Leclere. J. Catal. **48** 217-228 (1977).

[3] F.C.M.J.M. van Delft, A.D. van Langeveld, B.E. Nieuwenhuys. Surface Science **189/190** 1129-1134 (1987).

[4] M. Ahmad, T.T. Tsong. Surface Science **149** L7-L12 (1985).

[5] P.A. Dowben, A. Miller. CRC Press pp. 408-409 and references within. (1990).

[6] P.T. Wouda, B.E. Niewenhuys, M. Schmid, P. Varga. Surface Science **359** 17-22 (1996).

[7] A.D. van Langenveld, J.W. Niemantsverdriet. J. Vac. Sci. Technol. A **5** (4) 558-561 Jul/Aug (1987).

[8] J. Florencio, D.M. Ren, Tien T. Song. Surface Science **345** L29-L33 (1996).

[9] S.S. Bharadwaj, L.D. Schmidt. Ind. End. Chem. Res. **35** pp. 152-1533 (1996).

9. Appendices

9.1 Appendix 1. Example G.C. Traces

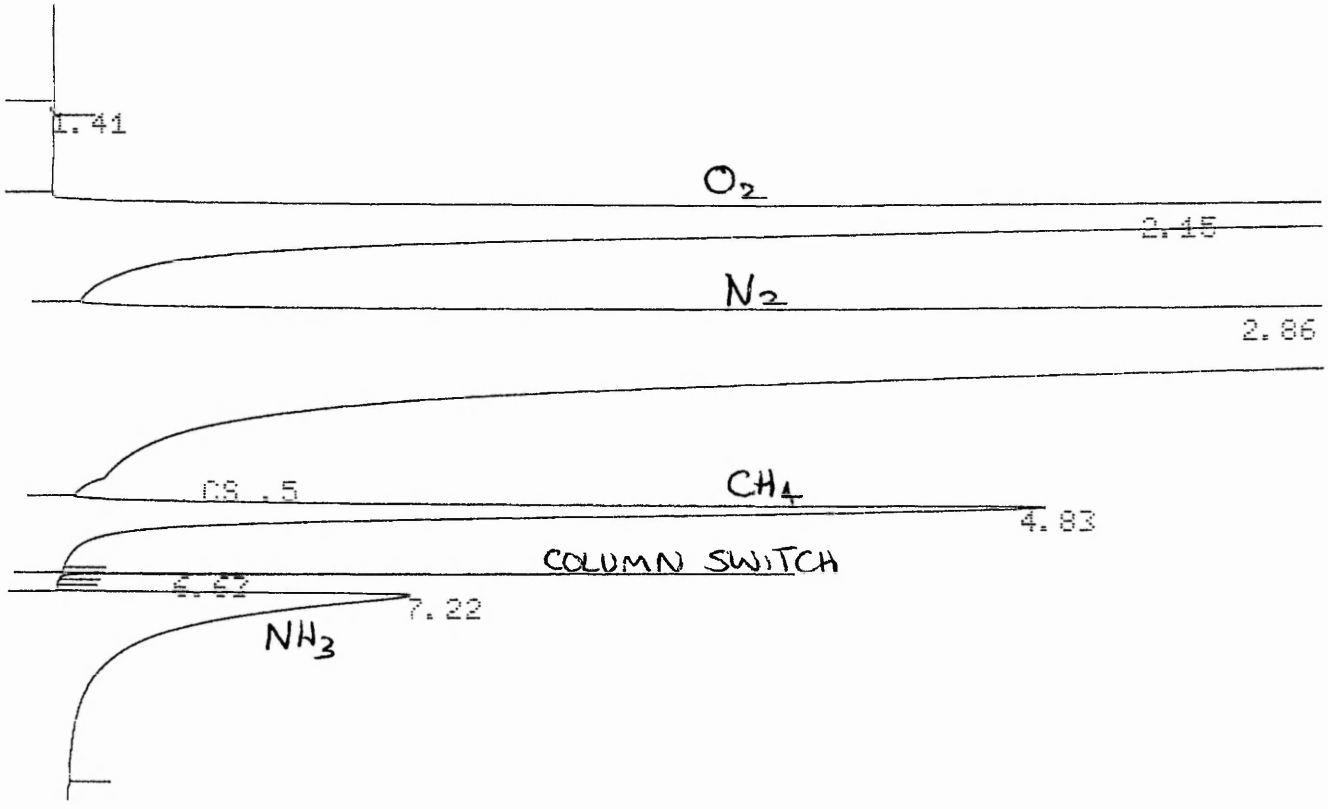

9.1.1 Feed Gas Analysis

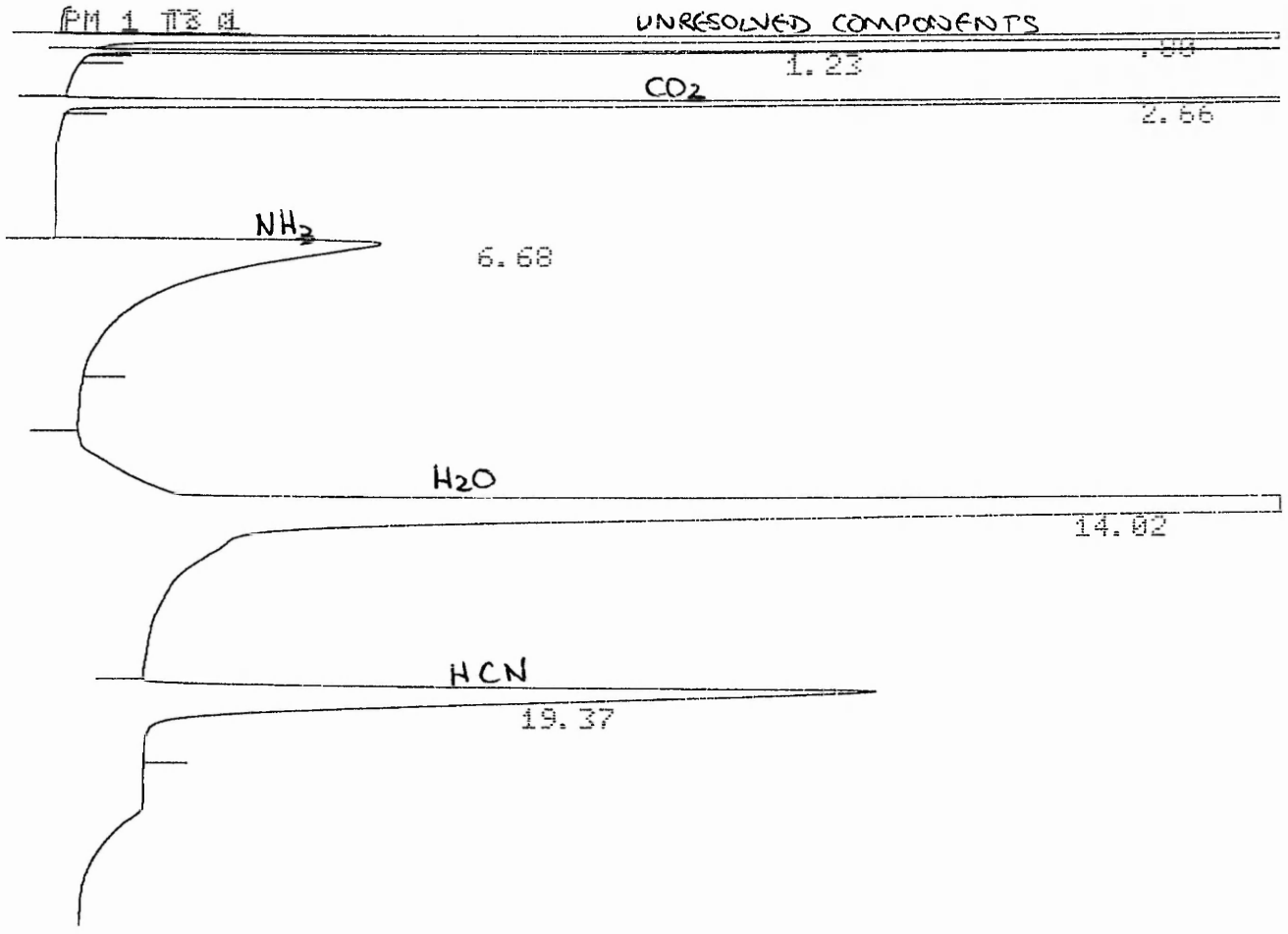

9.1.2 CO_2 / Product Analysis

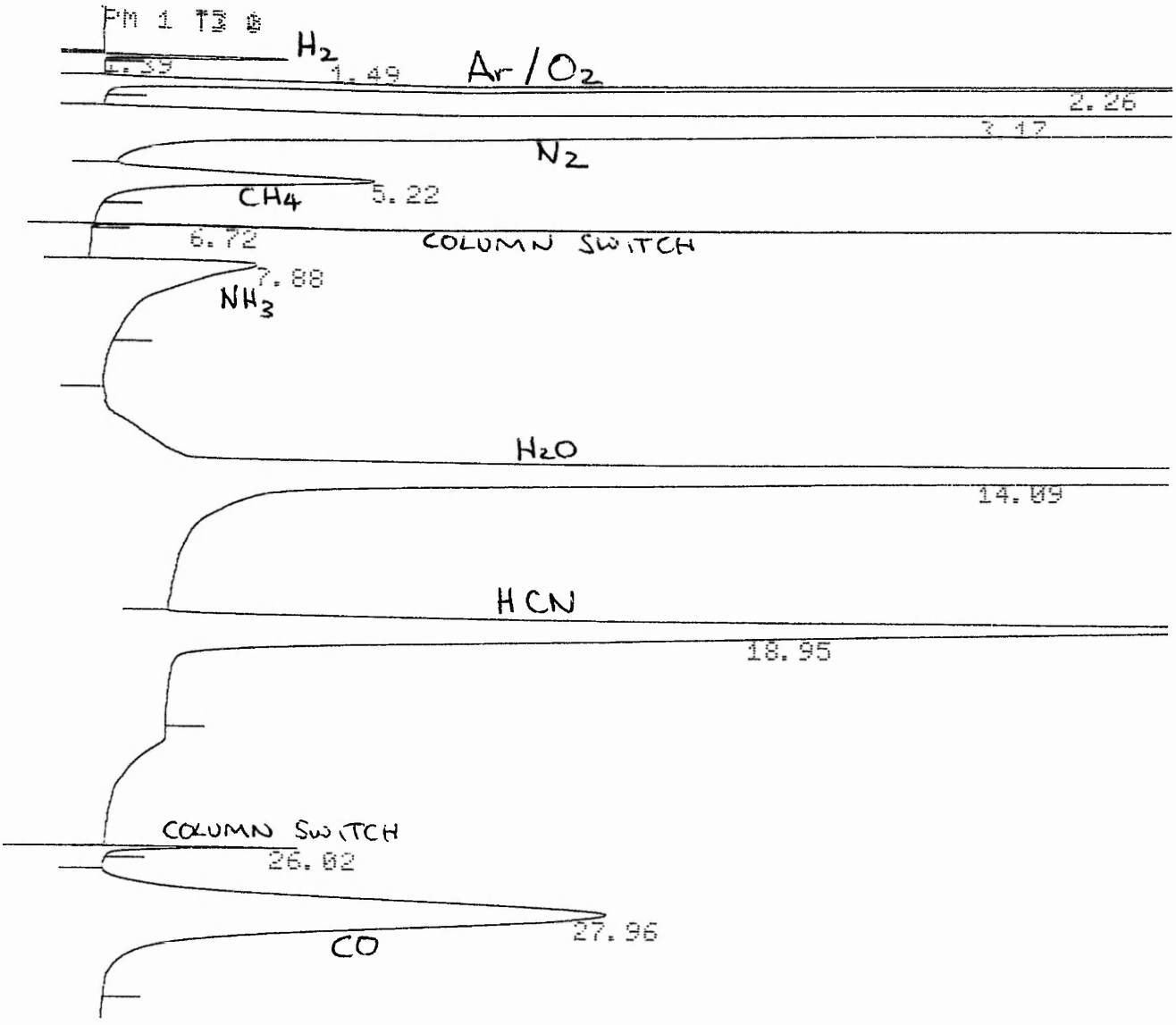

9.1.3 Standard Product Analysis

9.2 Appendix 2 G.C. Calibration Curves

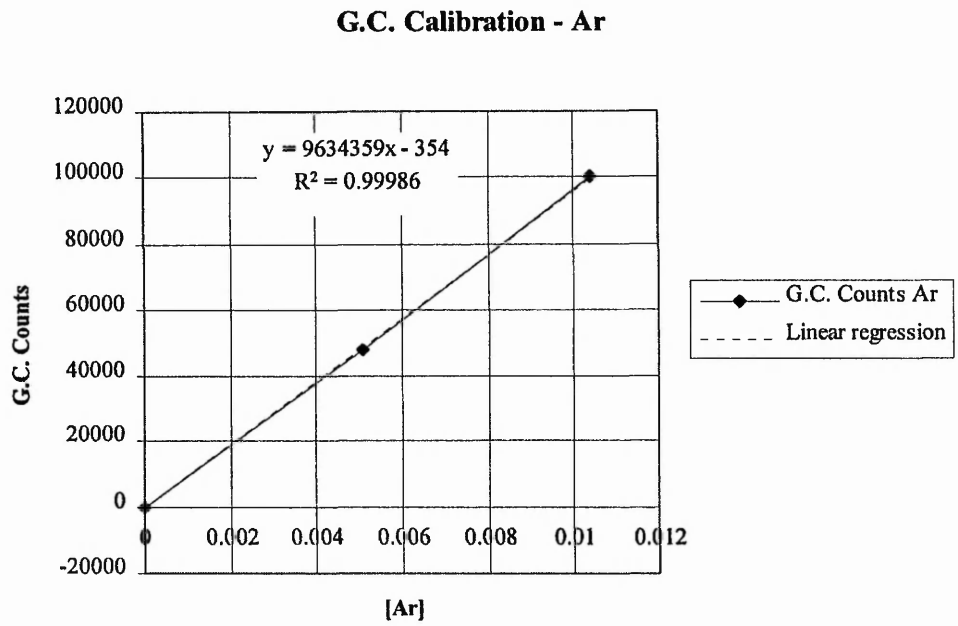

9.2.1 Argon Calibration

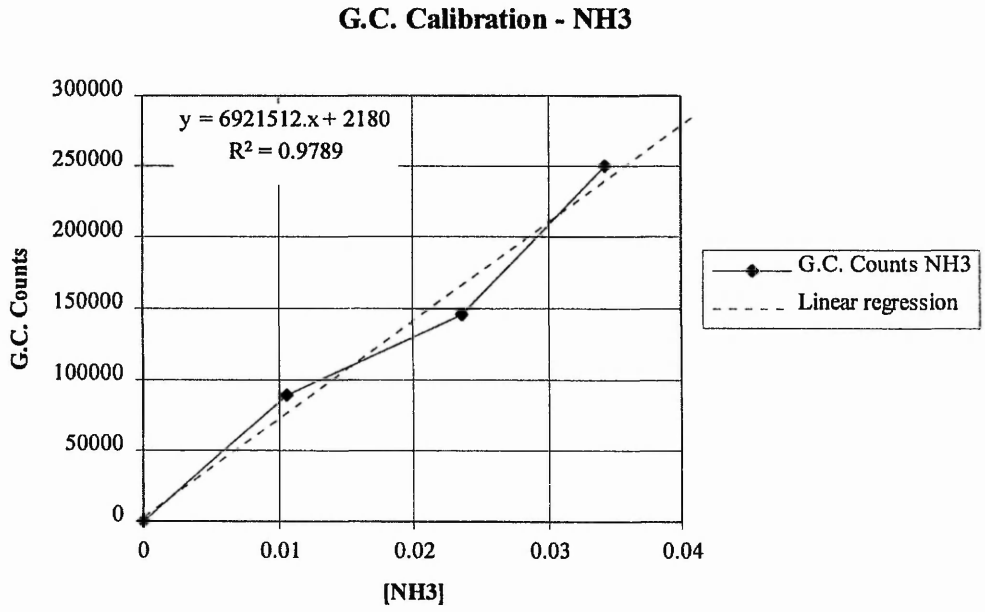

9.2.2 Ammonia Calibration

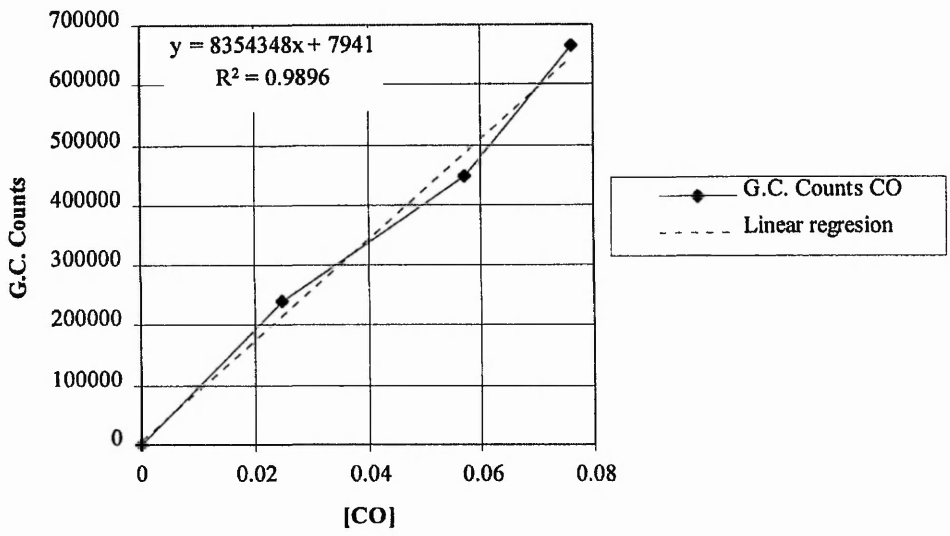

9.2.3 Carbon Monoxide Calibration

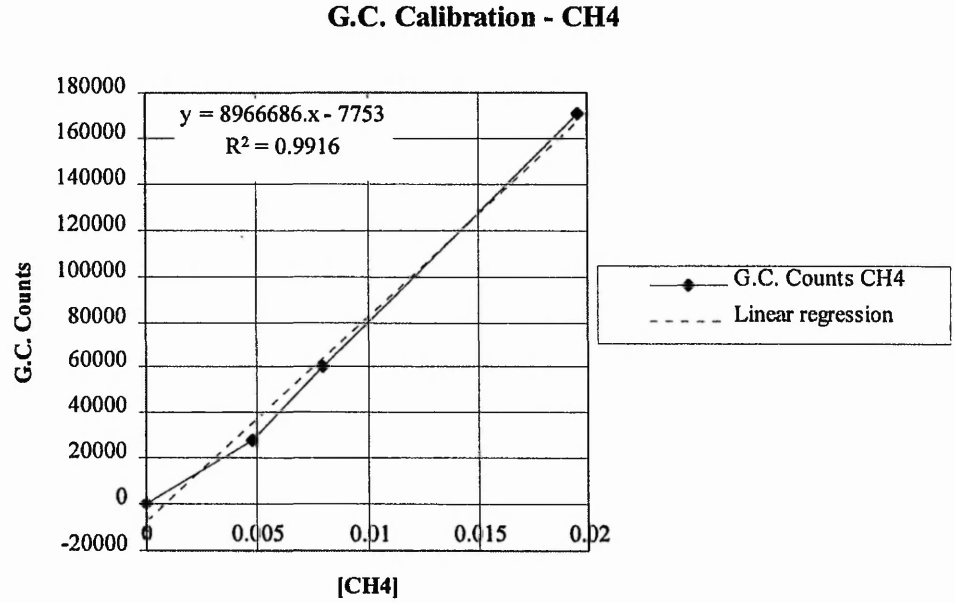

9.2.4 Methane Calibration

9.3 Appendix 3 - Mass and Heat Balance Calculations

9.3.1 83-17 Catalyst After 30 Minutes Activation

Product Distribution : 4 Layers of 83-17 (Woven) after 34 Minutes of Activation

Feed : From 100 moles feed

13.0	Methane
13.0	Ammonia
14.8	Oxygen
59.2	Nitrogen
100.0	

Expansion 1.097

Feed Eq. 100 moles in

11.9	Carbon	(C)
83.0	Hydrogen	(H)
27.0	Oxygen	(O)
107.9	Nitrogen	(N) From Air
11.9	Nitrogen	(N) From NH3

Products	Fraction	Content H	Content O	Content C	Content N	Moles Out Per Mole CH4		Exother	Total
H2		29.83	0.00	0.00	0.0	H2	1.2585		
H2O		38.88	19.44	0.00	0.0	H2O	1.6406	-241.80	-396.71
CH4	0.010	4.04	0.00	1.01	0.0	CH4	0.0852		
CO	0.063	0.00	6.34	6.34	0.0	CO	0.5350	-35.80	-19.15
CO2	0.006	0.00	1.20	0.60	0.0	CO2	0.0506	-318.80	-16.14
HCN	0.039	3.90	0.00	3.90	3.9	HCN	0.3291	252.60	83.13
NH3	0.021	6.30	0.00	0.00	2.1	NH3	0.1772		
O2	0.000	0.00	0.00	0.00	0.0	O2	0.0000		
N2		0.00	0.00	0.00	103.4	N2	4.3624		
TOTAL	1.000	82.95	26.98	11.85	109.4	Carbon	1.0000		
						Feed NH	1.00		
		Total Moles Of NH3 --> HCN		+	Unreacted NH3 =		0.51		
					Therefore Decomposed =			45.98	22.70

-326.17 KjMol-1

Shaded boxes = calculated figures via mass balance.

9.3.2 83-17 Catalyst After 1000 Minutes Activation

Product Distribution : 4 Layers of 83-17 (Woven) after 1000 Minutes of Activation

Feed : From 100 moles feed

13.0	Methane
13.0	Ammonia
14.8	Oxygen
59.2	Nitrogen
100.0	

Expansion 1.096

Feed Eq. 100 moles in

11.9	Carbon	(C)
83.0	Hydrogen	(H)
27.0	Oxygen	(O)
108.0	Nitrogen	(N) From Air
11.9	Nitrogen	(N) From NH3

Products	Fraction	Content H	Content O	Content C	Content N	Moles Out Per Mole CH4		Exother	Total
H2		27.23	0.00	0.00	0.0	H2	1.1480		
H2O		42.39	21.19	0.00	0.0	H2O	1.7870	-241.80	-432.11
CH4	0.008	3.36	0.00	0.84	0.0	CH4	0.0708		
CO	0.050	0.00	5.03	5.03	0.0	CO	0.4241	-35.80	-15.18
CO2	0.004	0.00	0.78	0.39	0.0	CO2	0.0329	-318.80	-10.48
HCN	0.056	5.60	0.00	5.60	5.6	HCN	0.4722	252.60	119.27
NH3	0.015	4.44	0.00	0.00	1.5	NH3	0.1248		
O2	0.000	0.00	0.00	0.00	0.0	O2	0.0000		
N2		0.00	0.00	0.00	103.7	N2	4.3718		
TOTAL	1.000	83.02	27.00	11.86	110.8	Carbon	1.0000		
						Feed NH	1.00		
					Total Moles Of NH3 --> HCN +	Unreacted NH3 =	0.60		
						Therefore Decomposed =		45.98	18.53

-319.97 KjMol-1

Shaded boxes = calculated figures via mass balance.

9.3.3 100% Platinum Catalyst After 1100 Minutes Activation

Product Distribution : 4 Layers of 100%Pt (Woven) after 1133 Minutes of Activation

Feed : From 100 moles feed Expansion 1.089

13.0	Methane
13.0	Ammonia
14.8	Oxygen
59.2	Nitrogen
100.0	

Feed Eq. 100 moles in

11.9	Carbon	(C)
83.6	Hydrogen	(H)
27.2	Oxygen	(O)
108.7	Nitrogen	(N) From Air
11.9	Nitrogen	(N) From NH3

Products	Fraction	Content H	O	C	N	Moles Out Per Mole CH4		Exother	Total
H2		22.79	0.00	0.00	0.0	H2	0.9542		
H2O		43.53	21.77	0.00	0.0	H2O	1.8230	-241.80	-440.80
CH4	0.014	5.40	0.00	1.35	0.0	CH4	0.1131		
CO	0.044	0.00	4.40	4.40	0.0	CO	0.3685	-35.80	-13.19
CO2	0.004	0.00	0.78	0.39	0.0	CO2	0.0327	-318.80	-10.41
HCN	0.058	5.80	0.00	5.80	5.8	HCN	0.4858	252.60	122.70
NH3	0.020	6.06	0.00	0.00	2.0	NH3	0.1692		
O2	0.001	0.00	0.24	0.00	0.0	O2	0.0101		
N2		0.00	0.00	0.00	105.5	N2	4.4188		
TOTAL	1.000	83.58	27.19	11.94	113.3	Carbon	1.0000		
						Feed NH	1.00		
		Total Moles Of NH3 --> HCN		+	Unreacted NH3 =		0.65		
					Therefore Decomposed =			45.98	15.87

-325.83 KjMol-1

Shaded boxes = calculated figures via mass balance.

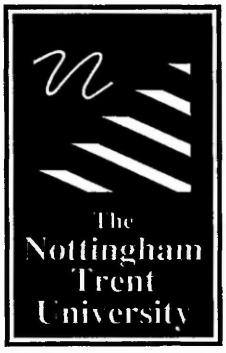

Libraries &
Learning
Resources

The Boots Library: 0115 848 6343
Clifton Campus Library: 0115 848 6612
Brackenhurst Library: 01636 817049